UNIVERSITÀ
DI TRENTO

X-ray induced temperature dependent amorphous-amorphous transitions in the GeO_2 glass

Fabio Brugnara

Department of Physics, University of Trento

Doctoral School in Physics

XXXVIII Cycle

Supervisor	Prof. Marco Zanatta
Co-supervisor	Prof. Giacomo Baldi
Committee members	Prof. Sebastiano Mariazzi
	Prof. Giulio Monaco
	Prof. Eloi Pineda Soler

June 11th, 2026

Acknowledgments

Vorrei dedicare questo spazio a tutti coloro che mi hanno seguito in questo percorso, che si conclude con la stesura di questa tesi. Ma un viaggio così, non si riassume in una tesi.

Grazie prima di tutto a Marco e a Giacomo, che mi hanno seguito e sopportato in tutti questi anni, dandomi un sacco di idee per andare avanti, cercare cose, letture da cui studiare, corretto cose, e molto altro. Grazie anche a Flavio, troppo divertente lavorare con te, peccato che è un po che non lo facciamo più. Goditi la pensione. Voglio soprattutto ringraziare i miei amici-colleghi di dottorato, Ziglio, Denis, Irene, AG, ed Erica, con cui insieme, oltre che lavorare e passare le notti nei beamtime a impazzire, ne abbiamo fatte di cose belle.

Ringrazio la famiglia come si fa sempre un po' istituzionalmente. Ma in realtà se lo meritano anche. Grazie mamma e papa, che mi avete sopportato quando compaio a salutarvi (e a mangiare) a orari improponibili. E grazie ancora papa per insegnarmi nuove cose a 62 anni, anche se non propriamente favorevoli all'università. Grazie mille alla mia vicina di casa, nonna Luciana, per la super compagnia e probabilmente gli oltre 500 caffè di questi ultimi anni. Grazie zia per i consigli davanti ai tanti caffè, i piatti e la verdura. E grazie nonna Concetta, anche se ci vediamo meno ora, non mi dimentico le mille cose che abbiamo fatto inseme.

E infine, GRAZIE VERAMENTE A TUTTI GLI AMICI che mi sono stati vicini in questi ultimi anni: quelli che ci sono oggi, quelli nuovi, quelli vecchi, quelli che non vedo da un po e non vedo l'ora di rivedere, e quello che non c'è più. Ora, sapete che sono sfaticato, e che mi dimentico i nomi. E quindi, sicuro non mi metto a dire qualcosa a uno per uno. Però, anche se ci metto meno righe, questi non-ringraziamenti sono i più importanti. E queste non-identificate persone, sono o sono state, le più importanti nella mia vita, o almeno quelle che hanno creato più felicità in questi anni (dopo le sbronze, le placche poggiate e le termiche).

Grazie

Introduction

Glasses can be regarded as liquids that have fallen out of equilibrium: upon cooling, the rapid increase in viscosity progressively slows structural rearrangements until the system becomes kinetically arrested in a disordered, liquid-like, configuration. As a consequence, glasses are intrinsically non-ergodic systems, and their properties depend not only on thermodynamic variables but also on their thermal and mechanical history.

Despite their apparent rigidity, atoms in glasses are not completely arrested. Even below the glass transition temperature, they can undergo structural rearrangements, especially when subjected to external perturbations. Among these, interaction with radiation plays a particularly relevant role in this thesis. The absorption of energetic particles or photons can induce local excitations, bond breaking, and defect formation, leading to modifications of the glass structure. In glasses, irradiation effects have long been investigated in terms of local defects, densification, and modification of the absorption spectrum, motivated by studies in the context of nuclear waste vitrification and radiation-resistant materials.

More recently, starting with the first work of Ruta *et al.* (2017), a different perspective has emerged with the observation that intense X-ray beams can directly induce atomic dynamics in glasses, even far below the glass transition temperature. It was shown that the high flux and tight focusing available at modern third- and fourth-generation synchrotron sources can trigger beam-induced dynamics in both chalcogenide and oxide glasses. This dynamics, revealed by X-ray photon correlation spectroscopy, does not probe intrinsic relaxation processes but reflects the response of the material to irradiation. At the same time, structural modifications related to a decrease in medium-range order have been reported, demonstrating the close coupling between radiation-induced dynamics and structural evolution. These observations raise fundamental questions regarding the microscopic mechanisms involved, their dependence on temperature, and their generality across different glassy systems.

This thesis is motivated by these observations and focuses on the response of vitreous germanium dioxide (v-GeO_2), a prototypical strong oxide glass, to intense X-ray irradiation. To address this problem, we employ a combination of complementary experimental techniques to probe both structure and dynamics over a broad range of length and time scales. X-ray photon correlation spectroscopy

(XPCS) probes the temporal evolution of speckle patterns generated by coherent scattering, providing access to the intermediate scattering function $F(Q,t)$ and thus to slow dynamics on timescales ranging from milliseconds to hours. X-ray diffraction (XRD) yields information on the static structure factor $S(Q)$, and in particular on medium-range order and density fluctuations through the low-Q limit. Inelastic X-ray scattering (IXS) at small angles provides access to the dynamic structure factor $S(Q,\omega)$, enabling the investigation of vibrational dynamics in the terahertz regime. The combination of these techniques allows for a comprehensive description of the system, bridging fast vibrational processes and slow structural relaxation.

The central objective of this thesis is to understand how vitreous GeO_2 responds to high X-ray doses. First, we demonstrate the existence of X-ray–induced dynamics at room temperature. In particular, we study the evolution of such dynamics with the total absorbed dose and whether it finally reaches a stationary state, as previously reported in other glasses in the literature. A related point is the role of temperature: we examine whether this induced dynamics displays a temperature dependence and how it is modified when standard thermal relaxation processes, at temperatures close to the glass transition, occur on similar timescales.

The investigation of such dynamics has become possible thanks to the development of novel data analysis methodologies. In particular, we introduce the multi-tau two-time-correlation (MTTTC) approach and advanced detector corrections, which are essential for reliably extracting dynamical information from long XPCS measurements under low-signal conditions.

A second objective is to characterize the structural transformations that accompany this dynamics. This is measured by monitoring, in parallel with the dynamics using XRD, the evolution of the first sharp diffraction peak and the low-Q scattered signal related to spatial density fluctuations in the glass. The structural dependence on the irradiation temperature, and its evolution from the pristine glass, are investigated in depth. The presence of a unique final steady structure of the glass that depends solely on the irradiation temperature is one of the central outcomes of this work.

In particular, we measure that irradiation produces an increase in the small-angle scattered signal, compatible with an increase in spatial density fluctuations in the system. A central issue is to determine whether the observed changes arise from modifications of the frozen-in (quasistatic) structure or from the dynamic component associated with vibrational motion. Within this framework, IXS measurements are used to analyze the origin of density fluctuations by separating their frozen-in and dynamical contributions. This will allow relating the final stationary state of the irradiated glass to a melt-quenched glass with a high fictive temperature. The

corresponding fictive temperature, like the glass state, changes with the irradiation temperature.

Finally, we compare the non-ergodicity factor obtained from XPCS at low frequencies with that inferred from IXS measurements in the high-frequency regime. This comparison offers insight into the degree of dynamical arrest across different timescales and contributes to a more unified description of relaxation processes in irradiated glasses.

The thesis is organized as follows. **Chapter 1** introduces the fundamental physics of supercooled liquids and glasses, including the concepts of glass transition, viscosity and fragility, the potential energy landscape, and density correlation functions. Particular attention is given to relaxation processes, density fluctuations, and the role of the fictive temperature, with a final focus on the structural properties of vitreous GeO_2. **Chapter 2** presents the X-ray experimental techniques used throughout this work. It introduces the interaction of X-rays with matter and the theoretical framework of scattering processes, and describes inelastic X-ray scattering (IXS), X-ray diffraction (XRD), and X-ray photon correlation spectroscopy (XPCS), together with their implementation at synchrotron beamlines. **Chapter 3** is devoted to the development of novel data-analysis methodologies for XPCS experiments. In particular, it presents the multi-tau two-time correlation (MTTTC) approach and advanced detector corrections, which enable reliable analysis of long timescale dynamics under low-signal conditions. **Chapter 4** reviews radiation damage in glasses under ionizing irradiation. It discusses the microscopic mechanisms of defect formation, radiolysis, and structural modifications, and introduces the physical framework underlying X-ray–induced dynamics. **Chapter 5** presents the XPCS investigation of X-ray–induced dynamics and structural transformations in vitreous GeO_2. The dose and temperature dependence of the dynamics are analyzed, together with the evolution toward a stationary irradiated state and its structural properties. **Chapter 6** focuses on the study of density fluctuations by means of IXS. The inelastic spectra are analyzed to separate frozen-in and dynamical contributions, providing insight into the dynamical origin of density fluctuations and enabling a comparison of non-ergodicity factors across different timescales. Finally, the main results of the thesis are summarized in the Conclusions.

Contents

1 The physics of supercooled liquids and glasses

This chapter introduces the fundamental physics of supercooled liquids and glasses. It outlines the nature of the glass transition describing the role of viscosity and fragility, and defining the potential energy landscape framework. Structural and dynamical properties are described through correlation functions, relaxation processes, and density fluctuations. Particular attention is given to the concepts of aging, rejuvenation, and the role of the fictive temperature. The discussion on the structure is finally focused on vitreous GeO_2, the system investigated in this thesis.

1.1 Supercooled liquids, glasses, and the glass transition

Glasses can be regarded as liquids that have lost their ability to flow: their microscopic structure remains essentially indistinguishable from that of the corresponding liquid. However, they are non-ergodic and no longer fully explore the phase space accessible to a fluid [Ang95]. Unlike crystals, which are characterized by a periodically ordered lattice at the atomic scale, glasses are amorphous solids that lack long-range structural order.

The most conventional method of obtaining a glass consists of quenching a melt fast enough to cross the melting point without triggering crystallization [Ang95; Cav09; DS01]. Figure 1.1 illustrates the temperature dependence of the volume (or alternatively, the enthalpy) of a liquid at constant pressure. If the liquid is cooled below its melting temperature T_m at a sufficiently slow rate, the molecules have time to rearrange into an ordered, thermodynamically stable crystalline phase. However, if the cooling rate is fast enough, the phase transition is avoided, and the liquid enters a metastable state known as the *supercooled liquid* state [EH12]. As the temperature drops further, the molecular motion slows down while the viscosity of the liquid increases. Consequently, the time required for the system to reach structural equilibrium becomes increasingly long.

At a certain point, the characteristic timescale for structural rearrangement exceeds the experimental observation time, and the atoms become virtually frozen in their disordered configuration: the system falls out of equilibrium, transitioning

from a supercooled liquid to a glass [DS01]. The *glass transition temperature*, T_g, is conventionally defined as the temperature at which the shear viscosity reaches 10^{12} Pa·s [Ang95]. At this stage, the material behaves macroscopically as a solid [Göt09]. Experimentally, during the glass transition an abrupt (but continuous) change of the thermal expansion coefficient $\alpha_p = \frac{1}{V}(\frac{\partial V}{\partial T})_p$ and the heat capacity $C_p = (\frac{\partial h}{\partial T})_p$ is observed.

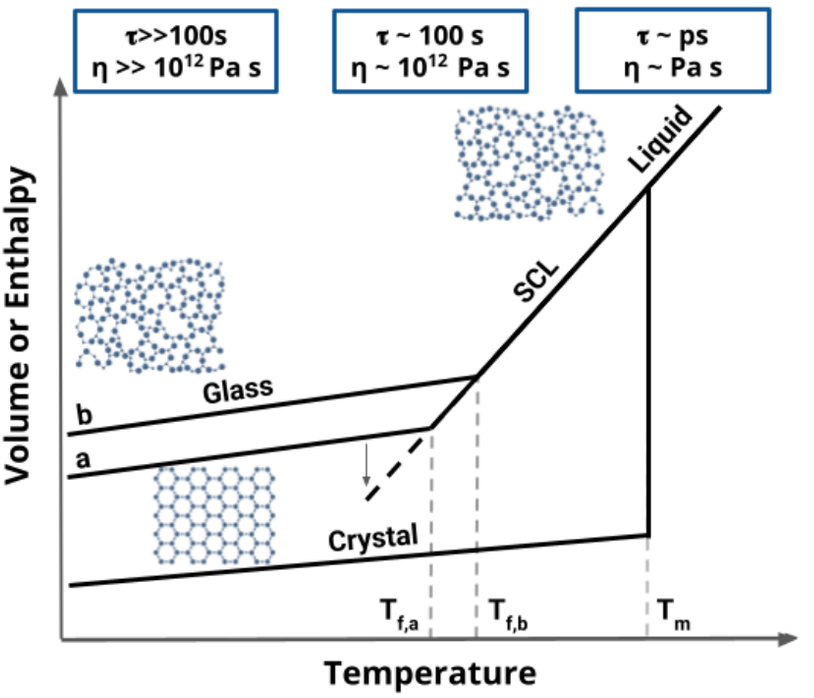

Figure 1.1: The molar volume (or enthalpy) as a function of temperature. Below the melting temperature T_m, a slow cooling leads to crystallization. A faster quench bypasses T_m, forming a supercooled liquid. At the glass transition temperature T_g, the system falls out of equilibrium, forming a glass. Different cooling rates lead to different T_g values. Isothermal aging below T_g allows the glass to slowly relax toward the supercooled liquid equilibrium line.

The glass transition is not thermodynamic phase transition: there are no discontinuities in the volume or heat capacity, and the exact value of the glass transition temperature, as well as the structure of the final glass, strictly depends on the system's thermal history, particularly the cooling rate [DS01]. Because the characteristic timescale for structural rearrangements grows exponentially upon cooling

(see the following Sec. 1.2), a liquid subjected to a rapid quench has less time to equilibrate. Consequently, it falls out of equilibrium and undergoes the glass transition at a higher temperature. A fast-cooled glass essentially freezes in a configuration that represents a higher temperature liquid; thus, it is characterized by a higher degree of structural disorder, a larger volume, and a higher enthalpy. Conversely, a slower cooling rate enables the liquid to follow the equilibrium supercooled curve down to lower temperatures before the kinetic arrest occurs, yielding a denser, more structurally relaxed, and thermodynamically stable glass [EH12].

To quantitatively describe the final state of a glass, which is inherently out of equilibrium, A. Q. Tool introduced the concept of the *fictive temperature* T_f [Too46]. The fictive temperature is defined as the temperature at which the non-equilibrium structure (and macroscopic properties like volume or enthalpy) of the glass would correspond to the equilibrium structure of the supercooled liquid. For a liquid cooled at a constant rate of few K/s, T_f roughly coincides with T_g at the onset of the transition and remains constant in the deep glassy state. Since this change of derivative takes place over a range of temperatures, the fictive temperature can be located as the virtual intersection of the liquid line with the extrapolation of the glassy one (see Fig. 1.1).

If a glass is held at a temperature just below T_g for an extended period, it undergo *physical aging*. This involves a slow, spontaneous densification as the system minimize its free energy and reach the extrapolated equilibrium supercooled liquid curve (as illustrated by the dashed line in Figure 1.1). In parallel, its fictive temperature relaxes towards the annealing temperature T of the system. Because the mobility is extremely low, this process can take up to geological timescales, and become more rapid approaching T_g [MGL07; Rut+12].

1.2 The strong temperature dependence of the viscosity

The viscosity η is a fundamental macroscopic observable for describing the kinetic arrest of supercooled liquids. Upon cooling, the viscosity of a glass-forming liquid can increase by more than 14 orders of magnitude within a relatively narrow temperature window [Ang95]. It is important to note here that the macroscopic fluidity of a system is intrinsically linked to the characteristic timescale of observation. For instance, when subjected to an external stress at terahertz (THz) frequencies, water at ambient temperature exhibits a solid-like elastic response [Mas+04].

The temperature dependence of the viscosity provides a useful empirical criterion for classifying glass-forming liquids. This is traditionally visualized using an Angell

plot, where the logarithm of the viscosity, $\log_{10}(\eta)$, is plotted against the inverse reduced temperature T_g/T [Ang95; Phi81]. Based on the curvature observed in this plot, liquids are characterized by their *kinetic fragility* [Bou08].

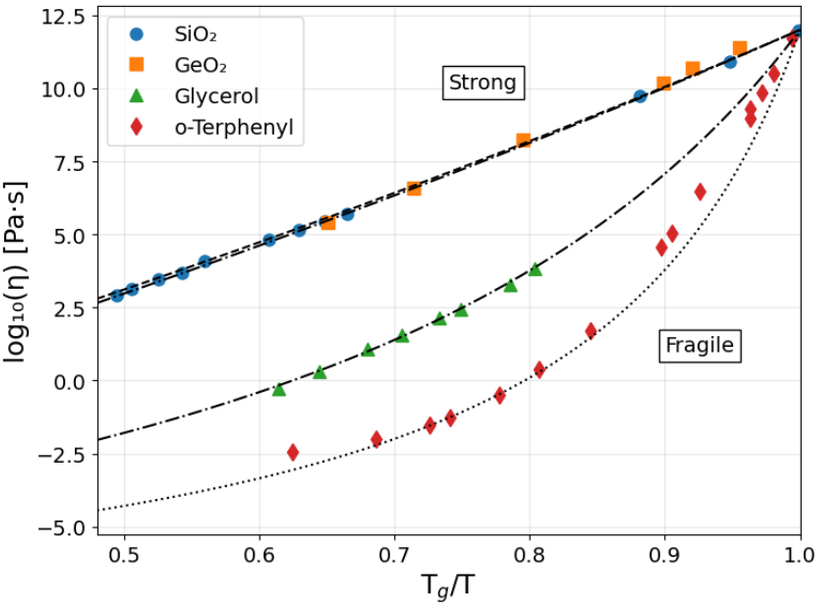

Figure 1.2: The Angell plot: logarithm of the viscosity η as a function of the inverse reduced temperature T_g/T. Strong glass formers (e.g., SiO_2 and GeO_2) show a linear, Arrhenius-like behavior, while fragile liquids exhibit a super-Arrhenius curve (e.g. Glycerol and o-Terphenyl).

As shown in Figure 1.2, *strong* glass formers (such as silica and germania networks) display the so-called Arrhenius temperature dependence:

$$\eta(T) = \eta_0 \exp\left(\frac{E_a}{k_B T}\right) \tag{1.1}$$

where E_a is a constant effective activation energy, k_B is the Boltzmann constant, and η_0 is the high-temperature limit of viscosity (almost 10^{-5} Pa·s for any glass forming liquuids). In the Angell plot, this relation appears as a straight line. Strong liquids typically possess open networks and covalent bonds [Phi81].

Conversely, *fragile* glass formers exhibit a super-Arrhenius behavior, implying that the effective activation energy for structural rearrangement grows as the temperature drops towards T_g. The standard empirical description for fragile systems

is the Vogel-Fulcher-Tammann (VFT) equation:

$$\eta(T) = \eta_0 \exp\left(\frac{DT_0}{T - T_0}\right) \tag{1.2}$$

where D and T_0 are phenomenological parameters [Cav09].

The degree of fragility is quantified by the fragility index m, defined as the slope of the viscosity curve at the glass transition T_g:

$$m = \lim_{T \to T_g} \frac{\partial \log_{10}(\eta(T))}{\partial(T_g/T)} \tag{1.3}$$

This index typically ranges from $m \approx 16$ for strong systems to $m \geq 100$ for highly fragile molecular and polymeric liquids [Ang95].

1.3 The potential energy landscape

From a statistical mechanics perspective, glasses are kinetically arrested supercooled liquids that have lost the ability to explore their entire phase space. Consequently, they break ergodicity and can no longer be treated as equilibrium statistical ensembles. Instead, a glass is confined to a restricted region of the phase space, exploring only a local subset of microstates permitted by its thermal energy. An example of these microstates are the vibrations about the "frozen-in" atomic positions. The slow dynamics that persists in glasses is called physical aging: a slow and spontaneous structural relaxation as the system attempts to reach the true thermodynamic equilibrium. The Potential Energy Landscape (PEL) formalism, first introduced by Goldstein in 1969 [Gol69], provides a powerful framework to visualize this ergodicity breaking and the phase-space dynamics of glasses [DS01; Gol69; Sci05].

The PEL represents the multi-dimensional hypersurface of the potential energy $\Phi(\mathbf{r}_1, \ldots, \mathbf{r}_N)$ mapped over the $3N$ coordinates of the N particles of the system. As sketched in Figure 1.3, this landscape is rugged, populated by a vast number of local minima known as *inherent structures* and characterised by shallow valleys (basins) grouped into larger dales, known as metabasins. Changes in the system density determine the deformation of the landscape, which for a system of N particles in a volume V is fixed. Each minimum corresponds to a metastable configuration, while the system's dynamic is governed by transitions between these basins [Sci05].

At high temperatures, the liquid has enough thermal energy to explore the entire PEL homogeneously, overcoming the energy barriers. As the temperature decreases and the system enters the supercooled liquid, transitions between basins occur

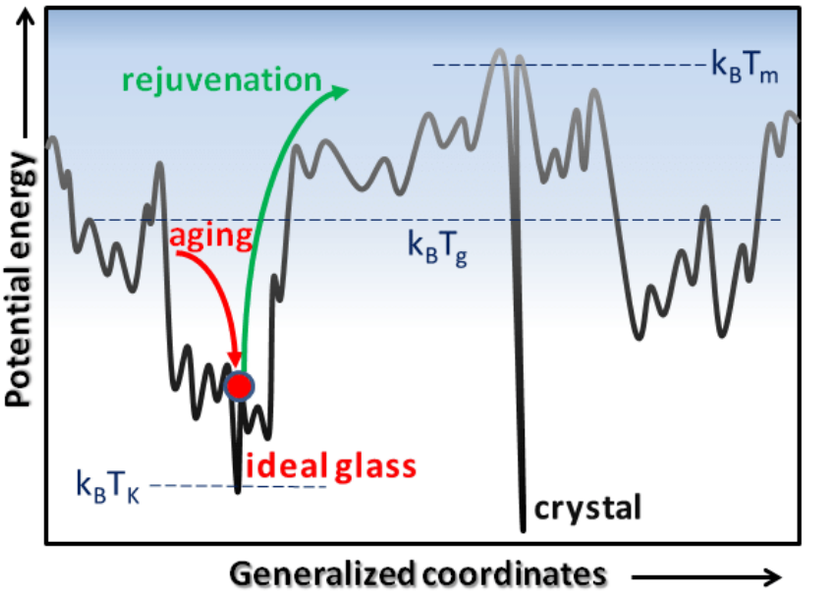

Figure 1.3: A schematic one-dimensional representation of the Potential Energy Landscape (PEL). The landscape is composed of deep minima (inherent structures) organized into broader metabasins. At high temperatures, the liquid continuously explores the entire landscape, whereas near T_g, the system gets trapped in deeper valleys, with dynamics dominated by activated jumps across energy barriers. Reprinted from [PJR15] by permission of Informa UK Limited, trading as Taylor and Francis Group.

via thermally activated jumps and the dynamics slows down. When the thermal energy k_bT becomes lower than the barrier heights of a metabasin, the system's configurational trajectory become confined. This trapping marks the loss of the ergodicity of the system and the transition into the arrested glassy state. Compared to the supercooled liquid, the glass than can explore a very limited region of the PEL on experimental timescales.

In this picture, aging corresponds to the slow cascade of the system from low-depth minima into progressively deeper, more thermodynamically stable structures [Sci05]. In contrast to physical aging, a glass can also be forced out of its deep local minima and driven into higher-energy, more disordered configurations within the potential energy landscape [PJR15]. This phenomenon, known as *rejuvenation* (as schematically depicted in Figure 1.3), is typically achieved by transferring energy into the system through external perturbations such as mechanical deformation or rapid thermal cycling.

More recently, it has been shown that particle irradiation [Bag+24; Kri+17] can also induce rejuvenation in glasses. This radiation-induced rejuvenation constitutes a central concept of the present thesis.

1.4 Density correlation functions

A microscopic description of the structural and dynamical properties of amorphous systems requires the definition of appropriate physical observables. In the context of liquids and glasses, these are given by space-time density correlation functions. Such quantities provide a powerful tool to describe microscopic molecular structures and motions, and they are routinely accessed via both experimental techniques and molecular dynamics simulations [Göt09].

A statistical mechanical description of an N-particle system occupying a volume V starts by specifying the particle coordinates $\{\mathbf{r}_i(t)\}$. The quantity of interest is the microscopic local density, $\rho(\mathbf{r}, t)$, defined as a sum of Dirac delta functions centered at the instantaneous positions of the particles:

$$\rho(\mathbf{r}, t) = \sum_{i=1}^{N} \delta(\mathbf{r} - \mathbf{r}_i(t)) \tag{1.4}$$

While this function formally contains the complete spatio-temporal evolution of every particle in the system, it is too much detailed for practical usage. From an experimental standpoint, $\rho(\mathbf{r}, t)$ is never directly accessible. Conversely, even though exact particle trajectories are accessible through molecular dynamics simulations, it yields little physical insight into the overall molecular behavior [BY80; BZ94].

Instead, scattering experiments and theoretical descriptions rely on statistical averages of the microscopic density. The simplest statistical measure we can define is the single-particle density correlation $\rho^{(1)}(\mathbf{r}, t) = \langle \rho(\mathbf{r}, t) \rangle$. However, for a macroscopically uniform and translationally invariant system, such as a liquid or an amorphous solid, this ensemble average simply yields the constant macroscopic density $\rho^{(1)}(\mathbf{r}, t) = N/V$: ensemble-averaging the absolute atomic positions in space completely loses the microscopic structural description. We therefore need at least two-particle correlation to describe the system dynamics [BZ94].

1.4.1 The density-density correlation function

This naturally leads to the introduction of the space-time density-density correlation function, known as the van Hove correlation function. Assuming macroscopic

translational invariance, a condition satisfied by both liquids and glasses, the van Hove function is expressed as

$$G(\mathbf{r},t) = \frac{1}{N}\left\langle \int_V d\mathbf{r}'\rho(\mathbf{r}',0)\rho(\mathbf{r}'+\mathbf{r},t)\right\rangle = \frac{1}{\rho}\langle\rho(\mathbf{r},t)\rho(\mathbf{0},0)\rangle \tag{1.5}$$

where the angular brackets $\langle \dots \rangle$ denote an ensemble average. Physically, $G(\mathbf{r},t)$ is proportional to the probability of finding a particle at position $\mathbf{r}$ at time t, given that a particle was located at the origin at time $t = 0$. This interpretation is evident by substituting the definition of the microscopic density into this expression, which yields the particle-sum representation [Van54]:

$$G(\mathbf{r},t) = \frac{1}{N}\left\langle \sum_{i=1}^{N}\sum_{j=1}^{N}\delta(\mathbf{r} - [\mathbf{r}_j(t) - \mathbf{r}_i(0)])\right\rangle \tag{1.6}$$

In a homogeneous and isotropic system, macroscopic rotational invariance ensures there is no preferred spatial direction. Consequently, the correlation between particles depends strictly on the modulus of their separation distance, $r = |\mathbf{r}|$. By taking the angular average over all solid angles Ω, the vector dependence is eliminated, and the van Hove function simplifies to a scalar function of radial distance and time:

$$G(r,t) = \frac{1}{4\pi}\int G(\mathbf{r},t)d\Omega = \frac{1}{4\pi r^2 N}\left\langle \sum_{i=1}^{N}\sum_{j=1}^{N}\delta(r - |\mathbf{r}_j(t) - \mathbf{r}_i(0)|)\right\rangle. \tag{1.7}$$

1.4.2 Reciprocal Space and Scattering Functions

While real-space correlations provide a direct picture of atomic arrangements, experimental techniques such as inelastic neutron scattering (INS), inelastic X-ray scattering (IXS) or X-ray photon correlation spectroscopy (XPCS) do not probe real space directly. Instead, they operate in the reciprocal momentum space, measuring momentum transfer $\hbar\mathbf{Q}$.

The relevant physical quantity is the spatial Fourier transform of the van Hove correlation function, known as the *intermediate scattering function* (ISF) [HM86]

$$F(Q,t) = \int_0^\infty 4\pi r^2 G(r,t)\frac{\sin(Qr)}{Qr}dr \tag{1.8}$$

where we have exploited the isotropy of the amorphous system to reduce the three-

dimensional Fourier transform to a one-dimensional spherical sine transform. The intermediate scattering function measures the time-dependent structural relaxation of the system at a specific length scale $2\pi/Q$. As we will see in chapter 2, the momentum $\hbar Q$ is directly set by the probe in scattering experiments, and the ISF is the output of XPCS experiments.

To connect with the energy transfer $\hbar\omega$ measured in inelastic scattering, we perform a temporal Fourier transform of $F(Q,t)$. This yields the *dynamic structure factor* [HM86]

$$S(Q,\omega) = \frac{1}{2\pi}\int_{-\infty}^{\infty} F(Q,t)e^{-i\omega t}dt \tag{1.9}$$

The dynamic structure factor is the key quantity in energy resolved experiments, as it is directly proportional to the double-differential scattering cross-section $\frac{d^2\sigma}{d\Omega d\omega}$ (see Ch. 2), making it the bridge between theoretical models of dynamics and experimental observations. Moreover, it allows looking at the dynamics in the frequency space, evidencing, for example, the presence of collective acoustic modes propagating over the length-scale $2\pi/Q$ of interest [Squ78].

1.4.3 The static limits: $g(r)$ and $S(Q)$

While $S(Q,\omega)$ and $F(Q,t)$ describe the dynamics of the system, the information on the structure of the amorphous state is encoded in their static ($t = 0$) limits. This limits leads to the definition of (i) in real space, the pair distribution function $g(r)$, and (ii) in reciprocal space, the static structure factor $S(Q)$. Figure 1.4 illustrates these two complementary functions for a typical amorphous system.

The pair distribution function

The Van Hove function $G(r,t)$ contains both spatial and temporal information. For $t = 0$, it reduces to the instantaneous spatial distribution of particles, i.e. a static picture of their correlations [BZ94]

$$G(r) = \rho\frac{\langle\rho(r)\rho(0)\rangle}{\rho^2} = \rho g(r) \tag{1.10}$$

where g(r) is the radial distribution function, or pair distribution function. Physically, $\rho g(r)$ (where $\rho = N/V$ is the macroscopic number density) represents the average density of particles at a distance r from a reference particle.

Unlike a crystalline lattice characterized by discrete, sharp peaks extending to infinite r (in this case, one has to recover the vector dependence on $\mathbf{r}$), amorphous

systems are topologically disordered. As shown in the left panel of Figure 1.4, the $g(r)$ of a glass or liquid displays pronounced, relatively narrow oscillations at small radial distances. The peaks are sharper the more ordered the structure, tending to the Dirac deltas of the perfect crystal. These peaks signify well-defined short-range order (SRO), typically corresponding to the constrained and packed firsts coordination shells. The main peak describes the nearest neighbor shell (or cage) of particles. However, these oscillations rapidly decay, and $g(r) \to 1$ for larger distances. This asymptotic behavior is the manifestation of the absence of long-range order, confirming that at extended distances, the local density simply averages out to the macroscopic bulk density.

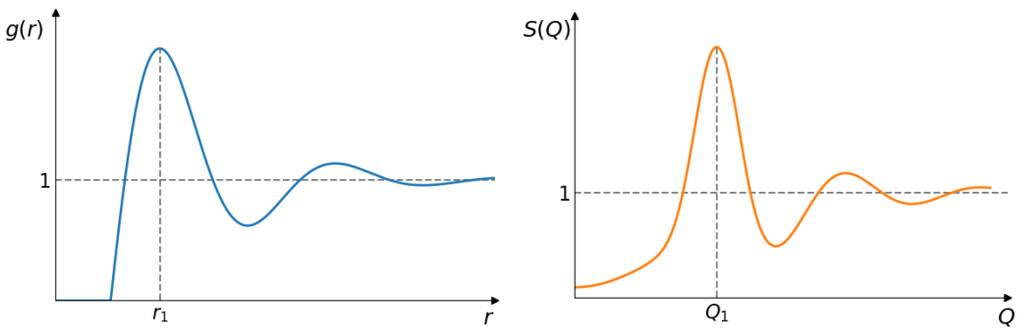

Figure 1.4: Left: Radial distribution function $g(r)$ exhibiting distinct short-range oder at low r and a lack of long-range periodicity as $g(r) \to 1$. Right: Corresponding static structure factor $S(Q)$ highlighting the First Sharp Diffraction Peak (FSDP), indicative of Medium-Range Order.

The static structure factor

In reciprocal space, the complementary structural information is captured by the static structure factor, $S(Q)$. It is defined as the instantaneous ($t = 0$) density correlation or, equivalently, the frequency integral of the dynamic structure factor [BZ94]:

$$S(Q) = F(Q, 0) = \int_{-\infty}^{\infty} S(Q, \omega) d\omega \tag{1.11}$$

Also, $S(Q)$ is linked to the real-space $g(r)$ via the Fourier transform:

$$S(Q) = 1 + 4\pi\rho \int_0^{\infty} r^2 [g(r) - 1] \frac{\sin(Qr)}{Qr} dr \tag{1.12}$$

The right panel of Figure 1.4 displays a typical $S(Q)$ for a glass or liquid. Despite the lack of long-range periodicity, a distinct signature of glasses and liquids is the presence of the First Sharp Diffraction Peak (FSDP), often emerging at low values of momentum transfer (typically $Q_1 \approx 1 - 2$ Å^{-1}). The FSDP is the signature of medium-range order (MRO), i.e. structural organization that extends beyond the immediate coordination shells (SRO) but remaining of finite extent compared to true macroscopic periodicity (like crystals).

The properties of the FSDP provide insights into the amorphous network. The full width at half maximum (FWHM), ΔQ, is inversely proportional to the characteristic correlation length of the medium-range order, $L \approx 2\pi/\Delta Q$. Thus, the FSDP width serves as a measurement of structural disorder: a broader peak signifies a lower MRO and a reduced structural correlation length [Ell91; Sal+07]. The peak position Q_1 is sensitive to macroscopic density and correlates with the first coordination shell r_1 in $g(r)$, often following an Ehrenfest-like relation ($Q_1 r_1 \approx$ const.). Consequently, density modifications (e.g., via pressure) correlates with Q_1, but the behavior depends on the system [BZ94].

Finally, we note that in the long-wavelength limit ($Q \to 0$), the static structure factor is linked to the thermodynamic properties of the liquid. Specifically, $S(Q)$ is proportional to the isothermal compressibility χ_T according to [HM86]

$$S(0) = \lim_{q \to 0} S(q) = \rho k_B T \chi_T \tag{1.13}$$

where ρ is the number density, k_B is the Boltzmann constant, and T is the absolute temperature. We will describe the behavior of $S(0)$ across the glass transition and deep in the glass in Sec. 1.6.

1.5 Relaxations in supercooled liquids and glases

The decay of the intermediate scattering function contains the dynamical signature of the glass transition. In high-temperature simple liquids, the intermediate scattering function $F(Q,t)$, after vibrations, is generally characterized by a single-exponential decay, which reflects the random and uncorrelated Brownian motion of particles. In contrast, supercooled liquids (SCLs) and glasses display a far more intricate dynamical behavior, in which distinct relaxation regimes can be identified [Bou08; Cav09; EH12] (see Fig. 1.5 left).

At very short times, in the picosecond range, the dynamic is dominated by vibrational motion of particles within transient cages formed by their nearest neighbours. These fast, oscillations, generally described as “rattling” inside the

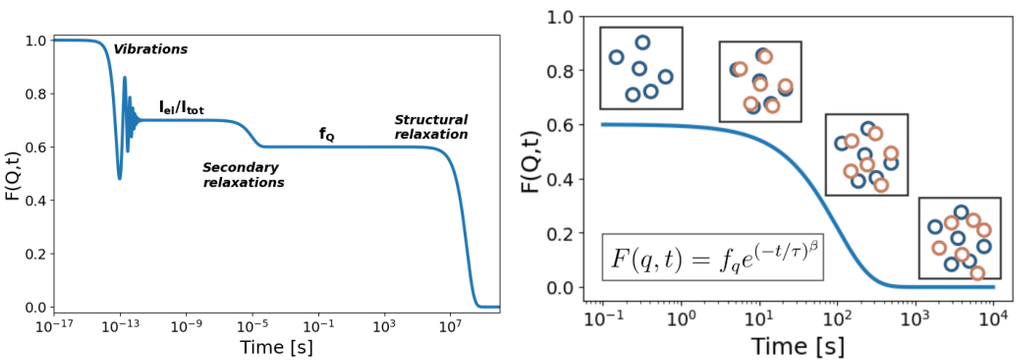

Figure 1.5: left) Schematic representation of the intermediate scattering function $F(q,t)$ in a supercooled liquid. At very short times, the ballistic regime is visible. The plateau corresponds to the rattling of particles inside their neighbor cages (β-relaxation). The final long-time decay is the structural α-relaxation, well-described by a stretched exponential function. right) Schematic representation of the intermediate scattering function $F(Q,t)$ in the α-relaxation regime. Insets depict the system's microscopic configuration over time, illustrating the gradual loss of structural correlation.

cage, keeps the atoms localized in contrast with long-range diffusion. Upon cooling, the amplitude of these vibrations progressively decreases, indicating an increasing rigidity of the cage structure [SN04]. In the macroscopic regime (i.e., at low Q), these vibrational modes correspond to the propagation of longitudinal sound waves in the system. Due to dissipative processes, however, such waves are progressively damped, ultimately leading to a decorrelation of the atomic positions over time.

Following this initial regime, the intermediate scattering function develops a plateau. On longer timescales, secondary relaxation processes emerge, commonly referred to as β-relaxations. Among them, the Johari–Goldstein (JG) β-relaxation plays a central and universal role in glass-forming systems [JG70]. In this regime, particles remain confined within their cages but undergo slower, collective motions that give rise to local structural rearrangements. The characteristic timescale of β-relaxations typically spans the interval between 10^{-6} and 10^{-3} s. Within the framework of the potential energy landscape (PEL), the JG β-relaxation is interpreted as localized transitions occurring within the same metabasin. β-relaxations are typically pronounced in fragile glass formers, where a clear separation between secondary and structural relaxation processes is observed. In contrast, the dynamics of strong glass formers are generally characterized by an extended plateau region that connects the fast vibrational regime to the α-relaxation, spanning many

orders of magnitude in time and reflecting the absence of well-resolved secondary relaxation processes [Sco+03].

At even longer times, $F(\mathbf{q}, t)$ exhibits its final decay, corresponding to the α-relaxation (or structural relaxation) [Jan18]. This process is associated with the escape of particles from their cages and with transitions between distinct metabasins in the PEL. Such rearrangements require the cooperative motion of many particles and the crossing of energy barriers. The structural relaxation time may vary from a few picoseconds in high-temperature liquids to hundreds of seconds close to the glass transition temperature T_g, and can even reach geological timescales in deeply glassy states [AG65b]. A schematic illustration of the α-relaxation is shown in Fig. 1.5 right, where the insets depict the progressive loss of correlation between the instantaneous configuration of the system and the initial one.

1.5.1 The α-relaxation

As anticipated, the α-relaxation is the primary relaxation process in supercooled liquids and plays a fundamental role in the dynamical arrest associated with the glass transition. A direct link exists between microscopic dynamics and macroscopic response quantified by the viscosity: the Maxwell's viscoelastic model [Nga11]. In this framework, the structural relaxation time τ_α is directly related to the macroscopic viscosity η through

$$\eta = G_\infty \tau_\alpha, \tag{1.14}$$

where G_∞ is the infinite-frequency shear modulus, i.e., the shear modulus measured under oscillatory deformation at high frequency. Its typical magnitude of the order of 10^9 Pa, and it is approximately constant across the SCL and glassy states. Upon cooling toward the glass transition temperature T_g, the structural relaxation time increases dramatically, reaching values of the order of 100 s at T_g. According to the viscoelastic description, materials, whether liquid or solid, do not respond instantaneously to an applied stress, but instead relax over a characteristic timescale. Figure 1.6 present the temperature dependence of the strong glass former v-GeO_2, which, following Eq. 1.14, mimic the behavior of the viscosity of Fig. 1.2.

Experimentally, the structural relaxation is not generally described by a simple exponential decay. Instead, it is commonly modeled by the Kohlrausch – Williams – Watts (KWW) function [Gol69] (see Fig. 1.5 right)

$$F(Q, t) = f_Q \exp\left[-\left(\frac{t}{\tau_Q}\right)^{\beta_Q}\right], \tag{1.15}$$

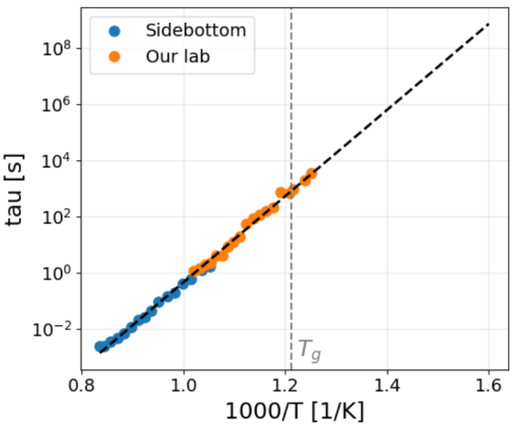

Figure 1.6: Temperature dependece of the structural relaxation time of v-GeO_2 measured with visible photon correlation spectroscopy. The blue points are data from [Sid23] while the extensions to lower temperatures are data taken in our laboratory. As can be seen, the strong glass former v-GeO_2 follows an Arrhenius behavior and the relaxation time mimics the viscosity of Fig 1.2.

where f_Q is the non-ergodicity factor, τ_Q the characteristic relaxation time at wavevector Q, and β_Q the stretching exponent, which quantifies the deviation from a single-exponential behaviour. In supercooled liquids, one typically finds $\beta_Q < 1$, corresponding to a stretched exponential decay. In this case, the relaxation initially proceeds relatively rapidly but develops a long-time tail, such that correlations persist longer than in the case of a purely exponential process. In this sense, the relaxation appears effectively slower and reflects the presence of a broad distribution of relaxation times, commonly attributed to dynamical heterogeneity (see in the following).

The *non-ergodicity factor* f_q corresponds to the height of the long-time plateau of the intermediate scattering function preceding the α-relaxation, and depends both on the amplitude of atomic vibrations and on the degree of structural disorder of the glass. It quantifies amount of phase-space the systems still have to explore (before structural relaxation) to become ergodic [Jan18].

1.5.2 Q-dependence of the KWW parameters

The KWW parameters τ_Q, β_Q, and f_Q depend on the structure, temperature, and the probed wavevector Q. In the case of simple Brownian diffusion, the dynamics

follows the Fick's law with

$$\tau_Q = \frac{1}{DQ^2} \qquad \beta_Q = 1 \tag{1.16}$$

where D is the diffusion coefficient. Deviations from the Q^{-2} scaling of the relaxation time indicate anomalous diffusion. A weaker Q-dependence ($n < 2$ in $\tau_q \propto q^{-n}$) is characteristic of faster-than-diffusive dynamics, often observed in colloidal glasses and gels under internal stress [Dur+05]. In particular, $n = 1$ means perfectly ballistic dynamics. Conversely, a stronger Q-dependence ($n > 2$) corresponds to sub-diffusive behavior, typical of systems with constrained dynamics, such as polymers or colloids close to the glass transition.

De Gennes narrowing

The Brownian scaling strictly holds in the low-Q limit, corresponding to the hydrodynamic (macroscopic) regime. At intermediate wavevectors, however, both the relaxation time τ_Q and the stretching exponent β_Q (less), are influenced by the static structure factor $S(q)$. This phenomenon is called *De Gennes narrowing* [De 59] and implies a slowing down of the dynamics at wavevectors close to the FSDP of $S(q)$

$$\tau_q \sim \frac{S(q)}{Dq^2} \tag{1.17}$$

This behavior reflects the fact that structurally favored configurations are dynamically more stable: relaxation processes occurring over intermolecular length scales are slowed down because particles must move into regions that are already densely populated by neighbouring molecules. De Gennes narrowing has been observed in simple liquids, supercooled liquids, and certain glasses, and it is the manifestation of the coupling between structure and dynamics [De 59; WIE18].

1.5.3 Dynamical heterogeneities

KWW with stretched exponential decay ($\beta < 1$) can arise from either an intrinsically non-exponential relaxation or from a superposition of spatially varying regions, each exhibiting a purely exponential decay but with different characteristic timescales [BB11; EH12]. Numerical simulations and experimental observations on colloidal and glassy systems have validated the latter scenario: the dynamics of supercooled liquids becomes deeply heterogeneous as T_g is approached [KB00; Tra+98]. These spatial fluctuations in mobility are referred to as *dynamical heterogeneities*. In the supercooled state, one can identify domains of particles that

are orders of magnitude more mobile than the average, coexisting with domains of particles that are nearly frozen [CR14; Wee+00]. The length scale associated with these cooperative rearranging regions grows continuously upon cooling [AG65a].

1.6 Spatial density fluctuations $S(0)$ across the glass transition

In any thermodynamic system, the local density ρ of a material is not uniform on microscopic length scales, but exhibits spatial fluctuations around its average value. *Density fluctuations* $\psi(v)$ can be defined by considering a reference volume v of arbitrary size and shape. As this reference volume is moved throughout the sample, the number of atoms N contained within it fluctuates about its mean value $\langle N \rangle$. The magnitude of these fluctuations, quantified by the variance, defines the density fluctuations:

$$\psi(v) = \left\langle \frac{(N - \langle N \rangle_r)^2}{\langle N \rangle_r} \right\rangle_r, \tag{1.18}$$

where $\langle \cdots \rangle_r$ denotes a spatial average over the sample.

Diffraction experiments provide direct access to density fluctuations: in the small-angle limit, the scattered intensity is proportional to the macroscopic-volume limit of $\psi(v)$ [CR83],

$$\psi(\infty) = \lim_{Q \to 0} \frac{1}{\rho} I(Q), \tag{1.19}$$

making $\psi(\infty)$ an experimental accessible quantity by light (to some extent), X-ray and neutron scattering.

According to statistical mechanics, within the grand canonical ensemble for a single-component system[1], density fluctuations are directly related to the isothermal compressibility [HM86]:

$$\psi(\infty) = \rho k_B T \chi_T, \tag{1.20}$$

where $\chi_T = \left(\frac{\partial V}{\partial P}\right)_T$ is the isothermal compressibility. This relation reflects the fact that, in liquids, density fluctuations are entirely of dynamical origin and arise from thermal motion in a medium characterized by the bulk compressibility.

The validity of Eq. 1.20 has been extensively verified for ordinary liquids and gases, as well as for supercooled liquids above T_g [CR83]. However, when the

1 A single-component system refers to a system composed of a single chemical species, so that density fluctuations arise purely from number-density variations rather than from composition fluctuations.

small-angle scattering intensity is measured as a function of temperature across the glass transition, the expected discontinuity associated with the jump in χ_T at T_g is not observed. Instead, only a change in the temperature dependence occurs at T_g, such that the $I(0)$ versus temperature curve resembles the typical behaviour of volume V or enthalpy H as a function of temperature (Fig. 1.1). Moreover, the experimentally measured $I(0)$ values are significantly larger than those obtained by inserting the glass compressibility into Eq. 1.20 [CR83; LAB+73; Lev+05].

To account for this discrepancy, one must consider that structural rearrangements become effectively frozen on experimental timescales at the glass transition [LAB+73; Roe83]. Consequently, density fluctuations in glasses can be separated into dynamic and quasistatic contributions [Roe83]:

$$\psi(v) = \psi_{\mathrm{dyn}}(v) + \psi_{\mathrm{qst}}(v). \tag{1.21}$$

Equation 1.21 decomposes a static quantity, namely the density fluctuations related to the low-Q limit of the static structure factor, into two distinct contributions of dynamic and quasistatic origin.

To clarify this distinction, we consider a reference volume v_i located at position $\mathbf{r}_i$ within the sample. The dynamic fluctuations $\psi_{\mathbf{r}_i}(v)$ inside this volume are obtained by replacing the spatial average in Eq. 1.18 with a time average [Roe83]:

$$\psi_{\mathbf{r}_i}(v) = \left\langle \frac{(N - \langle N \rangle_t)^2}{\langle N \rangle_t} \right\rangle_t, \tag{1.22}$$

where $\langle \cdots \rangle_t$ denotes the time average evaluated for the volume v located at $\mathbf{r}_i$.

In equilibrium liquids, ergodicity holds; therefore both $\langle N \rangle_i$ and $\psi_{\mathbf{r}_i}(v)$ coincide with their corresponding spatial averages. In a glass, however, many structural features become frozen at the glass transition. As a consequence, when the reference volume is moved to a different position $\mathbf{r}_j$, the time-averaged quantities $\langle N \rangle_j$ and $\psi_{\mathbf{r}_j}(v)$ differ from $\langle N \rangle_i$ and $\psi_{\mathbf{r}_i}(v)$. The point-to-point fluctuations of the local time-averaged density $\langle N \rangle_i$ thus define the quasistatic contribution $\psi_{\mathrm{qst}}(v)$ appearing in Eq. 1.21. This term represents the spatial variation of the locally averaged density across the sample.

The dynamic component $\psi_{\mathrm{dyn}}(v)$ of the total density fluctuation is instead obtained as the spatial average of the local dynamic fluctuations $\psi_{\mathbf{r}_i}(v)$ defined in Eq. 1.22. In liquids, where density fluctuations are entirely dynamic, they are directly related to the isothermal compressibility through Eq. 1.20. In glasses, the dynamic contribution $\psi_{\mathrm{dyn}}(v)$ is similarly connected to the glass compressibility by

[CR83; LAB+73; Roe83]

$$\psi_{\mathrm{dyn}}(\infty) = \rho k_B T \chi_T^g, \tag{1.23}$$

provided that both $\psi_{\mathrm{dyn}}(v)$ and χ^g are measured on the same experimental timescale.

Although the glass structure is commonly regarded as frozen, numerous atomic motion modes persist with relaxation times much shorter than the experimental timescale over which the compressibility is probed. These fast modes are responsible for the volume change under applied pressure and therefore contribute directly to the dynamic component of the density fluctuations.

1.6.1 Density fluctuations from structural relaxation and sound propagation

We now reformulate Eq. 1.21 in terms of thermodynamic quantities. For a system at thermodynamic equilibrium, following Laberge *et al.* [LAB+73], density fluctuations can be decomposed into contributions arising from isobaric–entropy and adiabatic–pressure fluctuations:

$$\psi(\infty) = \rho k_B T(\chi_T - \chi_S) + \rho k_B T \chi_S, \tag{1.24}$$

where χ_S denotes the adiabatic compressibility.

The second term, $\rho k_B T \chi_S$, contains two distinct physical contributions: (i) adiabatic density waves (i.e. sound waves or phonons), and (ii) density variations associated with structural relaxation processes in the equilibrium system. When the material becomes sufficiently viscous such that structural rearrangements occur on timescales much longer than the rapid oscillations of sound waves, the compressibility can be separated into two independent components. The phonon contribution is governed by the instantaneous (high-frequency) adiabatic compressibility χ_S^∞, whereas the density fluctuations associated with structural relaxation are determined by the relaxational part $\chi_S^r = \chi_S - \chi_S^\infty$ [LAB+73].

In a viscoelastic material capable of sustaining high-frequency shear stress, the high-frequency compressibility is related to the longitudinal elastic modulus through the high-frequency longitudinal sound velocity as $\chi_S^\infty = \frac{1}{\rho v_{l,\infty}^2}$. For an equilibrium system, density fluctuations can therefore be written as

$$\psi(\infty) = \rho\left[k_B T(\chi_T - \chi_S) + k_B T\left(\chi_S - \frac{1}{\rho v_{l,\infty}^2}\right) + k_B T \frac{1}{\rho v_{l,\infty}^2}\right]. \tag{1.25}$$

In a glass, Eq. 1.25 must be modified to account for the fact that the system is no

longer in thermodynamic equilibrium. The third term describes vibrational modes and remains unchanged, since these modes are equilibrated at the measurement temperature T.

The first term can generally be neglected in oxide glasses because $\chi_T^g \simeq \chi_S^g$ [2] [Ana+08]. The central term requires special consideration. During glass formation, as the melt is cooled, structural density fluctuations become kinetically arrested at the fictive temperature T_f. Upon further cooling, these fluctuations remain permanently frozen in, as their relaxation times exceed any experimentally accessible timescale (see Fig. 1.6). The magnitude of these frozen-in fluctuations corresponds to the equilibrium relaxational contribution evaluated at T_f.

Accordingly, the density fluctuations in the glass can be expressed as [Lev+05]

$$\psi^g(\infty) = \rho\left[k_B T_f\left(\chi_S(T_f) - \frac{1}{\rho v_{l,\infty}^2(T_f)}\right) + k_B T \frac{1}{\rho v_{l,\infty}^2(T)}\right]. \tag{1.26}$$

The adiabatic compressibility at T_f can be obtained by linear regression in the supercooled liquid regime using Eq. 1.20. Thus, the density fluctuations in the glass (or equivalently the scattered intensity $I(0)$) consist of a constant frozen-in component, determined solely by the thermal history of the sample (through T_f and the equilibrium structure at the glass transition), and a vibrational contribution that increases linearly with temperature between 0 K and T_f.

1.6.2 The role of the fictive temperature

The decomposition introduced above provides a direct interpretation of the low-Q scattered intensity in glasses prepared with different thermal histories. As shown in Fig. 1.7, silica samples characterized by different fictive temperatures T_f exhibit distinct values of $I(0)$ at a given measurement temperature.

According to Eq. 1.26, the extrapolated intensity in the glass can be written as the sum of two contributions: a vibrational term, governed by the high-frequency elastic response and therefore dependent on the measurement temperature T, and a frozen-in relaxational term, determined by the equilibrium structural fluctuations at the fictive temperature T_f. The vibrational contribution increases smoothly with temperature and is common to all samples, while the frozen component depends on the thermal history of the glass [Lev+05; Lev+07; WSI03].

2 More generally, the difference can be evaluated using the thermodynamic relation $\chi_T - \chi_S = \frac{\alpha_p^2 T_f}{\rho C_p}$, where α_p and C_p are the thermal expansion coefficient and the specific heat, respectively [LAB+73].

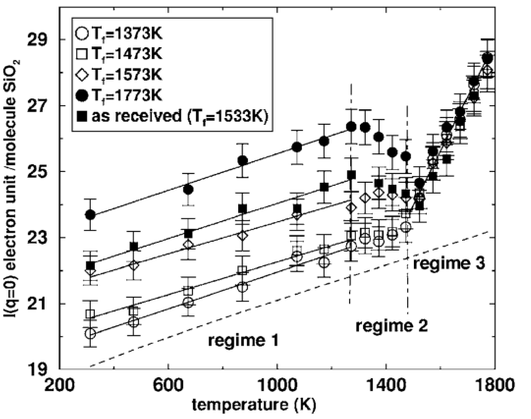

Figure 1.7: Scattered intensity at $Q = 0$ as a function of temperature for five samples characterized by different fictive temperatures. The temperature-dependent contribution arising from phonons, I_{ph}, calculated from Brillouin measurements, is shown as a dashed line to illustrate the slope of this term with temperature. For clarity, the curve has been vertically shifted upward. Figure reproduced with permissions from [Lev+05].

As a consequence, glasses quenched at different cooling rates and thus characterized by different fictive temperatures, retain different amplitudes of frozen-in density fluctuations. Faster cooling rates lead to higher T_f, meaning that structural fluctuations are arrested at higher temperatures where the relaxational compressibility is larger. This results in a larger residual (quasistatic) contribution to $I(0)$. Conversely, slowly cooled or annealed glasses, with lower T_f, exhibit smaller frozen-in density fluctuations. This framework explains why the $I(0)$ versus T curves for glasses with different histories appear vertically shifted while sharing a similar temperature-dependent slope: the slope reflects the vibrational (phonon-like) contribution, whereas the vertical offset encodes the fictive temperature and therefore the cooling history of the sample.

1.6.3 Non-ergodicity factor and fragility

The concept of non-ergodicity provides a complementary perspective on density fluctuations, focusing on their dynamical arrest. The non-ergodicity factor $f_q(T)$ is defined as the long-time limit of the normalized intermediate scattering function,

$$f_Q(T) = \lim_{t\to\infty} \frac{F(q,t)}{S(q)}, \tag{1.27}$$

and represents the fraction of density correlations that remain frozen at long times. In an ergodic liquid $f_Q = 0$, whereas in a glass f_q is finite, reflecting the persistence of structural correlations.

In the harmonic regime well below T_g, the temperature dependence of $f_Q(T)$ in the low-Q limit can be expressed in a simple form [Sco+03]

$$f_{Q\to 0}(T) = \frac{1}{1 + \alpha \frac{T}{T_g}}, \tag{1.28}$$

where α is a dimensionless parameter that encapsulates the microscopic vibrational properties of the glass.

The same temperature dependence of the non-ergodicity factor can be directly recovered from Eqs. 1.19 and 1.26. In the long-wavelength limit (low-Q limit), we have seen that the total density fluctuations are proportional to the static structure factor $S(Q \to 0)$. Instead, the long-time limit of the intermediate scattering function, $\lim_{t\to\infty} F(Q = 0, t)$ is proportional only to the frozen-in (quasistatic) term. Therefore, the non-ergodicity factor can be written as the ratio between quasistatic and total density fluctuations:

$$f_{Q\to 0}(T) = \frac{\psi_{\text{qst}}}{\psi_{\text{qst}} + \psi_{\text{dyn}}} = \frac{1}{1 + \frac{\psi_{\text{dyn}}}{\psi_{\text{qst}}}}. \tag{1.29}$$

Using Eq. 1.26, this expression becomes

$$f_{Q\to 0}(T) = \frac{1}{1 + \frac{M_\infty^{-1}(T)}{\chi_S(T_f) - M_\infty^{-1}(T_f)} \frac{T}{T_f}}, \tag{1.30}$$

where $M_\infty^{-1}(T) = 1/(\rho v_{l,\infty}^2(T))$ is the high-frequency longitudinal modulus.

Equation 1.28, or equivalently 1.30, shows that the decrease of f_q with temperature in the glassy state is approximately linear at low T, with a slope controlled by α. Physically, $1 - f_q$ measures the amount of decorrelation induced by vibrational motion; therefore, α quantifies how rapidly density correlations are lost upon increasing temperature within the harmonic solid.

A remarkable result reported by Scopigno *et al.* [Sco+03] is that the parameter α correlates strongly — and approximately linearly — with the kinetic fragility m of the corresponding liquid. In other words, fragile liquids (large m) correspond to glasses in which $f_q(T)$ decreases more rapidly with temperature, while strong glass formers (small m) display a much weaker temperature dependence of f_q. This

result bridge the vibrational dynamics of the glass well below T_g with the structural relaxation of the supercooled liquid above T_g, suggesting that the fragility of a liquid is encoded in the shape of the potential energy landscape explored by the glassy state.

1.7 The structure of glasses and supercooled liquids: the case of GeO_2

We go more in depth into the structure of glasses by looking at the system investigated in this thesis. Vitreous germanium dioxide (germania) (v-GeO_2) is a covalent oxide glass and a prototypical strong glass-former [Ang85]. Germania is the chemical, and to some extent structural, analogue of the archetypal oxide glass silica (v-SiO_2). Compared to silica, however, germania exhibits a supercooled liquid and liquid regime that is far more experimentally accessible, with a melting temperature $T_m = 1388$ K and a glass transition temperature $T_g \simeq 818$ K [Böh+93].

GeO_2 crystalline structure

The crystalline polymorphs of GeO_2 exhibit short-range structural motifs closely related to those of the amorphous phase, making it useful to briefly review their structures.

At ambient conditions, crystalline GeO_2 exists in two polymorphisms: an α-quartz hexagonal structure [SI64] and a rutile tetragonal structure [BK71]. The α-quartz phase is the stable high-temperature polymorph and is structurally analogous to α-quartz SiO_2, although important differences are present.

In the quartz-like structure, Ge atoms are tetrahedrally coordinated. However, the GeO_4 tetrahedra are more distorted than their SiO_4 counterparts. The O–Ge–O bond angles range from 106.3° to 113.1°, with an average Ge–O–Ge intertetrahedral angle of 130.1°. In contrast, O–Si–O angles in SiO_4 tetrahedra are more uniform (from 108.3° to 110.7°), and the Si–O–Si angle is significantly larger (144.0°) [Jor78]. The two independent Ge–O bond lengths in α-quartz GeO_2 are very similar, 1.737 Åand 1.741 Å[MCH06].

The rutile polymorph is the stable room-temperature phase and transforms into the α-quartz structure at 1281 K. In rutile GeO_2, germanium is sixfold coordinated within GeO_6 octahedra. The two axial Ge–O bonds (1.902 Å) are longer than the four equatorial ones (1.872 Å) [BK71].

GeO_2 amorphous structure

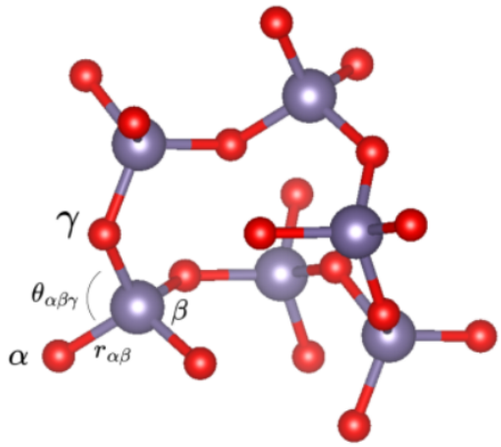

Figure 1.8: Short and medium-range order in GeO_2. Ge (purple) and O (red) atoms are arranged in structural units made by GeO_4 corner-sharing tetrahedra, here connected in a 6-memebered ring. Distance $r_{\alpha\beta}$ between atom α (O) and β (Ge) and bond angle $\theta_{\alpha\beta\gamma}$ between atoms α, β and γ are reported. Image reprinted with permission from [Zig24].

The structure of vitreous GeO_2 has been extensively characterised by neutron diffraction (ND) and x-ray diffraction (XRD) (details on the experimental techniques will be presented in the following chapters). As in the α-quartz polymorph, Ge atoms in v-GeO_2 are predominantly arranged in tetrahedral GeO_4 units. The O–Ge–O bond-angle distribution is broader than in silica and comparable to that of α-quartz GeO_2 (106.3°–113.1°) [DWS88]. This larger distortion is generally attributed to the larger ionic radius of Ge compared to Si, which allows oxygen atoms greater positional flexibility around the central cation.

The mean Ge–O–Ge intertetrahedral angle has been measured by x-ray diffraction to be $133 \pm 8.3°$ [NL96], smaller than the corresponding value in v-SiO_2. Overall, the structure of v-GeO_2 can be described as a continuous random network of corner-sharing tetrahedra, analogous to silica but more distorted and characterized by a higher proportion of three-membered rings.

X-ray diffraction studies of liquid and supercooled GeO_2 [Kam+86] show that the Ge–O bond length remains essentially unchanged with respect to the glass, consistent with the very small thermal expansion of the Ge–O bond, similarly to Si–O in silica. The GeO_4 tetrahedral units are thus preserved in the melt. However, the Ge–Ge distance increases from approximately 3.16 Å at room temperature to

3.25 Å at 1373 K. This shift is interpreted as a widening of the Ge–O–Ge bond angle upon heating.

2 X-Ray Experimental Techniques in disordered systems

This Chapter provides an overview of the X-ray–based experimental techniques used to probe the structure and dynamics of disordered systems. We begin by discussing the fundamental interaction mechanisms between X-ray photons and matter, introducing the concepts of scattering cross section and attenuation, and establishing the connection between measured signals and correlation functions.

On this basis, we present inelastic X-ray scattering (IXS), with some detail on its experimental implementation and on the inelastic ID28 beamline at ESRF. X-Ray diffraction (XRD) is rapidly introduced after IXS as it shares similar, but simpler, experimental principles. The focus here is on the XRD setups at X-ray photon correlation beamlines, which typically allows monitoring the medium-range order in the reciprocal space.

The chapter then focuses on coherent scattering techniques, introducing X-ray photon correlation spectroscopy (XPCS) as a powerful method to access slow dynamics in disordered materials. In this context, we discuss the partial coherence of synchrotron radiation, the properties of the speckle patterns generated by disordered matter, and the extraction of dynamical information through temporal correlation functions. Finally, we describe the experimental implementation of these techniques at state-of-the-art synchrotron beamlines: ID10 at ESRF and P10 at DESY.

2.1 Interaction of X-ray photons with matter

X-rays are high-frequency electromagnetic waves that interact with matter primarily through their coupling to charged particles. This interaction arises from the electric component of the electromagnetic field, which induces motion of charges. Owing to the very high frequency of X-rays, only the lightest particles, electrons, can effectively respond to the oscillating field, while the much heavier protons (about 2000 times more massive) remain essentially at rest.

Figure 2.1 shows the three main processes may happen when an X-ray photon interacts with an atom. The relevant one for scattering experiments is *Thomson scattering* (classical scattering), in which the X-ray photons induce oscillations of the electronic charge distribution. The oscillating electrons emit secondary radiation with (almost) the same frequency as the incoming photon, so that the

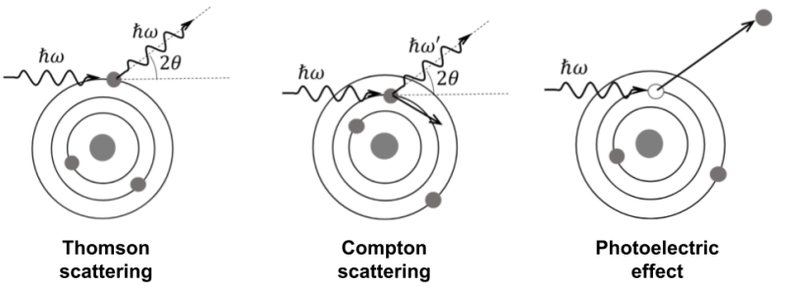

Figure 2.1: Main interaction mechanisms between X-ray photons and atoms: Thomson (elastic) scattering, Compton scattering with energy transfer to an electron, and photoelectric absorption followed by relaxation processes such as Auger emission or X-ray fluorescence.

scattered photon preserves its energy while its propagation direction changes. Other 2 interaction mechanisms may also occur: *Compton scattering*, where the photon transfers part of its energy to an electron, and *photoelectric absorption*, in which the photon is completely absorbed, and an electron is ejected from the atom. To revert to a stable state, the atom must then fill the hole in the inner shell by rearranging the electron orbitals via the transition of an electron from one of the outer orbitals to fill the core vacancy. The excess energy can be given off either by the emission of other photoelectrons from an outer shell orbital, the Auger effect, or by emitting a photon, the X-rays fluorescence.

X-ray photons Thomson scattered have (almost) the same frequency as the incident photons, and their phases are fixed with the phases of the incident photons. This means that the Thomson scattered photons are also able to interfere with each other, as long as the incident radiation is coherent. For this reason, Thoomson scattering is often referred as coherent scattering. In contrast to that, Compton scattering and fluorescence are called incoherent scattering and are generally treated as a background in scattering experiments.

The probability of these scattering processes is quantified in terms of the *scattering cross section*, which represents the effective area that a scatterer presents to the incident radiation. The atomic scattering cross section can be written as the sum of the cross sections corresponding to the interaction processes described above,

$$\sigma_{\text{tot}} = \sigma_{\text{Thom}} + \sigma_{\text{Com}} + \sigma_{\text{ph}}. \tag{2.1}$$

An X-ray beam of intensity I_0 passing through a material slab of thickness d is

attenuated due to scattering and absorption according to the Lambert–Beer law

$$I = I_0 e^{-\mu d}, \tag{2.2}$$

where μ is the linear attenuation coefficient,

$$\mu = \frac{\rho N_A}{M} \sigma_{\text{tot}}, \tag{2.3}$$

with ρ the mass density (g/cm^3), $N_A = 6.022 \times 10^{23}$ mol^{-1} the Avogadro number, and M (g/mol) the atomic mass. The characteristic length $l = 1/\mu$, over which the intensity decreases to $1/e \simeq 0.37$, is referred to as the *attenuation length*.

For X-ray energies below approximately 100 keV (those we will work with within this thesis), Compton scattering is generally negligible. For photon energies above a few keV and for most elements ($Z > 4$), the total absorption cross-section is dominated by photoelectric absorption processes (which scales as Z^4) rather than by Thomson scattering (which scales as Z^2).

Optimizing the Thomson scattering

I n an experiment, the Thomson scattered signal can be maximized by choosing an optimal sample thickness d^* that balances the increase in scattering probability with the reduction caused by beam absorption. Considering $\mu_{\text{ph}} \gg \mu_{\text{Thom}}$, the Thomson scattering can be linearized, and, accounting for absorption, we can write

$$I_{\text{Thom}} \propto I_0 (\mu_{\text{Thom}} d)\, e^{-\mu_{\text{ph}} d}.$$

The maximum value of I_{Thom} is obtained the optimal thickness

$$d^* = \frac{1}{\mu_{\text{ph}}}.$$

If, on the one hand, the high absorption of X-rays forces the use of thin samples, thus limiting the Thomson scattered signal, on the other hand it makes multiple scattering events generally negligible compared to neutron and light scattering.

2.2 Theory of the X-ray scattering processes

Spectroscopy experiments are among the most powerful tools for investigating the properties of matter. A beam of X-ray photons characterized by a narrow energy

spread, small angular divergence, and well-defined polarization impinges on a sample and is scattered in all directions. A detector counts the particles scattered at an angle 2θ within a small solid angle $d\Omega$ (see Fig. 2.2). Before reaching the detector, the scattered particles may pass through optical elements that control their properties: monochromators and analyzers select the energy, collimators restrict the angular divergence, and, in some cases, polarizers select the polarization state.

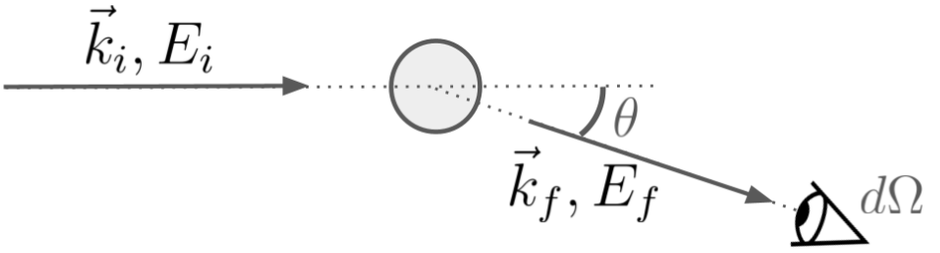

Figure 2.2: Schematic representation of a generic scattering experiment.

The instrument used to perform such measurements is referred to as a *spectrometer* (or diffractometer if no fianl energy selection is performed), whose complexity clearly depends on the physical problem under investigation. Regardless of the specific experimental configuration, the ultimate goal is to probe the properties of the sample through the detection of particles that have interacted with it via a scattering event. During this interaction, the energy of the probe particles may either remain unchanged or be exchanged with the sample, corresponding to *elastic* and *inelastic* scattering, respectively[3]. Here, it is useful to define the energy and wave vector (momentum) exchanged within the scattering process as

$$\hbar\omega = E_i - E_f, \qquad \vec{Q} = \vec{k}_i - \vec{k}_f, \qquad Q = |\vec{Q}| = \frac{4\pi}{\lambda} sin\frac{\theta}{2} \tag{2.4}$$

In general, the interaction time between probe and target system can be assumed to be much shorter than any other timescale relevant to the experiment. The scattering process can therefore be approximated as an instantaneous collision between the incident X-ray beam and the scatterers (electrons of the atoms or molecules of the sample). This approximation holds strictly for X-rays, whereas for thermal neutrons corrections must be introduced to account for the finite interaction time relative to the characteristic timescales of matter excitations.

3 The inelastic processes we are referring here, and from now on, are inelastic on the scale of meV - few eV, i.e. the typical excitations of matter. In these terms, also Thomson scattering may be inelastic.

We now consider a scatterer located at the origin, infinitely massive and at rest. The incident electromagnetic radiation is described as a plane wave impinging on the scatterer. As a consequence of the interaction with the electric field, the scatterer re-radiates the electromagnetic radiation following the inhomogeneous Helmholtz equation [Cun16]. Therefore, at large distances $r = |\mathbf{r}|$ from the origin, the resulting field can be interpreted as the superposition of the transmitted plane wave and a spherical wave emitted by the scatterer of the form $\psi_{\text{sc}} \propto \frac{e^{ikr}}{r}$ where k is the wave number of the scattered radiation. In this picture, the scattering event can be viewed as a process in which photons are partially removed from the incident plane wave and re-emitted as spherical waves originating from the scatterer, similarly to the Huygens principle of optics [Cun16].

The photons scattered at an angle 2θ within a solid angle $d\Omega$ pass through the energy filter (analyzer) and are finally detected after impinging on the sensitive area of the detector $dA = r^2 d\Omega$. The intensity scattered into the solid angle within an energy interval dE_f can be written as

$$I = K I_0 \frac{\partial^2 \sigma}{\partial \Omega \, \partial E_f} \, d\Omega \, dE_f, \tag{2.5}$$

where I_0 is the intensity of the incident beam impinging on the sample, and K is a factor accounting for detector efficiency, sample self-absorption, and other geometrical and instrumental effects. Here we also define the *double differential scattering cross-section*:

$$\frac{\partial^2 \sigma}{\partial \Omega \, \partial E_f} = \frac{\text{rate of photons scattered into } d\Omega \text{ with final energy in } E_f \text{ and } E_f + dE_f}{I_0 \, d\Omega \, dE_f}$$

The explicit form of the double differential scattering cross-section can be obtained by considering the interaction between the electromagnetic radiation and the electronic charge density of the sample within the framework of quantum electrodynamics, using the Fermi's golden rule. The derivation involves evaluating the transition probability between the initial and final photon–matter states using perturbation theory. In the case of X-ray scattering from disordered condensed matter some approximations can be introduced [Cun16]:

1. The dominant interaction mechanism is assumed to be Thomson scattering. This approximation is valid in the non-resonant regime and for photon energies far from electronic absorption edges, i.e. neglecting florescence phenomena.

2. The *Born–Oppenheimer approximation* is employed, allowing the electronic and nuclear degrees of freedom to be separated. In this framework, the electrons are assumed to instantaneously follow the motion of the much heavier nuclei, so that the electronic charge distribution can be expressed as a function of the instantaneous atomic positions. Closely related to this is the *adiabatic approximation*, which allows the electronic contribution to be incorporated into an effective atomic form factor $f(Q)$.

3. Liquids and disordered systems are isotropic. As a consequence, the scattering signal depends only on the magnitude of the momentum transfer $Q = |\mathbf{Q}|$ rather than on its direction.

Under these assumptions, the double differential X-ray scattering cross-section for a disordered system composed of a single atomic species can be written in terms of correlation functions, specifically in terms of the dynamic structure factor defined in Sec. 1.4.2:

$$\boxed{\frac{\partial^2\sigma}{\partial\Omega\,\partial E_f} = r_e^2\,\frac{k_f}{k_i}\,|\hat{\boldsymbol{\epsilon}}_i\cdot\hat{\boldsymbol{\epsilon}}_f|^2\,|f(Q)|^2\,S(Q,\omega)} \tag{2.6}$$

Here, $r_e = e^2/(mc^2)$ is the classical electron radius, i.e. the Thomson atomic cross section, k_i (k_f) is the incident (scattered) photon wave number, and $\hat{\boldsymbol{\epsilon}}_i$ and $\hat{\boldsymbol{\epsilon}}_f$ are the polarization unit vectors of the incident and scattered photons: the factor $|\hat{\boldsymbol{\epsilon}}_i\cdot\hat{\boldsymbol{\epsilon}}_f|^2$ is the polarization dependence of Thomson scattering. The quantity $f(Q)$ is the atomic (electronic) form factor, obtained as a Fourier transform of the electronic cloud density of the atom

$$f(Q) = \int \rho_e(\vec{r})e^{i\vec{Q}\cdot\vec{r}}d\vec{r} \tag{2.7}$$

Finally, $S(Q,\omega)$ is the same dynamic structure factor defined in Sec. 1.4.2.

The cross-section of Eq. 2.6 is valid for a system composed of a single atomic species. This derivation can however be generalized to molecular or crystalline systems by replacing the atomic form factor with either the molecular form factor or the unit-cell form factor, respectively. The situation becomes more complex when the system is multi-component and disordered. In this case, the factorization of the form factor leads to the appearance of an incoherent contribution in the X-ray scattering cross-section [Cun16].

2.3 X-ray inelastic scattering

The target of inelastic X-ray scattering is to measure the dynamic structure factor exploiting the relation of Eq. 2.6. However, while the highest frequency vibrations in these experiments are in the Thz region ($\hbar\cdot$Thz$\sim$ meV), as, for example, the longitudinal sound propagation at the interatomic distances, the typical X-ray energy used is of the order of tens of keV. To detect these phenomena within the dynamic structure factor we therefore have to distinguish X-ray photons with keV energy differing of few meV ($\Delta E/E \sim 10^{-7}$). The energy resolution requirements of IXS instruments are therefore very demanding both for the incident X-rays monochromaticity and for the energy analysis of the scattered photons.

An effective method to obtain X-rays with high resolving power is based on Bragg reflection from perfect crystals. It can be shown that the resolving power is given by [Cun16]

$$\frac{\Delta E}{E} = \frac{d_{hkl}}{\pi L_{ext}} \tag{2.8}$$

where d_{hkl} denotes the lattice spacing associated with the Bragg reflection (hkl), and L_{ext} is the extinction length, the characteristic depth inside a perfect crystal over which the incident X-ray wave is converted into the diffracted wave through multiple coherent scattering events (for example, the (111) reflection of Si has an extinction length of 7.2 μm for 1.54 Å X-rays). L_{ext} increases with increasing reflection order. Therefore, to achieve a high energy resolving power it is necessary to employ high-order Bragg reflections [Zac44]. Also, Eq. 2.8 requires the use of highly *perfect crystals*, i.e. a crystal for which defects or distortions produce relative variations of the lattice spacing $\Delta d/d$ smaller than the desired relative energy resolution. Such a requirement restricts the choice of materials to silicon single crystals.

Furthermore, to preserve the energy resolution without significantly reducing the photon flux, the divergence of the incoming photon beam must fall within the intrinsic angular acceptance of the monochromator reflection, called the Darwin width ω_D. Within the dynamical theory of X-ray diffraction [Zac44], this quantity is given by

$$\omega_D = \left(\frac{\Delta E}{E}\right)_h \tan\theta_B, \tag{2.9}$$

where h and θ_B denote the Bragg reflection order and the Bragg angle, respectively. Since $\tan\theta_B$ diverges for $\theta_B \to 90°$, approaching a backscattering geometry leads to a strong increase of the Darwin width. In backscattering geometry, ω_D become

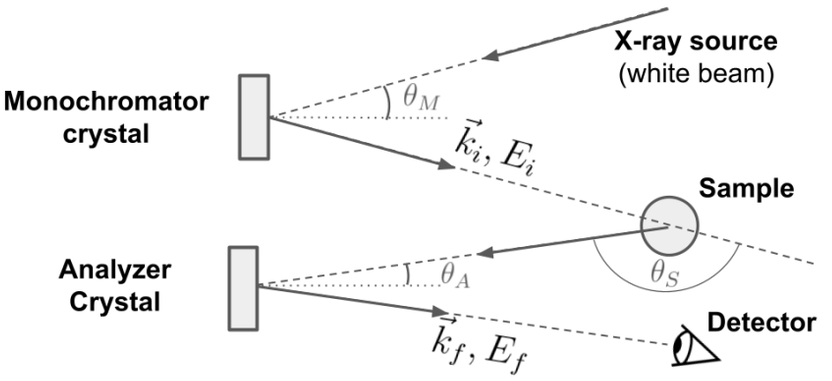

Figure 2.3: Schematic layout of an inelastic X-ray scattering (IXS) spectrometer based on the triple-axis concept. The monochromator selects the incident energy E_i, the sample defines the momentum transfer $\mathbf{Q}$, and the analyzer determines the scattered photon energy E_f.

large enough to accept the angular divergence of the X-ray beam delivered by standard undulator sources.

As shown in Fig. 2.3, the design of an IXS spectrometers is based on the concept of three-axis spectrometers. The first axis is located at the monochromator crystal to select the energy of the incident photons, E_i. Rotations around the second axis, located at the sample position, change the momentum transfer $\mathbf{Q}$. Finally, the third axis corresponds to the analyzer crystals and selects the energy of the scattered photons, E_f. Differently from the traditional triple-axis schemes, where energy scans of the scattered intensity are performed through rotations of the analyzer crystal, modern IXS beamlines vary the d-spacing of the reflecting crystals by changing their temperature. Here, achieving a relative energy resolution of 10^{-7}–10^{-8} requires millikelvin accuracy in the temperature control of the monochromator and analyzer crystals.

2.3.1 The ID28 beamline at ESRF

The measurements discussed in this thesis are taken at the ID28 beamline of the European Syncrothron radiation source (ESRF). The beamline layout is outlined in Fig. 2.4. The ID28 X-ray source consists of three undulators with a magnetic period of 32 mm, installed in a straight section of the electron storage ring. The

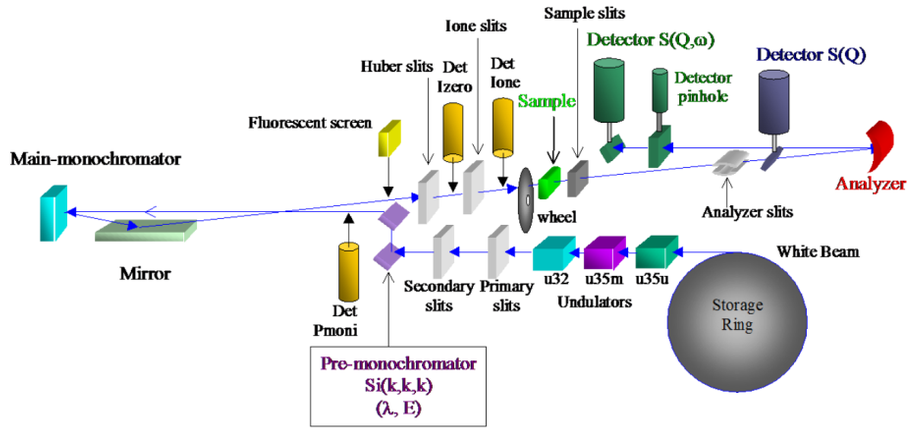

Figure 2.4: Schematic design of the ID28 beamline experimental apparatus. Figure taken from the ID28 user manual [Eur15].

photon energies used in the experiment correspond to the third or fifth harmonic of the undulator radiation. At these harmonics the emitted beam has a relative bandwidth $\Delta E/E \approx 10^{-2}$, an angular divergence of approximately $40 \times 15\ \mu$rad, and an integrated power of about 200 W [Cun16] (see more information of synchrotron X-Ray production in Fig. 2.9).

Before reaching the high-resolution optics, the beam is pre-monochromatized to $\Delta E/E \approx 2 \times 10^{-4}$ by means of a cryogenically cooled silicon Si(111) channel-cut crystal. The primary role of this element is to absorb most of the incident power, reducing the heat load on the main monochromator to minimize thermal distortions that would otherwise degrade the energy resolution. At present, after the EBS synchrotron upgrade at ESRF, this is one of the main challenges of the beamline: working with all three undulators without degrading the resolution because of heat load of the main monochromator.

The pre-monochromatized beam is subsequently reflected by the high-resolution main monochromator, which consists of an asymmetrically cut silicon crystal oriented along the [111] direction and operated in backscattering geometry at a Bragg angle of approximately $\theta_B = 89.98°$. In this configuration, the angular acceptance of the monochromator becomes larger than the divergence of the incoming beam, ensuring that all photons are reflected within the selected energy bandwidth. As already mentioned, achieving the required relative resolution $\Delta E/E \sim 10^{-7}$–10^{-8} requires the use of high-order Bragg reflections (h, h, h) with $h = 7, 8, 9, 11, 12, 13$.

The monochromatic beam is then focused at the sample position by a toroidal mirror (mirror with two different curvatures) located approximately 25 m before the

sample. Under standard conditions the beam size at the sample is about $250 \times 80\ \mu m^2$ (FWHM), but by focusing optics $10 \times 10\ \mu m^2$ beam sizes are achievable.

The energy of the photons scattered by the sample is analyzed by a set of nine spherical analyzers mounted at the end of a horizontal arm. The arm can be rotated by an angle 2θ to select the desired momentum transfer. These nine analyzer units have a mutual angular offset, which permit the simultaneous collection of IXS spectra at nine different Qs.

The required energy resolution is the same for both the monochromator and the analyzer, but the required angular acceptance is significantly different. For the analyzer, the optimal angular acceptance results from a compromise between count rate and momentum resolution: while reducing the angular acceptance improves the momentum resolution, it simultaneously decreases the detected photon flux. In typical IXS experiments, an acceptable momentum spread at low Q is $\Delta Q \lesssim 0.1$–$0.5\ nm^{-1}$. This corresponds to an analyzer angular acceptance of a few milliradians (working at keV energies), which is much larger than the Darwin width of the Bragg reflections commonly employed. Achieving such a large acceptance therefore requires the use of a focusing optical system. On ID28 this is accomplished by using a spherical analyzer composed of a mosaic of $\sim 12\,000$ small silicon square single-crystal glued onto a spherical surface. Each analyzer is then equipped with motorized entrance slits that define the Q-resolution, and focus the backscattered radiation on the cooled silicon diodes placed on the side of the sample.

The spectrometer arm rotates around the sample's vertical axis and can reach scattering angles up to about 55°. The best measured instrumental energy resolution has a full width at half maximum of about 1.5 meV, which is suitable for investigating the high-frequency dynamics of disordered systems. The typical shape of this energy resolution feature long tails following a Lorentzian (or better Voight) function.

2.4 X-ray Diffraction

X-ray diffraction (XRD) experiments consist of a monochromatic X-ray source that illuminates the sample, and a detector that collects the scattered radiation regardless of the energy. During the measurement the scattering angle can be varied by rotating the detector around the sample. The detector can be either a single-area detector or, more commonly, a two-dimensional pixel detector so that the scattered intensity can be recorded simultaneously over a range of angles.

In X-ray diffraction experiments the detector measures the scattered radiation without resolving the energy of the photons. As a consequence, Eq. 2.6 must be

integrated over all possible final energies,

$$\boxed{\frac{d\sigma}{d\Omega} = \int \frac{\partial^2\sigma}{\partial\Omega\,\partial E_f}\,dE_f = r_e^2\,|\hat{\boldsymbol{\epsilon}}_i \cdot \hat{\boldsymbol{\epsilon}}_f|^2 |f(Q)|^2 S(Q)} \tag{2.10}$$

Therefore, X-ray diffraction directly probes the static structure factor defined in Eq. 1.11. We recall that this equation holds for monoatomic and isotropic systems.

Differently, single crystals are characterized by a periodic arrangement of atoms organized in lattice planes. Constructive interference of the scattered waves occurs when the Bragg condition is satisfied,

$$2d_{hkl}\sin\theta/2 = n\lambda, \tag{2.11}$$

where d_{hkl} is the spacing between lattice planes with Miller indices (hkl) and λ is the X-ray wavelength. In crystalline systems this relation acts as a selection rule for the allowed scattering directions. As a consequence, the scattered intensity cannot be expressed solely as a function of the modulus Q, and consists of a series of sharp Bragg peaks reflecting the periodic atomic arrangement. In this case the orientation of the crystal also plays an important role, since rotating the sample moves the Bragg spots circularly with respect to the beam axis.

In powder diffraction the sample consists of many small crystallites randomly oriented with respect to the incident beam. As a consequence, for each set of lattice planes there is always a subset of crystallites that satisfies the Bragg condition. The diffracted intensity is therefore distributed over all azimuthal angles, giving rise to concentric rings in reciprocal space known as Debye–Scherrer rings (see the left panel of Fig. 2.5).

In contrast, as discussed in the first chapter, amorphous materials lack of long-range periodic order and are therefore isotropic, with no preferred crystallographic directions. Their scattering pattern does not show sharp Bragg peaks but is instead characterized by a broad diffuse maximum at low momentum transfer, often referred to as the first sharp diffraction peak [Ell91], followed by weaker and broader features at larger Q (see the right panel of Fig. 2.5).

2.4.1 Diffraction at XPCS beamlines

Typical XPCS beamlines allow the sample structure to be monitored using a dedicated diffraction detector (see, for example, the ID10 beamline at ESRF or P10 at DESY). These detectors are usually placed on the free side of the scattering plane—i.e. the side not occupied by the fast XPCS detector—and, when measuring

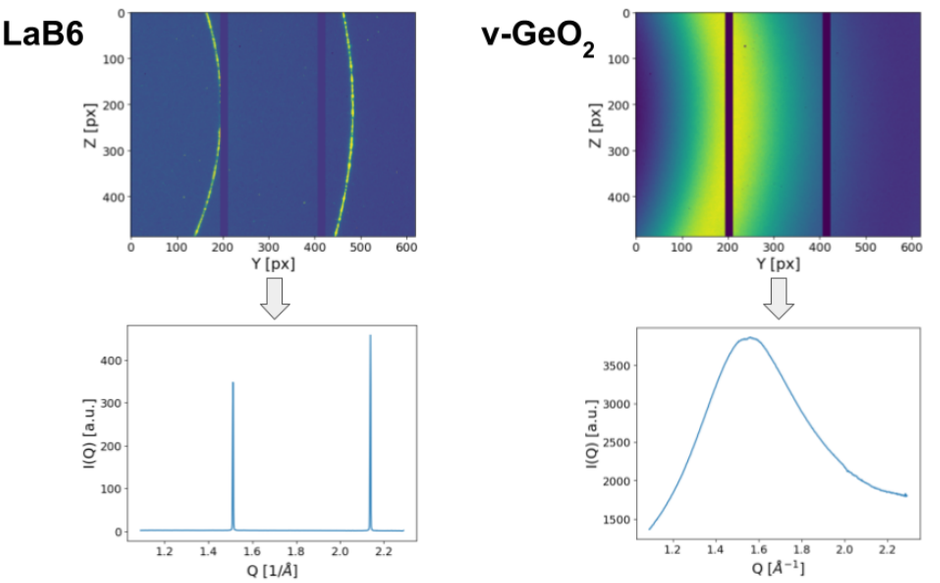

Figure 2.5: Examples of diffraction measurements taken at the ID10 beamline. Left: powder diffraction pattern of the LaB_6 (lanthanum hexaboride) calibrant used for detector calibration. Right: diffraction pattern of vitreous GeO_2 at room temperature, displaying the broad features characteristic of amorphous systems.

disordered systems, as close as possible to the sample in order to maximize the accessible momentum transfer range. However, due to the relatively low photon energies typically used in XPCS experiments (see next section), the accessible Q window generally extends from about 0.5 $Å^{-1}$ to a few inverse angstroms. This range mainly allows the observation of the first sharp diffraction peak (FSDP) in disordered systems.

The detector commonly employed for this purpose is the Dectris Pilatus detector [Kra+09], which is the standard configuration at the ESRF ID10 beamline. In our recent experiment at the DESY P10 beamline, however, the fast XPCS detector (Dectris Eiger 500k) [Din+11] was used instead.

The detector is mounted as close as possible to the sample, typically at a distance of about 15–20 cm. Small-angle scattering is often difficult to access because several components—such as the beamstop, transmission diode, and fast detector—occupy the central region of the scattering plane and limit the available solid angle.

Examples of diffraction measurements performed at the ID10 beamline are shown in Fig. 2.5. The left panel displays the powder diffraction pattern of a LaB_6 (lanthanum hexaboride) calibration sample [Nat15]. Using the `pyFAI` software package

[Ash+15], developed at ESRF, and by identifying the crystalline planes that generate at least two Debye–Scherrer rings on the detector, it is possible to determine the correct azimuthal integration that maps the detector pixels into reciprocal $|Q|$ space. The result of this integration is shown below the detector image of LaB_6, where the Debye–Scherrer rings are converted into sharp peaks in reciprocal space. Once the detector geometry is calibrated, the diffraction detector can be used to monitor the structure of the sample under investigation, as illustrated in the right panel of Fig. 2.5.

2.5 X-ray Photon Correlation Spectroscopy

To derive the differential cross-section equation of Eq. 2.6, we assumed the isotropicity of disordered matter and lost the vector dependence on the exchanged momentum $\hbar\vec{Q}$. Later, we derived the energy integrated equation for the cross section (Eq. 2.10) that relates the direction of the scattered photons, regardless of their energy, with the structure of the system. Also here, no vector dependence appears. However, when working with coherent radiation, as visible in Fig. 2.6, the scattering intensity $I(\vec{Q})$ defined in Eq. 2.10 can retain the orientational dependence of the scattering vector $\vec{Q}$. The structure factor $S(Q)$ usually reported for glasses in the case of coherent radiation corresponds to the orientational average $S(Q) \propto \langle I(\vec{Q}\rangle_Q$ where $\langle \cdots \rangle_Q$ is the average over the orientation of the wavevector at a fixed magnitude Q. This vector dependence of the scattered intensity forms the basis of X-ray photon correlation spectroscopy.

If coherent light (either X-rays or visible) is scattered from a disordered system it gives rise to a random diffraction or 'speckle' pattern (see the example in Fig. 2.6). Speckle patterns are related to the exact spatial arrangement of the (disorderdered) atoms [Pec85]. Such information is not accessible with incoherent light because, in this case, the diffraction pattern observed is an average containing information on the correlations in the sample only, and interference phenomena do not superimpose the diffraction pattern. Then, if the spatial arrangement of the disorder changes with time the corresponding speckle pattern will also change and the intensity fluctuations of the speckles provide information on the underlying dynamics.

X-ray Photon Correlation Spectroscopy (XPCS) probes the dynamic properties of matter by analyzing the temporal correlations among photons scattered by the studied material. It can measure the low frequency dynamics, from μs up to few hours, in a Q range from typically 10^{-3} Å^{-1} up to several Å^{-1}, depending on the sample and the scattering geometry.

Figure 2.7 shows the frequency-scattering vector range accessible by this tech-

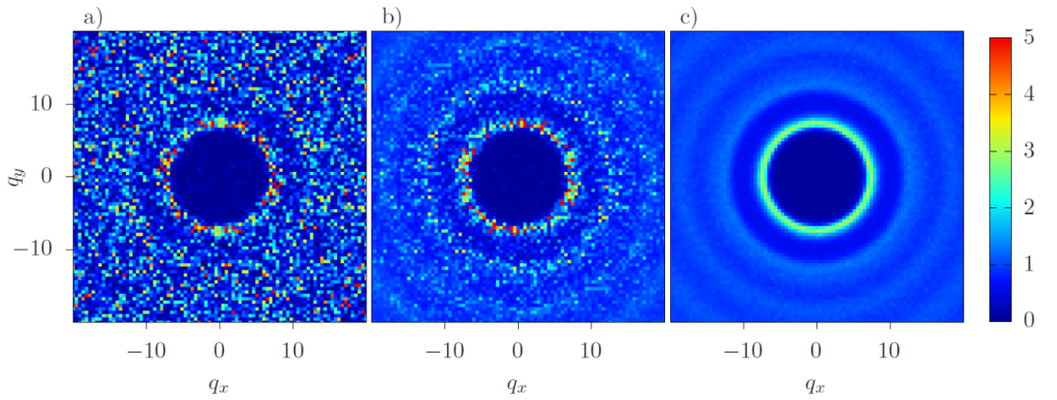

Figure 2.6: Simulated scattering intensity $S(\vec{Q})$ with intensities indicated by color as shown, in the (q_x ,q_y) plane for three reduced temperatures a) T = 0.0 b) T = 0.3 and c) T = 0.6 for a binary $A_{80}B_{20}$ model glass former (more details in ref. [PH23]). The reduction of the intensity fluctuations (speckle) with increasing temperature is evident. Figure reprinted with permission from [PH23].

nique compared to other methods frequently used to study the dynamics in disordered systems. X-ray Photon Correlation Spectroscopy is in particular complementary to Photon Correlation Spectroscopy (PCS) with visible coherent light which probes also slow dynamics (μ s to hours) but can cover only the small $Q < 4 \cdot 10^3$ Å^{-1}) regime [Pec85]. As we previously discussed, XPCS is furthermore not subject to multiple scattering, a phenomenon frequently complicating the analysis of PCS data in optically opaque systems. As we have seen, Inelastic X-Ray Scattering, as well as neutron based techniques (inelastic and quasi-elastic neutron scattering, neutron spin-echo), can access a similar Q range of XPCS but probe the dynamic properties of matter at high frequencies.

2.5.1 Partially coherent X-rays from synchrotron sources

Coherence controls the ability of scattered waves to interfere constructively or destructively and is therefore essential for extracting dynamical information from speckle fluctuations. Real X-ray beams from synchrotron sources, however, are only partially coherent: unlike optical lasers, they have a finite spectral bandwidth and a finite angular divergence. These two deviations from the ideal monochromatic plane wave limit the beam coherence in time and space and thus determine the experimentally accessible coherence lengths [Jae+16].

Accordingly, the coherence of an X-ray beam is characterized by one longitudinal

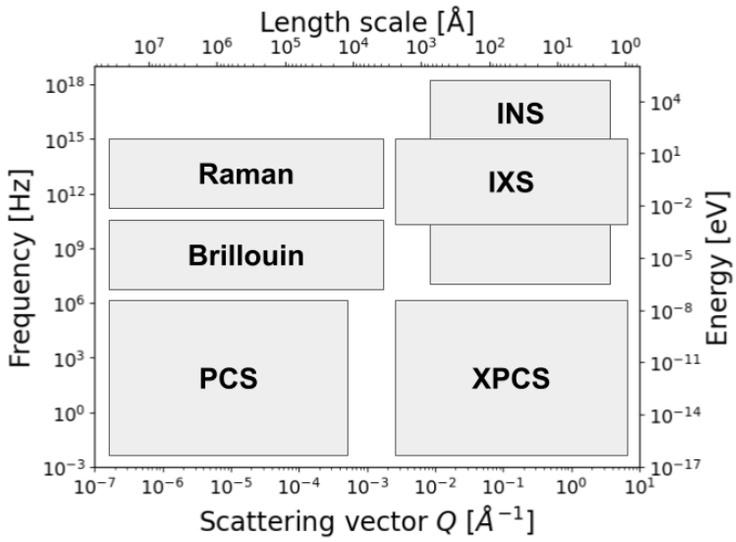

Figure 2.7: Frequency–Scattering vector space covered by X-ray Photon Correlation Spectroscopy (XPCS) and complementary techniques (PCS-Photon Correlation Spectroscopy, INS-Inelastic Neutron Scattering and IXS-Inelastic X-ray Scattering).

coherence length, L_L, and two transverse coherence lengths, $L_T^{(y)}$ and $L_T^{(z)}$ (horizontal and vertical).

The longitudinal coherence length originates from the finite relative bandwidth $\Delta\lambda/\lambda$ and, for two waves of wavelengths λ and $\lambda - \Delta\lambda$ propagating in the same direction (Fig. 2.8, left), one finds under the approximation $\Delta\lambda \ll \lambda$:

$$L_L = \frac{\lambda^2}{2\,\Delta\lambda}.$$

The transverse coherence length arises from the finite angular spread $\Delta\theta$ (or, thanks to the Huygens principle, the finite apparent source size) and, for two rays separated by an angle $\Delta\theta$ (Fig. 2.8, right), is written as

$$L_T = \frac{\lambda}{2\,\Delta\theta}.$$

In practice, achievable coherence lengths depend both on the source parameters and on beamline optics. For example, at third-generation synchrotrons the vertical source size is typically of order 100 μm: for an experimental station placed $\sim$ 20 m

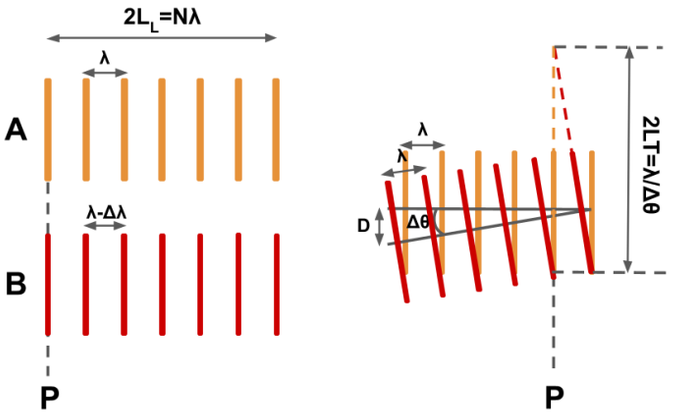

Figure 2.8: Coherence of an X-ray beam. Left: longitudinal coherence arises from finite spectral bandwidth; two waves with slightly different wavelengths accumulate a relative phase shift along propagation and become uncorrelated beyond L_L. Right: transverse coherence arises from finite angular divergence (or finite source size); rays separated by angle $\Delta\theta$ lose phase correlation across the wavefront over a distance L_T.

downstream this implies a vertical transverse coherence length of order $L_T^{(z)} \sim 10\ \mu$m for $\lambda = 1$ Å. The longitudinal coherence length is set by the monochromator bandwidth: a Si(111) double-crystal monochromator commonly delivers $\Delta\lambda/\lambda \sim 10^{-5}$, giving $L_L \sim 5\ \mu$m at $\lambda = 1$ Å [GMR08; Jae+16].

The dimension of the source and the intensity of the coherent photon flux intrinsically depends on the X-Ray production mechanism. Synchrotron radiation is generated when relativistic electron bunches are deflected by magnetic fields. Bending magnets emit broad angular and spectral radiation, while insertion devices such as undulators force electrons onto a periodic (sinusoidal) trajectory of period λ_u, producing radiation confined to a much narrower angular and spectral window (Fig. 2.9). For bending magnets, typical brilliances are $B \sim 10^{12}$–10^{14} ph/s/(mrad)^2/mm^2/0.1%BW. In contrast, undulator beamlines can reach brilliances exceeding $B \sim 10^{21}$ ph/s/(mrad)^2/mm^2/0.1%BW [GMR08]. The high brilliance of these sources is the key factor that enables coherent X-ray scattering experiments despite the intrinsically low coherence.

2.5.2 Static speckle patterns in disordered systems

As anticipated, when a coherent electromagnetic beam is scattered by a disordered system, it can give rise to a random diffraction pattern, commonly referred to as a

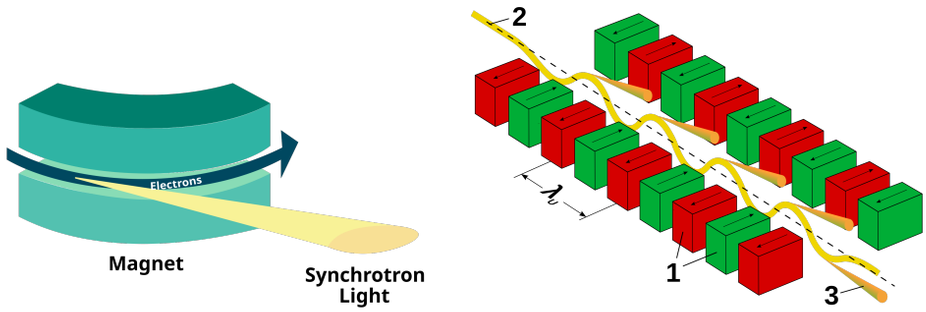

Figure 2.9: Schematic representation of synchrotron radiation generation. Left: electrons accelerated to relativistic energies are guided along a circular trajectory by bending magnets, emitting X-rays tangentially to their path. Right: insertion devices, such as undulators, force electrons onto a sinusoidal trajectory, enhancing the brilliance and coherence of the emitted radiation. Reproduced from Ref. [BP; Hol] under CC BY 3.0 and CC BY-SA 3.0 licenses, respectively.

speckle pattern. Such patterns originate from the interference of waves scattered with different phases, produced by independent regions within the illuminated volume, which may also evolve in time.

Let us consider a coherent beam with incident wave vector $\vec{k}_i$, scattered by a disordered sample into an outgoing wave vector $\vec{k}_f$. The instantaneous intensity measured in the far field at a given detector position can be expressed as the squared modulus of the total scattered electric field $E(\vec{Q}, t)$:

$$I(\mathbf{Q}, t) = |E(\vec{Q}, t)|^2 = r_e^2 \, |\hat{\boldsymbol{\epsilon}}_i \cdot \hat{\boldsymbol{\epsilon}}_f|^2 \left| \sum_n f_n(\vec{Q}) \exp\left[i\vec{Q} \cdot \vec{r}_n(t) \right] \right|^2, \tag{2.12}$$

where $f_n(\mathbf{Q})$ denotes the scattering amplitude of the n-th scatterer located at position $\mathbf{r}_n(t)$. The summation extends over all scatterers within the illuminated volume, assuming the incident beam is fully coherent over this region.

In an experiment, the measured intensity corresponds to a time average $\langle I(\vec{Q}, t) \rangle_T$ over the acquisition time T, rather than to an ensemble average. For non-ergodic systems, i.e., systems with static disorder, this time-averaged intensity exhibits strong fluctuations as a function of $\vec{Q}$, which constitute the speckle pattern (see the first two patterns in Fig. 2.6). Conversely, if the system is ergodic and its intrinsic fluctuations occur on time scales much shorter than the measurement time, the time average becomes equivalent to an ensemble average. In this case, $\langle I(\mathbf{Q}, t) \rangle_T$ can be

replaced by the ensemble-averaged intensity $\langle I(\mathbf{Q}, t)\rangle$, and the resulting scattering pattern appears smooth, reflecting only the average structural correlations in the sample, as in conventional experiments with incoherent radiation (see the last pattern in Fig. 2.6).

A static speckle pattern carries information not only about the structural disorder of the sample, but also on the properties of the incident radiation, such as its degree of coherence and the size of the illuminated volume. For a fully coherent beam, it can be demonstrated [GMR08] that the intensity measured at a given point in the speckle pattern follows negative exponential statistics, provided that the scattering amplitudes $b_n(\vec{Q})$ and the phases $\vec{Q} \cdot \vec{r}_n$ (see Eq. 2.12) are statistically independent and that the phases are uniformly distributed over the interval $[0, 2\pi]$. Under these conditions, the probability distribution of the intensity $P(I)$ takes the form

$$P(I) = \frac{1}{\langle I\rangle} \exp\left(-\frac{I}{\langle I\rangle}\right), \tag{2.13}$$

where $\langle I\rangle$ denotes the mean intensity. The corresponding standard deviation is given by $\sigma = \left(\langle I^2\rangle - \langle I\rangle^2\right)^{1/2} = \langle I\rangle$. The ratio $\beta = \sigma^2/\langle I\rangle^2$ provides a measure of the *speckle contrast*. Under fully coherent conditions, this quantity reaches unity, indicating maximum contrast. In practice, speckle patterns are recorded by 2D pixel detectors. In this way, the photon statistics can be analyzed by grouping pixels that correspond to the same momentum transfer Q, effectively averaging over an ensemble of equivalent speckles.

The finite pixel size limits the spatial resolution. If the observed intensity pattern results from the sum of M independent speckle patterns, the intensity distribution generalizes to the gamma distribution [Goo84]

$$P_M(I) = \frac{M^M I^{M-1}}{\langle I\rangle^M \Gamma(M)} \exp\left(-\frac{MI}{\langle I\rangle}\right), \tag{2.14}$$

where $\Gamma(M)$ is the gamma function. This distribution has the same mean $\langle I\rangle$ but a reduced variance $\sigma^2 = \langle I\rangle^2/M$, implying $\beta = 1/M$. This model describes partially coherent speckle patterns with good photon counting statistics.

Physically, M can be approximated as the ratio between the scattering volume and the coherence volume $L_L \cdot L_T^{(y)} \cdot L_T^{(z)}$. The limiting case of perfect contrast ($\beta = 1$) corresponds to a scattering volume equal to the coherence one. A reduction in contrast ($M > 1$) may also arise from detector effects, such as pixel sizes larger than the speckle size, leading to a smearing of the speckle pattern. Therefore, M

accounts for coherence losses originating both from the incident beam and from the detection system.

In the regime of weak speckle patterns dominated by photon counting noise (with discrete photon numbers $k = 0, 1, 2, \ldots$ per pixel), the gamma distribution must be convolved with the Poisson distribution ruling the photon shot noise leading to the Poisson–gamma distribution (also known as the negative binomial distribution) for integer k:

$$P_P^M(k) = \frac{\Gamma(k+M)}{\Gamma(M)\Gamma(k+1)} \left(\frac{M}{M+\langle k\rangle}\right)^M \left(\frac{\langle k\rangle}{M+\langle k\rangle}\right)^k. \tag{2.15}$$

For low photon counts and weak speckle contrast (large M), which is the typical situation in coherent X-ray experiments, distinguishing Poisson–gamma statistics from pure Poisson noise becomes challenging. This difficulty constitutes the main limitation of a technique closely related to XPCS, namely X-ray speckle visibility spectroscopy (XSVS), which probes sample dynamics by measuring the reduction of speckle contrast in images recorded with progressively longer exposure times T. In this approach, detector images must be carefully processed to correctly assign photon numbers to each pixel. In particular, spurious signals such as parasitic scattering or background counts from environmental radioactivity can lead to a systematic underestimation of the speckle contrast if not properly removed.

By contrast, as we now see, XPCS extracts dynamical information by computing temporal correlations of the scattered intensity. This procedure effectively separates the speckle signal from shot noise and background contributions, since these unwanted signals are temporally uncorrelated, whereas the speckle pattern retains time correlations that reflect the dynamics of the sample.

Finally, the speckle size plays a crucial role in determining the measured contrast, as controls the number of speckles per detector M. The linear speckle size at the detector plane, often associated with the transverse coherence length, is approximately given by [Pec85]

$$\sigma_s \sim \frac{\lambda D}{d}, \tag{2.16}$$

where λ is the X-ray wavelength, D is the sample-to-detector distance, and d is the effective source size. To maximize the detected contrast, the detector pixel size should be matched to σ_s. If the pixel size is significantly larger than the speckle size, multiple speckles are averaged within a single pixel, leading to a reduction in the measured contrast.

2.5.3 From speckle patterns to XPCS

If the spatial configuration of the scatterers evolves in time, the corresponding speckle pattern will also fluctuate. Measuring these intensity fluctuations provides direct insight into the system dynamics. Temporal correlations are commonly quantified through the normalized second-order intensity autocorrelation function, which quantifies the correlation between intensity values at times separated by a lag t. Considering a point-like detector measuring the intensity $I(\vec{Q},t)$ at a specific $\vec{Q}$, this intensity autocorrelation function (also known as homodyne autocorrelation function) is given by [Pec85]

$$g_2(\vec{Q},t) = \frac{\langle I(\vec{Q},0)I(\vec{Q},t)\rangle}{\langle I(\vec{Q})\rangle^2} = 1 + \beta(\vec{Q})\frac{\langle E(\vec{Q},0)E^*(\vec{Q},t)\rangle}{\langle I(\vec{Q})\rangle^2}, \tag{2.17}$$

where $\beta(\vec{Q})$ denotes the experimental contrast. This function represents the probability that, given an intensity $I(0)$ at a certain time, the intensity after a time t remains correlated.

In this context, it is useful to explicitly write the intermediate scattering function (Eq. 1.8) in terms of scatterers as

$$F(\vec{Q},t) = \frac{1}{N\langle f^2(\vec{Q})\rangle}\sum_{n=1}^{N}\sum_{m=1}^{N}\left\langle f_n(\vec{Q})f_m(\vec{Q})\exp\left[i\vec{Q}\cdot(\vec{r}_n(0)-\vec{r}_m(t))\right]\right\rangle, \tag{2.18}$$

where N is the number of scatterers and $\langle f^2(\vec{Q})\rangle$ is the scattering amplitude averaged over the particle size distribution. The brackets $\langle\cdots\rangle$ denote an ensemble average, and $F(\vec{Q},0)$ corresponds to the static structure factor. Now, assuming the scattered field $E(\vec{Q},t)$ is a zero-mean (complex) Gaussian variable, a situation typically satisfied when the speckle pattern arises from the interference of many independent scatterers, the correlation function can be expressed in terms of the normalized intermediate scattering function through the Siegert relation [GMR08]

$$\boxed{g_2(\vec{Q},t) = 1 + \beta(\vec{Q})\left|\frac{F(\vec{Q},t)}{F(\vec{Q},0)}\right|^2} \tag{2.19}$$

Therefore, measuring $g_2(\vec{Q},t)$ enables the extraction of the normalized ISF, which reveals the sample's relaxation dynamics. The stationarity of the process is required so that correlation functions depend only on the time delay. In particular, ergodicity

is necessary to ensure that time averages of the intensity fluctuations of a single speckle are equivalent to ensemble averages. This approach is best suited for stationary systems with sufficiently fast dynamics. For slow dynamics acquisition times required to obtain reliable statistics become long, and beamline stabilities can interfere.

Moreover, in non-ergodic systems (e.g. aging or out-of-equilibrium materials), the time-averaged $g_2(\vec{Q}, t)$ obtained from a single speckle no longer reflects the true ensemble dynamics, since the system explores only a limited region of phase space during the measurement. To overcome this limitation, the multi-speckle approach was introduced [Dur+05]. By simultaneously recording a large number of speckles at the same $|Q|$ using a 2D detector, the statistical sampling is significantly improved, enabling the investigation of slowly evolving and non-ergodic systems. For this reason, multi-speckle measurements with pixelated detectors have become the standard implementation at synchrotron beamlines. This approach will be discussed in detail in the following Chapter (Sec. 3.2), including the computation of the correlation function from speckle "movies" and the advanced detector corrections required to suppress background noise.

2.5.4 Experimental setups: ID10 at the ESRF and P10 at PETRA III

The requirements of high brilliance and partial coherence restrict the number of suitable XPCS beamlines. The experiments discussed in this thesis were carried out at two European synchrotrons: the European Synchrotron Radiation Facility (ESRF, Grenoble, France) and PETRA III at DESY (Hamburg, Germany). Detailed descriptions of these beamlines can be found in Refs. [Deu26; Fac25].

Figure 2.10 (top) shows a simplified representation of the ID10 beamline at ESRF. The radiation emitted by the undulator (U35 or U27) is first shaped using high-power slits to reduce its angular divergence, and subsequently monochromatized by a silicon channel-cut monochromator located in the first optics hutch (OH1). The beam then propagates through additional optical components (OH2) before entering the first experimental hutch (EH1), where techniques such as grazing-incidence diffraction (GID), X-ray reflectivity (XRR), and grazing-incidence small-angle scattering (GISAXS) can be performed.

Further downstream, in OH3, the beam is focused using compound refractive lenses (CRLs) and can be additionally monochromatized with a pseudo channel-cut monochromator if required. Guard slits are used to select the coherent portion of the beam. In the XPCS hutch, located approximately 60 m from the source, a beam

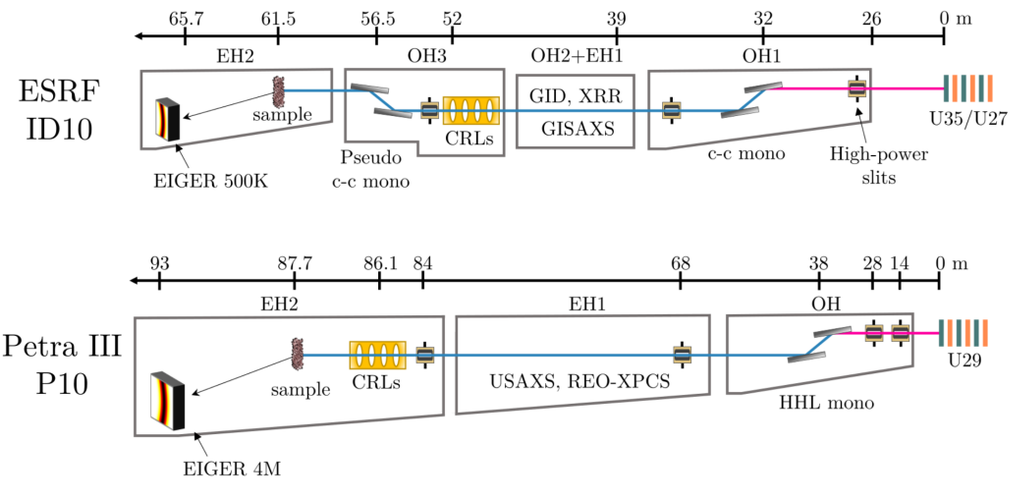

Figure 2.10: Top: schematic layout of the ID10 beamline at ESRF (Grenoble, France). The polychromatic (pink) beam produced by the undulator is monochromatized and focused onto the sample using optical elements such as slits and mirrors. The scattered radiation is recorded with a pixelated single-photon counting detector. Bottom: schematic layout of the P10 beamline at PETRA III (DESY, Hamburg, Germany). The overall configuration is similar to ID10, and only the main elements relevant for XPCS are shown. A detailed description and the complete layout can be found in [Deu26; Fac25]. Figure reprinted from [Mar21].

spot of about 8×10 μm^2 (vertical $\times$ horizontal) is typically achieved, with a flux on the order of 10^{12} photons per second at 8 keV [Fac25] after the EBS upgrade [Cor+24]. The sample is placed in a controlled environment (often under vacuum), and the scattered intensity is detected using a pixelated single-photon counting detector (e.g., Dectris Eiger).

The sample-to-detector distance is adjusted to match the speckle size to the detector pixel size (e.g., 75×75 μm^2 for the detector considered). Figure 2.10 (bottom) also presents the layout of the P10 beamline at PETRA III, which follows a similar design. In this case, the beam is monochromatized using a high-heat-load monochromator and focused near the sample using CRLs. The beam size at the sample is typically around 3×3 μm^2 (vertical $\times$ horizontal), with a lower photon flux of the order of 10^{11} photons per secondat 8 keV.

3 Novel data analysis pipelines at XPCS beamlines

In this chapter I present two advancements in XPCS data analysis pipelines that I developed during my PhD.

The first part of the chapter introduces the multi-tau two-time correlation (MT-2TC) method, a novel data-reduction scheme designed to efficiently compute two-time correlation functions over extremely large datasets. Beyond its technical development, the introduction of MT-2TC also provides an opportunity to present and discuss the standard data analysis approaches used in multi-speckle XPCS (multi-tau, and two-time correlation). The method was developed in the last year of my PhD in discussion with supervisors and collaborators. The presented experimental applications to v-GeO_2 and v-Ta_2O_5 were carried out at the ID10 beamline.

The second part of the chapter focuses on advanced detector corrections for the Eiger 4M detector, particularly addressing noise sources specific to CdTe sensors installed at the ID10 beamline. These effects were identified and characterized during beamtime and subsequent data analysis, leading to the development of dedicated correction procedures, including the masking of out-of-average pixels and the filtering of environmental radiation events.

3.1 Recent improvements at XPCS beamlines

In the previous chapter, we introduced X-ray photon correlation spectroscopy (XPCS). As we have seen, the technique exploits the coherent fraction of synchrotron (or free-electron laser) X-rays: when a coherent beam is focused onto a sample, the scattered radiation produces a speckle pattern, i.e. a granular interference fingerprint of the instantaneous spatial arrangement of scatterers. Recording the temporal fluctuations of this pattern with a fast area detector enables direct measurements of dynamical processes such as diffusion, relaxation, and flow [MFR16; Shp14; Sut08].

At modern synchrotrons, XPCS takes advantage of the exceptional brightness and coherence of the focused beam. As anticipated, to face non-ergodicity, to mitigate radiation damage (see Ch. 4) and to maximize weak scattered signals, pixelated detectors are employed to improve the signal-to-noise ratio (SNR) at fixed dose by averaging over multiple coherence areas (multi-speckle XPCS) [FLM06;

Lum+00]. In this case, the correlation function SNR is given by

$$\mathrm{SNR} = \langle I(q) \rangle C \sqrt{\tau_{\mathrm{min}} T N_{\mathrm{px}}}\,, \tag{3.1}$$

which increases linearly with the average scattered intensity $\langle I(q) \rangle$ and scales with the square root of the number of pixels N_{px}, the minimum sampling time τ_{min}, and the measurement time T. Here, C denotes the contrast, i.e. the speckle visibility expected for a fully static sample, and directly related to the coherence of the X-Ray beam [Pec85].

Dedicated XPCS beamlines are now standard installations at leading synchrotron facilities worldwide. We discussed ID10 at ESRF and P10 at PETRA III, but also 8-ID-E at APS and 11-ID at BNL exist. Over the past decade, these facilities have seen major developments:

- **Coherent flux at fourth-generation synchrotron radiation sources –** Third-generation synchrotron radiation sources typically delivered a coherent flux of 5×10^9 to 5×10^{10} photons s^{-1} in the 8–11 keV range (e.g. ID10 at ESRF [Fav+17], 8-ID-E at APS [Jia+23], P10 at PETRA III [Spr+23]). The advent of fourth-generation facilities, such as ESRF-EBS and APS-U, has produced a substantial increase in brilliance, and consequently in coherent flux, by up to two orders of magnitude, mainly due to the dramatic reduction of horizontal emittance in the electron beam [Cor+24; Fav+17; RBB+23].

- **Ultra-fast photon-counting pixel array detectors (PADs) –** Photon-counting PADs have become the detectors of choice for XPCS thanks to their large dynamic range, negligible readout noise and dark current, and large collection areas [Zha+18]. The Eiger 4M is today's standard detector, offering frame rates up to 4 kHz [DEC25]. Recent developments in ultra-fast PADs now enable access to even shorter delay times. Continuous measurements have been demonstrated at 50 kHz for about 50 s and at 1.2 MHz for 4 s in burst mode using the UFXC32k chip [Zha+16; Zha+17] and the related Rigaku XSPA-500k detector [Zha+18]. Burst-mode operation of the AGIP detector has reached 195 ns delay times over 700 μs [Jo+21], while the TEMPUS detector has recently achieved $\sim$ 450 ns in continuous operation using its event-driven mode [Chu+25].

- **Raw data sparsification –** To handle the huge data rates produced by ultra-fast PADs, raw data sparsification was introduced at the 8-ID-E beamline [Zha+21] and is now standard at ID10 (ESRF), 8-ID-E (APS) and 11-ID (BNL). The approach, motivated by the measured low-count rate frames of

typical XPCS experiments [CCM12], stores only non-zero values and their positions, drastically reducing data throughput while preserving the entire measurement information.

- **Beamline stability –** Improvements in mechanical and thermal stability have significantly extended the upper dynamical limit of XPCS. Relaxation times of several hours can now be reliably measured, as shown in slow-dynamics experiments [Rut+13].

The combination of increased coherent flux and ultra-fast PADs dramatically expands the probed range towards faster times. Concurrently, improvements in instrumental stability and data sparsification pipelines enable measurements over hours or even days at high frame rates. For instance, as we will see in this chapter, we recently continuously tracked the relaxation dynamics of v-GeO_2 and v-Ta_2O_5 for up to 16 hours with 1 ms resolution, generating over 40 million frames with the Eiger 4M detector at ID10. These advances allow XPCS to span an unprecedented dynamical window, from microseconds to days. This opens new scientific opportunities, such as capturing both α and β relaxations within a single correlation function, or simultaneously resolving fast and slow dynamics in aging systems.

However, these capabilities introduce significant computational challenges, demanding increased processing power and memory for the calculation of correlation functions. In parallel, measuring spackle patterns at such high frequencies results in very low count rates per frame, and, especially when measuring glasses such that v-GeO_2, the measured signal on the fast XPCS detector become comparable, and is affected, by detector noises.

To compute reliable correlation functions, it is essential to quantify and mitigate these noise sources. Recent improvements at XPCS beamlines, together with the new challenges they introduce, motivate the two works presented in this chapter.

3.2 Time-resolved XPCS analysis across broad time-scales using multi-tau two-time correlations

As we have seen, multi-speckle detection constitutes the standard operating mode at XPCS beamlines. Three distinct approaches are commonly used for the data analysis in multi-speckle XPCS: standard intensity correlation (IA) [Lum+00], multi-tau intensity autocorrelation (MT-IA) [CW99; Sch87], and two-time correlation (2TC) [Bik17; Cip+02; Sut+03]. The standard correlation consist of the direct implementation of Eq. 2.17 The multi-tau scheme is widely employed for systems where the dynamics do not change significantly during the measurement. It improves the signal-to-noise ratio at long delay times and dramatically reduces computational complexity (from $O(N^2)$ to $O(N \log N)$) by correlating progressively time-averaged frames. In contrast, the two-time correlation approach is necessary for systems with time-dependent dynamics, such as those driven by external stimuli, undergoing aging, or relaxing toward equilibrium. This method calculates the correlation as a function of both measurement time and delay time, yielding a 2D correlation map.

In this section, we first introduce these data analysis schemes, but the ultimate goal is to define a new data-reduction approach that combines the advantages of both methods: the *multi-tau two-time correlation* function (MT-2TC). This approach mitigate computational complexity and largely reduce the memory limitations that constrain the number of frames in standard two-time calculations, and provides a more direct quasi-logarithmic visualization of the correlation matrix. Furthermore, the measurement-time average of our function reduces to the classical multi-tau correlation function, allowing for the straightforward recovery of the standard autocorrelation, as in the two-time formalism.

This work is also reported in recently published open-access paper [Bru+26].

3.2.1 Multi-speckle correlation functions

Intensity autocorrelation (IA)

Photon correlation spectroscopy with area detectors was first demonstrated in XPCS by Dierker *et al.* [Die+95] and in DLS by Kirsch *et al.* [Kir+96], and later further developed by Cipelletti *et al.* [CW99] and Lumma *et al.* [Lum+00]. In the standard multi-speckle scheme, the intensity autocorrelation (IA) function $g_2(q, \tau)$ is calculated by averaging over detector pixels with the same scattering vector q,

following what we introduced in Eq. 2.17 for a single detector,

$$g_q^{(2)}(\tau) = \langle \frac{\langle I_p(t) \cdot I_p(t+\tau) \rangle_p}{\langle I_p(t) \rangle_p \langle I_p(t+\tau) \rangle_p} \rangle_t \tag{3.2}$$

Here, $I_p(t)$ is the intensity at the pixel p and time t; the brackets $\langle \cdot \rangle_p$ and and $\langle \cdot \rangle_t$ denote ensemble (pixel) and time average, respectively. The order of averaging and normalization is important: taking the ensemble average first preserves information on ergodicity [JGP90], while the chosen normalization suppresses fluctuations in the incident beam [Dur+05][4].

In a typical XPCS experiment, the detector records a series of speckle patterns (frames) at constant spacing Δt. The data can be arranged as an intensity matrix $\mathbf{I}$ of dimensions $N_f \times N_{\text{px}}$ where N_f is the number of frames and N_{px} the number of pixels. When stored as a dense matrix, besides the challenges of data storage, a direct calculation of the numerator in the above expression scales as $N_f^2 \cdot N_{\text{px}}$, which quickly becomes computationally prohibitive.

As depicted at the beginning of the chapter, when detectors operate at high frame rates and scattering signal is low, most entries of $\mathbf{I}$ are zero. Using sparse storage formats, mainly compressed sparse row (CSR) or column (CSC) representations [ST23], can drastically reduce the computational cost of evaluating Eq. 3.2, since only nonzero elements are processed[5]. However, row or column indexing in sparse matrices is intrinsically slow, limiting the efficiency of a direct element-wise evaluation of Eq. 3.2. A more practical solution is provided by two-time correlation functions exploiting the sparse linear algebra.

Two-time correlation (2TC)

Omitting the time averaging in Eq. 3.2, the two-time correlation (2TC) function can be defined as [Sut+03]

$$G_S^{(2)}(t_1, t_2) = \frac{\langle I_p(t_1) \cdot I_p(t_2) \rangle_p}{\langle I_p(t_1) \rangle_p \, \langle I_p(t_2) \rangle_p}, \tag{3.3}$$

where t_1 and t_2 are the times of the correlated frames. Independently, Cipelletti [Cip+02] introduced an equivalent form, $G_C^{(2)}(t_w, \tau)$, expressed in terms of the

4 Different definitions of $g_2(q, \tau)$ exist in literature, varying in both the order of averaging and the choice of normalization [Bik17; CCM12; CW99; Dur+05; Lum+00]

5 A related approach based on event correlators was proposed by Chushkin et al. [CCM12], showing dramatic speed-ups.

waiting time $t_w = \frac{t_1+t_2}{2}$ and the lag time $\tau = |t_1 - t_2|$. Using the symmetric definition of the waiting time [Bik17], $G_C^{(2)}(t_w, \tau)$ corresponds to a 45° rotation of the $G_S^{(2)}(t_1, t_2)$ matrix. Within both representations, the standard IA can be computed by time averaging [Dur+05]

$$g^{(2)}(\tau) = \langle G_C^{(2)}(t_w, \tau)\rangle_{t_w} = \langle G_S^{(2)}(t, t+\tau)\rangle_t \tag{3.4}$$

Equations 3.3 and 3.4 give a practical computational pathway to compute both 2TC and IA taking advantage of the efficiency of matrix multiplication algorithms:

$$\mathbf{G}_{\mathrm{S}}^{(2)} = ((\mathbf{I}\cdot\mathbf{I}^{\mathrm{T}}) \odot_r \mathbf{n}) \odot_c \mathbf{n}^{\mathrm{T}} \quad \text{with} \quad [\mathbf{n}]_i = (\sum_{p_j} I_{t_i,p_j})^{-1} \tag{3.5}$$

The matrix product $\mathbf{I}\cdot\mathbf{I}^{\mathrm{T}}$ computes the pixel-averaged correlations in the numerator of Eq. 3.3. The subsequent element-wise multiplications, $\odot_r$ (row-wise) and $\odot_c$ (column-wise) with the normalization vector $\mathbf{n}$ ensures the proper normalization. The entries of the resulting matrix ($N_f \times N_f$ large) correspond directly to the 2TC: $[\mathbf{G}_{\mathrm{S}}^{(2)}]_{i,j} = G_S^{(2)}(i\Delta t, j\Delta t)$[6]. The IA vector is then obtained by averaging over the offset diagonals of this matrix, i.e. averaging over constant lag times: $[\mathbf{g}^{(2)}]_k = \frac{1}{N_f-k}\sum_{i=0}^{N_f-1}[\mathbf{G}_{\mathrm{S}}^{(2)}]_{i,i+k}$.

This matrix-multiplication approach leverages optimized linear algebra routines and is especially powerful for sparse data, where direct indexing is slow. However, it comes at the cost of memory: $\mathbf{G}_{\mathrm{S}}^{(2)}$ is a dense matrix of dimension $N_f \times N_f$. For large datasets, this rapidly exceeds available resources (e.g. $\mathbf{G}_{\mathrm{S}}^{(2)}$ from 1 million frames requires several terabytes). A general workaround is time-binning, where data are coarse-grained to longer frame-times, however, at the expense of losing access to the fastest dynamics. Alternatively, multi-tau autocorrelation offers a way to overcome time-scale limitations.

Multi-tau autocorrelation (MT-IA)

Multi-tau calculation of intensity autocorrelation was first proposed by Schätzle [Sch83] for single area detectors, and later extended to multi-speckle DLS by Cipelletti [CW99]. Instead of following the prescription of Eq. 3.2, which requires evaluating all possible frame pairs and thus scales as N_f^2, multi-tau algorithms maintain a nearly constant ratio between the delay time τ and the sampling time Δt, still maintaining the temporal resolution $\frac{\Delta t}{\tau} \ll 1$. This leads to a quasi-logarithmic

6 Since $\mathbf{G}_{\mathrm{S}}^{(2)}$ is symmetric, only one half of the matrix needs to be computed.

sampling of lag times: the correlation function spans several decades of τ with far fewer points, reducing both computational cost and memory requirements, as well as increasing the SNR at large τ as a consequence of the non-constant Δt.

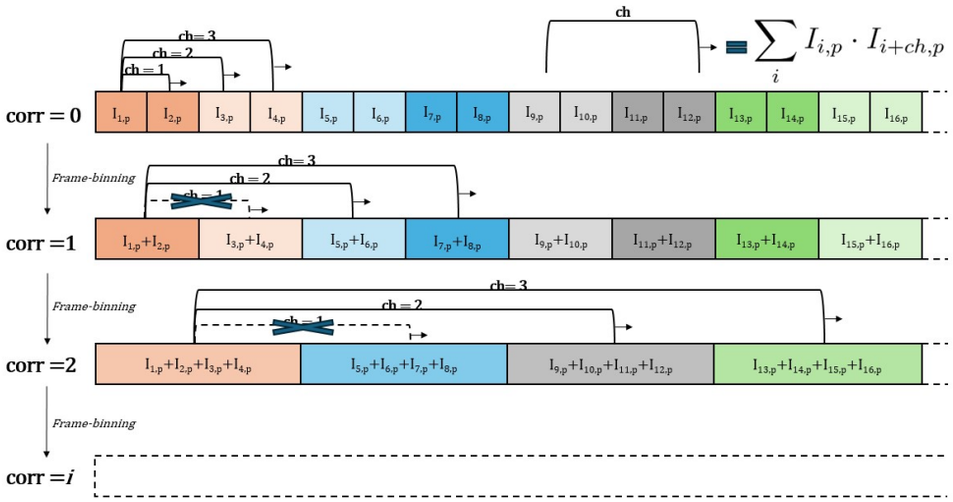

Figure 3.1: Multi-tau correlator scheme for a single pixel p with four channels. Data sampled at Δt are correlated in corr=0 by all channels but the first, then binned and passed to subsequent correlators, each doubling the delay times. Only new lag times (second half of channels) are computed at each stage [CW99].

Let us first focus on the calculation of the un-normalized IA for a single pixel. The multi-tau algorithm organizes the computation into a cascade of linear correlators (levels), each with a fixed number of channels (four in the example of Fig. 3.1).

- **First correlator (corr=0):** The pixel intensity stream, sampled at Δt, is fed into the channels. All channels except the first (which corresponds to zero lag time, i.e. the speckle pattern variance) compute correlations at linearly spaced delays $\tau_{ch} = ch * \Delta t$.
- **Subsequent correlators (corr = 1, 2, ...):** Before feeding the signal to the next correlator, pairs of consecutive frames are summed, effectively doubling both the sampling time and the accessible delay times. In these correlators, only the second half of the channels are used, since the first half corresponds to lag times already computed at higher temporal resolution.

- **Iteration:** This binning–correlation process is iteratively repeated, each stage doubling the frame time and extending the correlation function to longer τ. The multi-tau autocorrelation (MT-IA) function is obtained by merging the outputs of all correlators.

Finally, the MT-IA functions calculated for all pixels with the same scattering wave vector are averaged and normalized[7]. Multi-speckle multi-tau autocorrelation is the starting point of our novel correlation scheme.

3.2.2 Multi-tau two-time correlation (MT-2TC)

The 2TC matrix defined in Eq. 3.5 is a standard tool in XPCS data analysis. It provides information on sample ergodicity and stationarity, allows verification of measurement stability, and highlights temporally correlated noise sources [Bik17] (e.g. spurious high-count signals from environmental radioactivity appearing in consecutive frames). Once stationarity is established, the IA is obtained by time-averaging over the selected stationary time ranges. As already noted, the main limitation of this method lies in the size of the $\mathbf{G}_S^{(2)}$ matrix. In addition, when the measurement time far exceeds the sample decorrelation time, visualizing the entire matrix becomes uninformative. In such cases, data are either inspected through sub-matrices or, as in recent studies [CZN24; Per+17], reformulated in the $G_C^{(2)}(t_w, \tau)$ representation and plotted with a logarithmic τ axis. To overcome these limitations, we propose a multi-tau definition of the $G_C^{(2)}(t_w, \tau)$ function, quasi-logarithmically spaced in τ. This approach extends the standard multi-tau scheme of Fig. 3.1 by avoiding temporal averaging.

We denote frame-shifts as follows: $\mathbf{I}[i:]$ is the sub-matrix of $\mathbf{I}$ starting from row i , and $\mathbf{I}[:-j]$ excludes the last j rows. Frame binning for the $corr$-th correlator is defined as $[\mathbf{I}^{\mathbf{corr}}]_{f,p} = \sum_{k=0}^{2^{corr}} I_{f\cdot 2^{corr}+k,p}$[8]. The non-normalized multi-tau 2TC is then defined as a set of vectors of different sizes, one for each correlator index $corr = 0, 1, \ldots$ and channel index $ch = 0, 1, \ldots, N_{ch} - 1$:

$$C^{(2)}_{MTcorr,ch} = \sum_{\text{pixels}} \mathbf{I}^{\mathbf{corr}}[:-ch] \odot \mathbf{I}^{\mathbf{corr}}[ch:] \tag{3.6}$$

where $\odot$ is the element-wise (Hadamard) product. For each correlator and channel, the intensity matrix is first binned by 2^{corr}, then element-wise multiplied with its

7 The autocorrelation functions are first averaged over pixels, and later normalized. This order is essential for non-ergodic samples, since it directly yields the ensemble-averaged IA function [CW99].

8 The last frames are discarded if 2^{corr} is not a divisor of N_f.

frame-shifted copy (by ch rows), and finally summed over pixels. Normalization follows Eq. 3.3:

$$G^{(2)}_{MTcorr,ch} = C^{(2)}_{MTcorr,ch} \odot \mathbf{n}^{\mathbf{corr}}[:-ch] \odot \mathbf{n}^{\mathbf{corr}}[ch:] \tag{3.7}$$

As in the standard multi-tau scheme, the correlator and channel indices determine the lag time τ, while the i-th element of the vector $G^{(2)}_{MTcorr,ch}$ corresponds to a waiting time t_w:

$$\begin{aligned} \tau(corr, ch) &= 2^{corr} \cdot ch \cdot \Delta t \\ t_w(i, ch, corr) &= (\frac{ch+1}{2} + i) \cdot 2^{corr} \cdot \Delta t \end{aligned} \tag{3.8}$$

Computationally, each Hadamard product in the denominator requires roughly $N_{\mathrm{px}} N_f / 2^{corr}$ multiplications per correlator and channel. Computing the full object thus involves about $2N_{\mathrm{px}} N_{ch} N_f$ operations[9]. Similarly, the number of elements in $G^{(2)}_{MT\,corr,ch}$ scales as $2 \cdot N_f \cdot N_{ch}$. For large datasets, both the computational cost and storage requirements are therefore reduced from quadratic to linear in N_f. This enables calculation and storage of 2TC functions irrespective of frame rates and measurement times, thus allowing operation at the full detector speed. Visualization is naturally achieved in a $t_w - \tau$ plot with logarithmic τ, which conveniently displays the full dynamics of the sample—even when relaxation times are much shorter than the total acquisition time—and facilitates verification of stationary ranges.

As an example, Fig. 3.2 compares the standard 2TC (top) with the MT-2TC (bottom), computed on a v-Ta_2O_5 128 frames measurement at low frame rate $\Delta t \sim 4$ s (details in Sec. 3.2.3). In the multi-tau calculation, we used 16 channels, which is sufficient to avoid time-blurring effects as, apart for the first half of the first correlator's channels, always keeps $\frac{\tau}{\Delta t} > 8$. The MT-2TC can be viewed as a 45° rotation of the 2TC matrix, but with the lag time τ quasi-logarithmically sampled: the rectangle-rows corresponding to each correlator and channel double in both height and width every 8 rows (except for the first correlator, which has 16 channels). In this example, both the 2TC and the MT-2TC reveal the same physical information, namely the sample dynamics evolving with an increasing relaxation time. However, important practical differences arise: i) Although both are computed from the same 128 frames, they contain very different numbers of elements. The 2TC has $N_f^2 = 16384$ entries, while the MT-2TC contains fewer than $2 \cdot n_{ch} \cdot N_f = 4096$ entries. This gap grows quadratically with N_f. ii) To perform this comparison, we simulated

9 This estimate follows a geometric series and overestimates the true number of multiplications.

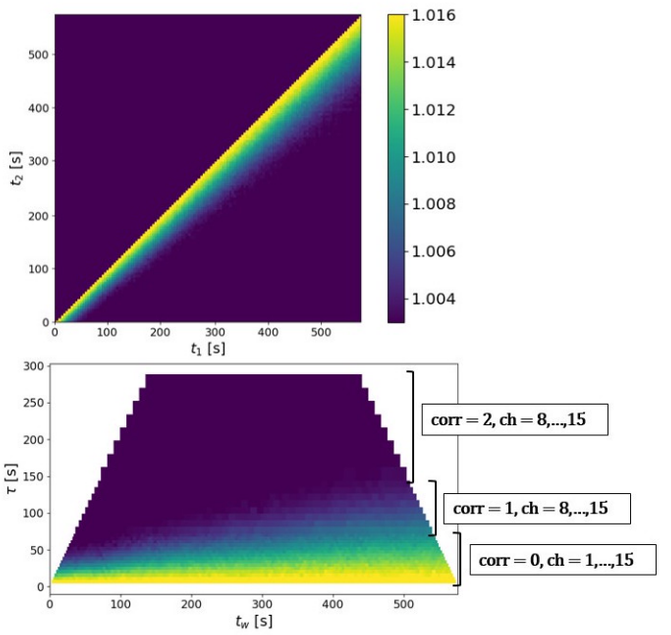

Figure 3.2: Comparison of the standard 2TC (top) and MT-2TC (bottom) computed for a v-Ta_2O_5 measurement at a low frame rate ($\Delta t \sim 4$ s), chosen to improve the signal-to-noise ratio (see Sec. 3.2.3 for details). The labels indicate which correlator and which set of channels correspond to the rows of the MT-2TC. Notably, the first correlator consists of 15 channels (the first channel is omitted, as it corresponds to the self-correlation of frames), while the other two correlators consist of 8 filled channels each.

4 s frames by binning the original 1 ms data, so that the standard 2TC achieves a reasonable SNR. At much higher frame rates the 2TC would become unusable, dominated by noise. By contrast, the MT-2TC remains robust: for each lag time it shows the same SNR irrespective of the frame rate, since its SNR naturally improves with increasing τ.

Finally, the IA function, consistent with that of Sec. 3.2.1, can be recovered by averaging over t_w, and errors can be computed accordingly[10]:

$$g^{(2)}_{MT\,corr,ch} = \frac{1}{N_{t_w}} \sum_{t_w} G^{(2)}_{MT\,corr,ch}. \tag{3.9}$$

10 When averaging over a restricted observation-time range, care must be taken to truncate at the appropriate correlator index, since higher-order correlators may correlate frames lying outside the chosen t_w interval under the symmetric definition.

MT-2TC from sparse matrices

In principle, Eq. 3.7 enables the calculation of both IA and 2TC for arbitrarily large N_f. In high-frame-rate and long-duration measurements, however, data are typically stored in sparse formats to circumvent memory limitations. Therefore, an efficient implementation of Eq. 3.7 must explicitly operate on sparse data structures. A key difficulty arises in the binning step: binning sparse intensity matrices is highly inefficient, as it neither reduces memory usage nor simplifies subsequent calculations. In fact, binning a sparse matrix by a factor of 2 usually results only in a frame re-indexing of the events, since two consecutive frames rarely record photons in the same pixel. To address this, we propose a two-step implementation of Eq. 3.7 that fully advantage of the sparse formalism.

Step 1 – Sparse-domain 2TC sub-matrices

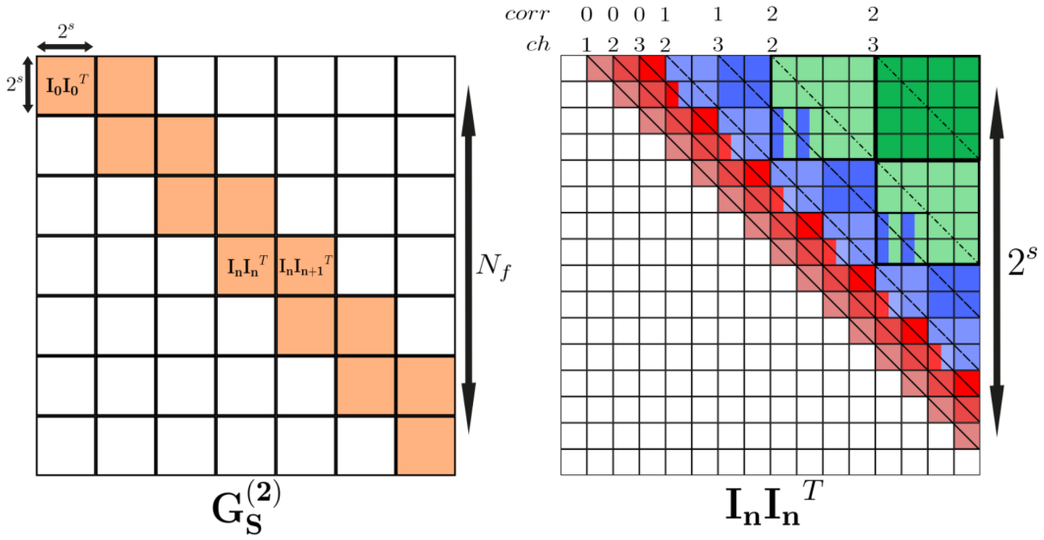

Figure 3.3: Illustration of the two-step sparse implementation of the multi-tau 2TC. **Left:** Decomposition of the full $\mathbf{G}_\mathbf{S}^{(2)}$ into diagonal and off-diagonal sub-matrices computed from sparse blocks of $\mathbf{I}$. **Right:** Mapping of a 2TC sub-matrix into the multi-tau representation via successive binning and extraction of *ch*-offset diagonals. In this example, $s = 4$ and 4 channels are used. Double-colored entries indicate values used in different multi-tau correlators.

We first compute the linear 2TC matrices using Eq. 3.5, but restricted to small sub-matrices of $\mathbf{I}$. These are defined by a parameter s as $\mathbf{I}_n = \mathbf{I}[n \cdot 2^s : (n+1) \cdot 2^s]$

with $n = 0, 1, \ldots, N_f/2^s$. For each n, two consecutive 2TCs are calculated: (i) the autocorrelation of $\mathbf{I}_n$, and (ii) the cross-correlation of $\mathbf{I}_n$ with $\mathbf{I}_{n+1}$[11]. These correspond to the diagonal blocks of the entire $\mathbf{G}_\mathrm{S}^{(2)}$ matrix (Fig. 3.3, left). Each 2TC sub-matrix is then converted into its multi-tau version, subsequently filling the first correlators of $G^{(2)}_{MT\,corr,ch}$ by appending the correlation values at the end of its vectors. For each correlator, this conversion is achieved by binning the 2TC sub-matrices, both by rows and columns, by 2^{corr}, and extracting the channel vectors from the corresponding ch-offset diagonals (Fig. 3.3, right). The cross-correlation matrices $\mathbf{I}_n\mathbf{I}_{n+1}$ are treated analogously, except that their first correlators and channels start from the corner rather than from the diagonal. It can be shown that this algorithm fills the first correlators equivalently to Eq. 3.7, but moves time-binning after the correlation computation. The advantage of this approach is that it avoids explicit frame binning, still avoiding high memory consumption, since only two small $\mathbf{I}$ sub-matrices are processed at each step, which are then transformed from the linear 2TC into its multi-tau representation.

Step 2 – Dense-domain computation

The second stage follows Eq. 3.7. The intensity matrix $\mathbf{I}$ is time-binned by a factor 2^{s+1} and converted into a standard dense matrix. From this point, subsequent correlators are computed via the Hadamard product and binning scheme of Eq. 3.7. In practice, the optimal choice of s is such that $2^s \sim \frac{1}{\text{sparsity}}$, i.e. binning becomes advantageous once the resulting matrix is effectively dense.

Implementation and memory considerations

As described in Sec. 3.2.2, the MT-2TC calculation for sparse data is divided into two main stages. In the first stage, standard two-time correlation (2TC) sub-matrices are computed from successive batches of 2^s frames. At this stage, only a limited number of intermediate quantities are required. Two arrays, I_0 and I_1 (each of dimension $2^s \times N_\mathrm{px}$), store the frame batches used to compute diagonal and off-diagonal 2TC sub-matrices. The corresponding correlation results are stored in an intermediate matrix $G^{(2)}_\mathrm{sub}$ of dimension $2^s \times 2^s$. The output of this stage consists of (i) a time-binned version of the original frame sequence, denoted I_dense (of dimension $N_f/2^s \times N_\mathrm{px}$), and (ii) a partially filled MT-2TC object, in which only the channels associated with the first correlators are populated.

11 The extension of Eq. 3.5 to this case replaces the transposed $\mathbf{I}_n$ matrix with $\mathbf{I}_{n+1}$. The same happens in the normalization

The first-stage computation is performed by iterating over the dataset in steps of 2^s frames. At each iteration, two consecutive frame batches, I_0 and I_1, are loaded into memory. These batches are used to compute both the diagonal and off-diagonal two-time correlation (2TC) sub-matrices, which are temporarily stored in the intermediate array $G^{(2)}_{\text{sub}}$. The resulting sub-matrices are then transformed into their multi-tau representation and accumulated in the corresponding channels of the MT-2TC object. Finally, the frames I_0 are time-binned by summation to produce the corresponding dense frame, which is stored in the vector I_{dense} for subsequent processing in the dense stage of the algorithm.

In the second stage, the MT-2TC is completed by operating on the dense (time-binned) frames. This step involves matrix slicing and dense matrix elementwise multiplications, followed by successive binning of I_{dense} by a factor of two at each iteration, as described by Eq. 3.6 and 3.7.

In the present implementation, the computation of sparse 2TC sub-matrices relies on Intel MKL sparse matrix-multiplication routines [Int23], while the frame-binning step and all dense operations are implemented using the NumPy library [Har+20].

Computational time

The computational time of the MT-2TC algorithm scales linearly with the number of frames N_f. In the first stage, the number of loop iterations scales as $N_f/2^s$. In the second stage, the initial number of dense frames to be processed is also $N_f/2^s$, and the first iteration dominates the computational cost, since subsequent iterations operate on progressively halved frame sequences. As a result, the total computational time increases approximately linearly with N_f.

This behavior contrasts with the standard 2TC approach, whose computational cost and memory usage scale quadratically with the number of frames. However, the standard matrix-multiplication-based 2TC benefits from highly optimized linear algebra routines and remains faster until memory limitations come into play. As N_f increases and the full 2TC matrix can no longer be stored in memory, the standard approach becomes impractical. In this regime, the MT-2TC retains linear scaling with N_f, providing a decisive advantage in terms of feasibility for large datasets.

Memory considerations

The main advantage of the MT-2TC method is the strong reduction of memory usage. In standard 2TC calculations, the dominant memory limitation arises from storing the full 2TC matrix, whose size scales as $N_f \times N_f$. For example, on typical beamline computing infrastructure such as that available at the ESRF, storing the full 2TC

matrix for a dataset of 200,000 frames using 32-bit floating-point numbers would require approximately 160 GB of memory, already at the limits of workstations equipped with a few hundred gigabytes of RAM.

In contrast, the MT-2TC correlation object scales linearly as $2 \times N_f \times N_{\mathrm{ch}}$. For the same dataset and using 16 channels, the MT-2TC object occupies only about 25.6 MB. This directly addresses the dominant memory bottleneck associated with the size of the two-time correlation matrix in large-frame XPCS datasets.

Additional memory is required for intermediate quantities. The sparse frame batches I_0 and I_1 each contain on the order of N_{px} non-zero values and therefore require limited memory[12]. The largest intermediate objects are the correlation sub-matrix $G^{(2)}_{\mathrm{sub}}$ and the dense, time-binned frame sequence I_{dense}, whose sizes depend on the choice of the parameter s. For the example shown in Fig. 3.4 (top), the optimal choice is $s = 14$. In this case, computing the MT-2TC for 1 million frames requires approximately 1 GB of memory for each of $G^{(2)}_{\mathrm{sub}}$ and I_{dense}. Given the number of frames involved, a total memory requirement of a few gigabytes represents a substantial reduction compared to standard two-time correlation calculations.

Importantly, the algorithm does not require the full dataset to be loaded into memory at once and therefore supports chunked processing, in which data are handled in successive time blocks. At any given time, only the frame batches I_0 and I_1 need to reside in memory. As a result, the method supports datasets that approach or exceed available RAM, with practical limitations progressively determined by the speed of data loading from disk and computation, rather than by memory capacity.

3.2.3 Experimental demonstrations and perspectives

From a practical standpoint, the MT-2TC approach is particularly well suited to high–frame-rate XPCS experiments involving large numbers of frames. By preserving access to the full two-time information while drastically reducing memory requirements, it enables efficient storage and visualization, as well as flexible a posteriori selection of time windows without recomputing correlations, simplifying both online inspection and post-processing of large datasets.

In this section, we illustrate the versatility and effectiveness of the proposed tool through two recent experiments we carried out at the ID10 beamline of ESRF using the Eiger 4M detector working at a frame rate of 1 kHz. The first case concerns the relaxation dynamics of v-GeO_2, where our aim is to study the temperature dependence of the contrast and its connection to the non-ergodicity of the glass. These case will be in-depth discussed within the next chapters as constitute the

12 Here we assume the optimal choice $s \sim \log_2(1/\mathrm{sparsity})$, as discussed previously.

core of this thesis. Here the objective is to demonstrate the functioning of the MT2TC method. The second example addresses X-ray-induced dynamics in a thin film of v-Ta_2O_5, obtained by ion beam sputtering, comparing as-deposited and annealed samples. Here, the focus was on relaxation processes occurring on the millisecond timescale, which are particularly relevant because they dominate the noise response of ground-based gravitational-wave detectors, such as Advanced Virgo [Ae14], Advanced LIGO [Ae15] and KAGRA [Ae13], at frequencies in the range between 10 and 1000 Hz [Ste18].

For both oxide samples, the dynamics observed at temperatures below the glass transition are dominated by X-ray induced processes (see Ch. 4), i.e. relaxations activated by the interaction of the intense coherent X-ray beam with the sample, primarily through bond breaking due to the radiolysis process, which superimpose on the intrinsic material dynamics [Mar+23; Rut+17].

XPCS at ms time resolution on v-GeO_2

The experiment was performed in the small-angle configuration of the ID10 beamline with the detector centered at 1.75° using a 9.7 keV X-ray beam, giving access to the 1.2–2.2 nm^{-1} Q-range. More details on this experiment are described at the beginning of Ch. 5. In the room temperature measurement rapidly discussed here, the X-Ray induced relaxation time is of about 6 s, however, because of the very low scattered signal ($\sim$ 0.2 ph/px/s), we took about 1 hour scans exploiting the stationary dynamics of the sample to improve the SNR (see Eq. 3.1). The sample under irradiation initially displayed non-stationary dynamics: during the first $\sim$ 200 s of beam exposure the relaxation slows down, from millisecond to second time scales. After this transient regime, the dynamics became stationary. In the experiment, we investigated the dynamics of this "damaged" glass, thus measuring on the same irradiated spot, within the regime of stationary dynamics.

The stationarity of the dynamics is quantified using the novel MT-2TC. An example computed for a 400 K scan at $Q = 1.7 \pm 0.1$ nm^{-1} (1, 000, 000 frames at 1 ms) is shown in Fig. 3.4. The two-time correlation function, naturally represented with the lag time on a logarithmic scale, allows the relaxation process to be monitored across the entire measurement time, even when the relaxation itself is much shorter than the measurement time. As expected, correlations at shorter lag times are noisier due to the limited number of correlated photons, while at longer lag times the statistics improve and averaging is no longer needed to obtain stable values. Once stationarity is established, the $g^{(2)}$ function is obtained by averaging over the rows of the $G^{(2)}_{MT\,corr,ch}$ object, as shown in the lower panel of Fig. 3.4 (here computed skipping the first 200 s in which the dynamic is in evolution). Here, the agreement

with the Kohlrausch-Williams-Watts (KWW) relaxation function over six decades in time is significant.

The multi-tau IA is compared with the standard linear definition of Eq. 3.2, computed from 20,000 frames obtained by binning the original 1 million frames by a factor of 50 in order to avoid memory limitations. Otherwise, when using 32-bit floating-point numbers, the full 2TC matrix would require approximately 4 terabytes of memory. The two methods give consistent results, but the multi-tau calculation provides a significant advantage in terms of SNR, especially at long lag times, and, more importantly, extends the accessible time window by almost two decades. Given the objectives of this experiment, in particular accessing the contrast (see next chapters), reliable access to the low–lag-time regime, i.e. lag times much shorter than the X-ray–induced relaxation time, is essential to resolve the plateau before the initial decay of the correlation function and thus to accurately determine the contrast, which would otherwise be compromised by excessive frame binning.

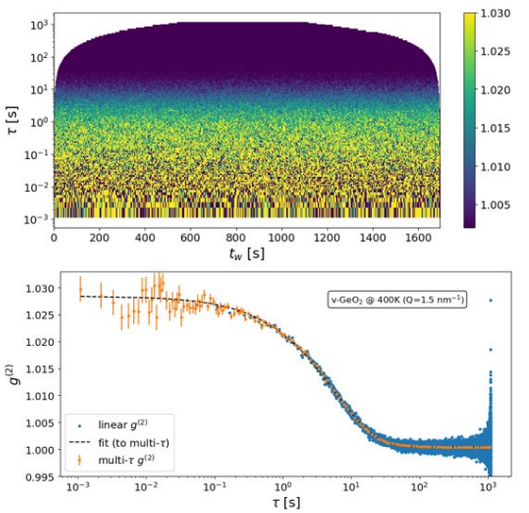

Figure 3.4: MT-2TC (top) and IA (bottom) computed on X-ray–damaged v-GeO_2 at 400 K, using sixteen channels to preserve temporal resolution. **Top:** Two-time correlation function on $1,000,000$ frames at 1 ms, plotted with lag time on a logarithmic axis, allowing visualization of the relaxation process across the entire measurement window. **Bottom:** Comparison of the multi-tau IA (orange error bars) with the standard linear definition of Eq. 3.2 (blue dots), the latter computed from 20,000 frames at 50 ms to avoid memory limitations.

X-Ray induced relaxation dynamics in v-Ta_2O_5

The experiment was carried out in the wide-angle configuration of the ID10 beamline, with the detector angle varied between 1.5° and 10° to probe the Q-dependence of the induced relaxation within the range 3–20 nm^{-1}, using a working energy of 21.7 keV. The samples consisted of two 2.5 μm-thick v-Ta_2O_5 films deposited on Si substrates by ion-beam sputtering at the Laboratoire des Matériaux Avancés (LMA): one in the as-deposited state and the other annealed at 500° C for 10 hours (additional details on sample preparation will be provided in a forthcoming publication, as well as a discussion on the XPCS results). The $0.8 \cdot 10^{12}$ ph/s X-ray beam was tightly focused to a spot size of 10×7 μm^2 in order to increase the dose rate and accelerate the beam-induced dynamics. The experiment is performed in transmission geometry through the 0.5 mm Si substrate, which is almost transparent at this working energy.

Subjected to such X-ray dose, the relaxation dynamics evolves on the scale of a day, requiring measurements to be monitored over several hours. Figure 3.5 shows this evolution for the as-deposited sample at $Q = 20$ nm^{-1}. The MT-2TC plot (top), computed from 60,000,000 frames at 1 ms, captures the full evolution of the dynamics across the measurement window. The characteristic relaxation time starts at a few tens of seconds and rapidly increases to thousands of seconds, and the relaxation function progressively stretches, evidencing the heterogeneous nature of the sample dynamics. The MT-2TC representation also guides the choice of stationary time-windows for computing autocorrelation functions and extracting KWW relaxation parameters. In practice, it suggests exponentially increasing window widths during the first hours, followed by equally large windows at later times (vertical red dashed lines). The $g^{(2)}$ functions are then obtained by t_w-averaging over the appropriate segments of the MT-2TC (according to Eq. 3.8), ensuring that the averaged correlations are calculated from frames belonging to the selected stationary windows.

From a practical perspective, the MT-2TC for this dataset, comprising 60 million frames, was computed only once and required approximately 30 minutes on a standard analysis workstation. Subsequent calculations of the $g^{(2)}$ functions for different waiting times and window selections involve only cuts and averages of the precomputed MT-2TC, and therefore incur negligible additional computational cost. This illustrates a key practical advantage of the method for long-duration experiments, where repeated recalculation of two-time correlations would otherwise be prohibitive.

Figure 3.5 (bottom) shows the resulting $g^{(2)}$ functions calculated for the selected time windows. As expected from Eq. 3.1, the signal-to-noise ratio improves with

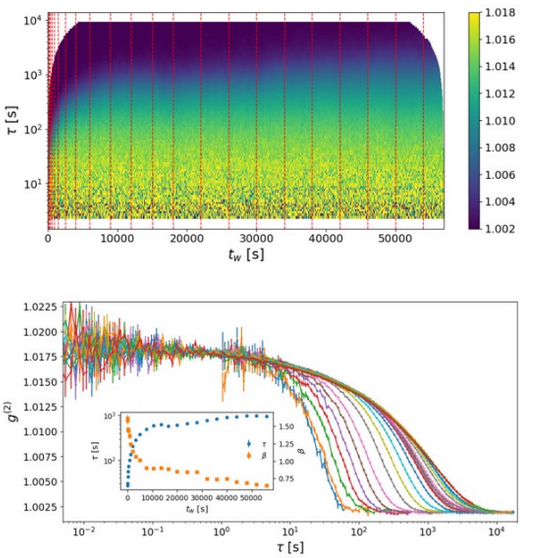

Figure 3.5: X-ray induced relaxation dynamics of the as-deposited v-Ta_2O_5 sample at $Q = 20$ nm^{-1}. **Top:** *Multi-tau two-time correlation* (MT-2TC) function for lag times $\tau > 1$ s, computed from 60,000,000 frames at 1 ms, capturing the evolution of the relaxation dynamics during beam exposure. Vertical dashed red lines indicate the stationary time windows selected for IA analysis. **Bottom:** Corresponding $g^{(2)}$ functions obtained by averaging over the selected windows. Access to faster dynamics is limited to the wider time windows, which exhibit improved SNR; therefore, only $g^{(2)}$ from these windows are shown for short lag times ($\tau < 1$ s). **Inset:** Extracted relaxation times and stretching exponents, which progressively increase and decrease, respectively, with dose, both following an approximately exponential trend.

increasing window width. Consequently, access to faster dynamics is restricted to the wider time windows, since the correlations computed over shorter intervals are dominated by statistical noise. The fitted t_w dependence of the relaxation time τ and the stretching exponent β is presented in the inset. For the as-deposited sample, the relaxation time progressively increases with exposure, following an approximately exponential trend.

We note that, when the induced decorrelation becomes very long, in contrast to the v-GeO_2 measurements, the relaxation over the full dynamical range cannot be adequately described by a single KWW function. In particular, in the fast lag-time range between 10 ms and 10 s, the correlation function exhibits a slow decay that precedes the main relaxation and cannot be captured by a stretched exponential form. We are currently investigating whether this behavior is indicative

of the presence of a secondary relaxation process, possibly related to the thermal Brownian noise in gravitational waves detectors. Access to this extended time window is therefore essential to correctly characterize the dynamics and to avoid oversimplified fits based on a restricted lag-time range.

Further potential applications of the MT-2TC

Beyond the experimental demonstrations presented above, the MT-2TC approach is expected to be broadly applicable to XPCS measurements involving large datasets, high frame rates, and time-evolving dynamics. By providing access to the full two-time information while drastically reducing data size, the method enables flexible a posteriori analysis and efficient handling of long-duration measurements.

More generally, one of the most promising applications of the MT-2TC is the detection of two-step relaxation processes in glassy systems, such as the coexistence of α and β relaxations. While such phenomena are well known in light scattering and XPCS studies [RB25], they have not yet been clearly resolved with X-rays in the regimes targeted here. Access to correlation functions over lag-time ranges significantly wider than the characteristic decorrelation region is essential to identify these behaviors and to avoid masking slow or intermediate relaxation components.

In addition, the MT-2TC representation is particularly valuable for experiments exhibiting non-stationary or heterogeneous dynamics, where the identification of stationary time windows is nontrivial. In these cases, it provides an efficient and intuitive way to monitor the temporal evolution of the dynamics and to guide the selection of appropriate averaging intervals, especially in dose-dependent or aging experiments.

In practice, the advantages of the MT-2TC become most apparent when large numbers of frames must be handled simultaneously. While for small datasets the standard matrix-multiplication-based two-time correlation remain faster due to highly optimized linear algebra libraries, this situation changes as soon as memory limitations prevent computing and storing the full $N_f \times N_f$ correlation matrix. The MT-2TC is specifically designed to operate in this regime, which is increasingly common in high–frame-rate XPCS experiments involving long acquisition times and evolving dynamics.

Code availability

The implementation of the multi-tau two-time correlation method presented in this section is publicly available under an open-source license at the following link. *https://github.com/FabioBrugnara/XPCS_library*

3.3 Advanced Eiger 4M detector corrections for XPCS experiments

The DECTRIS EIGER 4M detector has become the standard at XPCS beamlines in recent years. It is available in two versions, differing in the sensor material: silicon (Si) and cadmium telluride (CdTe). The Si-based detector is employed at P10 (PETRA III), whereas the CdTe version is used at ID10 (ESRF).

The main advantage of the CdTe detector is its extended detection energy range (8–100 keV), compared to 6–40 keV for Si [DEC25]. This capability allows the ID10 beamline to safely operate at photon energies up to 21 keV [Fac25]. However, as we will see, this extended range comes at the cost of a higher background signal and reduced fabrication uniformity.

In this section, we discuss three detector-related corrections that we have implemented. Two of them address background noise arising from ambient radioactivity (primarily γ radiation) and from high-energy particles (e.g. muons and energetic electrons) depositing energy in the detector. Ambient radioactivity constitutes the dominant background in CdTe detectors and is not negligible in low-flux experiments, although it can be effectively mitigated through data processing. In contrast, particle-induced events are much rarer and become observable mainly in Si detectors, where the contribution from ambient radioactivity is negligible. Both effects are generally well controlled and become less relevant at high photon flux. The first correction, however, addresses a more intrinsic issue: an efficiency-dependent signal originating from a subset of pixels that deviate significantly from the average response. This effect, probably linked to the CdTe fabrication process, is absent in Si detectors. We have developed an effective procedure to identify and correct for these anomalous pixels.

3.3.1 Out-of-average behavior pixels in the CdTe detector

The first noise source we discuss is the presence, within the DECTRIS EIGER 4M CdTe detector, of pixels that behave (i.e. count) markedly differently from the average. To highlight this effect, we analyze a long 8 keV measurement on germania glass at ambient temperature. The detector is placed 5 m from the sample at the FSDP ($Q \sim 1.5$ Å^{-1}) to maximize the scattering signal, and ensure a uniform detector illumination. The acquisition we now use as an example consists of 200,000 frames

recorded at 0.02 ms. This measurement was performed in 2021 within the HC5721 experiment at the ID10 beamline[13].

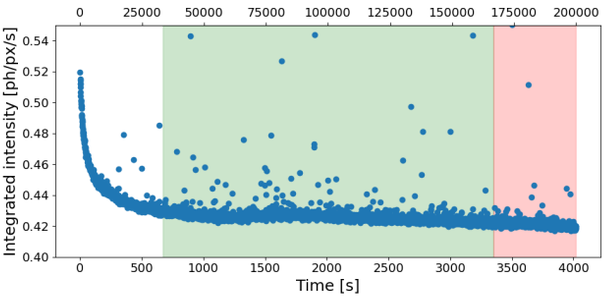

Figure 3.6: Integrated detector intensity as a function of time. The intensity is computed by integrating all detector pixels (masked by the **e4m_htmask**, see below). The green-shaded frames are used for analysis, while the red-shaded frames are reserved for testing.

Figure 3.6 shows the temporal evolution of the detected intensity under X-ray exposure. To identify pixels with anomalous behavior, we require an approximately constant photon flux at the detector. Therefore, we exclude the initial frames, where the intensity varies significantly due to the rapid structural transformation of germania under X-ray irradiation (this will be discussed in detail in the next chapter). The motivation of the random higher-counts frames will be clarified in the following Sec. 3.3.2. We restrict the analysis to frames between $200{,}000 \times \frac{1}{6}$ and $200{,}000 \times \frac{5}{6}$ (green interval), while reserving the final frames (red interval) for validation.

The standard procedure to construct a detector mask consists of computing two maps from the selected frames: i) the average flux per pixel ([ph/px/s]), and ii) the maximum photon count per pixel ([ph/px]). These maps are shown in Fig. 3.7, together with the respective population histograms. Using these maps, we identify regions that deviate significantly from the average detector response. These include:

- The detector modules edges
- A distinct line in the upper-right corner
- Cross-like patterns visible in the maximum-count map

13 The data analyzed in this thesis refer to more recent measurements, taken in 2025 and 2026. In particular, the ID10 measurements with the CdTe detector were performed in SAXS configuration. Here, we use these earlier preliminary measurements because they were acquired at the same enrgy (8 keV) on the FSDP, ensuring that the entire detector is illuminated and that the beamstop shadow is absent.

- Junctions between thin and thick detector lines

In addition, we remove hot pixels by identifying those that consistently register counts over multiple consecutive frames. In this dataset, four hot pixels were identified at (15, 1007), (15, 1008), (16, 1008), and (1495, 1264). The final mask, referred to as **e4m_mask**, is shown in Fig. 3.8.

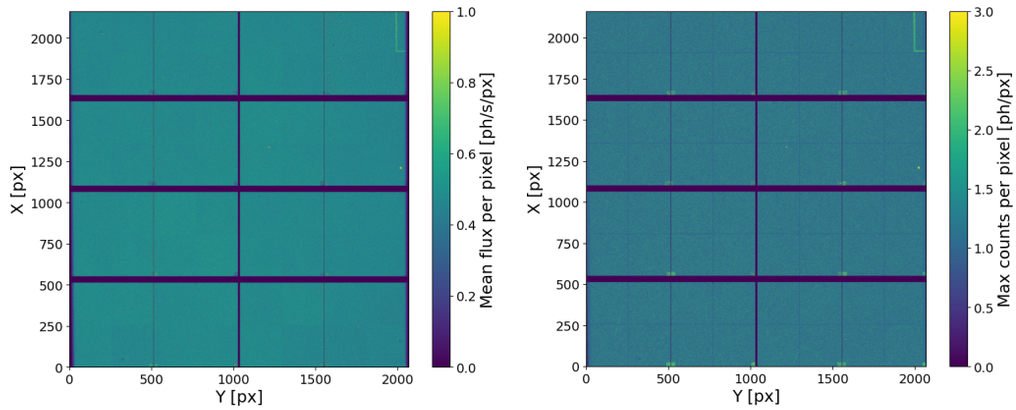

Figure 3.7: Maps of average flux per pixel $[ph/px/s]$ and maximum photon count per pixel $[ph/px]$, together with the corresponding pixel histograms.

Under the assumption of uniform illumination, the distribution of the average flux per pixel is expected to be Gaussian (or Poissonian in the low-count regime), centered around the mean X-ray flux over the detector. While small deviations from an ideal Gaussian are expected—for example due to the non-uniform static structure factor of GeO_2—the distribution obtained after applying the **e4m_mask** deviates markedly from this expectation (see Fig. 3.7). Although the masking procedure effectively removes many low-count pixels without affecting the central Gaussian-like component, the overall distribution still exhibits significant non-Gaussian features. In particular, while the core of the distribution appears consistent with a Gaussian profile, an additional broad tail extends to values several times larger than the mean, indicating the presence of pixels with anomalously high count rates.

To identify pixels with anomalous behavior, we apply thresholding to the flux distribution using two limits, a lower and a higher one, which enclose approximately 90% of the detector pixels (see Fig. 3.9). Pixels lying outside this interval correspond to the low- and high-flux tails discussed above. Figure 3.10 shows the spatial distribution of these out-of-average pixels on the detector, distinguishing between those exceeding the upper threshold and those falling below the lower one.

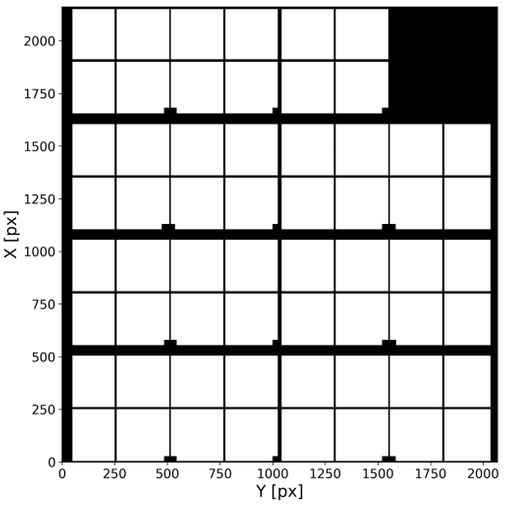

Figure 3.8: Manually defined detector mask (**e4m_mask**). In addition to the rectangular regions masking unwanted detector areas, four hot pixels (not visible at this scale) have been removed: (15, 1007), (15, 1008), (16, 1008), and (1495, 1264). The reason for masking the entire upper-right region will be clarified later.

The structured patterns observed in Fig. 3.10 are independent of the sample, scattering angle, and experimental configuration. This confirms that these out-of-average pixels originate from detector-related effects, thereby excluding non-uniform illumination as the source of the non-Gaussian flux-per-pixel distribution. The thresholds introduced in Fig. 3.9 therefore effectively isolate these anomalous pixels. We refer to the mask generated from these out-of-threshold pixels as **e4m_htmask**, obtained by combining the black pixels in the two maps shown in Fig. 3.10. A limitation of this approach is that a small fraction of statistically valid ("good") pixels may also be classified as outliers, since the procedure removes the tails of the Gaussian distribution. However, their number is negligible compared to the extended structured patterns identified above.

We attribute the presence of these anomalous pixels to non-uniformities arising from the CdTe detector fabrication process. Importantly, masking the out-of-threshold pixels significantly improves the flux distribution. This is demonstrated in Fig. 3.11, where the histograms are computed using the reserved test frames (red interval in Fig. 3.6). The distribution obtained after applying **e4m_htmask** is compared with both the raw data and the **e4m_mask**-only case. As shown, the application of **e4m_htmask** nearly restores the expected Gaussian profile.

In practice, these hidden out-of-average pixels predominantly exhibit higher-

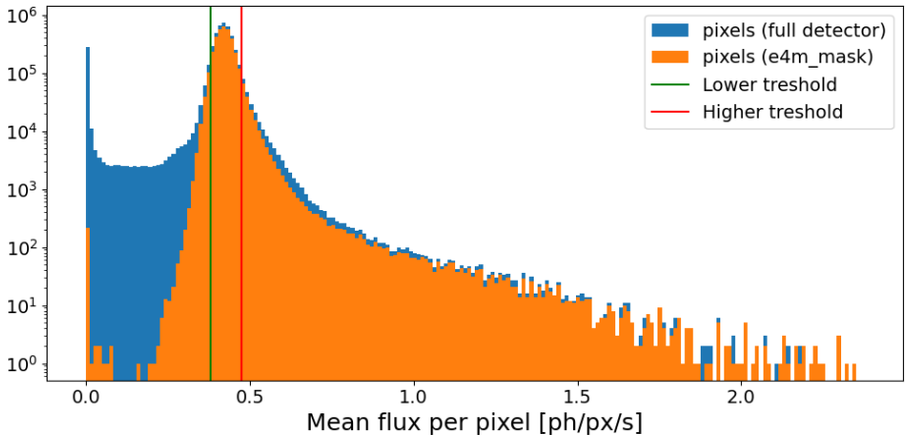

Figure 3.9: Histogram of the mean flux per pixel after applying the **e4m_mask** (orange), compared to the distribution obtained from the full detector (blue). The central peak is approximately Gaussian and represents the average X-ray flux over uniformly illuminated pixels. The vertical green and red lines indicate the lower ($l_{\text{th,low}}$) and upper ($l_{\text{th,high}}$) thresholds used to further filter anomalous pixels. While the masking procedure removes a large fraction of low-count pixels, the distribution still exhibits a pronounced high-flux tail extending well beyond the Gaussian core, highlighting the presence of pixels with anomalously high counting rates.

than-average counts. While this leads to a slight overestimation of the mean detector intensity, their most significant impact is on the intensity autocorrelation function: their removal substantially lowers the baseline of the measured $g^2(t)$, indicating that these pixels contribute spurious correlations across all time scales.

It is worth noting that this effect is not observed at the P10 beamline, which employs a silicon-based detector rather than CdTe. This difference likely reflects the higher material uniformity and maturity of silicon detector fabrication.

Finally, a residual non-Gaussian contribution remains, visible as a small population of high-count pixels on the right-hand side of the distribution of Fig. 3.11. As discussed in the next section, this contribution originates from environmental noise and can be effectively removed without introducing additional masking procedures.

3.3.2 Environmental radioactivity noise in the CdTe Detector

Unlike the out-of-average pixels described in the previous section, which are stable over time, the remaining noisy pixels on the right-hand side of the Gaussian distribution in Fig. 3.11 vary from scan to scan. Moreover, these pixels generally

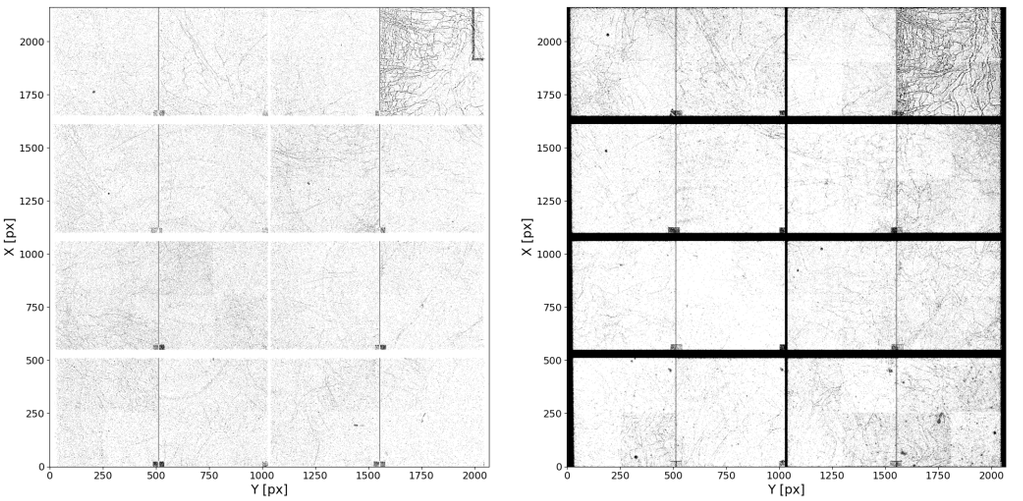

Figure 3.10: Detector map showing pixels (black) above the higher threshold (left) and below the lower threshold (right). These thresholds are those shown in the histograms of Fig. 3.9).

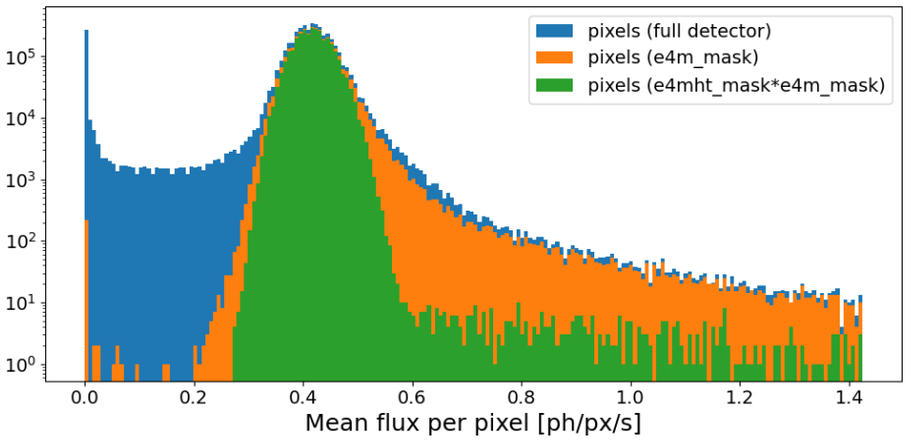

Figure 3.11: Mean flux per pixel computed on the test frames (red interval in Fig. 3.6). The blue histogram corresponds to the raw data, while the orange histogram is obtained after applying both **e4m_mask** and **e4m_htmask**. Except for a small residual contribution at high flux, the resulting distribution is close to Gaussian.

behave correctly, except for sporadic events in which they register counts far exceeding the expected signal (ranging from 10 to 1000 counts, compared to the typical 1–2 maximum photons per pixel per frame). This behavior is consistent with energy deposition from high-energy photons (e.g. γ rays) originating from environmental radioactivity. Such events are particularly relevant in CdTe detectors due to their extended detection efficiency, which can reach into the MeV range. As a result, a single high-energy photon (hard X-Ray or γ-Ray) can produce multiple counts when the detector operates at keV energies, with an approximate count given by $E_{\text{ray}}/E_{\text{th}}$, where E_{th} is the pixel threshold energy used to discriminate electronic noise from photon events. In practice, E_{th} is set slightly above half of the incident photon energy to minimize charge sharing (cross-talk) between neighboring pixels, where the deposited energy may be split between adjacent channels.

To isolate these high-count events, it is sufficient to set to zero any pixel counts exceeding a chosen threshold within each run. Owing to the large difference between the counts produced by environmental radioactivity and those from the scattered X-ray signal, selecting an appropriate threshold to separate the two contributions is straightforward. Even better, the recent advances in speed of XPCS detectors, together with sparse data acquisition pipelines that enable operation at these higher frame rates, further enhance this separation: the number of "good" counts per pixel decreases with shorter integration times, while the energy deposited (i.e. the counts) by a γ event remains unaffected. As a result, the contrast between the two signals becomes even more pronounced.

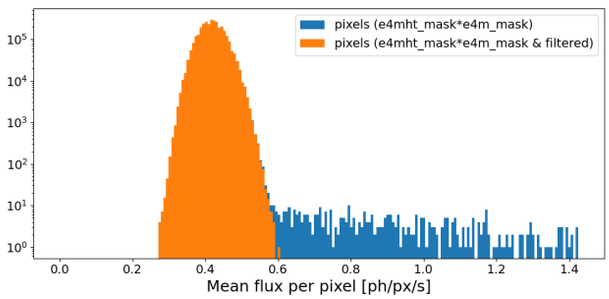

Figure 3.12: Mean flux per pixel computed on the test frames (red interval in Fig. 3.6). Both histograms are masked using **e4m_mask** and **e4m_htmask**. The blue histogram corresponds to the raw data, while the orange histogram shows the distribution after removing high-count (γ) events. The Gaussian profile is fully restored.

Figure 3.12 compares the flux-per-pixel histograms before and after the high-

count filtering, both obtained using **e4m_htmask**. The expected Gaussian distribution is fully recovered after the correction. Notably, this result is achieved by removing only the few counts exceeding the threshold within each run, rather than excluding entire pixels from the analysis.

The impact of this correction on the $g_2(t)$ function clearly depends on the strength of the scattered X-ray signal. For the test frames analyzed here, the γ-ray contribution (in term of counts) amounts to approximately 0.04% of the total signal (evaluated after applying **e4m_htmask**). The detection rate, i.e. the fraction of frames containing at least one γ event detected by the threshold counts, is about 1.2%. This corresponds to an average contribution of roughly 500 counts/s within the entire detector at an operating energy of 8 keV. Notably, we observe an additional contribution at short times in the computed $g_2(t)$ without filtering these events: these locally deposited high-count events tend to correlate across temporally adjacent frames, producing a spurious bump in $g_2(t)$ at millisecond timescales.

Following the identification of this effect and the implementation of the corresponding correction, the ID10 beamline incorporated an online filter in the data acquisition pipeline. This filter automatically sets to zero any pixel counts exceeding a predefined threshold (for example, ~ 5 counts when operating at millisecond frame rates) before storing the data.

3.3.3 Cosmic-ray signal in the Si detector

The final source of noise we consider arises from what we broadly refer to as "cosmic rays" or residual environmental radiation not removed by the methods described above, i.e. any spurious signal produced by particles depositing energies of the order of tens of keV in the detector pixels. This contribution is mainly attributed to muons, high-energy protons, and residual soft X-ray background. For instance, a minimum-ionizing particle (MIP), such as a muon, is expected to deposit approximately 10 keV when traversing 100 μm of silicon, that is the thickness of the detector [Gro22].

To detect these events efficiently under low X-ray flux conditions, we developed a simple algorithm that exploits their higher spatial correlation compared to the "good" scattered X-ray photons. The data are treated as a 2D sparse matrix, where rows correspond to frames and columns to pixels (~4M pixels per frame). For each frame, we evaluate the spatial correlation of the detected events by counting the number of neighboring pixels firing within a distance d_{px} (measured by a linear metric).

Cosmic-ray events are identified by applying a lower threshold N_{max} on the number of neighboring active pixels within d_{px}. Computationally, this is efficiently

implemented as a sparse matrix multiplication using a kernel matrix $K(d_{\text{px}})$, which maps each event to its local neighborhood[14]:

$$\text{events} = [(\text{data} \neq 0)@K(d_{\text{px}})] \geq N_{\text{max}},$$

where the (sparse) matrices have dimensions $N_{\text{frame}} \times N_{\text{pixel}}$ (data) and $N_{\text{pixel}} \times N_{\text{pixel}}$ (K).

This method is effective under the assumption of low photon occupancy, where genuine X-ray scattering events are sparse. Under these conditions, the spatial signature of cosmic-ray events—typically extended clusters or linear tracks—can be clearly distinguished from isolated photon detections. This assumption is well justified, as the correction becomes relevant only in very low signal regimes.

To quantify this contribution, we analyze a measurement at PETRA III (Si detector) over a 1-hour acquisition on v-GeO_2 at room temperature in small angle configuration ($Q = 0.2$ Å^{-1})[15]. Figure 3.13 (left) shows the spatial distribution of detected cosmic-ray events over this run. The image is obtained by summing all identified events across frames, and shows the effectiveness of the matrix multiplication method in recognizing events characterized by spatial patterns. For examples, muons producing straight lines are well recognized, as well as high energy electrons producing "spaghetti" like shapes. On average, we detect ~5 events/s, corresponding to an integrated intensity of ~50 counts/s (each event, on average, affects about 10 pixels). Assuming similar values for the CdTe detector (ID10), it is evident that in within the CdTe γ-induced counts dominate the detector background, and these lower counting events can be neglected.

Once these events are identified, the correction procedure follows the same approach introduced in the previous section: pixels identified as cosmic-ray events are set to zero on a frame-by-frame basis. Figure 3.13 right shows the effect of this correction by looking at the histogram of the average detector flux per frame. The inset shows the time evolution of the average flux at the detector. As observed, the intensity initially increases due to the structural changes undergone by germania under irradiation (see following chapters), and subsequently reaches a stationary regime. The figure compares the filtered signal (orange) with the unfiltered one (blue), clearly highlighting the presence of spurious high-count frames in the latter. After filtering, the expected Gaussian distribution of the signal is fully restored.

14 We skip the details on the specific form of the kernel matrix.

15 These measurements are test data acquired in 2024. The measurements discussed later in this thesis were performed in 2026 at the FSDP of germania. The reason for presenting this contribution using small-angle test measurements lies in the lower scattered flux, which facilitates the identification of the background signal discussed here.

In any case, this contribution remains negligible under typical experimental conditions, as evidenced by the minimal change in the counting distribution after filtering. In our measurements at PETRA III on v-GeO_2, this correction was never relevant, and no effect on the $g_2(t)$ function was observed. Although these experiments were performed under very low flux conditions, this contribution may become relevant when working at even lower fluxes. Therefore, in the following, we neglect this effect and only correct for the two contributions discussed above.

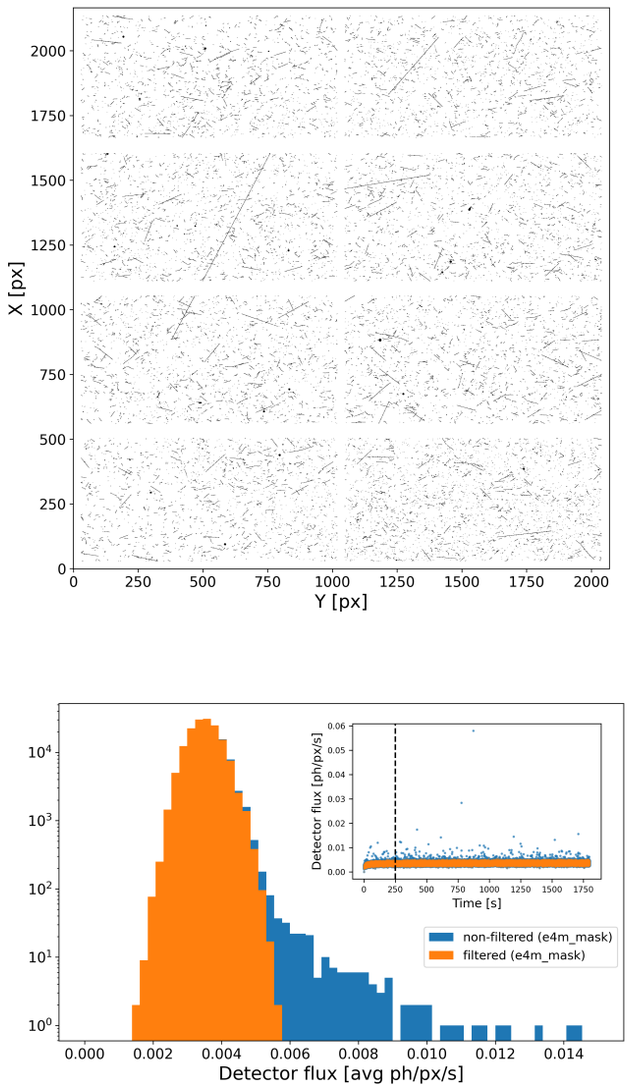

Figure 3.13: left) Spatial map of detected cosmic-ray events in a low-flux measurement at PETRA III (Si detector) over a 1-hour scan. The image is obtained by summing all identified events across frames. right) Flux-per-pixel histogram for a very low signal measurement at PETRA III (v-GeO_2, $Q = 0.4$ Å^{-1}) before and after cosmic-ray filtering. The expected Gaussian distribution is recovered after correction.

4 Radiation Damage in Glasses under Ionizing Irradiation

Ionizing radiation induces both microscopic and macroscopic changes in glasses, affecting their structural, optical, and dynamical properties. Initially studied in the context of nuclear waste vitrification and radiation-resistant materials, these phenomena have become a framework for understanding how disordered networks respond to non-thermal perturbations.

In this Chapter, we introduce the main mechanisms of radiation–matter interaction in oxide glasses, namely radiolysis, atomic displacement (knock-on damage), and electron rearrangement processes. These mechanisms lead to the formation of point defects whose populations are governed by the interplay between generation and recovery, controlled by dose, dose rate, and temperature. We also discuss how the accumulation of such defects produces structural modifications extending from the atomic to the nanometric scale.

Particular attention is devoted to the dynamical perspective that has recently emerged with XPCS. Under intense irradiation, glasses exhibit beam-induced atomic rearrangements even far below the glass transition temperature. In this regime, radiation modify the glass structure up to a steady state governed by the balance between defect creation and annihilation.

Understanding this radiation-driven dynamics, the related structural modifications, and its dependence on experimental parameters as photon flux and temperature, constitutes the main focus of this Chapter and is essential for interpreting the results presented in this thesis.

4.1 Natural intrinsic defects in crystals and glasses

Crystals can be imagined as the idealized limit in which atoms occupy periodic lattice sites with complete translational symmetry. However, real crystalline materials contain defects, such as chemical impurities, vacant lattice sites, and atoms occupying non-regular lattice positions.

An analog situation happen in glasses. In this case, the ideal glass structure is commonly described by the continuous random network (CRN) model, whereas real glasses, like real crystals, always contain defects. In many instances, these defects are closely analogous to those found in crystalline materials [Gri85].

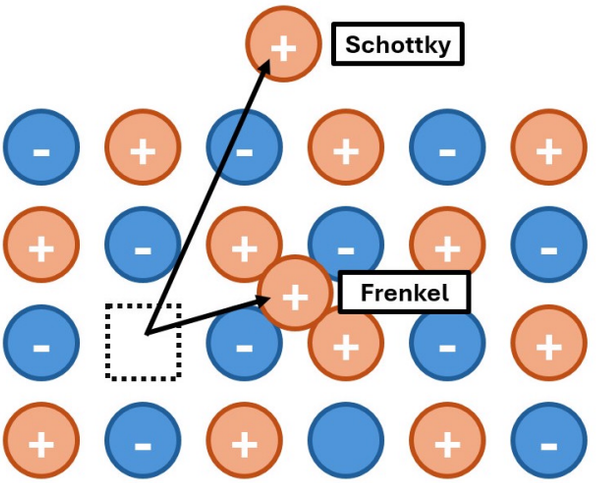

Figure 4.1: Schematic representation of intrinsic point defects in an ionic crystal. In a Schottky defect, an ion is removed from the lattice and transferred to the surface, creating a vacancy. In a Frenkel defect, an ion is displaced from its lattice site to an interstitial position, forming a vacancy–interstitial pair. Figure inspired from [Kit05].

For this reason, we begin by introducing *intrinsic point defects*, namely, defects that involve only the atoms of the host material and not impurities or dopants, by considering the case of crystalline solids at thermal equilibrium. In the following sections, we will extend this discussion to intrinsic point defects in oxide glasses, considering both defects naturally present in the as-prepared material and those induced by irradiation. In this context, intrinsic defects are defined as those associated solely with a pure glass matrix composed of a single type of network-forming cation R and oxygen (or, more generally, a chalcogen) O.

4.1.1 Schottky defects

The simplest type of defect is a lattice vacancy, corresponding to a missing atom and commonly referred to as a *Schottky defect*. In a perfect crystal, a Schottky defect can be created by transferring an atom from a lattice site in the interior to a site on the crystal surface (see Fig. 4.1). At thermal equilibrium, a finite number of lattice vacancies are always present in an otherwise perfect crystal, since the introduction of disorder increases the entropy of the system [Kit05].

In metals with close-packed structures, the fraction of vacant lattice sites at temperatures just below the melting point is typically on the order of 10^{-3} to 10^{-4}.

In some alloys, however the fraction of vacant sites for one of the components can be as high as 50%.

The probability that a given lattice site is vacant is governed by the Boltzmann factor $P \propto \exp(-E_V/k_BT)$, where E_V is the energy required to remove an atom from a lattice site in the interior of the crystal and place it at a site on the surface. If the crystal contains N lattice sites, the equilibrium number of vacancies n is therefore given (for $n \ll N$) by [Kit05]

$$\frac{n}{N} \underset{n<<N}{\simeq} \exp\left(-\frac{E_V}{k_BT}\right), \tag{4.1}$$

with E_V typically of the order of few eV.

4.1.2 Frenkel defect

The other type of difect is the *Frenkel defect* (Fig.4.1), in which an atom is displaced from a regular lattice site to an interstitial position—namely, a site that is not normally occupied by an atom. The dominant intrinsic defect type depends on the system.

If the number of Frenkel defects n is much smaller than both the number of lattice sites N and the number of available interstitial sites N', the resulting expression for the equilibrium defect concentration is given by [Kit05]

$$n \simeq \sqrt{NN'} \exp\left(-\frac{E_I}{k_BT}\right). \tag{4.2}$$

where E_I is the energy necessary to remove an atom from a lattice site to an interstitial position.

We found that the equilibrium concentration of vacancies and vacancy-interstitial pairs decreases with decreasing temperature. However, if a crystal is grown at elevated temperature and subsequently cooled rapidly, the vacancy concentration may exceed the equilibrium value at lower temperatures, as vacancies become frozen into the lattice due to limited atomic diffusion [Kit05].

The above disussion can be extended to the case of glasses. Intrinsic defects are naturally present in glasses quenched from the high temperature melt. As in crystals, these are Frenkel (vacancy-interstitial pairs) and Schottky (vacancy) defects. Following Eq. 4.1 and 4.2, their equilibrium concentration increases strongly with temperature, and when a glass is quenched from the melt, the high-temperature population of intrinsic defects is frozen into the structure. Subsequent annealing or slow cooling can partially reduce this intrinsic defect concentration, therefore, the

defect concentration is directly connected, and naturally increase, with the glass fictive temperature. For example, these defects are naturally present in silica with a concentration of $\sim 10^{18}$ cm^{-3} (resulting in 0.1% of defects per atom) [Gri85].

4.2 Radiation Damage Mechanisms in Glasses

Radiation damage processes in glasses are generally the same as in crystals, and arises from the interaction of energetic radiation with both the electronic and atomic structure of the material. Although the primary interaction depends on the radiation type and energy, the subsequent relaxation processes ultimately determine the nature and stability of the induced damage. Following the framework introduced by Griscom [Gri85], radiation damage mechanisms in glasses can be classified into three categories:

- radiolysis (ionization and recombination of electrons),
- displacement or knock-on damage,
- electron rearrangement processes.

In all cases, what we define as "damage" is the existence of post-irradiation local structures (either atomic or electronic) which differ from the structures present before irradiation [FG79]. In these terms, we can think of the glass undamaged (pristine) structure in terms of an ideal continuous random network (CRN), although, as we have just seen, deviations from the ideal CRN exist in any real glass [Gri85].

4.2.1 Irradiation and dose

The amount of radiation absorbed by a system is quantified through the dose D, defined as the average energy absorbed per unit mass. The dose can be delivered in two different ways: i) a focused beam can hit the sample, or ii) the sample can be fully bathed in a radiation rich environment. The first case is typical of X-ray and electron irradiation, while the second for neutrons and γ-rays.

In the case of an X-ray beam of steady photon flux Φ (ph/s) and energy ε t impinging on sample volume of mass M over an exposure time, the absorbed dose can be written as

$$D = \frac{\Phi(1-T)\varepsilon}{M} \cdot t, \tag{4.3}$$

where $T = \exp(-\mu d)$ is the transmission of a sample of thickness d and attenuation coefficient μ. The scattering volume mass can be computed by $M = Ad \cdot \rho$, where ρ is

the density of the sample and A the area of the focal spot, calculated by considering an ellipse with semi-axes equal to 2σ.

In neutron irradiation experiments, by contrast, the entire sample is generally exposed inside the reactor. In this case, M corresponds simply to the total sample mass, and Φ represents the average number of neutrons per second impinging on the sample within its solid angle. Also, an integration over the neutron energy spectra should be taken. Similarly, for gamma irradiation, the sample is placed close to the radioactive source.

The unit of dose is the gray Gy=J/kg, or, in older texts, the radiation unit rad = 0.01 Gy.

4.2.2 Radiolytic processes

Radiolysis encompasses atomic and structural modifications driven by the energy released during non-radiative recombination of electrons and holes. When ionizing radiation (X- or γ-ray photons, ultraviolet light, or charged particles such as electrons or protons) traverses a glass, and its energy exceeds the band gap, electrons are ionized from the valence band. The promotion of electrons from the valence band to the conduction band generates electron–hole pairs, with the excess energy converted into kinetic energy. These excited electrons then move through the glass matrix and undergo several possible processes: they can be trapped at pre-existing flaws to form defect centers in the glass structure, recombine with positively charged holes, or, in the case of high-energy electrons, produce a cascade of secondary electrons through knock-on collisions with bound electrons. These secondary electrons continue to propagate through the matrix, ionizing additional bound electrons via Coulomb interactions and losing approximately 20 eV per ionization event. Eventually, the electrons lose sufficient energy such that further ionization is no longer possible, at which point they either become trapped at defect sites (here categorized as electron rearrangement processes, see subsection 4.2.4), or recombine with positive holes in the matrix [FG79]. These recombinations are the processes that transfer energy to the glass network and are what we refer to as radiolytic damage creation.

In oxide glasses such as silica and germania, the band gap is large ($E_g \approx 9$ eV), and electron-hole recombination happens through inelastic scattering processes [Gri85; OGP21]. While radiative recombination may occur, non-radiative recombination is often dominant. In this case, the released energy is transferred to nuclear motion, leading to highly localized vibrational excitation. The energy released during a single non-radiative recombination event can be comparable to or greater than typical bond energies. For example, the Si–O bond energy in silica is approximately

$E_{\mathrm{Si-O}} \approx 4.5$ eV (see Tab. 4.1). As a result, localized recombination events can induce bond rupture, atomic rearrangement, or the conversion of pre-existing structural precursor sites into stable defect centers [Gri85].

Table 4.1: List of bond energies of typical oxide glasses [Kil95].

Type	Bond energy (eV)	Type	Bond energy (eV)
O–O	5.2	Si–Si	4
Si–O	4.5	Ge–Ge	2.0

4.2.3 Displacement (knock-on) damage

Displacement damage occurs when the incident particle directly transfers momentum and energy to an atom in the glass network, such that it is sufficient to break bonds and drive the atom from its equilibrium site into an interstitial position, producing vacancy–interstitial pairs. The minimum amount of energy transfer to have knock-on events has to be of the same order as the strengths of the bonds which must be broken (see Tab. 4.1), usually 4-20 eV. This energy must be compared to the maximum energy that can be transferred per collision. In the following we discuss knock-on damage for different particles.

Electrons An electron must travel at relativistic speeds to impart enough energy to an atom in the glass matrix to cause a displacement. From relativistic scattering theory the maximum energy T_m that can be transferred to an atom of mass M by an electron of energy E is

$$T_m = \frac{4m_e ME}{(m_e + M)^2}\left(1 + \frac{E}{2m_e c^2}\right)$$

where m_e is the mass of the electron. Thus, assuming $T_m = 20$ eV is required, the incident electron must have an energy of

$$E(\mathrm{MeV}) = 0.52\left(\sqrt{1 + 0.45A} - 1\right) \tag{4.4}$$

to cause a displacement of an atom of mass number A. For example, in amorphous silica, the threshold electron energies required to displace oxygen and silicon atoms are on the order of 160 keV and 260 keV, respectively [Gri85].

Neutrons In the case of neutrons, non-relativistic scattering theory applies, yielding to

$$T_m = \frac{4nME}{(n+M)^2}E$$

where n is the mass of the neutron. Thus, requiring 20 eV, yields

$$E(\text{eV}) = 6.25\frac{(1+A)^2}{A} \tag{4.5}$$

High-energy photons If the incident particle is a high-energy photon (X- or γ-rays), atomic displacements occur indirectly through energetic secondary electrons. These electrons are primarily generated by Compton scattering, since radiolytic electrons produced by lower-energy photons do not have sufficient kinetic energy to induce direct atomic displacements. Such displacements would require X-rays in the hundreds of keV range (as described above), where Compton scattering dominates over radiolysis [Gri85]. For a photon of energy E_p scattered at an angle θ, the resultant Compton electron have an energy

$$E = E_p(1 - \frac{m_e c^2}{E_p(1-\cos\theta + m_e c^2)} \tag{4.6}$$

where m_e is the electron mass. For $E_p = 1.5$ MeV gamma rays at 180° scattering angle the resulting Compton electrons carry an energy of $E = 1.3$ MeV. Instead, for 100KeV X-rays, the highest energy Compton electron have an energy of 28 keV. Therefore, equation 4.4 compared to the typical oxide glasses bond strengths (see table 4.1), says that gamma rays are capable of directly displacing atoms after Compton scattering, while lower energy X-rays can't.

However, it does not follow that knock-on events predominates whenever T_m exceed the bond threshold energy. In fact, experimental observations demonstrate that atomic displacement plays a minor role in defect formation in silica under ionizing irradiation [Gri85; PK68]. Defect yields scale with absorbed ionization dose rather than with calculated displacement rates without showing any discontinuity at T_m, indicating that knock-on damage contributes only marginally compared to radiolysis (see Fig. 1 from ref. [Gri85]).

Finally, for the soft X-rays primarily considered in this thesis—typically in the energy range of 8–25 keV and employed at modern synchrotron beamlines for XPCS and inelastic X-ray scattering experiments—displacement damage can be safely neglected.

4.2.4 Electron rearrangement processes

Electron rearrangement processes involve the trapping of radiation-generated electrons or holes at pre-existing defects within the glass network, since no materials are known wherein both electrons and holes can be self trapped. In glasses, such precursor sites include oxygen vacancies, strained bonds, non-bridging oxygens, hydroxyl groups, and impurity-related complexes [Gri11; Gri85]. Charge trapping alters the local electronic configuration and generally lead to the formation of paramagnetic or optically active defect centers without necessarily producing new atomic displacements.

Damage sites created radiolitically or by knock-on processes, as well as intrinsic defects naturally present in glasses quenched from the high temperature melt (Sec. 4.1), work as precursors for the electron rearrangements, serving as a trap for the radiation-induced free carriers. We have seen that intrinsic defects are naturally present in silica with a concentration of $\sim 10^{18}$ 1/cm^3. In contrast, intrinsic defects created by radiolysis or by knock-on events increase monotonically up to $\sim 10^{20}$ cm^{-3}, where defect annihilation due to electron wave function overlaps begin [Gri11; Gri85].

In silica and germania, oxygen Frenkel defects consist of an oxygen vacancy and a complementary interstitial oxygen. The vacancy leads to the formation of an $R{-}R$ bond, while the interstitial oxygen binds onto a normal oxygen site to form a peroxy linkage of the type $R{-}O{-}O{-}R$. Upon irradiation, these natural defects, as well as those formed by knock-on events or recombination of electron-holes pairs, may trap holes, resulting in paramagnetic centers such as oxygen hole centers or peroxy radicals. Another intrinsic defect arises from the presence of strained $R{-}O{-}R$ bonds, which naturally occur in glasses due to the distribution of bond lengths and bond angles inherent to the disordered network. Under irradiation, rupture of one bond in such a strained configuration with a successive rearrangement of the electronic structure can lead to the formation of stable dangling bond on the network former and a non-bridging oxygen hole center.

A common feature shared by many of these defect centers is the local structural relaxation that occurs following charge trapping. Such relaxation stabilizes the defect by lowering its energy and inhibiting recombination. This stabilization may involve local rearrangement of the glass network, such as bond reorientation, or the diffusion of nearby modifier cations toward or away from the defect site to preserve charge neutrality. Together, these processes contribute to the formation and long-term stability of radiation-induced defect centers in glasses.

4.2.5 An illustrative case: 1 MGy ^{60}Co γ radiation on silica

Here we consider the well-studied case of silica irradiated by the ~1.5 MeV γ rays emitted by a ^{60}Co source, as described in Ref. [FG79]. This case provides a clear illustration of the relative roles of knock-on and radiolytic processes and allows quantitative estimates of recombination probabilities and ionization yields.

About 1 Si atom is displaced for about 100 γ photons. Therefore, a ^{60}Co dose of 1 MGy results in approximately 10^{16}–10^{17} displacements of Si atoms per gram of material. A similar number of displacements occurs for oxygen atoms. Structural defects produced in this manner can serve as trapping sites for radiation-generated electrons and holes, thereby acting as precursors for electron rearrangement processes.

However, as discussed previously, ionization dominates over atomic displacement. For the same 1 MGy dose, approximately 10^{25} ionizations per gram are produced, corresponding to more than 10^4 ionization events per silicon atom in the glass. Despite this extremely large number of ionizations, the concentration of stable defect centers observed in monocomponent glasses such as SiO_2, B_2O_3, and GeO_2 after ^{60}Co irradiation to 1 MGy is typically on the order of 10^{16} cm^{-3} (order 10^{15} g^{-1}).

This comparison clearly indicates that the vast majority of radiation-induced ionization events result in rapid electron–hole recombination, with only a very small fraction leading to the formation of stable defect centers. Similarly, most short-range atomic displacements recombine through vacancy–interstitial annihilation and do not contribute to long-lived structural damage.

4.3 Radiation-induced defect centers in oxide glasses

As introduced above, the microscopic manifestation of radiation damage in oxide glasses is the formation of point defects, which have been extensively investigated using electron spin resonance (ESR) and optical spectroscopy [Gri11; Gri85], largely in the case of silica.

ESR is a spectroscopic technique that probes transitions induced by electromagnetic radiation between electron spin energy levels in the presence of a static magnetic field. The method is applicable to species containing one or more unpaired electrons, including radicals, triplet states, and complexes of paramagnetic ions. Spectral characteristics such as resonance positions, hyperfine splittings, line shapes, and line widths are sensitive to the electronic structure, molecular orientation and local environment of the paramagnetic species. Since all the glasses

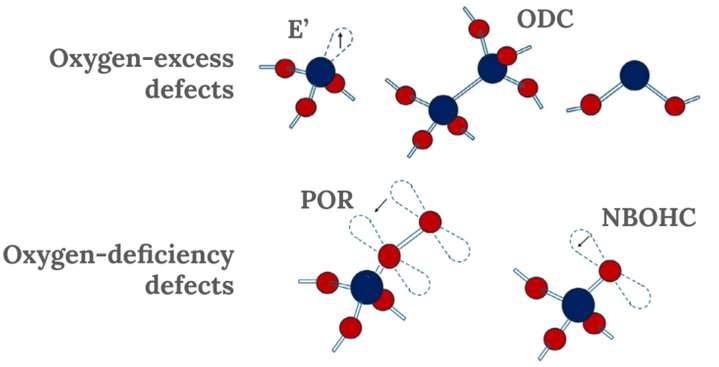

Figure 4.2: Main point defects in oxide glasses, divided as oxygen deficiency-related and oxygen excess-related color centers. E') The general E' center showing the dangling bond of the sp3 hybrid orbital associated with an oxygen vacancy with a trapped hole or under-coordinated silicon, ODC) the so-called wrong bond (ODC = oxygen deficiency center), associated with a neutral oxygen vacancy or with a divalent (twofold coordinated) Si/Ge atom, NBOHC) non-bridging oxygen hole center associated with the 2px dangling bond of an under-coordinated oxygen atom, POR) the peroxyl radical. Figure adapted from [JB25; OGP21].

of interest are diamagnetic in their as-prepared forms, ESR-active defects result only when the radiolytic fragment or displaced atom contains an odd number of electrons or if an electron rearrangement process happened. In these terms, radiation-induced defects in glasses can be broadly classified into ESR-active and ESR-silent centers. ESR-active defects contain unpaired electrons and can be directly detected, for example the trapping of a hole at a vacancy site which result in a paramagnetic defect, namely the E' center (see Fig. 4.2). Differently, ESR-silent defects are inferred from optical absorption or luminescence measurements [Gri85].

Defect centers in oxide glasses can be classified by defect type. The aim is to organize the complex landscape of radiation-induced point defects into a limited number of defect types common to most oxide glasses. For a more detailed treatment of this subject, the reader is referred to the works of David L. Griscom [FG79; Gri11; Gri85].

4.3.1 E′ centers

The E′ center consists of a pyramidal AO_3 unit with an unpaired electron localized on a dangling sp^3 hybrid orbital of the network-forming apex atom A, where (in general) all three oxygens are bridging to the other atoms in the glass (or crystal)

network (see Fig. 4.2). This defect is associated with three-coordinated atoms present as "defects" in the otherwise tetrahedral network. For example, an oxygen vacancy in the SiO_2 or GeO_2 network, would give rise to two AO_3 units. The E′ center is commonly represented as

$$\equiv \mathrm{R}\cdot \tag{4.7}$$

where the symbol "≡" represents three back bonds to three oxygens in the crystal structure or glass network and "·" represents an unpaired electron [Gri11; Gri85].

E′ centers are readily produced under both X-ray and γ-ray irradiation, even in regimes where atomic displacement is negligible. Their formation is attributed primarily to radiolytic processes and to electron rearrangement at oxygen-deficient precursor sites. A strong correlation has been established between the concentration of E′ centers and optical absorption bands in the ultraviolet, particularly near 5.8 eV [Luo+11].

The germanium E′ center

Detailed information on the germanium E′ center is reported in Ref. [FG79]. Since this system plays the central role in the present thesis, the most relevant results are summarized here.

The ESR signal attributed to the Ge E′ center was first reported by Weeks and Purcell [WP65] in a study of crystalline and glassy GeO_2 subjected to γ-ray and electron irradiation. This resonance has been associated with oxygen-vacancy-related structures, as demonstrated by the significantly higher defect production rate observed in reduced materials (about 50% more) compared with samples annealed in oxygen [FG79].

Garlick [GNO71] further demonstrated that, for a fixed X-ray dose (15 min irradiation), the concentration of Ge E′ centers formed in a given phase (hexagonal, tetragonal, or glassy) increases with increasing temperature of annealing treatments performed prior to irradiation. This behavior is attributed to the progressive quenching-in of intrinsic Frenkel and Schottky defects during high-temperature annealing, as described in Sec. 4.1. An exception to this trend is observed for heat treatments performed within the stability range of the tetragonal phase, evidencing the inability of this phase to support stable defects. In hexagonal and glassy GeO_2, the formation of Ge E′ centers under ionizing radiation is generally attributed to hole trapping at pre-existing Ge–Ge bonds, as a threshold energy of approximately 120 keV has been determined for the production of additional Ge E′ centers via oxygen displacement processes [GNO71].

4.3.2 Non-bridging oxygen hole centers (NBOHC)

Non-bridging oxygen hole centers (NBOHCs) correspond to hole trapped in a non-bonding oxygen 2p orbital perpendicular to the Si–O (or Ge-O, ...) bond (see Fig. 4.2)

$$\equiv \mathrm{R{-}O}\cdot. \tag{4.8}$$

Several processes may lead to the formation of NBOHCs under ionizing irradiation. In the case of silica, the following reactions has been identified:

1. The greatest numbers of NBOHCs are observed in high-OH silicas, where they result from radiolysis of the OH group:

$$\equiv \mathrm{Si{-}O{-}H} \xrightarrow{\text{ionization}} \equiv \mathrm{Si{-}O}\cdot + \mathrm{H}\cdot. \tag{4.9}$$

2. Hole trapping at pre-existing non-bridging oxygen sites may occur through direct capture of radiation-generated holes, without requiring bond rupture,

$$\equiv \mathrm{Si{-}O^-} + h^+ \rightarrow \equiv \mathrm{Si{-}O}\cdot. \tag{4.10}$$

   This process converts an inactive precursor into an optically and magnetically active NBOHC.

3. Radiolytic rupture of strained or distorted R–O–R bridging bonds may also produce NBOHCs together with a complementary R-related defect,

$$\equiv \mathrm{Si{-}O{-}Si} \equiv \xrightarrow{\text{radiolysis}} \equiv \mathrm{Si{-}O}\cdot + \equiv \mathrm{Si}\cdot. \tag{4.11}$$

NBOHCs formed through these processes are optically active and contribute to absorption bands in the visible and ultraviolet spectral regions [Gri85; OGP21].

4.3.3 Oxygen deficiency centers (ODC)

Oxygen deficiency centers (ODCs) are intrinsic defects associated with the absence of an oxygen atom in the glass network. They are generally ESR-silent but play an important role in the optical properties of irradiated oxides, particularly through absorption bands in the ultraviolet spectral region [Gri11; Gri85]. As visible in Fig. 4.2, two main classes of oxygen deficiency centers are commonly distinguished.

- A first class, often referred to as ODC(I), is associated with an oxygen vacancy forming a R–R bond,

$$\equiv \mathrm{R{-}R} \equiv . \tag{4.12}$$

  Such defects may act as precursors for the formation of paramagnetic centers under ionizing irradiation.

- A second class, denoted ODC(II), is commonly attributed to a twofold-coordinated silicon atom, which may be represented as

$$= \mathrm{R} :. \tag{4.13}$$

  ODC(II) centers are optically active and are responsible for characteristic absorption and luminescence bands in the ultraviolet region.

The formation of oxygen deficiency centers may occur during glass synthesis or as a result of radiolytic rupture of R–O–R bonds under ionizing irradiation.

4.3.4 Peroxy radical defects (POR)

Radiation can induce the formation of oxygen-related defects such as peroxy radicals and interstitial oxygen species. The peroxy radical (POR) consists of a superoxide ion (O_2^-) bonded to one R atom in the glass structure (see Fig. 4.2):

$$\equiv \mathrm{R{-}O{-}O} \cdot . \tag{4.14}$$

The formation of such defects may occur through hole trapping at pre-existing peroxy linkages or through secondary reactions involving oxygen species generated by radiolytic rupture of R–O–R bonds.

4.4 Dose-rate effects and competing annealing mechanisms

The response of oxide glasses to irradiation depends not only on the total absorbed dose but also on the dose rate. In general, the observed behavior reflects a competition between the rate of defect generation and the various annealing processes that reduce the defect population. In the present context, the term *annealing* is used in a broad sense to denote any mechanism that decreases the concentration of radiation-induced defects.

Three distinct annealing processes may operate on defects [Gri85]:

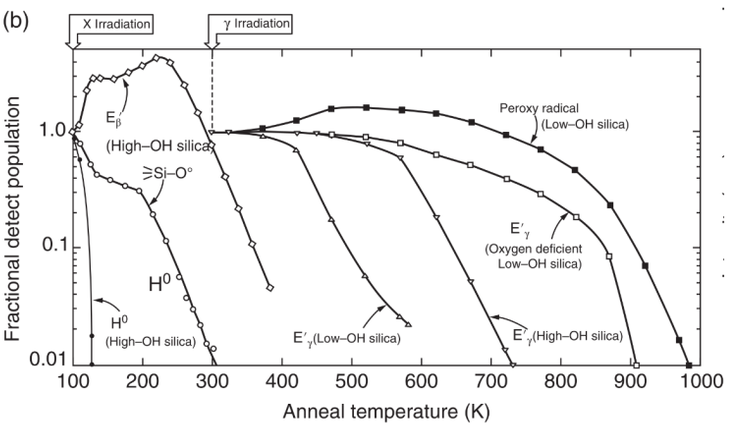

Figure 4.3: Isochronal annealing curves (5-10 min anneals) for radiation induced defect centers in high purity Type-III (1200 pp, OH) and Type IV (<5 ppm OH) fused silicas. Figure taken with permission from [OGP21].

1. thermal annealing,
2. radiation annealing,
3. photobleaching.

If thermal annealing is the only mechanism active and the dose rate remains constant, the defect concentration is expected to approach a steady-state value at sufficiently high total doses. This steady-state concentration depends both on the dose rate and on the temperature-dependent annealing rate.

Defect thermal annealing rates are typically determined from isochronal annealing experiments, which consist of heating a defect-containing sample through successive temperature steps, each held for the same fixed time, in order to monitor how defect concentration decreases as a function of temperature. These experiments show that defects generated at a given temperature can anneal within minutes after only a modest temperature increase. As shown in Fig. 4.3, silica irradiated at 77 K already exhibits recovery upon heating by about 20 K. Although annealing is commonly associated with temperatures near or above the glass transition, radiation-induced defects can anneal at temperatures far below T_g, reflecting localized rather than large-scale structural relaxation.

An investigation of the growth of the 5.8 eV optical absorption band, associated with the E′ center in amorphous silica, has demonstrated the existence of radiation annealing processes in addition to thermal annealing [PG72]. At sufficiently high dose rates (above approximately 0.004 MGy/s), the steady-state absorption at 5.8 eV

(reached after tens MGy irradiation) decreases with increasing dose rate at a given temperature. A similar behavior has firstly been reported by [MKG59] on crystal Ge that, quantifying defect population trough conductivity measurements, demonstrate for the first time a radiation-annealing process capable of reconstructing radiation generated-defect centers by irradiation at lower doses. This behavior indicates that radiation itself can promote structural recovery processes, not merely the depopulation of trapped electron or hole centers: radiation annealing can contribute to the healing of network damage.

In addition, radiation-induced optical losses may be reduced under illumination through photobleaching annealing, an effect of particular relevance in fiber-optic systems where attenuation depends on the propagating optical power. Notably, photobleaching does not restore the damaged structure, but rather deactivates optically absorbing defect centers [PG72].

Figure 10 of the review by Griscom [Gri85] presents a comparative overview of data obtained for amorphous SiO_2 subjected to various types of ionizing and particle irradiations over a broad dose range, including the effects of thermal annealing and defect stability. Experimental evidences strongly support the predominance of radiolytic mechanisms in the formation of point defects in silica, suggesting that many apparently distinct datasets may represent different manifestations of damage generated primarily through ionization processes. The compilation highlights the complexity of the observed behaviors and clearly illustrates the interplay of competing defect-generation and annealing mechanisms, demonstrating that radiation-induced defect evolution in oxide glasses cannot be described solely in terms of defect creation. Moreover, recently Griscom [Gri11] interpreted a turnover and subsequent decrease in paramagnetic defect concentration upon increasing dose in Al-doped silica as a defect conversion mechanism, involving the trapping of second electrons at defect sites that converts into ESR silent defects.

Overall, the observable defect concentrations arise from the dynamic balance between defect generation and multiple recovery mechanisms, whose relative importance depends on dose, dose rate and temperature.

4.5 Irradiation induced structural modifications in oxide glasses

In this section, we examine the modifications of the glass structure induced by irradiation. We focus on vitreous silica, as it is the most (and only) studied oxide glass in the literature. In this system, the short-range order is remarkably robust under irradiation: the fundamental SiO_4 tetrahedral units are largely preserved, and

silicon retains its fourfold coordination over a wide range of irradiation conditions [Dev94].

Although the local tetrahedral structure remains essentially intact, irradiation significantly affects the medium-range order of the glass network. In silica, changes in the Si–O–Si angular distribution are commonly observed. Raman spectroscopy shows a shift of the R-band (450 cm^{-1}) toward lower frequencies, consistent with a reduction of the average Si–O–Si bond angle, together with a broadening of the band, indicating an increased dispersion of angular values. The maximum reported decrease of the average bond angle is of the order of 10% [OGP21]. Neutron diffraction measurements further support an average Si–O–Si angle reduction of approximately 9.5°, accompanied by a slight decrease in the Si–O bond length and a small reduction in the Si–Si distance, consistent with the overall densification of the glass [BSG70; POH00]. Irradiation also modifies the ring statistics of the network. Irradiated silica exhibits a broader distribution of ring sizes, with an increased fraction of small-membered rings. This trend is evidenced by the enhanced intensity of the D_1 and D_2 Raman bands and supported by molecular dynamics simulations modeling the effects of nuclear collision cascades [OGP21].

Small-angle scattering measurements on silica provide additional insight into irradiation-induced structural heterogeneity. As first demonstrated by Bale *et al.* (see Fig.4.4), irradiation produces a pronounced increase in low-q scattering intensity, indicating enhanced density fluctuations at nanometric length scales. Importantly, these changes appear largely independent of the initial glass preparation route or impurity content, suggesting that the final irradiated structure is primarily governed by radiation-induced rearrangements rather than by pre-existing compositional differences. Consistent with the annealing behavior of defect centers discussed in Sec.4.4, the additional small-angle scattering signal decreases upon thermal treatment (see Fig.4.4). Notably, this recovery occurs at temperatures well below the glass transition temperature, demonstrating that the irradiation-induced structural modifications are metastable even at relatively low temperatures. This behavior is similar to the metastability of radiation-induced defect centers and supports the idea that irradiation drives the glass into a higher-enthalpy state that can relax upon moderate heating.

Interestingly, diffraction studies have shown that quartz and vitreous silica irradiated with neutron fluences exceeding 10^{18} n/cm^2 exhibit similar diffraction patterns, which differ from that of unirradiated vitreous silica [POH00]. This observation suggests that intense irradiation drives both crystalline and amorphous forms toward a structurally convergent, disordered state. This observation is further supported by recent simulations of neutron irradiated vitreous Silica, which shows the very same trend [Kri+17].

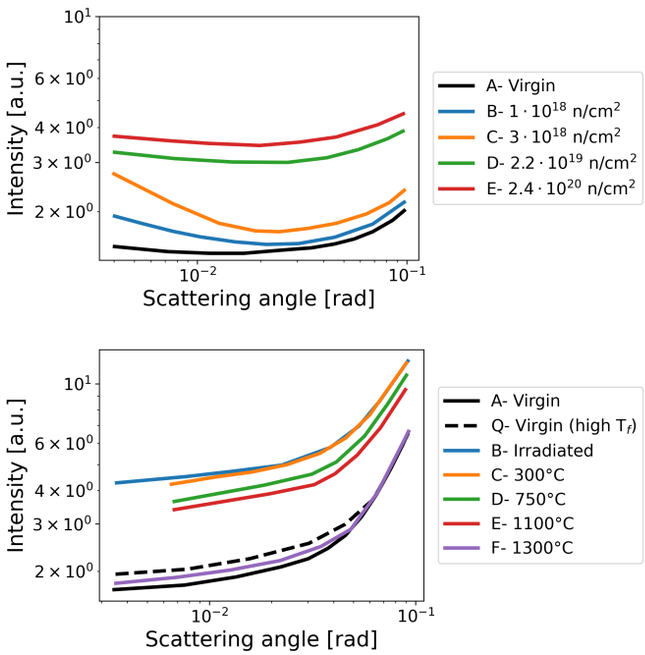

Figure 4.4: above) Small-angle scattering profiles of silica glass. Curve A corresponds to the unirradiated sample. Curves B-E represent samples irradiated with increasing neutron fluence. below) Small-angle scattering from Corning 7940 silica glass. Curve A corresponds to the unirradiated sample. Curve B represents the sample irradiated with a neutron fluence of 1.5×10^{20} n/cm^2. Curves C–F correspond to a sample irradiated with 1.5×10^{20} n/cm^2 and subsequently annealed at 300°C, 750°C, 1100°C, and 1300°C, respectively. Curve Q represents an unirradiated sample quenched from 1700°C. The X-ray wavelength used was 0.707 Å. The scattering curves have not been corrected for slit-height effects. Data taken from [BSG70].

4.5.1 Macroscopic changes Induced by Ionizing Radiation

The accumulation of microscopic defects and structural rearrangements ultimately leads to macroscopic changes in the physical properties of glass, which are of direct relevance for technological applications.

Volume changes in silica

Radiation-induced volume changes in amorphous silica have been known and extensively studied since the 1950s [PK68; Pri+64]. A connection exists between defect centers observed by ESR and optical absorption and the macroscopic density changes (observed photoelastically).

When virgin fused silica is exposed to ionizing radiation or heavy-particle bombardment, a volumetric compaction is typically observed. Much larger compaction per unit deposited energy occurs in the case of heavy-ion irradiation compared to purely ionizing radiation, but the same saturation compaction values

$$\Delta V/V \approx 3 \times 10^{-2}.$$

Optical changes

One of the most evident manifestations of radiation-induced attenuation in glasses is darkening or coloration. Since, as we have seen in Sec. 4.3, most radiation-induced defect centers absorb at relatively high photon energies, the resulting decrease in optical transmission is typically more pronounced at shorter wavelengths. Consequently, attenuation is strongest in the ultraviolet and visible spectral regions (200–700 nm), while it is generally less severe in the near-infrared range (700–2000 nm) [OGP21]. As the absorbed dose increases, the accumulated defect population leads to a progressive increase in optical losses, particularly in the visible domain.

When irradiation induces densification of the glass, corresponding changes occur in internal stress, electronic polarizability, and refractive index. In silica, radiation-induced variations of the refractive index are typically in the range $\Delta n \sim 5 \times 10^{-3}$ to 10^{-2} [OGP21]. Even such apparently small changes can have substantial consequences for optical systems, leading to lens defocusing and degradation of imaging performance.

Mechanical consequences of irradiation

Changes in density and medium-range order also affect mechanical properties such as hardness and elastic moduli. Although these effects are generally smaller than

optical changes, they are important for applications involving long-term radiation exposure as in nuclear-waste vitrification [BH88; OGP21].

4.6 X-ray induced dynamics as the manifest of damage creation and annihilation

The previous sections have shown that ionizing irradiation produces structural modifications in glasses, from local bond rupture and defect formation to medium-range rearrangements and macroscopic transformations. At the microscopic level, radiolysis continuously generates electron–hole pairs, broken bonds, and transient atomic displacements. However, as illustrated in Sec. 4.2.5 for γ-irradiation, only a very small fraction of these events leads to stable defect centers. The vast majority of ionization and displacement processes recombine on short timescales through vacancy–interstitial annihilation, electron–hole recombination, or local structural relaxation.

Radiation damage must therefore be understood as a dynamic balance between defect creation and defect annihilation. Each ionization event deposits energy into a confined region of the network, inducing short-lived atomic motion and local stress redistribution. Most of these perturbations relax back toward configurations close to the initial structure, while only a small subset becomes frozen as stable defects.

X-rays provide a particularly powerful platform to investigate this dynamic process. At modern synchrotron beamlines, intense coherent X-ray beams are everyday used in XPCS experiments. In this context, the X-ray beam acts simultaneously as a source of ionization and as a probe of atomic motion. The focus here shifts from the identification of individual defect centers to the collective dynamics of the network under continuous irradiation. Rather than considering radiation damage solely in terms of static defect populations, XPCS makes it possible to observe directly the atomic-scale dynamics caused by the balance between damage creation and recovery.

In the following, we review the main results obtained over the past decade on beam-induced dynamics in oxide glasses, which establish the foundations of this thesis.

4.6.1 Emergence and physical understanding of beam-induced dynamics

The possibility that irradiation may induce atomic rearrangements in disordered systems was first demonstrated in real space by Huang and coworkers, who recorded a video of a two–dimensional amorphous SiO_2 film under 80 kV electron irradiation using transmission electron microscopy [Hua+13]. In the experiment, the atomic network was observed to continuously reorganize through bond switching and ring rearrangements, producing what was described as the "dancing" of atoms. Although performed under electron irradiation and in a quasi–two–dimensional geometry, this work clearly demonstrated that the interaction between ionizing radiation and a glassy network can activate atomic motion, revealing radiation-induced dynamics at the interatomic scale.

A similar phenomenology emerged soon in bulk oxide glasses studied by means of XPCS. In 2014, Ruta and coworkers reported the observation of fast atomic-scale relaxations in a sodium silicate glass illuminated by 8 keV X-rays at a third-generation synchrotron source [Rut+14]. The measurements were performed at wave vectors corresponding to the first sharp diffraction peak, probing interatomic distances of a few Å. Remarkably, relaxation times of the order of 10^2–10^3 s were detected at room temperature, well below T_g, where structural relaxation should be completely frozen on experimental timescales. This apparent contradiction raised the fundamental question of whether the observed motion was intrinsic to the glassy state or instead driven by the probing radiation. As an explanatory example of these observations, Fig. 4.5 shows recent measurements of this glass dynamics at room temperature in v-GeO_2, which exhibit a perfect compressed exponential relaxation over six decades with $\tau = 5.7$ s and $\beta = 0.75$.

Induced dynamics dependence on the X-ray flux

In 2017, Ruta and coworkers revisited the problem by performing flux-dependent XPCS measurements on strong oxide glasses such as SiO_2 and GeO_2 [Rut+17]. Building on the earlier observation of unexpectedly fast relaxations, they demonstrated that **the characteristic relaxation time scales inversely with the incident photon flux**, $\tau \propto 1/\Phi$, or equivalently with the inverse of the dose rate (see Eq. 4.3). This behavior is illustrated in Fig. 4.6(a), where the relaxation time increases linearly with the inverse flux for silica. This result provided the first evidence that the detected motion is not an intrinsic equilibrium relaxation of the glassy state, but is instead directly triggered by the absorption of X-ray photons. In this perspective, XPCS experiments on oxide glasses must be regarded as *pump–probe*

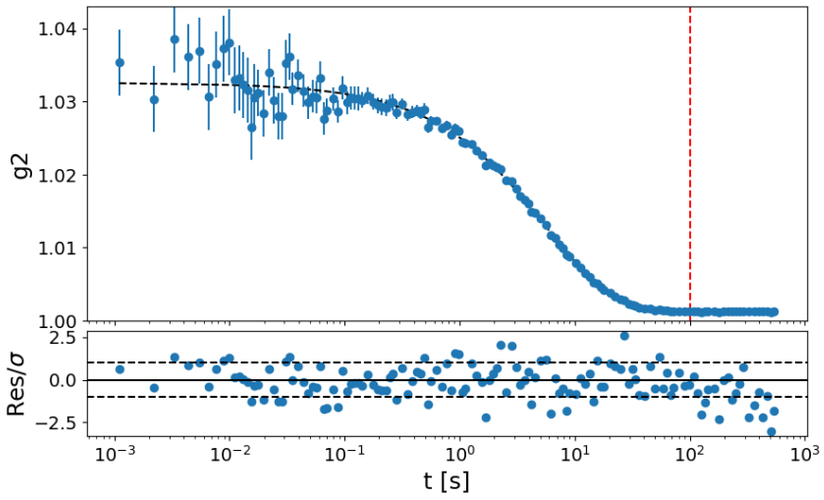

Figure 4.5: Intensity autocorrelation functions measured in vitrous germania at room temperature at Q=0.2 $Å^{-1}$ (more details in the following sections). The fit is computed on data with lag-time lower than 100 s (red-dashed vertical line). As can be seen from the residual plot, the accordance with the compressed exponential function with $\tau = 5.7$ s and $\beta = 0.75$ is remarkable.

measurements: the beam acts simultaneously as a pump, generating local radiolytic excitations in the network, and as a probe, monitoring the induced rearrangements through speckle decorrelation.

Within the same article, a comparison was performed with metallic glasses, which under identical experimental conditions exhibited no flux dependence and no measurable beam-induced dynamics, evidencing the **specificity of the phenomenon to oxide glasses**.

The competition between thermal and X-ray induced relaxation

The role of temperature was first investigated by Pintori *et al.* in 2019 through temperature-dependent XPCS measurements on B2O3 glass [Pin+19]. Measurements performed below and above T_g revealed the coexistence of **two relaxation channels**: the intrinsic structural relaxation, governed by temperature, and a beam-induced relaxation, governed by the absorbed photon rate. As shown in Fig. 4.6(b), the flux-dependent plateau observed deep in the glassy state progressively merges with the equilibrium relaxation curve near and above T_g. When $\tau_\alpha(T) < \tau_{\text{ind}}(\Phi)$, the measured dynamics follows the equilibrium behavior and becomes flux-independent; deep in the glassy state, the induced channel dominates

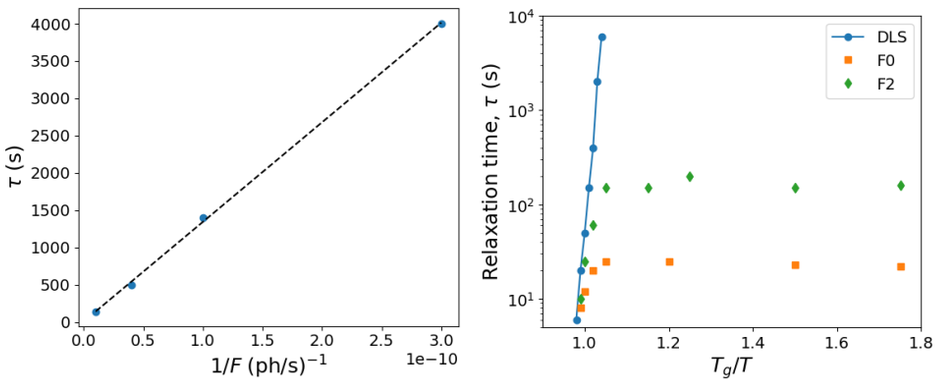

Figure 4.6: (a) Relaxation time as a function of the inverse x-ray flux for SiO_2 samples. The inverse proportionality between the flux and the induced relaxation time is evident. Figure modified from [Rut+17]. (b) Relaxation time as a function of T_g/T for B_2O_3 glass at different flux intensities. Blue circles represent macroscopic Dynamic Light Scattering (DLS) measurements performed with visible light. Orange squares correspond to data acquired at the maximum synchrotron flux (F_0), while green diamonds correspond to measurements performed with an attenuated beam ($F_2 < F_0$). XPCS measurements were carried out at the first sharp diffraction peak: $Q = 1.6$ Å^{-1} for SiO_2 and $Q = 1.5$ Å^{-1} for B_2O_3. Figure adapted from Ref. [Pin+19].

and τ scales with flux. The data are well described by a parallel model,

$$\frac{1}{\tau(T,\Phi)} = \frac{1}{\tau_\alpha(T)} + \frac{1}{\tau_{\text{ind}}(\Phi)}, \tag{4.15}$$

which has since been confirmed in oxide glasses such as boron oxide and sodium silicates [Alf+23; Chu20], supporting its general validity.

Cooperative response to defect creation and annihilation

Pintori *et al.* also provided a quantitative estimate of the number of structural units involved in a single photon-induced rearrangement [Pin+19]. By definition, a relaxation time τ corresponds to the average time required to decorrelate N_{tot}/e structural units within the illuminated volume[16], where N_{tot} is the number of structural units in the scattering volume. From the proportionality between decorrelation rate and absorbed photon rate, they calculated the number of units displaced per

16 We are approximating $f_Q \simeq 1$.

photon as

$$N_u = \frac{N_{\text{tot}}}{e\Phi(1-T)\tau}. \tag{4.16}$$

For B_2O_3, this gives $N_u \sim 600$ units, corresponding to $\sim 3 \times 10^3$ atoms and to a characteristic size of about 2 nm. **XPCS decorrelation therefore reflects cooperative nanometric rearrangements** rather than isolated bond-breaking events. The microscopic origin of this dynamics lies in radiolysis: each absorbed photon generates a cascade of ionization events that induces bond rupture and local structural relaxation. The observed motion represents the network response to the continuous creation and recombination of defects [Gri85; Pin+19; Rut+17]. The dynamics **spatial extent is not determined solely by the primary electronic cascade, but also by network connectivity and composition** [Pin+22], which control how the radiolytic perturbation is accommodated within the glass network.

Amorphus-amorphous structural transformations

Initial indications of dose-dependent effects, similar to dose reported in Sec. 4.5, were reported in [Dal+19; Pin+22], where prolonged irradiation produced measurable changes in the relaxation time and in the shape of the intensity correlation functions. Although not systematically addressed at the time, these observations suggested that cumulative structural modifications influence the induced dynamics. In light of the defect physics discussed in the previous sections, this behavior can be naturally interpreted as the consequence of the progressive accumulation of radiation-induced point defects with increasing absorbed dose, resulting in overlall structural changes in the system.

Subsequent studies explicitly investigated the role of the total absorbed dose [Alf+23; Mar+23]. Alfinelli *et al.* demonstrated that pure B_2O_3 and a series of sodium silicate glasses undergo an **amorphous–amorphous transformation under continuous X-ray irradiation** [Alf+23]. **The pristine glass progressively evolves toward a radiation-modified amorphous phase characterized by a decrease and broadening of the first sharp diffraction peak (FSDP)**, indicating enhanced medium-range disorder and a shift toward a higher-energy configuration in the potential energy landscape. The dose required for this transformation is strongly composition dependent and quantitatively correlates with network rigidity within the framework of constraint theory. Once formed, **the new amorphous phase remains structurally stable under further irradiation**, while continuing to display beam-induced dynamics with stretched exponential relaxation similar to that of the corresponding supercooled liquid.

Complementary results by Martinelli *et al.* on $LiBO_2$ glass provided a detailed

microscopic picture of how the dynamics evolves with accumulated dose [Mar+23]. At low doses, the induced dynamics is consistent with a dilute population of isolated defects acting as elastic dipolar stress sources, producing ballistic-like atomic displacements ($\tau \propto q^{-1}$) and compressed correlation functions ($\beta > 1$). As the absorbed dose increases, the defect density grows. This leads to a systematic decrease of the shape parameter β, a weakening of the simple q^{-1} scaling of the relaxation time, and the appearance of de Gennes narrowing in $\tau(q)$, a sign of collective dynamics. Structural measurements performed in parallel show a reduction and broadening of the FSDP, confirming the progressive increase in disorder.

Above a characteristic dose of the order of 1–2 GGy, both structure and dynamics reach a stationary regime. In this fully irradiated state, defect creation and annihilation balance each other, and the glass exhibits a stretched exponential relaxation with $\beta < 1$ and a q-dependence of the relaxation time closely resembling that of an undercooled liquid. Martinelli *et al.* interpreted this regime as a microscopic yielding condition: although the material does not flow macroscopically, its interatomic-scale response is fully plastic, analogous to a glass at the yield point in mechanical experiments

Uniqueness of the fully irradiated glass

Building on the dose-dependent structural and dynamical evolution described above, Baglioni *et al.* extended this framework by demonstrating the uniqueness of the radiation-induced yielding state in a series of $GeSe_3$ chalcogenide glasses [Bag+24].

Glasses prepared with different cooling rates, hence different initial stabilities and fictive temperatures, were X-ray irradiated at room temperature. Despite their different initial thermodynamic and structural states, all samples evolved toward the same stationary configuration under prolonged irradiation. Calorimetric measurements revealed that the enthalpy increases continuously with dose until a plateau is reached, corresponding to a radiation-modified glass of higher enthalpy, here ascribed as a rejuvenated state. Simultaneously, X-ray scattering shows a reduction and shift of the first sharp diffraction peak, indicating increased intermediate-range disorder. Crucially, **once this stationary state is reached, both structure and dynamics become dose-independent and remain stable under further irradiation**, evidencing a balance between defect creation and annihilation. The yielding state is also reversible: heating above T_g restores the pristine structure.

A central result of the paper is that **this stationary irradiated glass corresponds to a well-defined fictive temperature, independent of the initial preparation protocol**. All glasses converge toward a fictive temperature $T_f \approx 1.2, T_g$. This finding establishes a direct link between radiation-induced yield-

ing and the thermodynamic landscape of supercooled liquids: X-ray irradiation drives the glass toward a unique, moderately rejuvenated state equivalent to a liquid instantaneously quenched from $\sim 1.2, T_g$.

Therefore, while Alfinelli and Martinelli demonstrated the existence of dose-driven amorphous–amorphous transformations and stationary dynamical regimes, Baglioni *et al.* provided a thermodynamic picture: **X-ray irradiation drives glasses toward a unique yielding state, independent of their initial disorder, structurally equivalent to a glass quenched from a specific fictive temperature crossover temperature.** Also, Baglioni et al. guessed that the measured X-ray induced transformation is independent of temperature.

The uniqueness of the radiation-induced stationary state constitutes the starting point of this work, and the historical review presented above establishes the framework within which we will operate. In particular, we will show that, contrary to previous expectations, the irradiation temperature plays a crucial role in the X-ray–induced amorphous–amorphous transformation.

5 X-ray–induced transitions in v-GeO_2 probed by XPCS

This chapter presents the main results obtained during my PhD on the X-ray–induced dynamics and structural transformations of vitreous GeO_2, investigated by means of X-ray Photon Correlation Spectroscopy (XPCS).

We first describe the experimental conditions and measurement strategies adopted at the ID10 (ESRF) and P10 (PETRA III) beamlines. We then investigate the room-temperature beam-induced dynamics, focusing on its evolution with absorbed dose and the emergence of a stationary fully damaged state.

The structural counterpart of this dynamical evolution is then discussed, highlighting the modifications of the structure factor and the associated increase in disorder, densification, and density fluctuations.

We subsequently analyze the temperature dependence of both the dynamics and the structure of the fully damaged state, showing that the irradiation temperature controls the final glassy configuration.

The thermal stability of the irradiated state is addressed, demonstrating that the fully damaged structure is stable at the irradiation temperature and does not recover upon beam interruption, except close to the glass transition.

Finally, we discuss the uniqueness of the fully damaged state, showing that it depends only on the irradiation temperature and not on the previous history of the glass, and we interpret the irradiation process in terms of rejuvenation and annealing within the potential energy landscape framework.

5.1 Experimental conditions and measurement strategy

Within this chapter, we present the results of two XPCS experiments performed at the ID10 beamline of ESRF (HC6209, April 2025) and at the P10 beamline of PETRA III (11022045, January 2026). The focus of both experiments was the characterization of X-ray–induced dynamics and the associated structural changes in vitreous GeO_2, with particular attention to their temperature dependence.

A key advantage of these XPCS beamlines is the possibility to monitor both dynamics and structure (at least partially) simultaneously, as discussed in the

previous chapter. This is achieved through the combined use of a fast detector for correlation measurements and a slower detector for diffraction.

In Sec. 2.5.4, we described the general experimental layouts of these beamlines. In the following, we detail the specific configurations employed in the present experiments, which were optimized to address our scientific objectives on the germania sample.

5.1.1 P10 beamline configuration

As described in Sec. 2.5.4, the second experimental hutch (EH2) of the P10 beamline is dedicated to sample illumination and acquisition of the scattering signal. This is the hutch where the experimental setup is tailored to the specific scientific goals.

The sample is mounted between two copper slabs forming the so-called "hot finger", which allows local heating and precise temperature control. The copper foils have a 3 mm hole that allows mounting the thin slab samples freestanding. The temperature is monitored by three thermocouples (Fig. 5.1a). The sample holder is placed inside a vacuum chamber, and the X-ray beam is kept under vacuum up to the sample position. After the sample, a Kapton foil serves as an exit window (Fig. 5.1b).

The scattered signal is collected by two two-dimensional single-photon-counting detectors (Si Eiger500K, Dectris). One detector is used for XPCS measurements and is mounted at the end of a $\sim$ 2 m long vacuum tube aligned with the sample (Fig. 5.1c,d), featuring both entrance and exit Kapton windows (Fig. 5.1b,c). The Eiger500K corresponds to a smaller (one-quarter area) version of the Eiger4M discussed previously, which was not available during the experiment. The detector is mounted on a circular rail and was operated at a fixed scattering angle of $\theta = 19.5°$, corresponding to the First Sharp Diffraction Peak of GeO_2 at the photon energy of $E = 8.77$ keV used (Fig. 5.1d).

XPCS measurements were performed at a frame rate of 0.1 kHz, while the diffraction detector operated at 0.5 Hz. The choice of a lower frame rate, compared to the maximum available (1 kHz), was motivated by the data acquisition format at P10, where detector data are stored as dense arrays. We implemented a post-acquisition sparsification pipeline to convert these dense datasets into sparse formats; however, to keep this process computationally efficient, we opted to operate the detector at a reduced frame rate.

Due to the reduced detector size, the sample–detector distance was set to 2 m (instead of 5 m) to increase the solid angle and thus maximize the detected scattered intensity. The second detector, used for diffraction measurements, is positioned as close as possible to the sample ($\sim$ 10 cm) to cover the widest possible Q-range.

As discussed, the mapping between pixel position and Q is calibrated using a LaB_6 standard (Fig. 5.1b).

A movable arm located just after the sample chamber exit window allows insertion of a silicon diode to monitor the transmitted beam and quantify the photon flux. In this setup, it was not possible to install an internal beamstop, complicating the separation of sample scattering from Kapton window scattering. A retractable beamstop mounted on the diode arm, positioned a few millimeters from the Kapton window, serves as an external beamstop. Owing to the relatively large scattering angle, this configuration efficiently blocks parasitic scattering from the direct beam hitting the window. This approach could not be applied to the diffraction detector; however, parasitic scattering was mitigated using lead tape shielding directly applied on the chamber exit window.

The photon flux at the sample was approximately $5 \cdot 10^{10}$ ph/s, although an accurate measurement was not available during the experiment. As discussed, the dose rate (i.e. the X-ray flux per unit area) is inversely proportional to the induced decorrelation time. Therefore, slowing down beam-induced dynamics, so that it enters the measurable time-window, can be achieved either by reducing the flux using attenuators or by defocusing the beam to spread the same flux over a larger area. The first approach does not improve the quality of the measured correlation functions. For example, reducing the beam intensity by 50% slows the dynamics by a factor of two, but also reduces the scattered intensity by the same factor. If measurements are performed over a fixed multiple of the decorrelation time, Eq. 3.1 shows that the signal-to-noise ratio remains unchanged, while the total acquisition time increases. In contrast, defocusing the beam preserves the total scattered intensity while reducing the dose rate, thereby slowing the induced dynamics proportionally to the increase in beam size. Although defocusing slightly reduces the speckle contrast due to partial loss of transverse coherence, the overall gain from the reduced dose rate makes this approach preferable. Moreover, diffraction measurements benefit from this choice, as structural evolution is slowed without compromising signal intensity. After preliminary tests, the beam size at the sample was set to $(14.9 \times 8)\ \mu m^2$ (FWHM) by slightly detuning the incident energy from the optimal focusing condition (8.4 keV), shifting the focal point downstream of the sample and achieving controlled defocusing. This strategy effectively slows down X-ray-induced dynamics, moving it within the accessible time window of the experiment. Using Eq. 4.3 and assuming a sample thickness of $\sim 100\ \mu m$, we estimate a dose rate at P10 of ~ 0.3 MGy/s.

An incident-beam monitor, measuring the scattering from a Kapton foil, enables continuous monitoring of fluctuations in the incoming beam intensity, for instance due to synchrotron current injection and decay. Unfortunately, the available mon-

itor was placed in the first experimental hutch, therefor not directly monitoring the intensity at the sample, evidencing some systematic variations caused by beam spatial instability.

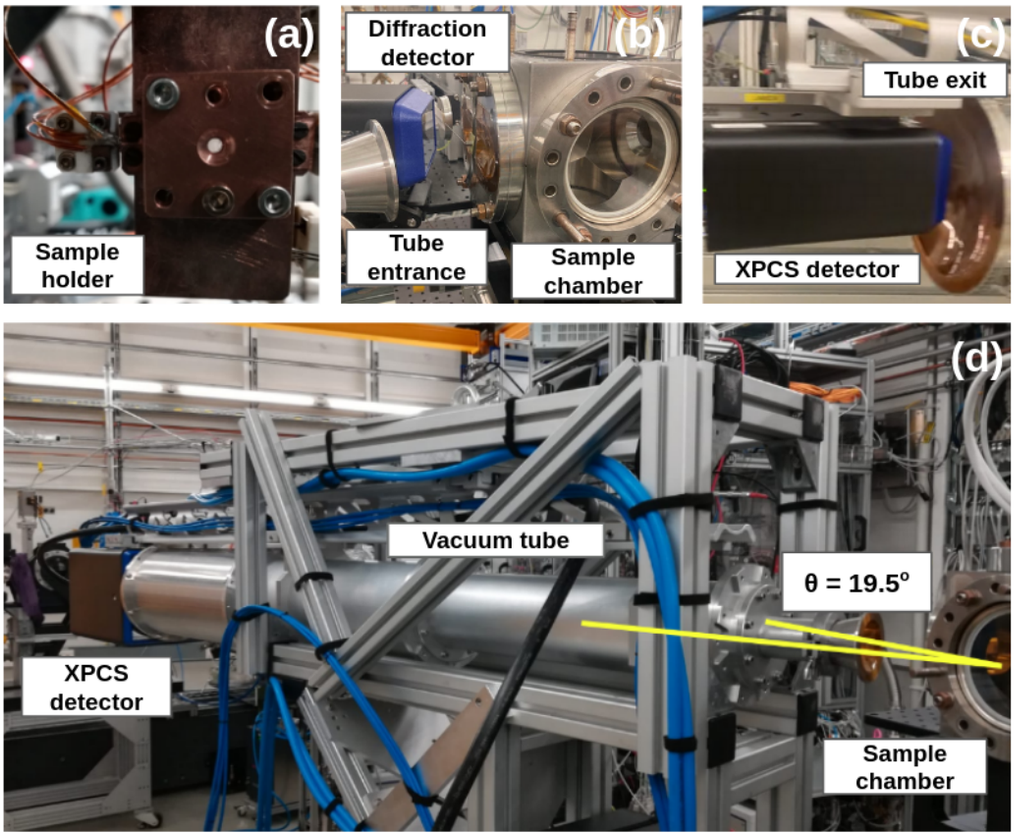

Figure 5.1: (a) Photograph of the sample holder ("hot finger"), which enables local heating and temperature control. (b) View of the sample stage inside the vacuum chamber, including the entrance window of the vacuum tube and the diffraction detector positioned close to the sample. (c) The XPCS detector (Eiger500K) mounted at the end of the vacuum flight tube. (d) Schematic of the scattering geometry, showing the detector positioned at a fixed angle $\theta = 19.5^\circ$ on a circular rail.

5.1.2 ID10 beamline configuration

The setup used at the ID10 beamline is conceptually similar to that described for P10. We therefore limit the discussion here to the main differences.

At ID10, the fast detector was a Dectris Eiger4M based on CdTe, while a Dectris Pilatus detector was used for diffraction measurements. The experiment was performed in SAXS configuration, with the XPCS detector positioned at a scattering angle of 1.75° and at a distance of 5 m from the sample, in order to improve the speckle contrast.

In contrast to the P10 setup, the entire beam path is maintained under vacuum, and no Kapton windows are present between the sample chamber and the vacuum tube leading to the XPCS detector. A removable internal beamstop is placed immediately downstream of the sample to prevent the direct beam from hitting the walls of the vacuum tube. The diode used to monitor the transmitted beam—thus providing information on both sample transmission and incident flux—is located at the end of the vacuum tube, on the side of the XPCS detector.

The beam monitor was not working during the experiment; however, normalization of the scattered intensity by the synchrotron current effectively corrects for beam intensity fluctuations, which are mainly driven by variations in the stored current.

To slow down the X-ray–induced dynamics and bring it within the accessible time window, the $1.2 \cdot 10^{12}$ ph/s beam was defocused to a spot size of 30×40 μm^2 on the $\sim$ 100 μm thick v-GeO_2 sample by working at the 9.7 keV energy. Owing to the EBS upgrade of the synchrotron, the ID10 beamline benefits from a coherent flux approximately 50 times higher than that available at P10 under comparable conditions. The defocusing result in a dose rate at the sample of 1 MGy/s.

XPCS measurements were performed at a frame rate of 1 kHz, while the diffraction detector operated at 1 Hz. Thanks to the beamline data acquisition pipeline, the fast detector data are directly stored in sparse format.

Table 5.1 summarizes the main experimental parameters of the P10 and ID10 beamlines used in this work.

5.1.3 Sample preparation

The samples were prepared starting from a bulk cylindrical piece of v-GeO_2, obtained using the standard melt-quenching method. Specifically, high-purity GeO_2 powder (99.99%, Sigma Aldrich srl) was poured into an alumina crucible and melted at 1600 °C and held at this temperature for 6 hours to remove air bubbles, before being rapidly quenched in air, after reducing the temperature down to 1200 °C. The glass was cut out from the crucible, taking only the central part of the sample, to prevent the alumina contamination. The resulting cylinder was cut into thin slices, which were subsequently thinned and optically polished using silicon carbide grinding paper down to a thickness of approximately 100 μm. This thickness is

Table 5.1: Summary of the main experimental parameters at the P10 and ID10 beamlines.

	P10 (PETRA III)	**ID10 (ESRF)**
Energy	8.8 keV	9.7 keV
Fast detector	Eiger500K	Eiger4M
Diffraction detector	Eiger500K	Pilatus
Scattering angle θ	19.5°	1.75°
Sample–detector distance	2 m	5 m
XPCS frame rate	0.1 kHz	1 kHz
Diffraction frame rate	0.5 Hz	1 Hz
Photon flux	$5 \cdot 10^{10}$ ph/s	$1.2 \cdot 10^{12}$ ph/s
Beam size (FWHM)	14.9×8 μm^2	30×40 μm^2
Dose rate	$\sim$ 0.3 MGy/s	1 MGy/s

slightly larger than the optimal value for XPCS measurements at $\sim$ 8 keV, in order to maximize the scattered intensity while maintaining good thickness uniformity across the sample. Indeed, producing flat and homogeneous samples is more reliable at larger thicknesses.

5.2 The room temperature induced dynamics

As introduced in Sec. 4.6, oxide glasses exhibit atomic dynamics under high-dose-rate X-ray irradiation even at room temperature, or more generally at temperatures well below the glass transition temperature. Here, we begin by presenting results on the room-temperature dynamics. In particular, we discuss the evolution of the dynamics as a function of the absorbed dose, although these experiments were not specifically designed for this purpose. In doing so, we analyze together the ID10 and P10 experiments, which probe the dynamics at low Q and at the FSDP, respectively.

Figure 5.2 shows the multi-tau two-time correlation function of vitreous germania at room temperature, measured at $Q = 0.2$ Å^{-1} at the ID10 beamline. The irradiated spot had not been previously exposed to the beam, initially corresponding to what we refer to as the pristine (or virgin) glass. Therefore, the t_w axis can be directly converted into absorbed dose using the known dose rate of 1 MGy/s. The plot displays correlations for $\tau > 0.1$ s, as shorter times (corresponding to the 1 kHz frame rate) are dominated by noise, and averaging over t_w is required to extract clean correlation curves.

The presence of X-ray–induced atomic dynamics is clearly observed, as evi-

denced by the complete decorrelation of the G_2 function at τ of the order of 10 s. Quantitatively, the characteristic relaxation time starts fast, and then slows down during the first $\sim$ 300 s of irradiation (see zoom in Fig. 5.2). After this initial regime, corresponding to an absorbed dose of $\sim$ 300 MGy, the system reaches a stationary state characterized by a well-defined relaxation time that remains constant, at least over the $\sim$ 30 min measurement shown here. We refer to this state as the "fully irradiated" (or "fully damaged") glass.

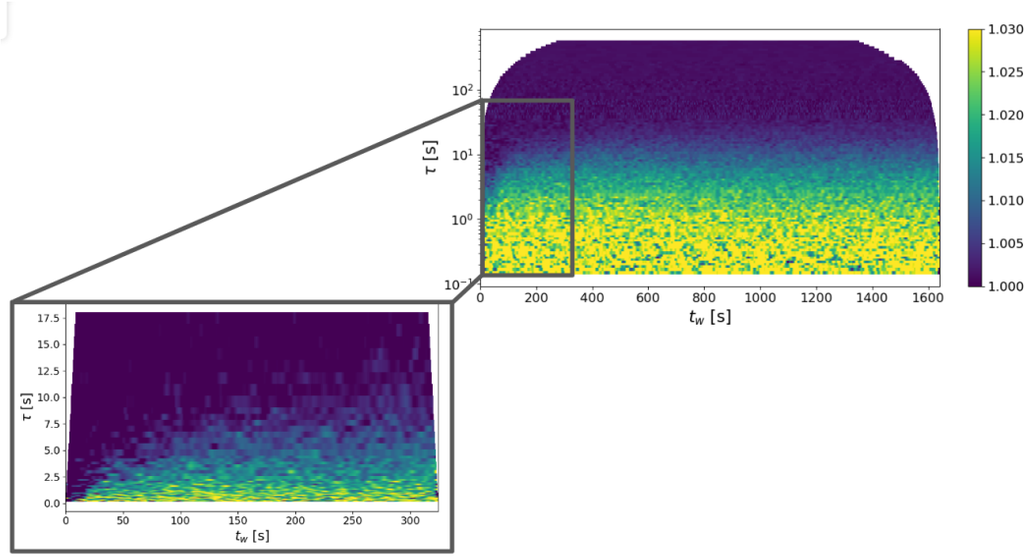

Figure 5.2: Multi-tau two-time correlation function $G^{(2)}(t_w, \tau)$ of vitreous GeO_2 at room temperature measured at ID10 ($Q = 0.2$ Å^{-1}). The horizontal axis represents the waiting time t_w, which can be directly converted into absorbed dose (1 MGy/s). The color scale highlights the decorrelation of the signal, showing the evolution from faster to slower dynamics during the first $\sim$ 300 s, followed by a stationary regime.

5.2.1 Dose dependence of the room-T induced dynamics

Although the primary goal of these experiments was to characterize the fully damaged germania state, and a proper investigation of dose dependence would require a mesh protocol (i.e. probing different sample positions to improve the signal-to-noise ratio of G_2), we attempt here a quantitative description of the dynamical evolution.

Figure 5.3 shows the evolution of the correlation function as a function of waiting time t_w, and thus absorbed dose, for both experiments. We recall that the corre-

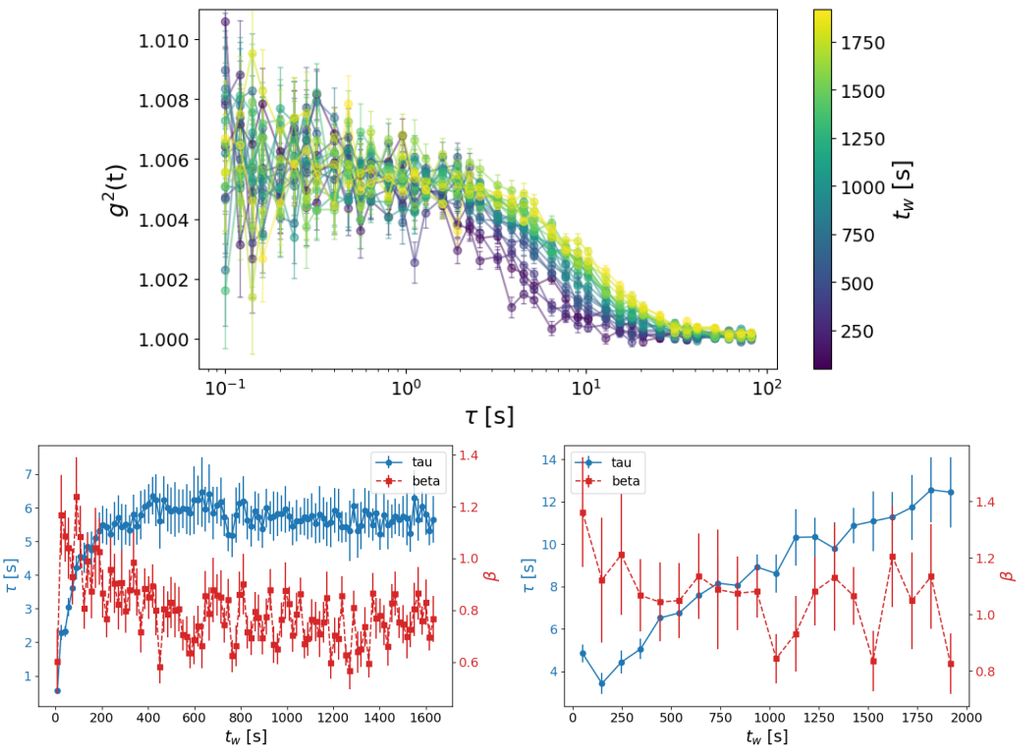

Figure 5.3: Dose dependence of the room-temperature dynamics in vitreous GeO_2. **Top:** Evolution of the $g_2(\tau)$ function at P10 ($Q = 1.55$ Å^{-1}) obtained from successive t_w slices (50 s width), showing the progressive slowing down of the dynamics with increasing dose. **Bottom left:** Evolution of the relaxation time τ and stretching exponent β at ID10 ($Q = 0.2$ Å^{-1}). The β parameter of the lowest-dose point can't be properly fitted. **Bottom right:** Same quantities for P10 ($Q = 1.55$ Å^{-1}).

sponding dose rates are 1 MGy/s (ID10) and 0.3 MGy/s (P10), and that the two experiments probe different Q values: 0.2 Å^{-1} and 1.55 Å^{-1}.

The upper panel displays the evolution of the correlation function measured at P10, obtained by vertically slicing and averaging the MT-2TC function (analogous to Fig. 5.2). Each slice spans 50 s in t_w, providing a compromise between temporal resolution and statistical accuracy. As the absorbed dose increases, the decorrelation shifts to longer τ, indicating that the glass evolves towards a more radiation-resistant state. This evolution progressively saturates at long waiting times, consistent with the stationary regime observed in Fig. 5.2.

The two lower panels of Fig. 5.3 show the evolution of the fit parameters (β and τ) as a function of t_w for the two experiments (ID10 on the left, P10 on the right). The fits are performed using the KWW function (Eqs. 1.15 and 2.19), including a small background contribution:

$$g_2(\tau) = (1 + y_0) + Ce^{-2\left(\frac{t}{\tau}\right)^{\beta}}. \tag{5.1}$$

Due to the limited SNR resulting from MT-2TC slicing, the background y_0 is fixed to the stationary-state value (e.g. as obtained from Fig. 5.4). This approximation is justified since y_0 is much smaller than the contrast and empty-cell measurements show negligible signal.

In both cases, the relaxation evolves over the first $\sim$ 300 MGy of absorbed dose, during which the relaxation time increases. At low Q, the dynamics initially occur on timescales shorter than 0.5 s (a precise value would require dedicated measurements) and slow down to a stationary value of about 6 s. The stretching exponent β initially takes a slightly compressed value ($\sim$ 1.2) and decreases to $\sim$ 0.8 in the stationary regime. This behavior is consistent with previous observations in oxide glasses [Alf+23; Mar+23], where compressed dynamics are associated with stress-release processes.

A similar behavior is observed at the FSDP in the P10 experiment, where the relaxation time increases from a few seconds to about 13 s. Due to the lower dose rate, the evolution occurs over longer timescales, reaching a stationary regime after $\sim$ 900 s (corresponding again to $\sim$ 300 MGy). The transition is smoother, and the stationary regime is less clearly defined from the dynamics alone. However, it is clearly identified from the structural evolution (see Sec. 5.3), which sets the characteristic timescale of the transformation to $\sim$ 1000 s. Also, a similar evolution of β is observed, however, with a more limited statistics.

The increase of τ with the absorbed dose indicates that the glass evolves toward a more radiation-resistant structure, a behavior already observed in the silica glass [Alf+23; Mar+23]. However, we have recently observed the opposite trend in a

vapor-deposited Ta_2O_5 glass film, where the relaxation time decreases with absorbed dose. This suggests that the evolution of the induced relaxation time—whether it increases or decreases—depends on the initial stability of the glass.

In both experiments, the contrast C remains constant within experimental uncertainty, indicating that it does not depend on t_w or absorbed dose.

5.2.2 The fully damaged room-T dynamics

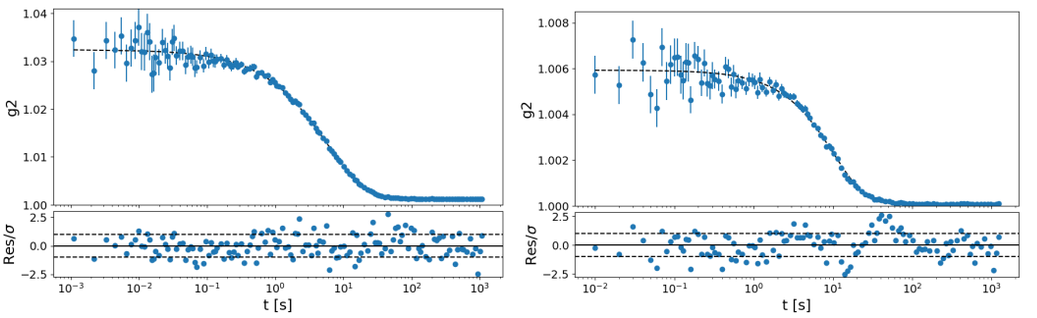

Figure 5.4: Intensity autocorrelation functions $g_2(\tau)$ in the stationary (fully damaged) regime at room temperature. **Left:** ID10 measurement at $Q = 0.2$ Å^{-1}. **Right:** P10 measurement at $Q = 1.55$ Å^{-1}. Solid lines represent KWW fits, and residuals highlight the excellent agreement over several decades in time.

Having described the transition toward the stationary regime, we now focus on the fully damaged state by averaging the correlation functions over the stationary time intervals: $t_w > 300$ s for ID10 and $t_w > 1000$ s for P10. The resulting $g_2(\tau)$ functions are shown in Fig. 5.4 for both low Q (left) and FSDP (right).

As demonstrated by the residuals, the agreement with the KWW function over more than six decades in time is remarkable. This is made possible by the MT-2TC approach, which allows the use of more than one million frames at 1 ms resolution. Exploiting the stationarity of the dynamics significantly improves the SNR (see Eq. 3.1), which is particularly important for accurately determining the contrast from the short-time plateau.

The fit parameters are summarized in Table 5.2. The background y_0 is very small compared to the contrast, reflecting the effectiveness of the detector corrections discussed in Sec. 3.3. The stretching exponent β is below unity at low Q and close to unity at the FSDP. This may indicate a weak effect of De Gennes narrowing, although a full Q-dependent study would be required to confirm this interpretation. To compare relaxation times from different experiments, it is necessary to express

them in terms of absorbed dose: $\tau_{\mathrm{ID10}} = 5.8$ MGy and $\tau_{\mathrm{P10}} \sim 3.15$ MGy[17]. The dose required for a complete structural rearrangement in the fully damaged glass is therefore of the order of a few MGy both on the macroscopic scale (low-Q) and at interatomic distances (FSDP).

At this stage, we do not further discuss the origin of this stationary dynamics, as its interpretation will become clearer after introducing the corresponding structural transformations and their thermal stability.

Q	τ	β	C	y_0
0.2 Å^{-1} (ID10)	(5.8 ± 0.1) s	0.76 ± 0.01	0.031 ± 0.002	$(1.2 \pm 0.1) \cdot 10^{-3}$
1.55 Å^{-1} (P10)	(10.5 ± 0.3) s	1.05 ± 0.04	0.0059 ± 0.0001	$(7.6 \pm 0.3) \cdot 10^{-5}$

Table 5.2: Fit parameters of the $g_2(\tau)$ functions in the stationary (fully damaged) regime at room temperature for the two Q values probed at ID10 and P10.

5.2.3 Q-dependence of the room-T induced dynamics

Within the ID10 experiment, we attempt a characterization of the Q-dependence of the fully damaged glass dynamics. However, the accessible Q-range is limited, since the detector optical table was mounted in SAXS configuration, allowing access only to the 0.1–0.5 Å^{-1} region.

Figure 5.5 shows the Q-dependence of the four fit parameters: τ, β, C, and y_0. The Q-dependence of τ is very weak and clearly does not follow the Brownian $1/Q^2$ behavior. This observation is consistent with the findings of Martinelli *et al.* (see Fig. 3 of [Mar+23]), who reports a progressive weakening of the $\tau(Q)$ dependence with increasing dose. Similarly, the stretching exponent β displays an approximately flat behavior, again in agreement with the same reference.

The contrast C, as expected, increases as Q decreases. This reflects the increase in transverse coherence of the scattered beam, due to the reduced path-length differences between photons scattered at different depths within the material. The 2 highest-Q points are less reliable because of the presence of parasitic background, visible in the time-averaged detector intensity images. This also leads to a larger y_0 value compared to the nearly background-free higher-Q regions, as well as the lower contrast.

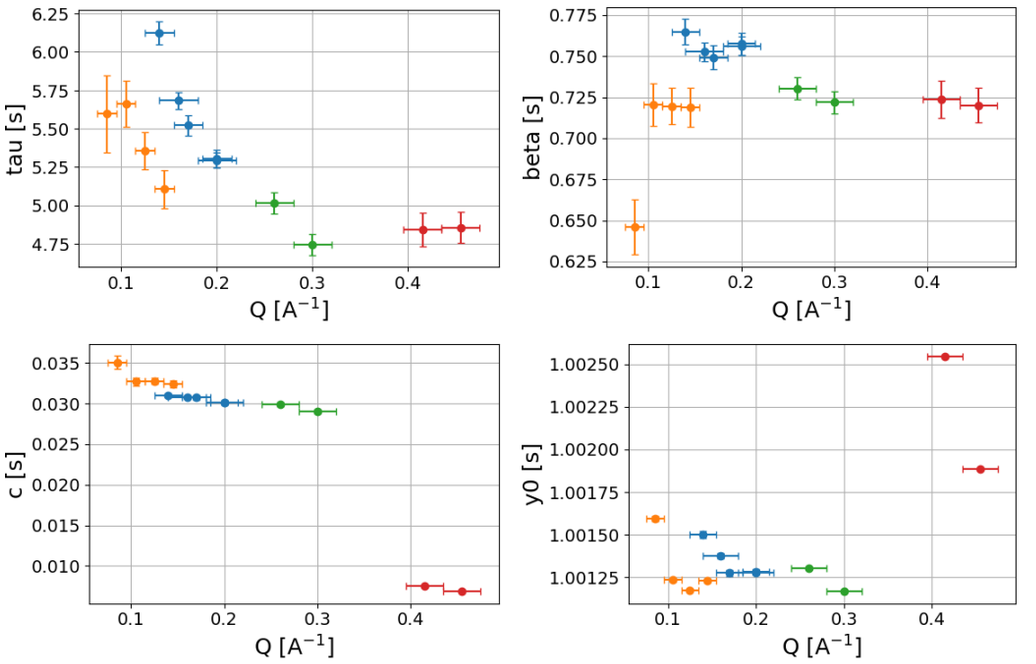

Figure 5.5: Q-dependence of the KWW fit parameters in the fully damaged room-temperature state measured at ID10. Different colors reflect different detector positions (different scattering angles). **Top left:** Relaxation time τ as a function of Q, showing a weak dependence and clear deviation from Brownian $1/Q^2$ scaling. **Top right:** Stretching exponent β, displaying an approximately constant behavior. **Bottom left:** Contrast C, increasing at lower Q due to enhanced transverse coherence. **Bottom right:** Background parameter y_0, with a higher value at the lowest Q due to parasitic scattering contributions.

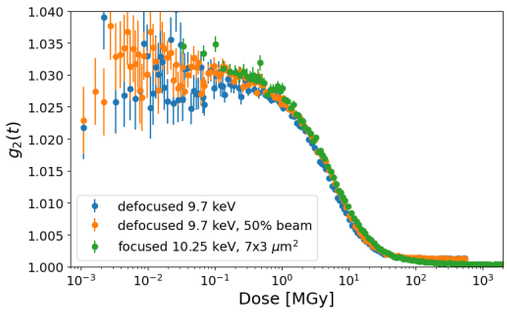

Figure 5.6: Room-temperature correlation functions measured in the fully damaged state under different experimental configurations, plotted as a function of rescaled time $\tau\times$ (dose rate). The datasets correspond to variations in beam energy, beam size, and attenuation. The collapse of all curves demonstrates the inverse proportionality between the relaxation time and the dose rate.

5.2.4 The standard dose-rate inverse proportionality

The inverse proportionality between the dose rate at the sample and the measured induced relaxation time was one of the first major results on X-ray–induced dynamics [Rut+17]. It is therefore standard to test this assumption in XPCS experiments probing induced dynamics.

Figure 5.6 shows the correlation functions measured at room temperature in the fully damaged state, plotted as a function of rescaled time, i.e. $\tau\times$ (dose rate), for four different experimental configurations:

- 9.7 keV energy, 30×40 μm^2 beam (standard configuration),
- 9.7 keV energy, 30×40 μm^2 beam, with 50% attenuation,
- 10.25 keV energy, 7.7×3.3 μm^2 beam, no attenuation,
- 8.67 keV energy, 7.2×3.4 μm^2 beam, no attenuation.

In these measurements, the dose rate was varied either by changing the incident beam intensity using attenuators or by modifying the beam size at the sample (via changes in the photon energy), thereby altering the area over which the photon flux is distributed.

As shown in Fig. 5.6, when the relaxation time is expressed in terms of absorbed dose, all correlation functions collapse onto a single master curve. To facilitate the

17 The photon flux at P10 is estimated rather than precisely measured.

comparison, the amplitude of the correlation functions was rescaled, as reducing the beam size leads to an increase in the contrast.

The expected inverse proportionality between the dose rate and the relaxation time is therefore verified, not only when varying the incident intensity through attenuation—as commonly done—but also when modifying the beam size, and thus the illuminated area over which the photon flux is deposited.

5.3 The room temperature structural transformation

The evolution of the induced dynamics discussed in the previous section is accompanied by a corresponding evolution of the structure. As introduced in Sec. 4.6, this behavior has been recently observed in the chalcogenide glass $GeSe_3$, and to some extent in earlier studies [Alf+23; Dal+19]. In addition, the classical works of Primak [PK68; Pri+64; Pri78] and Bale [BSG70] on neutron irradiation already evidenced a compaction of oxide glasses (e.g. silica) accompanied by modifications of the structure factor. As we now show, and as expected, a similar phenomenon occurs at room temperature in germania under X-ray irradiation. The present study benefits from a significantly improved signal-to-noise ratio in the diffraction measurements and negligible background. Moreover, germania exhibits particularly strong structural modifications under irradiation, making the fully irradiated room-temperature state markedly different from the pristine glass.

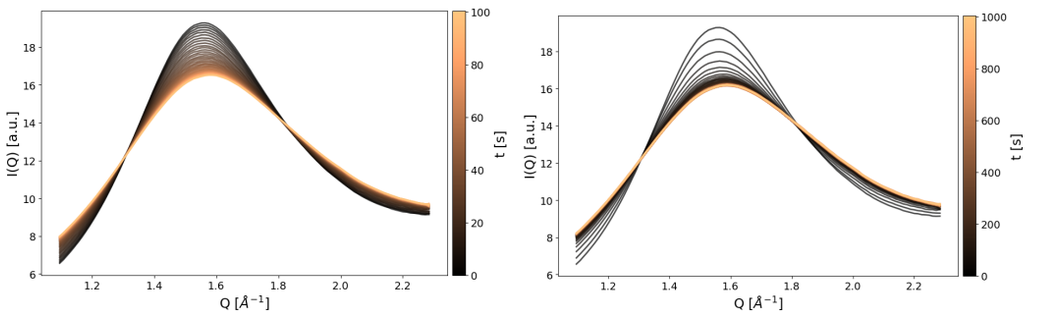

Figure 5.7: Evolution of the structure factor of vitreous GeO_2 at room temperature under X-ray irradiation (ID10, 1 MGy/s). **Left:** Zoom on the initial stage (first 100 s), with diffraction patterns acquired every 2 s, showing the rapid initial structural evolution. **Right:** Same evolution over a longer time scale, with patterns acquired every 10 s, highlighting the exponential-like approach toward a stationary (fully damaged) structure.

Figure 5.7 shows the evolution of the structure factor–focusing on the FSDP region–of vitreous germania at room temperature under X-ray irradiation. The data are obtained at the ID10 beamline (dose rate of 1 MGy/s), although the same evolution was observed at P10, occurring more slowly due to the lower photon flux.

The left panel displays the evolution of the FSDP during the first 100 s, with successive diffraction patterns spaced by 2 s (as indicated by the color scale). The system initially evolves rapidly toward a different structure, following an exponential-like behavior. The right panel shows the same evolution over a longer 1000 s time scale, with patterns spaced by 10 s. Here, the exponential character is even more evident, with the structural evolution saturating toward what we refer to as the fully damaged state.

After an absorbed dose of approximately 300 MGy, the structure essentially stops evolving. As discussed in the previous section, the system then exhibits stationary dynamics under continued irradiation. During this transformation, the FSDP widens by about 30%, its position shifts toward higher Q by approximately 1.3%, and its intensity significantly decreases. As discussed in the introduction, a broadening of the FSDP reflects an increase in disorder at the medium-range scale [Sal+07]. This increase in disorder is one of the main results reported by Baglioni *et al.* [Bag+24]. Furthermore, the shift of the FSDP position toward higher Q, according to the Ehrenfest relation, corresponds to a densification of the same order. This observation is consistent with the early studies of Primak [PK68; Pri+64; Pri78], which reported densification of silica glass by a few percent under neutron irradiation.

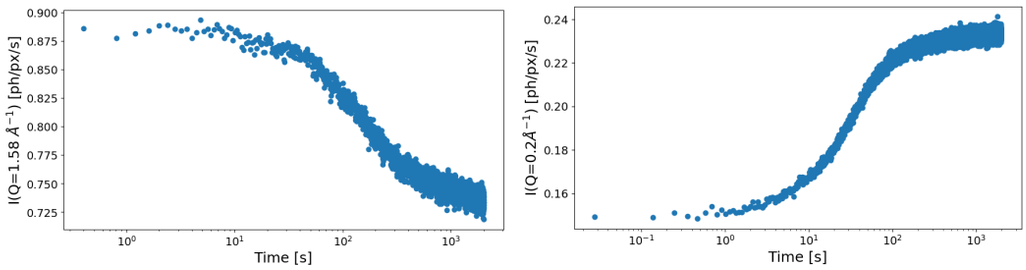

Figure 5.8: Time evolution of selected structural observables at room temperature. **Left:** Scattered intensity at the FSDP measured at P10 (integrated over the detector), showing an initial plateau corresponding to the pristine glass, followed by an exponential-like evolution and a final stationary regime. **Right:** Low-Q scattered intensity ($Q = 0.2$ Å^{-1}) measured at ID10, highlighting the transition from the pristine plateau to the fully damaged plateau, with an overall increase in intensity.

To better highlight the exponential character of these structural changes, Fig. 5.8

(left) shows the evolution of the scattered intensity at the FSDP measured with the fast XPCS detector (integrated over the full detector range) at the P10 beamline. The exponential behavior is clearly visible: on a logarithmic scale, an initial plateau is observed, corresponding to the linear-response regime in which the measurement probes the pristine glass structure. At P10 (dose rate $\sim$ 0.3 MGy/s), this regime extends over approximately the first 10 s. This pristine plateau is followed by an exponential-like structural evolution over a dose of about 300 MGy. Beyond this point, the evolution slows down and reaches a stationary plateau. Due to the lower dose rate at P10, therefore the lower maximum achievable total dose, the final plateau is more clearly defined in the ID10 measurements.

Figure 5.8 (right) shows the evolution of the low-Q scattered intensity (Q = 0.2 $Å^{-1}$) measured with the fast XPCS detector at ID10. As discussed in Sec. 1.6, the low-Q signal probes density fluctuations in the system[18]. As for the FSDP, two plateaus are observed: a pristine plateau for doses below $\sim$ 300 MGy, and a fully damaged plateau after the exponential-like transformation. The higher dose rate at ID10 allows measurements up to $\sim$ 2 GGy, providing a clearer definition of the final plateau. However, in this case the behavior is opposite to that observed at the FSDP: the low-Q scattered intensity increases by approximately 40%, corresponding to a substantial increase in density fluctuations.

At this stage, it is not possible to distinguish whether this increase arises from relaxational or vibrational contributions. Nevertheless, an increase in relaxational density fluctuations appears more plausible, as a comparable increase in the vibrational contribution would imply an unrealistically large change in the high-frequency longitudinal sound velocity (see Eq. 1.26). This point will be revisited in Chapter 6.

The existence of a final stationary state, in which both the dynamics and the structure become stationary—as in an equilibrium liquid—is non-trivial. It indicates that the rates of defect production and annihilation reach a balance after a certain absorbed dose, or, more precisely, after a given defect concentration is achieved. As discussed extensively in Chapter 4, defect production is driven by X-ray radiolysis, while defect annihilation can occur either through thermal annealing or radiation-induced annealing processes.

At the initial stage of irradiation, defect production is not compensated by annihilation, leading to a progressive increase in defect concentration. This results in the observed evolution of the structure factor: spatial density fluctuations and medium-range disorder increase, while the system becomes more compact. The

18 The assumption that Q = 0.2 $Å^{-1}$ is sufficiently small will be discussed in Sec. 6.1.5.

evolution of the structure, together with the increasing defect concentration, is accompanied by a slowing down of the induced dynamics.

We anticipate here, in agreement with the studies discussed in Chapter 4, that the fully damaged structure obtained at room temperature remains stable at the irradiation temperature. When the beam is switched off, the induced dynamics clearly ceases, yet the glass does not recover its initial state, instead preserving the saturated defect concentration. This result will be independently demonstrated for different irradiation temperatures in Sec. 5.13. This observation indicates that the saturation mechanism is not governed by thermal annealing, which would otherwise lead to at least partial recovery toward the pristine structure. Rather, it suggests that defect annihilation is primarily driven by radiation-induced processes.

5.4 Temperature evolution of the dynamics

In the previous sections, we have shown that v-GeO_2 at room temperature under X-ray irradiation exhibits beam-induced dynamics, in agreement with previous studies (see Sec. 4.6), which evolve with the absorbed dose. This evolution of the dynamics is accompanied by a structural evolution, eventually leading to a stationary state characterized by a more disordered structure, densification, and an increase in spatial density fluctuations. Once this fully damaged structure is reached, the beam-induced dynamics become stationary, with a stretched-exponential behavior and a relaxation time, expressed in dose units, of the order of a few MGy. Further irradiation still produces atomic displacements and decorrelation, but the structural state of the glass remains unchanged.

To better understand the processes governing this transformation, we now investigate the temperature dependence of the beam-induced dynamics and of the associated structural evolution. In the two experiments, several temperature ramps were acquired on different germania samples. In this section, we focus on the dependence of the dynamics of the fully damaged state on the irradiation temperature, for the two probed Q values. As will become clear throughout this chapter, the existence of a final stationary fully damaged state is independent of the irradiation temperature, and the dose required to reach it remains of the order of $\sim$ 300 MGy.

In both experiments, measurements were always performed on the same irradiated spot in order to avoid variations in sample thickness arising from non-perfectly flat sample preparation. In this way, the beamline contrast $\beta(\vec{Q})$ (Eq. 2.17) remains constant with temperature, allowing access to the temperature dependence of the non-ergodicity factor f_Q (Eq. 1.15). As discussed, the sample thickness strongly affects the contrast in WAXS XPCS experiments. However, after each temperature

change, the sample position shifts due to thermal expansion. To compensate for this effect, we acquired spatial maps of the scattered signal to relocate the previously irradiated spot. By analyzing the spatial variation of the scattered intensity (both at low Q and at the FSDP), it was possible to consistently recenter the beam on the same region (see Fig. 1.8 for examples of such maps).

We also verified, by monitoring the sample transmission, the absence of ablation: no measurable change in transmission was observed even after several days of exposure. Finally, as will be shown in this chapter, the fully damaged state is identical whether reached from the pristine glass or from a previously damaged state at a different temperature. This justifies the choice of measuring always on the same spot, which ensures comparable correlation functions, particularly with respect to the contrast.

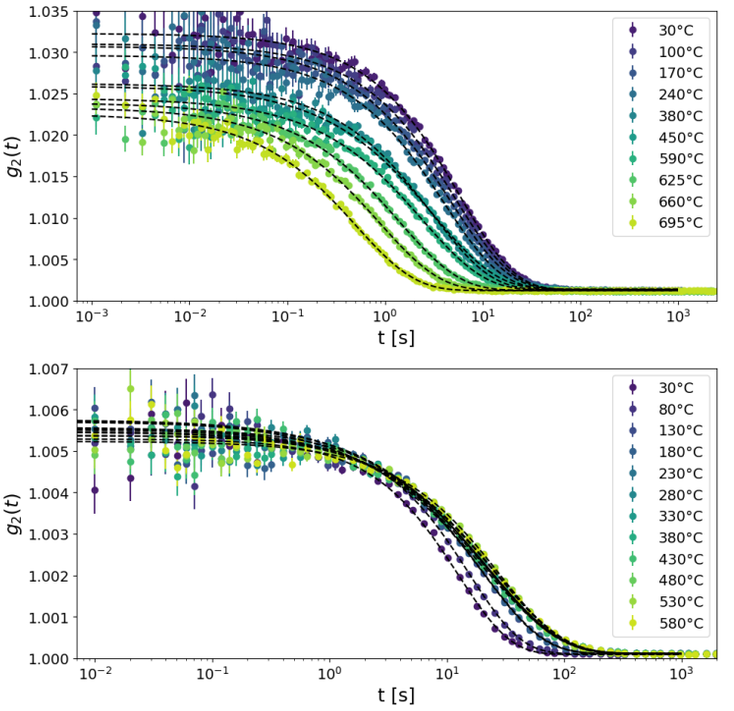

Figure 5.9: Temperature evolution of the intensity autocorrelation function $g_2(\tau)$ in the fully damaged state. **Top:** Low-Q measurements at ID10 ($Q \sim 0.2$ Å^{-1}). **Bottom:** FSDP measurements at P10 ($Q \sim 1.55$ Å^{-1}). Each curve is obtained by averaging the MT-2TC over the stationary time window, i.e. after the system has absorbed $\sim$ 300 MGy and reached the fully damaged state.

Figure 5.9 shows correlation functions measured at different irradiation tem-

peratures at low Q (top) and at the FSDP (bottom). The curves are obtained by averaging the MT-2TC over the stationary dynamical regime, excluding the initial frames corresponding to the structural transformation, i.e. after the system has absorbed approximately 300 MGy.

The corresponding fit parameters are presented in Fig. 5.10. At ID10, three nominally identical 100 μm thick samples were measured (samples 6, 7, and 3). Sample 6 was subjected to a fast heating ramp (about 10 minutes per temperature point), while samples 7 and 3 were measured with slower ramps (about 1 hour per point). For sample 7, additional measurements were performed during cooling.

At P10, two 100 μm thick samples were measured (samples 1 and 2). For sample 1, a heating ramp of about 2 hours per point was performed. For sample 2, the temperature was varied multiple times, both due to beamline issues and to specific experimental objectives (see Sec. 5.7). In all cases, the correlation functions and fits discussed here refer to the fully damaged stationary state at the corresponding irradiation temperature.

Both at low Q (ID10) and at the FSDP (P10), the relaxation time in the fully damaged state exhibits a weak temperature dependence below the glass transition temperature T_g (Fig. 5.10, top).

In the low-Q case, above T_g, the fitted τ decreases and bends toward the equilibrium curve measured by visible photon correlation spectroscopy, indicating the onset of intrinsic relaxational dynamics, qualitatively described by the parallel relation of Eq. 4.15. Interestingly, in the slower heating ramps, a bump in τ is observed when approaching T_g from below. This feature is not visible in the fast heating ramp (sample 6) nor in the cooling ramp (sample 7). By analyzing the t_w dependence of the correlation functions, similarly to Sec. 5.2.1, a slow linear increase of τ with t_w is observed above $\sim 450^\circ$C, following the initial beam-induced evolution. We attribute this behavior to a thermal annealing effect that progressively drives the glass toward the supercooled liquid state. However, X-ray–induced relaxation still dominates, and it remains unclear why the two processes do not equilibrate to produce a fully stationary dynamics.

In contrast, at the FSDP the relaxation time shows a very weak temperature dependence, slightly increasing with temperature and never approaching the equilibrium curve. This behavior can be attributed to De Gennes narrowing: the equilibrium relaxation time at the FSDP may be shifted to longer times due to the increase of $S(Q)$. A full verification would require a complete characterization of the relaxation time over the entire Q range.

The stretching exponent β (Fig. 5.10, bottom left) shows a well-defined, nearly constant value at low Q, remaining stretched at approximately $\beta \sim 0.75$. In contrast, the P10 data exhibit more scatter: sample 1 shows an approximately constant $\beta \sim 1$,

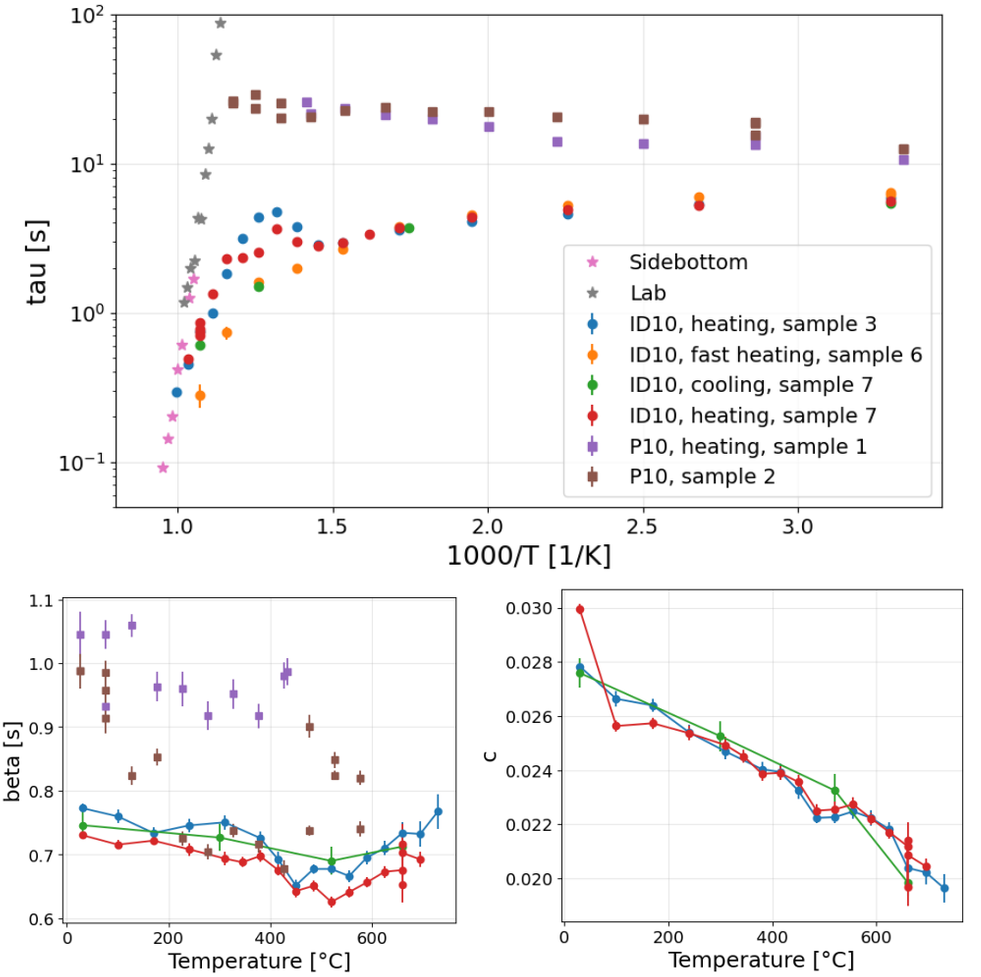

Figure 5.10: Temperature dependence of the KWW fit parameters in the fully damaged state. **Top:** Relaxation time τ as a function of temperature for both low-Q (ID10) and FSDP (P10) measurements. The equilibrium supercooled liquid data are obtained from visible photon correlation spectroscopy: low-temperature data from Sidebottom [Sid23] (pink stars), extended to higher temperatures by measurements performed in our laboratory (gray stars, to be published). **Bottom left:** Stretching exponent β as a function of temperature. **Bottom right:** Contrast C as a function of temperature for the low-Q measurement only.

while sample 2 displays values between 0.7 and 1. This variability is attributed to beamline instabilities rather than to intrinsic physical effects, as small variations in β can arise from fluctuations in the incoming flux.

Contrast and non-ergodicity of the glass

The overall contrast C (Eq. 5.1) exhibits a particularly interesting behavior. As already visible in Fig. 5.9, at low Q the contrast decreases with temperature, while at the FSDP it remains essentially constant. Assuming that the beamline contrast $\beta(\vec{Q})$ remains constant within each experiment, the observed behavior of C reflects the temperature dependence of f_Q^2 (see Eqs. 2.17 and 1.15).

As discussed in the introduction (Fig. 1.5), f_Q represents the ratio between decorrelation due to atomic vibrations and that due to structural relaxation frozen into the glass. In the present case, X-rays induce decorrelation, but the plateau preceding the decay still reflects the non-ergodicity of the system on timescales shorter than the induced relaxation time. Equivalently, as will be discussed in Sec. 5.6, it reflects the non-ergodicity of the damaged structure when the beam is switched off.

At the FSDP, f_Q is expected to be close to unity, due to the dominance of low-frequency contributions in $S(Q,\omega)$. In other words, the FSDP arises from structural correlations on long timescales, and persists even at zero temperature where vibrational contributions vanish. The constant behavior of C at the FSDP is consistent with this picture.

At low Q (Fig. 5.10, bottom right), the reduction of the contrast is consistent with the expected decrease of the non-ergodicity factor f_Q (see Sec. 1.28). While the zero-frequency contribution to the dynamic structure factor is only weakly temperature dependent, the vibrational contribution increases with temperature, and in this Q-range the two contributions are comparable.

To our knowledge, this represents the first measurement in a glass system capturing the temperature dependence of the non-ergodicity factor with XPCS. This result will be further discussed in Chapter 6, where it will be compared with the high-frequency non-ergodicity factor measured by inelastic X-ray scattering.

5.5 Dependence of the structure on the irradiation temperature

We have seen that, below the glass transition temperature, the beam-induced dynamics show a very weak temperature dependence, while approaching T_g the relaxation time bends toward the supercooled liquid line. As suggested by Baglioni

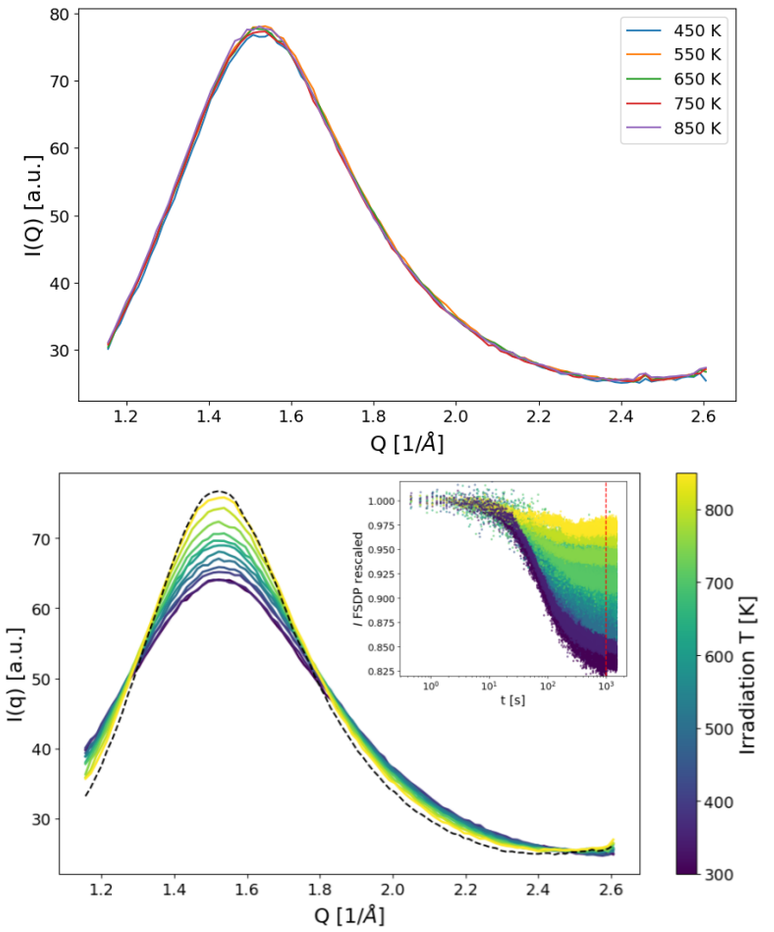

Figure 5.11: Temperature dependence of the structure factor $I(Q)$ of vitreous GeO_2 under X-ray irradiation. **Top:** Pristine glass measured at the P10 beamline at different temperatures, obtained from short exposures on a non-irradiated region of the sample. The structure shows only minor temperature dependence below the glass transition, as expected for a glass. **Bottom:** Fully damaged glass measured at different irradiation temperatures. In contrast to the pristine case, the final structure exhibits a strong dependence on the irradiation temperature: lower temperatures lead to a broader FSDP and a shift toward higher Q, indicating increased disorder and densification. The black dashed curve corresponds to the pristine glass at 850 K for comparison. **Inset:** Evolution of the FSDP intensity, measured by the fast XPCS detector, from the pristine to the fully damaged state. Intensities are normalized to the pristine value. The transformations follow an exponential-like evolution toward a stationary value, which depends approximately linearly on the irradiation temperature. The red dashed vertical line marks the time corresponding to an absorbed dose of 300 MGy, beyond which the structural evolution saturates.

et al. [Bag+24], one would therefore expect that the fully irradiated state exhibits little or no temperature dependence below the glass transition, while, approaching the temperature range where thermal relaxation dominates, the structure recovers toward that of the equilibrium supercooled liquid. Accordingly, a dependence of the final structure on the irradiation temperature is expected only in the vicinity of T_g.

Our experiments instead reveal a dramatically different situation. Figure 5.11 (top) shows the temperature dependence of the scattered intensity $I(Q)$ of the pristine glass measured at the P10 beamline. The structure was obtained by acquiring single diffraction patterns on a non-irradiated region of the sample, always probing the same spot to avoid thickness-related distortions and keeping the total acquisition time much shorter than the initial plateau ($\sim$ 1 s) discussed in Fig. 5.8 (left), thereby preventing X-ray–induced structural modifications. At almost-zero absorbed doses, the expected behavior of glasses is observed: below the glass transition, the structure shows only minor changes with temperature, at least in the FSDP region. Moreover, within an accuracy of about 20%, the thermal expansion coefficient—estimated from the small shift of the FSDP position Q_1, assuming a linear proportionality with density—is consistent with literature values [NM68].

In contrast, Fig. 5.11 (bottom) shows the structure factor of the fully damaged state measured at different irradiation temperatures. Contrary to expectations, the final structure exhibits a strong dependence on the irradiation temperature even well below T_g. In particular, the lower the irradiation temperature, the broader the FSDP becomes, and the more its position shifts toward higher Q values. Therefore, lower irradiation temperatures produce a glass that is both more disordered and denser. Conversely, when approaching and exceeding the glass transition, the fully damaged glass becomes increasingly similar to the pristine structure. However, in our experiments we did not reach sufficiently high temperatures for which irradiation no longer induces structural modifications in the supercooled liquid. We expect such a regime to occur several hundreds of kelvin above T_g, but the maximum accessible temperature was limited to 850 K at P10 by the furnace design, and to $\sim$ 1000 K at ID10 by the onset of crystallization.

The inset in Fig. 5.11 (bottom) shows the evolution of the FSDP intensity, measured by the fast XPCS detector, from the pristine glass to the fully damaged state. The intensities are normalized to unity at the pristine state (initial value), whose FSDP is nearly temperature independent. As already observed at room temperature, the FSDP height evolves exponentially toward the damaged state. The final FSDP intensity, in this temperature range, depends approximately linearly on the irradiation temperature. The red dashed vertical line indicates the time corresponding to

an absorbed dose of 300 MGy at the P10 beamline: beyond this dose, the structural evolution essentially saturates for all temperatures.

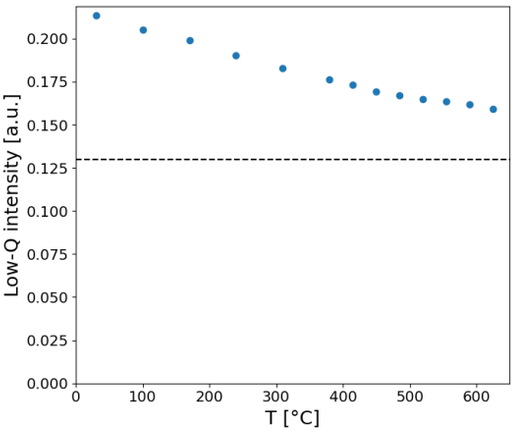

Figure 5.12: Irradiation temperature dependence of the low-Q scattered intensity (Q = 0.2 Å^{-1}) of the fully damaged state measured at the ID10 beamline. The horizontal dashed line represents the corresponding intensity of the pristine glass at room temperature.

To conclude this section, we again exploit the fast XPCS detector at the ID10 beamline to monitor the low-Q scattered intensity. Figure 5.12 shows the irradiation temperature dependence of the scattered intensity at $Q = 0.2$ Å^{-1} in the fully damaged state. The horizontal dashed line indicates the room-temperature value for the pristine glass.

The observed temperature dependence of the SAXS signal differs markedly from the expected behavior of a pristine glass (discussed in Sec. 1.6), where, below T_g, only a small increase in density fluctuations due to vibrational contributions is expected with increasing temperature. Instead, we observe an opposite and much more pronounced trend. This should not be surprising, as we have just seen that irradiation at different temperatures dramatically alters the resulting glassy state. Therefore, by changing the irradiation temperature, we are not simply varying the temperature of the glass, but also its position in the potential energy landscape.

We have seen that the SAXS signal increases by about 40% at room temperature upon irradiation. When varying the irradiation temperature, we find that the SAXS intensity decreases with increasing temperature, showing a trend opposite to that observed for the FSDP. This again indicates that the structural transformations induced by irradiation become progressively weaker as the temperature increases, approaching the pristine glass behavior above T_g. Therefore, while X-ray irradiation

enhances density fluctuations at all temperatures, the magnitude of this effect increases as the irradiation temperature decreases.

Overall, the fully irradiated structure of germania strongly depends on the irradiation temperature. In particular, lower irradiation temperatures lead to a more disordered and more compact structure, accompanied by a larger increase in density fluctuations. Therefore, X-ray irradiation up to the fully damaged state systematically shifts the glass within the potential energy landscape (PEL), with the irradiation temperature controlling its final position. Within our experimental range, the room-temperature case (Sec. 5.3) exhibits the largest structural transformation, whereas approaching and surpassing the glass transition X-ray irradiation produces only minor structural modifications.

From the point of view of local defects, this suggests that the lower the temperature of the glass, the larger the defect concentration it can sustain. This may arise either from a decrease in the defect annihilation rate with decreasing temperature, or from an increase in the defect production rate, or from a combination of both effects, ultimately requiring higher defect concentrations to reach a balance between the two processes. At present, we do not have a definitive explanation, as the simplest scenario of thermal defect annealing decreasing with temperature does not appear to dominate (see Sec. 5.13).

Within this framework, and in agreement with the results of Baglioni et al. [Bag+24], one may interpret irradiation up to the fully damaged state as a rejuvenation process, since it drives the glass toward a more disordered state with enhanced density fluctuations. In this view, the lower the irradiation temperature, the more rejuvenated the resulting glass. This interpretation will be further discussed after introducing additional experimental evidence in Chapter 6.

5.6 Stability of the fully-irradiated state

The thermal stability of the fully irradiated state after cessation of X-ray irradiation has so far been implicitly assumed, based on the literature results presented in Sec. 4.6. In this section, we demonstrate that the fully irradiated state obtained at a given temperature remains stable at that temperature. Specifically, once the X-ray beam is switched off after the transformation to the final state, the glass does not recover its pristine structure but retains the fully irradiated configuration, provided that the temperature is not significantly increased with respect to the irradiation temperature. This implies that the structural defects produced by X-ray radiolysis in germania are stable within the temperature range explored in this study. This behavior contrasts with the isochronal annealing curves discussed in Chapter 4 on

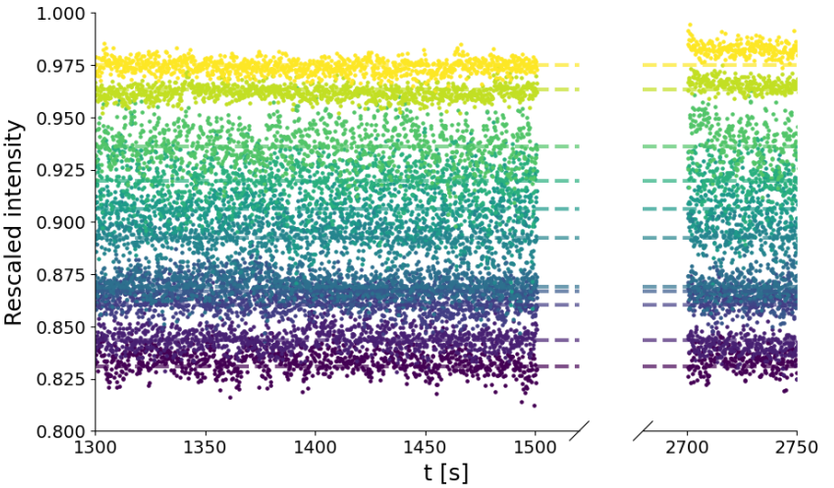

Figure 5.13: Time evolution of the FSDP intensity measured at the P10 beamline during and after irradiation. The intensity is normalized to the pristine value (not shown). After reaching the fully damaged state, the X-ray beam is switched off at $t_w = 1500$ s for 20 minutes, allowing the sample to thermally anneal at constant temperature. Upon re-irradiation, the FSDP intensity is measured again. Horizontal dashed lines indicate the average intensity before beam interruption. The absence of significant changes demonstrates the stability of the fully irradiated structure at most temperatures, with only minor recovery observed close to T_g (800–850 K).

other oxide systems, where defects evolve or anneal at temperatures only slightly above the irradiation temperature.

This stability is demonstrated in Fig. 5.13, where the FSDP intensity measured by the fast XPCS detector is reported as a function of time (P10 beamline). The waiting time axis is referenced to the pristine state (not shown), whose intensity is normalized to unity. The data shown start at $t_w \sim 1300$ s, when the structural transformation is already completed. At $t_w = 1500$ s, the X-ray beam is switched off for 20 minutes, allowing thermal annealing at constant temperature. The beam is then switched on again to probe the structure after this annealing period. As can be seen, the FSDP intensity remains unchanged after the interruption for all temperatures, except for the two closest to T_g (800 and 850 K), where a slight recovery toward the pristine structure is observed. In these cases, additional dose is required to re-establish the fully damaged state.

These results indicate that, deep in the glassy state, thermal annealing does not play a dominant role in limiting the defect concentration. If it did, the fully irradiated structure would depend on the X-ray dose rate, which is not observed

in our experiments nor in the literature. In contrast, close to and above T_g, where intrinsic structural relaxation becomes comparable to the experimental timescale, thermal annealing becomes effective and partial recovery is observed.

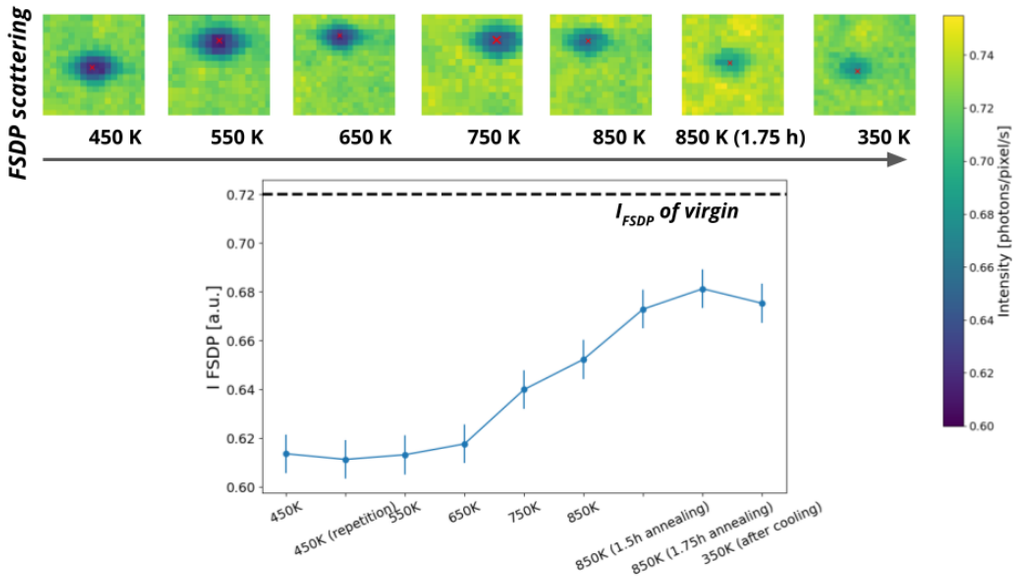

Figure 5.14: Thermal stability of a glass irradiated at 350 K. A pristine region is first irradiated to the fully damaged state at 350 K. The temperature is then increased stepwise, and the same region is monitored via spatial maps of the FSDP intensity (displayed at the top of the figure). The central plot shows the FSDP intensity at the center of the irradiated spot within the maps. The irradiated spot remains clearly visible up to ~ 650 K, indicating structural stability. Above ~ 750 K, the structure progressively evolves toward the pristine state. Even after prolonged annealing at 850 K, full recovery is not achieved. Upon cooling back to 350 K, the structure remains unchanged, confirming the persistence of the partially annealed state.

To further investigate thermal stability, we consider the evolution of a glass irradiated at low temperature (350 K) upon subsequent heating, as shown in Fig. 5.14. A pristine region is first irradiated at 350 K until the fully damaged state is reached. The temperature is then increased in steps of about 100 K, while the same region is monitored using fast, attenuated spatial maps of the FSDP intensity. These maps allow clear identification of the irradiated region due to the strong contrast in intensity.

As observed, the structure remains unchanged up to about 650 K. Above this temperature (around 750 K), the structure begins to evolve toward the pristine

state. At the maximum temperature of 850 K, a clear time dependence is observed, indicating ongoing annealing. However, even after 1.75 hours, the pristine structure is not fully recovered, nor is the structure corresponding to a fully irradiated state at 850 K reached; instead, the FSDP intensity remains at an intermediate value. Upon cooling back to 350 K, the structure remains unchanged, retaining the configuration reached at high temperature, as expected for a glass outside irradiation conditions. While this discussion focuses on the FSDP for simplicity, the same behavior is observed across the full structure factor.

From these results, we conclude that the defected structure is stable at the irradiation temperature and requires several hundred kelvin of heating to initiate annealing. Moreover, we observe a characteristic feature of radiation-induced defects in glasses, already discussed in Chapter 4: defects begin to evolve and partially anneal at temperatures below T_g (in this case at 750 K), as reflected by the progressive structural recovery. The incomplete annealing observed even after prolonged exposure at 850 K further highlights the intrinsic stability of the damaged state.

These findings reinforce the relevance of studying the X-ray–induced fully irradiated glass as a metastable but robust state, rather than a transient configuration existing only during or immediately after irradiation.

5.7 Radiation-induced rejuvenation and annealing

The final aspect addressed in this chapter is the uniqueness of the fully damaged state. As discussed in Sec. 4.6, Baglioni et al. [Bag+24] demonstrated, for the chalcogenide glass $GeSe_3$ at room temperature, that the fully irradiated state does not depend on the sample preparation, in particular on the fictive temperature of the glass. Here, we extend this concept by showing that the final state is unique irrespective of the irradiation history. Specifically, the same glass state is obtained whether one irradiates the pristine glass at a given temperature or irradiates, at the same temperature, a glass that has previously been irradiated at different temperatures. In other words, the fully irradiated structure depends solely on the irradiation temperature and not on the initial minimum in the potential energy landscape.

To demonstrate this behavior, we repeatedly irradiate the same spot of the sample up to the fully damaged state and change the irradiation temperature in a stepwise manner, both upon heating and cooling, while monitoring the FSDP intensity as well as the structure factor at the P10 beamline. For simplicity, we focus here on the FSDP intensity, noting that the same conclusions apply to the full structure factor.

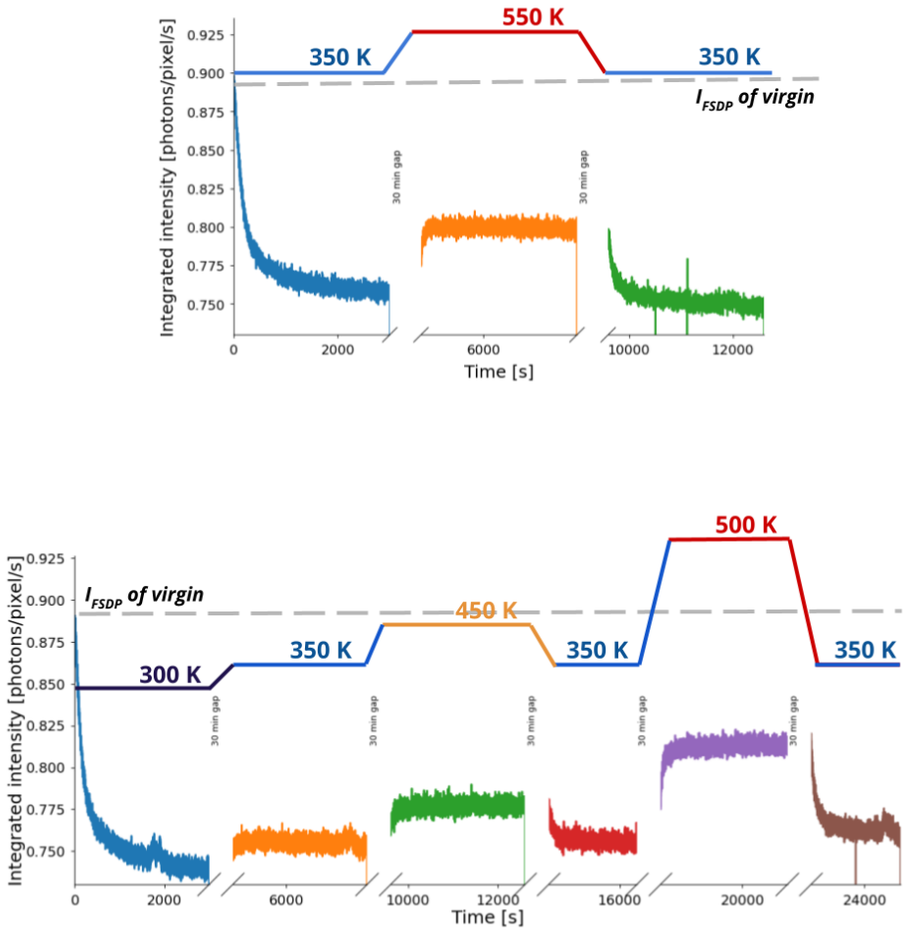

Figure 5.15: Evolution of the FSDP intensity during successive irradiation steps at different temperatures on the same sample spot (P10 beamline). **Top:** Starting from the pristine glass at 350 K, the sample is first irradiated to reach the fully damaged state. The temperature is then increased to 550 K, the same spot is recentered, and irradiation resumes, leading to a partial recovery toward the fully irradiated state at the higher temperature. Upon cooling back to 350 K and re-irradiating, the structure evolves again toward the corresponding low-temperature fully damaged state. **Bottom:** Same protocol applied over multiple temperature steps, showing reproducible transformations between fully irradiated states at different temperatures. The exponential evolution of the FSDP intensity upon re-irradiation highlights that structural changes are driven by the X-ray beam and not by thermal effects alone.

Figure 5.15 shows two repetition (top and bottom panels) of this procedure. In the top panel, we start from the pristine glass at 350 K. The sample (blue curve) is irradiated until the fully damaged state at this temperature is reached. The temperature is then increased to 550 K and, by acquiring spatial maps of the FSDP intensity (as in Fig. 5.14) while depositing a negligible dose, the previously irradiated spot is recentered. Irradiation is then restarted at the higher temperature. At this stage, the FSDP intensity partially recovers, evolving toward the fully irradiated state corresponding to 550 K[19]. The reverse process is subsequently performed: once the fully irradiated state at 550 K is reached, irradiation is stopped, the temperature is lowered back to 350 K, and the beam is switched on again. The structure then evolves once more, transforming from the fully irradiated state at 550 K to that corresponding to 350 K. The same up-and-down protocol is repeated over multiple temperature steps in the bottom panel of Fig. 5.15, with a typical time interval of about 30 minutes between temperature changes.

Importantly, the structural transformation start with the same exponential behavior previously observed only when the beam is switched on at the new temperature. This again demonstrates that structural modifications are induced by irradiation and not by thermal annealing alone. The temperature dependence of the fully damaged state is therefore activated only under irradiation and cannot be achieved by temperature changes in the absence of the beam.

These measurements demonstrate that the fully irradiated state is uniquely determined by the irradiation temperature and is independent of the previous history of the glass, i.e. of the initial minimum in the potential energy landscape. Moreover, in analogy with conventional thermal production mechanisms of glasses, we speculate that X-ray irradiation can act either as a rejuvenation or an annealing mechanism depending on the irradiation temperature: transitions toward more disordered states correspond to rejuvenation, while transitions toward structures closer to the pristine glass correspond to annealing. This analogy will become clearer in the following and final chapter (Chapter 6), where we will assign to the fully irradiated glass state a fictive temperature.

19 Small mismatches between consecutive curves are due to imperfect recentering of the irradiated spot, caused by step losses in the sample vertical motor during the P10 experiment.

6 Density fluctuations by IXS

In this chapter, we present an inelastic X-ray scattering (IXS) study on vitreous GeO_2 at the ESRF ID28 beamline, aimed at clarifying the origin of the low-Q scattering increase and the loss of contrast observed in XPCS measurements.

The ID28 beamline was optimized to work at small angle with negligible background to access weak inelastic signals in the small-Q regime. We show that, also here, X-ray irradiation drives the system to a fully damaged state, characterized by enhanced density fluctuations, affecting the elastic (frozen-in) component.

The spectra are well described by a model combining an elastic peak and a damped harmonic oscillator, allowing the extraction of the acoustic frequency, damping, and elastic fraction F_Q. The high-frequency longitudinal sound velocity is found to be temperature independent ($v_L^\infty \simeq 3900$ m/s), indicating that vibrational dynamics are essentially unaffected by irradiation.

By exploiting the linear temperature dependence of the vibrational contribution, we calibrate the scattered intensity and separate vibrational and frozen-in density fluctuations. This shows that irradiation increases the frozen-in component, consistent with a picture in which the glass is driven toward higher fictive temperatures.

Finally, we demonstrate a direct proportionality between the elastic fraction measured by IXS and the square root of the XPCS contrast, establishing that both techniques probe the same non-ergodicity factor across different timescales.

6.1 Experimental conditions and measurement strategy

Within this chapter, we present the results of the inelastic X-ray scattering experiment performed at the ID28 beamline of ESRF (HC6005, October 2025). The experiment had multiple goals. First, we aimed to better understand the origin of the increase in the low-Q scattered signal. Second, we wanted to clarify the origin of the loss of contrast observed during the temperature ramps measured at ID10 (see Fig. 5.9), which we have interpreted as a decrease of the non-ergodicity factor f_Q.

In this section, we describe in detail the beamline preparation and the experimental configuration. A significant effort was required to prepare the beamline, including a dedicated test week in June 2025, as small-angle (Brillouin) inelastic scattering measurements on glasses (or liquids) had not been performed on this instrument for a long time. These experiments impose specific requirements, in particular extremely low background and a highly symmetric and stable energy resolution, in contrast to the more common measurements currently carried out on crystalline and magnetic systems.

6.1.1 ID28 beamline configuration

The 100 μm slab sample, prepared as described for the previous two experiments (Sec. 5.1.3), is broken into an order $\sim 1 \times 1$ mm^2 piece and glued, using a high-temperature cement, onto the tip of a needle. The glue only partially covers the sample so that, once properly oriented, a 100 μm thick freestanding portion is available for measurements. The needle is in direct thermal contact with the three resistors of the furnace. The sample is kept under vacuum within a specifically designed 3D-printed chamber, which is air-cooled by airflow within its walls. The entrance Kapton window is placed about 11 cm upstream of the sample (with respect to the beam direction) to separate Kapton scattering from sample scattering. The exit window, instead, is placed 5 cm downstream of the sample.

In contrast to the ID10 experiment, in which the beam was kept under vacuum up to the detector, the presence of two Kapton windows close to the sample complicates the isolation of the scattered signal and requires two beamstops. An internal beamstop, built as a cylinder with entrance and exit holes, blocks the scattering from the entrance Kapton window while allowing the direct beam to reach the sample. An external beamstop, placed about 1 mm from the exit window, stops both the transmitted beam and the Kapton scattering from the exit window. The beamstop positions are adjusted by monitoring the scattered signal and allow measurements over only a finite angular range. In particular, the external beamstop limits the smallest accessible scattering angle, which in this configuration is about 0.7°.

We chose to work with the Si(11,11,11) reflection, corresponding to a photon energy of 21.747 keV (11th Bragg reflection in backscattering), as it is the highest-order reliable reflection previously tested. In particular, one of the main sources of resolution instability is the heat load on the main monochromator, and this configuration had already been verified to provide stable performance.

Of the nine crystal analyzers described in Sec. 2.3.1, only three detectors were operational. These analyzers are labeled a6, a2, and a7, with a6 at the smallest

scattering angle and a7 at the largest. Their angular separations are 0.78° between a6 and a2, and 0.746° between a2 and a7. The best resolution is provided by analyzer a6, which we therefore positioned at a scattering angle of 1°, matching the ID10 experiment and corresponding to $Q = 0.19$ Å^{-1}. The analyzer slits were set to 20×55 mm (horizontal × vertical), yielding a Q-resolution of about 20%. The unused analyzers were closed to prevent crosstalk.

The beam size, measured using the standard knife-edge method, was focused as tightly as possible to 14.5×26.6 μm^2 (FWHM). Although it was not possible to measure the photon flux precisely at the selected reflection, it is estimated to be on the order of 10^{10} ph/s, corresponding to a dose rate of about 0.1 MGy/s on the 100 μm germania sample.

The sample preparation procedure is identical to that described in Sec. 5.1.3.

Significant effort was devoted to isolating the scattered signal from fluorescence. As discussed in Eq. 2.6, the scattering model applies when fluorescence and Compton contributions are negligible. The working energy of 21.747 keV is relatively close to the 11.1 keV absorption edge of germania, and fluorescence can contribute as a spurious signal, particularly through lower-order silicon reflections. This contribution was reduced by applying thresholds to the detector multichannel analyzers: by inspecting the pulse-height distribution, the lower threshold was set to approximately 70% of the average pulse height.

The performance of this setup, namely the resolution, the empty-cell contribution, and the rate of radiation-induced damage in the germania glass at this beamline, is discussed in the following.

6.1.2 Resolution

The resolution is measured by performing inelastic scans of scattering from a plexiglass slab cooled down to about 20 K, in order to suppress inelastic contributions, and at the FSDP of plexiglass to maximize the elastically scattered signal. In this configuration, the energy spectrum of $S(Q, E)$ of plexiglass, at fixed Q, can be approximated by a delta function.

Inelastic scans of the monochromator temperature are performed with a temperature step of 5 mK. The integration time is set to 30 s for each temperature point, and the measurement is repeated three times to improve the statistics.

We briefly describe here the first step of the data analysis, which consists of transforming the measured intensities—recorded as a function of the silicon monochromator and analyzer resistances—into energy spectra. The measurement stores the resistance measured by thermocouples both on the monochromator and on the analyzer crystals (whose temperature is kept constant). The temperatures are then

computed using a Steinhart–Hart–like calibration, and, from the temperature shifts between monochromator and analyzer, together with the known thermal expansion of silicon, these variations are converted into energy shifts.

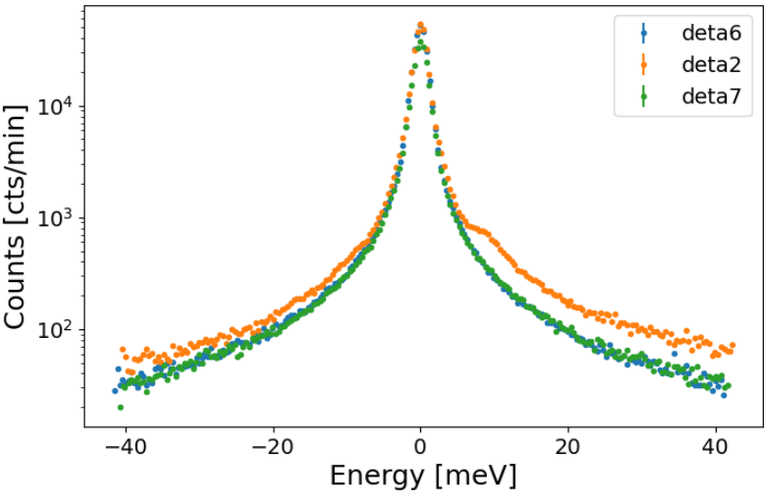

Figure 6.1: Energy resolution functions measured for the three analyzers used in the experiment using the plexiglass scattering. Analyzer a6 (deta6) exhibits the best and most symmetric resolution, with a Lorentzian FWHM of 1.7 meV. Analyzer a7 (deta7) shows a broader resolution of 1.9 meV, while analyzer a2 (deta2) provides a comparable width (1.7 meV) but with noticeable asymmetry.

The resolution measurements for the three detectors are shown in Fig. 6.1. Analyzer a6 (denoted deta6) exhibits the best and most symmetric resolution function, which is why it was selected for measurements at the Q value of interest. A Lorentzian fit yields a FWHM of 1.7 meV. The other two analyzers, whose data are mainly used as a complement in this work, show either a broader resolution of 1.9 meV (deta7) or a good but non-symmetric resolution of 1.7 meV (deta2). The non-symmetric resolution, in particular, makes it difficult to distinguish genuine inelastic vibrational contributions from spurious signals and is therefore not ideal for IXS measurements. Fortunately, analyzer a6 fulfills the required conditions.

At the end of the experiment, at the highest sample temperatures, the sample crystallized. The scattered signal increased significantly both at small angles, due to the presence of nanometric crystal grains, and at larger Q, where Bragg peaks appeared. By attenuating the incoming beam to avoid detector saturation, we exploited these Bragg peaks—which elastically scatter the incoming beam at well-defined (though broadened due to finite Q resolution) energies—to remeasure the

instrumental resolution, assuming that vibrational contributions are negligible compared to the strong elastic signal. Within experimental uncertainty, the resolution of all three analyzers remained essentially unchanged throughout the entire week of measurements, ensuring a controlled heat-loading at the monochromator.

6.1.3 Empty cell

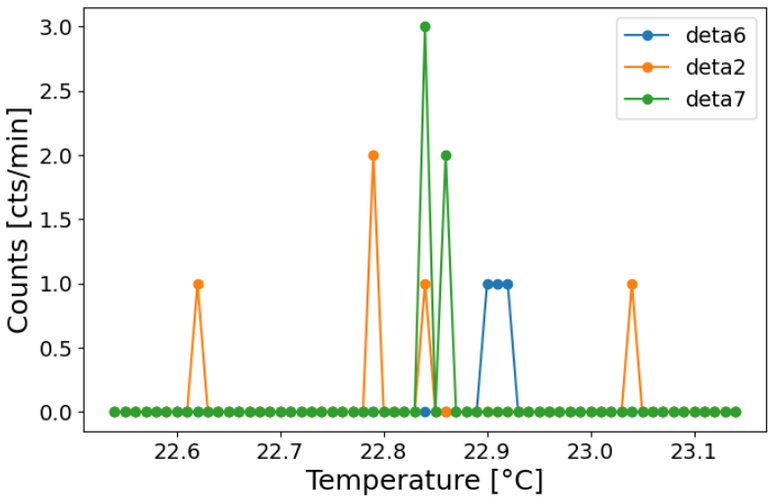

Figure 6.2: Empty-cell measurements for the three analyzers, acquired with temperature steps of 10 mK (faster scan) and an integration time of 1 min per point. The horizontal axis is expressed in analyzer temperature and spans the same energy range as the resolution measurements of Fig. 6.1, with half the temperature step. The absence of detectable signal demonstrates the effectiveness of the beamstop configuration and multichannel analyzer thresholds in suppressing spurious background contributions.

The inelastic signals we aim to measure, namely the longitudinal acoustic modes in germania, are very weak compared to the elastic signal and, as will be shown, differ from the resolution of only a few tens of counts per minute. An almost zero empty-cell background is therefore essential to distinguish the inelastic signal from the instrumental resolution.

Figure 6.2 shows the empty-cell measurements acquired with temperature steps of 10 mK (faster scan), with the horizontal axis expressed in analyzer temperature. The explored temperature range corresponds to the same energy range covered in the resolution measurements of Fig. 6.1, but with half the temperature step. The integration time for each point is 1 min.

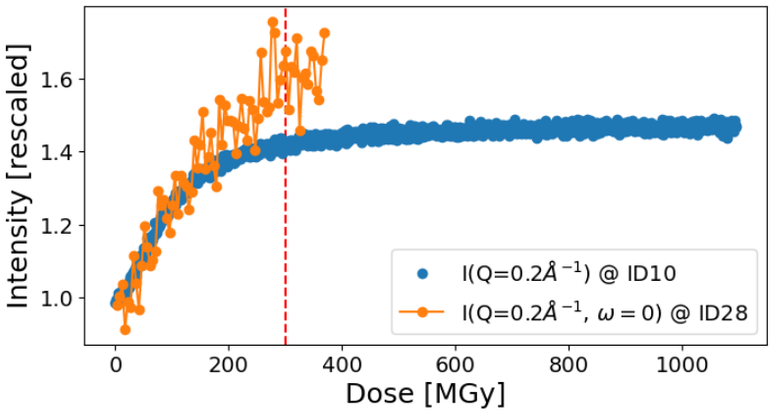

Figure 6.3: Comparison of the evolution of the low-Q scattered intensity during X-ray irradiation at ID10 and ID28. The ID10 data correspond to the total scattered intensity (Fig. 5.8, right), while the ID28 data represent the elastic ($E = 0$ meV) signal measured at low Q. Time is expressed in absorbed dose units, allowing direct comparison between the two experiments. The vertical red dashed line indicates the characteristic dose of $\sim$ 300 MGy required to reach the fully damaged state. Intensities are normalized to unity at the initial (pristine) state.

The measurements show, for all three analyzers, an almost zero empty-cell signal (y axis in cts/min), demonstrating the effectiveness of the beamstop configuration as well as of the multichannel analyzer thresholds in completely suppressing spurious contributions.

6.1.4 X-Ray structural modification of germania

As extensively discussed in Chapter 5, germania undergoes an irradiation-temperature-dependent structural transformation that, in particular for IXS, leads to an increase in density fluctuations of about 40% at room temperature. We have identified an absorbed dose of approximately 300 MGy for the completion of this transformation. The fact that, within an X-ray inelastic scattering experiment, a covalently bonded glass such as germania can undergo structural changes due to X-ray damage is, or at least was, largely unexpected. However, high dose rates are now also reached in IXS experiments as a consequence of the increased brilliance of third- and fourth-generation synchrotron sources and the tightly focused beams that can now be achieved.

For the present experiment, our goal is to measure the low-Q energy spectra of the fully irradiated germania, in order to compare with the ID10 results and

quantify the increase in small-angle scattering. It is therefore necessary to verify that the fully damaged state can be reached within the experimental timescales. The estimated dose rate of ~ 0.1 MGy/s already suggests that this is feasible.

Figure 6.3 shows the evolution of the small-angle scattered intensity measured at ID10 (data from Fig. 5.8, right), compared with the increase in the elastic scattering measured at ID28 during irradiation of pristine germania at room temperature. The latter is obtained by setting the monochromator and analyzer at the same temperature and starting irradiation (and measurement) on a pristine region of the sample. The time axis is expressed in absorbed dose units, allowing a direct comparison between the two experiments[20]. The intensities are normalized to unity at the initial state.

The dose required to complete the X-ray–induced transformation is comparable in both experiments, as indicated by the vertical red dashed line at $\sim$ 300 MGy. However, the relative increase in scattered intensity is larger for the ID28 data. This difference might arise because, while the detector at ID10 does not discriminate photon energy, IXS measurements selectively probe the elastic ($E = 0$ meV) contribution. As discussed in the introduction (Sec. 1.6), at low Q the inelastic signal is mainly associated with acoustic vibrations and is governed by the high-frequency longitudinal sound velocity, which, as we will show, is only weakly affected (or not affected) by the irradiation-induced transformation. A stronger sensitivity to structural modifications is therefore expected in the elastic signal. Also, a small temperature drift of the crystals can slightly move the elastic peak during the measurements, which cannot be recentered because the entire energy spectrum is not acquired here.

The final verification of radiation-induced damage in germania concerns the structure factor. By varying the scattering angle, we can measure $I(E = 0, Q)$ at different Q values and compare it with the ID10 measurements of $I(Q)$. The comparison for room temperature and 550 °C is shown in Fig. 6.4. The points with error bars correspond to data acquired at ID28 with a 30 s integration time using analyzer 6, while the dashed lines represent the ID10 measurements at the corresponding temperatures (rescaled to approximately match the intensity). We also verified that the other two analyzers (a2 and a7), apart from a scaling factor, follow the same $I(E = 0, Q)$ behavior.

At low Q, the effect of the beamstop blocking the signal below approximately 0.15 Å^{-1} is clearly visible. The agreement with the ID10 data around the FSDP is not perfect, probably, as discussed befor, because in the present case we measure

20 A slight horizontal mismatch of the ID28 data might be present, as the photon flux is estimated rather than directly measured.

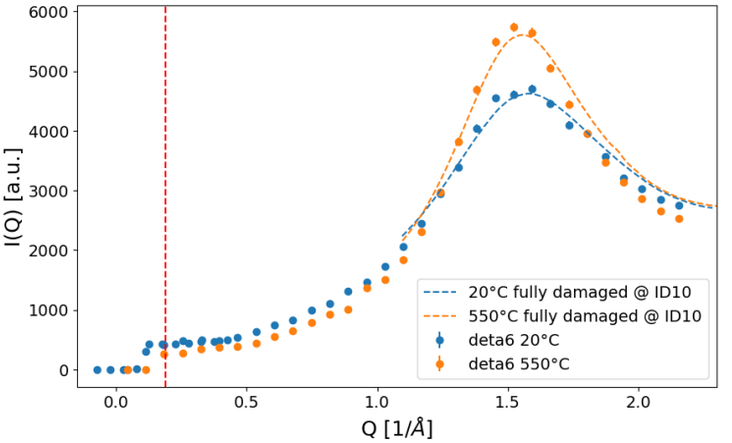

Figure 6.4: Comparison between the elastic scattering intensity $I(E = 0, Q)$ measured at ID28 and the structure factor $I(Q)$ measured at ID10. The points with error bars correspond to ID28 measurements (analyzer 6, 30 s integration time), while the dashed lines represent ID10 data at the same temperatures, rescaled for comparison. Measurements are shown for room temperature and 550 °C. The low-Q cutoff is due to the beamstop (around $Q \sim 0.15$ Å^{-1}).

only the elastic contribution ($E = 0$ meV), rather than integrating over all energies. Nevertheless, the comparison confirms that germania undergoes structural modifications under X-ray irradiation and, consistently with previous observations, that these modifications are more pronounced at lower irradiation temperatures.

We have therefore demonstrated that the complete transformation to the fully damaged state of germania can also be achieved at the IXS beamline ID28 within approximately half an hour of irradiation. In the following, all measurements are performed on fully irradiated samples; accordingly, an absorbed dose of ~ 300 MGy is delivered prior to each measurement.

6.1.5 Validity of the low-Q approximation at $Q = 0.2$ Å^{-1}

We briefly discuss the validity of the approximation—widely used in this work—of considering $Q \sim 0.2$ Å^{-1} sufficiently small to represent the low-Q limit. To do so, we refer to small-angle X-ray scattering measurements by Levelut *et al.* [Lev+05; Lev+07] on silica. As discussed in Fig. 1 of Ref. [Lev+05], for Q values in the range 0.2–0.6 Å^{-1}, the scattered intensity follows the empirical relation

$$I(Q) = I(Q = 0) \exp(bQ^2). \tag{6.1}$$

For silica, the parameter b is of the order of a few Å^{-2}, leading to a correction of approximately $\frac{I(0.2)-I(0)}{I(0)} \sim 5\%$. Although b is, in general, system-dependent, it typically falls within this order of magnitude [Lev+05], making the measurement at $Q = 0.2$ Å^{-1} a good approximation of $I(0)$.

More importantly, the parameter b shows no variation with sample preparation or temperature (both in the liquid and glassy phases), as shown in Fig. 1 of Ref. [Lev+05]. It therefore remains constant across different structural states of the same glass.

Since our measurements are expressed in arbitrary units and all data refer to germania measured at the same Q, the factor $\exp(bQ^2)$ can be absorbed into the overall intensity scale. As a result, the measured intensities can be directly interpreted as representative of the low-Q limit of the scattered intensity.

6.2 The inelastic spectra of germania

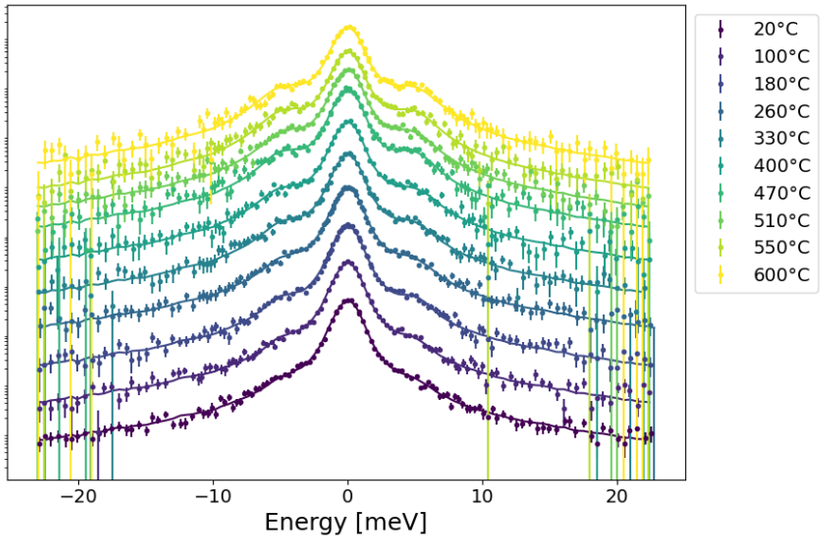

Figure 6.5: Inelastic spectra of vitreous GeO_2 measured at different temperatures and Q values (0.19, 0.34, and 0.49 Å^{-1}). The spectra are vertically shifted for clarity, from lower (bottom) to higher (top) temperature, and displayed on a logarithmic scale. Solid lines represent fits using the model described in the text.

Within this experiment, we measured the inelastic spectra at different temperatures for each of the three Q values corresponding to the analyzers, namely 0.19 Å^{-1},

0.34 Å^{-1}, and 0.49 Å^{-1}. A total of 10 temperatures were investigated, ranging from room temperature up to 600°C. At 640°C, the sample crystallizes. Each spectrum is obtained by summing four acquisitions, each with an integration time of 1 min per monochromator temperature, with temperature steps of 5 mK. Prior to summation, each individual acquisition is recentered to correct for systematic shifts arising from thermal fluctuations of the crystal analyzers and the monochromator. The spectra measured at these temperatures are shown in Fig. 6.5, vertically shifted for clarity and displayed on a logarithmic scale, with lower temperatures at the bottom and higher temperatures at the top. The solid lines represent the fitted models, which will be described in the following sections.

The inelastic spectra consist of a central peak, corresponding to low-frequency correlations, and two symmetric side peaks, which represent the longitudinal acoustic modes of the system [BY80]. In this analysis, we neglect the possible contribution of longitudinal–transverse mode coupling, assuming that the longitudinal acoustic modes dominate the inelastic scattering signal [Cun16].

6.2.1 Modeling of the inelastic spectra: elastic and DHO contributions

To model the measured inelastic spectra, we describe the dynamic structure factor $S(Q,E)$ as the sum of an elastic contribution and an inelastic component associated with longitudinal acoustic excitations.

The thermal population factor is introduced through the Bose distribution to account for the thermal asymmetry between the Stokes and anti-Stokes sides of the inelastic spectrum:

$$n(E) = \frac{1}{e^{\frac{E}{k_B T}} - 1}. \tag{6.2}$$

The inelastic contribution is modeled using a damped harmonic oscillator (DHO), which describes propagating density fluctuations [Buc14; BY80]

$$DHO(Q,E) = (n(E)+1)\frac{E}{k_B T}\frac{1}{\pi}\frac{2\Gamma(Q)\Omega(Q)^2}{\left(E^2 - \Omega(Q)^2\right)^2 + 4\Gamma(Q)^2E^2}. \tag{6.3}$$

Here, $\Omega(Q)$ represents the characteristic frequency of the acoustic mode, while $\Gamma(Q)$ is its damping coefficient. The term $(n(E)+1)\frac{E}{k_B T}$ ensures that the detailed balance condition,

$$\frac{S(Q,E)}{S(Q,-E)} = \exp\left(\frac{E}{k_B T}\right),$$

is satisfied, while preserving the continuity of the first derivative at $E = 0$.

The total dynamic structure factor is then written as:

$$S(Q,E) = A\Big[F_Q\,\delta(E) + (1 - F_Q)\,DHO(Q,E)\Big], \tag{6.4}$$

where A is an overall intensity scale and F_Q is the elastic fraction, i.e. the relative weight of the central (elastic) peak. As discussed by Scopigno *et al.* [Sco+03] and anticipated in the introduction, F_Q provides a measure of the high-frequency non-ergodicity factor f_Q. In the case of a strong glass such as germania, where secondary relaxation processes are absent or negligible, F_Q is therefore expected to coincide with the conventional (low-frequency) non-ergodicity factor.

Finally, to compare with the experimental spectra, the model is convoluted with the instrumental resolution function $R(E)$ dispayed in Fig. 6.1:

$$I(Q,E) = [S(Q,E)] \otimes R(E). \tag{6.5}$$

This model provides an effective description of the spectra, quantifying both the elastic contribution associated with frozen or slowly relaxing density fluctuations and the inelastic signal arising from longitudinal acoustic modes.

6.2.2 Extraction of dynamical parameters from the spectra

Each measured spectrum is independently fitted using the model described in the previous section. The free parameters are therefore A, F_Q, Ω, and Γ. No constraints on the parameters are required to obtain reliable results; consequently, the fitted parameters at different temperatures are fully uncorrelated and directly obtained from standard χ^2 minimization. The initial parameter guesses are identical for all temperatures and Q values, and are chosen as follows: the integral of the measured spectrum for A, $F_Q = 0.8$, $\Omega = 6$ meV, and $\Gamma = 2$ meV.

Examples of the fits are shown in Fig. 6.6 for room temperature (left column) and 600°C (right column), for the three Q values (0.19 Å^{-1}, 0.34 Å^{-1}, and 0.49 Å^{-1} from top to bottom). The y-axis is displayed on a logarithmic scale. The green dotted line represents the fitted resolution function (with area $A \cdot F_Q$), i.e. the convolution of the delta function with the instrumental resolution. The yellow dotted line corresponds to the DHO model, while the pink dotted line shows its convolution with the resolution function. Due to the smooth nature of the DHO, this convolution differs slightly from the analytical function. The final model is shown as a black solid line, and the residuals represent the difference between the data and the model, normalized by the standard deviation. In all displayed cases,

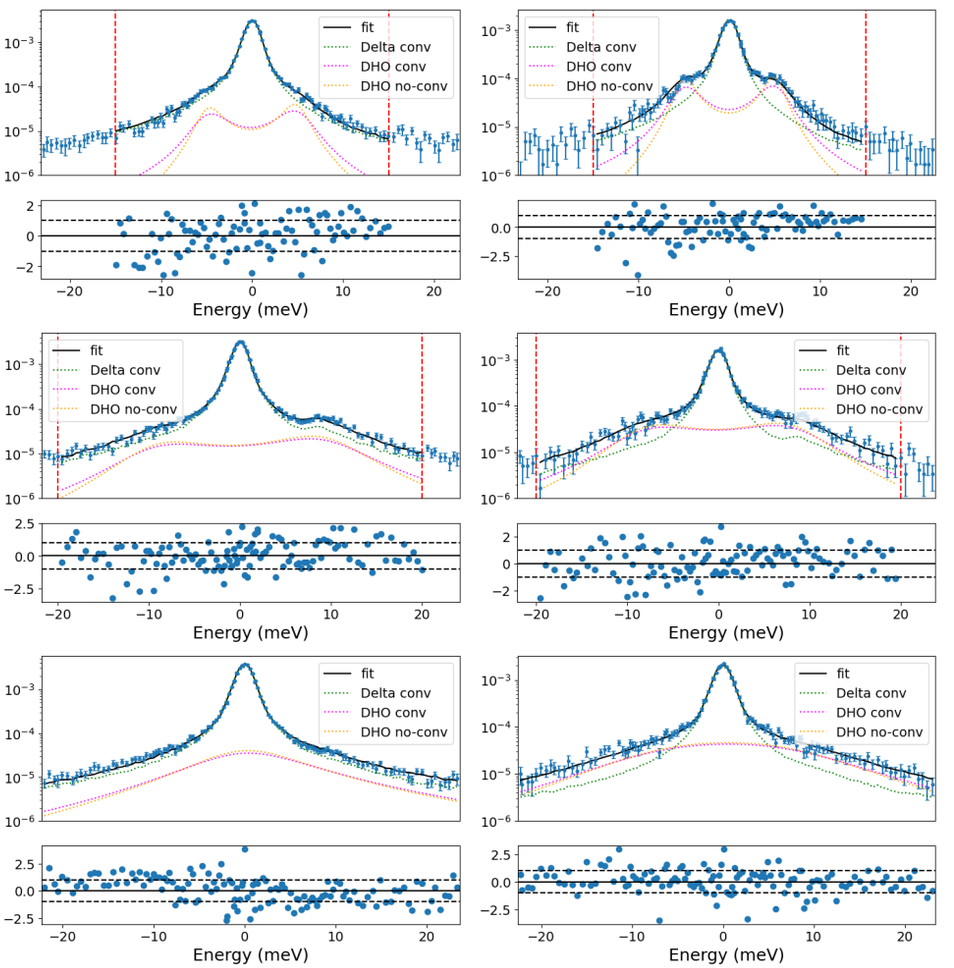

Figure 6.6: Examples of fits of the inelastic spectra at room temperature (left column) and 600°C (right column) for the three probed Q values: 0.19 Å^{-1} (top), 0.34 Å^{-1} (middle), and 0.49 Å^{-1} (bottom). The black solid line represents the total fit, the green dotted line the elastic contribution (resolution function), the yellow dotted line the DHO model, and the pink dotted line its convolution with the resolution. Residuals are shown below each spectrum.

the agreement between this simple model and the data is remarkable. The increase of the inelastic signal (i.e. the vibrational contribution) with temperature is clearly visible.

We also note the very small difference between the resolution function and the room-temperature data, which justifies the care devoted to empty-cell measurements and to achieving a symmetric and well-characterized resolution. In particular, the fits obtained with analyzer a2, which exhibits a non-symmetric resolution, are more difficult to interpret, and the presence of a small bump in the resolution function can be visually misleading.

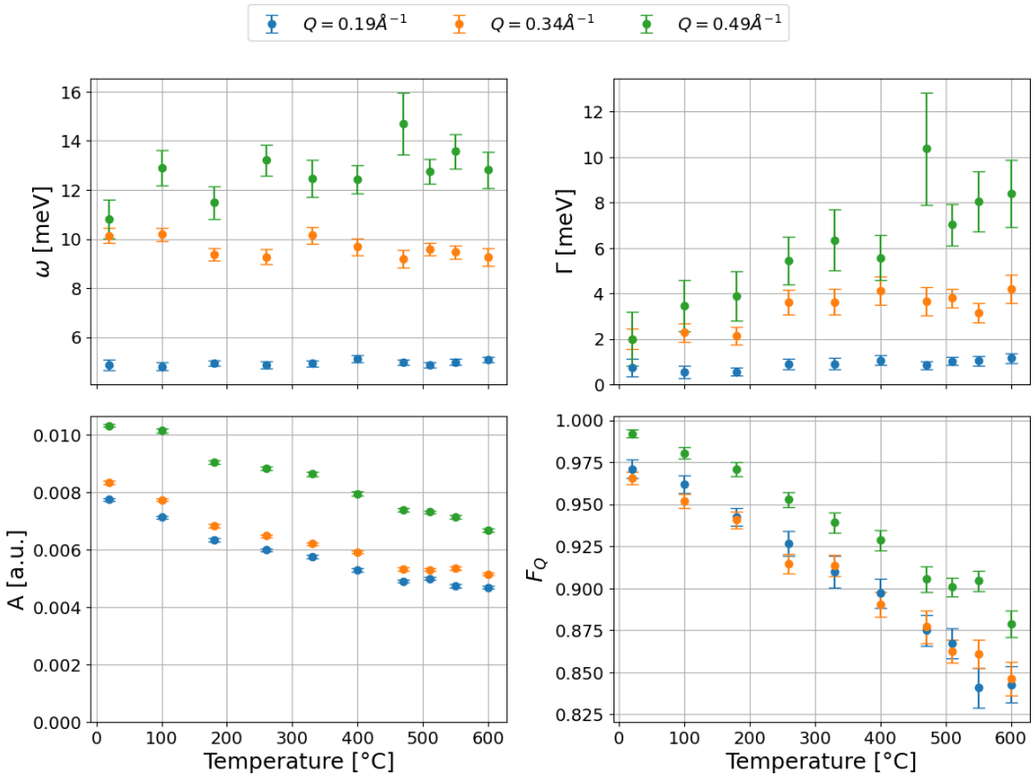

Figure 6.7: Temperature dependence of the fitted parameters for the three probed Q values.

The fitted parameters are summarized in Fig. 6.7. We recall that parameters at different temperatures are obtained independently and refer to the fully damaged state of germania irradiated at the corresponding temperature. The nearly constant behavior of the DHO frequency Ω as a function of temperature is significant. This anticipates that the derived longitudinal sound velocity will be essentially temperature independent. The parameter A, corresponding to the energy-integrated

scattered intensity $I(Q, E)$, exhibits the same trend observed in the ID10 measurements (Fig. 5.12): the lower the irradiation temperature, the larger the total small-angle scattering intensity of the fully damaged state.

Finally, the high-frequency non-ergodicity factor F_Q shows a decrease with increasing temperature, consistent with the behavior of the low-Q contrast measured at ID10. As already discussed, the correspondence between these quantities follows $f_Q \propto C^2$, and will be further addressed in Sec. 6.5.

6.3 The interpretation of the inelastic spectrum

In this section we interpretate the teperature dependences of the fitting parameters within our model presented in Fig. 6.7. The starting point is the measurement of the longitudinal velocity.

6.3.1 Temperature-independent sound velocity

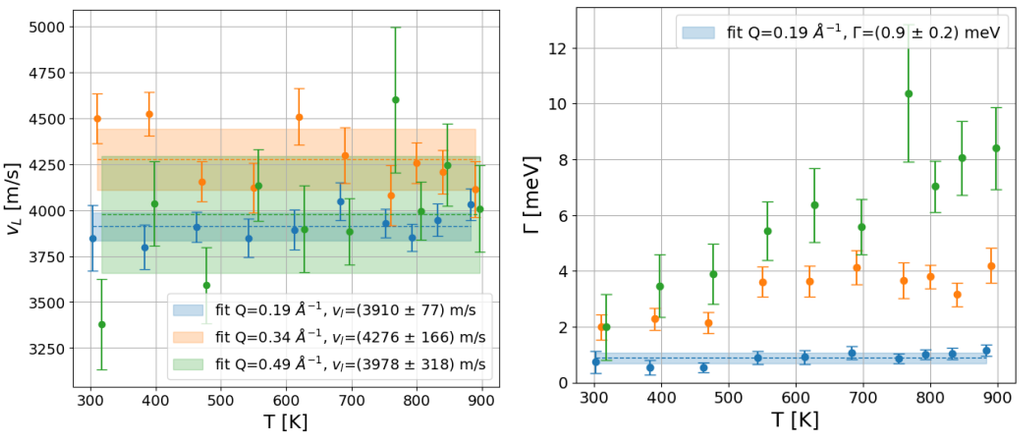

Figure 6.8: Left: Longitudinal sound velocity v_s extracted from the DHO peak position $\Omega(Q)$ as a function of temperature for the three probed Q values. Horizontal dashed lines represent the temperature-averaged values, while shaded areas indicate the corresponding standard deviations. Right: Temperature-averaged damping parameter $\Gamma(Q)$ as a function of Q, showing the expected increase with increasing Q.

The speed of sound is obtained from the dispersion relation of the acoustic phonon:

$$v_s = \frac{1}{\hbar}\frac{d\Omega}{dQ}. \tag{6.6}$$

In the present case, it can be approximated as the ratio between the fitted DHO peak position Ω and the corresponding Q value. For a dispersive propagation, this ratio is expected to be independent of Q, as in the case of low-frequency longitudinal sound, where all frequencies propagate at the same velocity.

The sound velocity is usually expressed in m/s rather than in meV Å. By expressing $\hbar$ in meV·s, the conversion becomes:

$$v_s\ [\mathrm{m/s}] \approx 152\,\frac{\Omega\ [\mathrm{meV}]}{Q\ [\mathrm{\AA}^{-1}]}. \tag{6.7}$$

The left panel of Fig. 6.8 shows the sound velocity extracted at each temperature. No significant temperature dependence of the longitudinal sound velocity is observed. We therefore determine a temperature-independent value by averaging over all temperatures. The corresponding standard deviations are shown as shaded areas, while the average values are indicated by horizontal dashed lines. The resulting velocities at the three different Qs, reported in the legend, are consistent within about one standard deviation, indicating that the dispersion relation is linear within experimental uncertainty.

As a reference value for the fully damaged state of germania, we consider the result obtained at $Q = 0.19$ Å^{-1}, where collective modes are more clearly defined, the resolution function is optimal, and the fitted parameters exhibit the smallest uncertainties. From this measurement, we obtain a longitudinal sound velocity of (3910 ± 77) m/s.

This value is consistent with previous inelastic neutron scattering measurements by L. E. Bove *et al.* [Bov+05], who reported $v_L^{\infty} \sim (3650 \pm 1000)$ m/s. In that work, a non-dispersive feature attributed to a transverse mode was also observed, becoming distinguishable from the longitudinal mode at higher Q. In our measurements, as indicated by the good agreement of the fits (Fig. 6.6), no additional modes are required to describe the data. The observation of such transverse modes with X-rays would likely require measurements at higher Q, where the separation between longitudinal and transverse excitations is larger. Moreover, the radiation-induced modifications of germania, which enhance the elastic peak, may further mask a weak transverse contribution located at low energies [Bov+05]. Also, the value we found is consistent with Brillouin light scattering measurements of the high-frequency longitudinal sound velocity reported by [Ana+08] that shows a weak temperature dependence within our temperature region with an average value of ~ 3750 m/s (see Fig. 4 from Ref. [Ana+08]).

Finally, the right panel of Fig. 6.8 shows the temperature-averaged DHO damping parameter Γ. The lowest Q measurement shows a temperature independent value

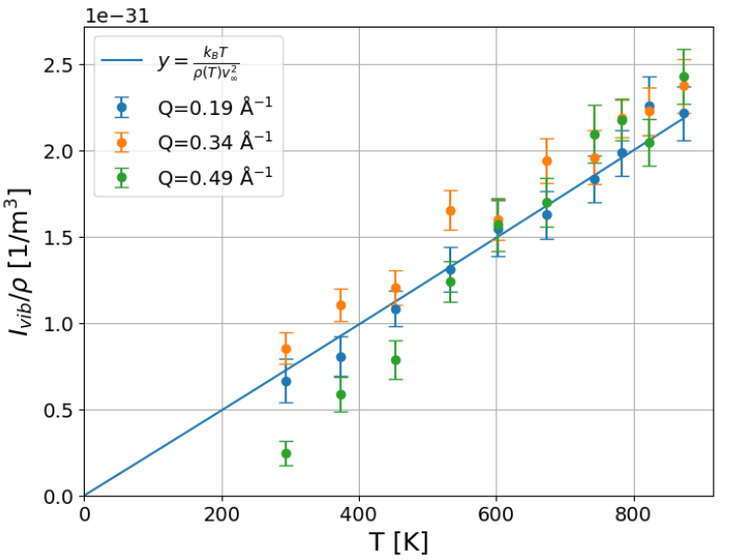

Figure 6.9: Temperature dependence of the vibrational contribution to the scattered intensity, $A(1 - F_Q)$, for the three probed Q values. For $Q = 0.19$ Å^{-1}, the data follow a linear trend passing through the origin, as expected from the vibrational contribution to density fluctuations. The slope is constrained to $\propto k_B/(\rho v_L^2)$, allowing calibration of the intensity scale in absolute units (m^{-3}).

of $\Gamma = (0.9 \pm 0.2)$ meV. Also at $Q = 0.34$ Å^{-1} displays an almost constant value, while the highest Q measurement shows an increase of Γ with temperature. This behavior may be attributed to the limited energy range of the measurements compared to the dispersion of the collective modes at high Q. As shown in Fig. 6.6, at $Q = 0.49$ Å^{-1} the collective modes are no longer well resolved, resulting in strong correlations among the fit parameters.

6.3.2 Using vibrations to calibrate the scattered intensity

We have established that the high-frequency longitudinal sound velocity of the fully damaged state of germania—whose behavior is comparable to that of pristine vitreous germania at room temperature—is $v_L^\infty \simeq 4000$ m/s and is independent of temperature. We also know the initial density of germania (~ 3.6 g/cm^3) and have shown that irradiation induces only a small densification, of the order of 1%.

As discussed in the introductory chapter, vibrational dynamics govern density fluctuations, and thus the low-Q scattered intensity in the glassy state (see Eq. 1.26). In this framework, the frozen-in contribution is expected to remain constant for a

standard glass, while the vibrational contribution scales as

$$k_B T \frac{1}{\rho v_L^2}.$$

Since the density varies only weakly with temperature (due to the small differences in irradiation-induced densification), and v_L^∞ remains constant, a linear dependence of the integrated inelastic signal on temperature is expected, with zero intercept. Within our model, this quantity corresponds to the vibrational contribution

$$A(1 - F_Q).$$

Figure 6.9 shows $A(1 - F_Q)$ as a function of temperature. The expected linear behavior is clearly observed for $Q = 0.19$ Å^{-1}, where the data follow a straight line passing through the origin.

By constraining the slope of this linear dependence to be proportional to $\frac{k_B}{\rho v_L^2}$, and including the additional density prefactor appearing in Eq. 1.26, we can calibrate the intensity scale and express it in absolute units (m^{-3}), as shown in the figure. This calibration will be useful in the next section, where we compare our results quantitatively with literature values of the compressibility.

6.4 Density fluctuations in fully damaged GeO_2

The central result of this analysis is the separation of the scattered signal into contributions arising from frozen-in and vibrational density fluctuations. The calibration procedure described in the previous section allows us to express the scattered intensity in absolute units. In particular, by plotting the intensity divided by $k_B T \rho$, as prescribed by Eq. 1.18, we express the data in compressibility units (m^2/N).

Figure 6.10 shows the total (blue dots), elastic (orange squares), and inelastic (green triangles) contributions to the scattered intensity. These quantities are obtained from the fit parameters as A, $A \cdot F_Q$, and $A \cdot (1 - F_Q)$, respectively. The orange horizontal line represents the elastic intensity of the pristine glass measured in Fig. 6.3, while the green dashed line corresponds to the linear fit of the vibrational contribution shown in Fig. 6.9.

The overall behavior of the total scattered intensity is consistent with that observed in the ID10 experiment (Fig. 5.12). However, the relative variation of the SAXS intensity with irradiation temperature between room temperature and T_g is approximately 15% larger than in the ID10 measurements. At present, we do

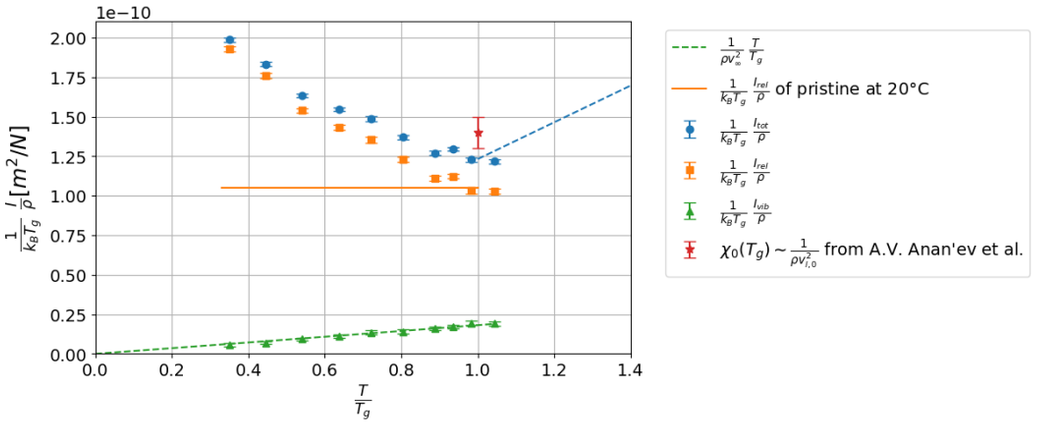

Figure 6.10: Total, elastic, and inelastic contributions to the low-Q scattered intensity of fully irradiated GeO_2, expressed in compressibility units (m^2/N). Blue dots represent the total intensity (A), orange squares the elastic (frozen-in) contribution ($A \cdot F_Q$), and green triangles the inelastic (vibrational) contribution ($A \cdot (1 - F_Q)$). The orange horizontal line indicates the elastic intensity of the pristine glass (estimated from Fig. 6.3), while the green dashed line corresponds to the linear temperature dependence of the vibrational contribution (Fig. 6.9). The blue-dashed line is the extrapolation of the intensity within the supercooled liquid fixed by the value of the small angle intensity at T_g, as, whithin the SCL regime, $I(0) \propto T$ (see Sec. 1.18).

not have a clear explanation for this discrepancy. One possible origin may be the different X-ray energies used in the two experiments, particularly in relation to the Ge K_α edge at 11.1 keV, which could lead to slightly different defect populations and, consequently, to structural differences.

Overall, as previously discussed, irradiation increases the frozen-in density fluctuations from the pristine to the fully damaged state. Assuming the validity of Eq. 1.26, the frozen-in density fluctuations of the pristine glass at room temperature (orange line) remain essentially unchanged below T_g. This confirms the previously proposed picture: the lower the irradiation temperature, the larger the structural modifications, and hence the greater the increase in small-angle density fluctuations. Conversely, close to T_g, where thermal structural relaxation becomes significant, irradiation produces negligible additional frozen-in density fluctuations, and the fully irradiated structure remains essentially unchanged.

Figure 6.10 also reports the isothermal compressibility at the glass transition estimated by A. V. Anan'ev *et al.* [Ana+08], obtained from the low-frequency longitudinal sound velocity as $\chi(T_g) = 1/(\rho v_{L,0}^2)$, where $v_{L,0}$ is measured by Brillouin light scattering. Assuming that the increase in frozen-in density fluctuations is

negligible around T_g, consistently with the data, we obtain $\chi(T_g) \sim 1.24{\times}10^{-10}$ m^2/N, compatible with the value $(1.4 \pm 0.1) \times 10^{-10}$ m^2/N reported in Ref. [Ana+08].

The damage process and the fictive temperature

Following the discussion in Chapter 1 on the dependence of frozen-in density fluctuations of the melt-quenched glass on the fictive temperature (see Fig. 1.7), it is natural to interpret the X-ray–induced structural transformation in these terms. Also, we have seen that in supercooled liquids, intrinsic defects (Schottky and Frenkel defects) are naturally present, with concentrations governed by Boltzmann statistics (Eqs. 4.1 and 4.2). Their concentration increases with temperature and, upon quenching to form the glass, the defects present at the fictive temperature T_f become frozen into the structure.

As shown in Chapter 5, irradiation produces defects in the glass matrix up to a saturation level, where defects are continuously created and annihilated by radiation. We have also demonstrated that thermal annealing does not play a significant role under these conditions, and that the structural transformations are entirely driven by irradiation. The fully defected structure shows a broadening and a reduction of the FSDP, indicating an increase in structural disorder at the medium-range scale. Also, as discussed in Sec. 4.6, Baglioni *et al.* [Bag+24] showed that in $GeSe_3$ the enthalpy increases under irradiation, and the structure evolves toward that of a glass with a fictive temperature of about $1.2\,T_g$, independently of the initial state.

In our case, while the vibrational contribution to density fluctuations remains essentially unchanged, consistent with the unchanged high-frequency sound velocity, the frozen-in contribution increases significantly under irradiation. This suggests the following interpretation: X-ray irradiation increases the defect concentration, driving the glass toward a state analogous to that obtained by quenching a supercooled liquid from higher temperatures, i.e. a higher fictive temperature T_f. Although the defects generated by irradiation may differ in nature or distribution from those frozen in during conventional quenching (see Sec. 4.1), their macroscopic effects on structure, density fluctuations, and enthalpy [Bag+24] are similar. This interpretation is further supported by molecular dynamics simulations by Krishnan *et al.* [Kri+17], which show that neutron irradiation drives quartz toward an amorphous state resembling high-fictive-temperature silica with $T_f = 4400$ K).

A key observation is that the irradiation temperature controls the final state of the glass. Lower irradiation temperatures lead to larger modifications and thus correspond to higher effective fictive temperatures. Conversely, increasing the irradiation temperature leads to progressively less modified structures, with the

fictive temperature approaching T_g. At, or slightly above, the glass transition, the fully irradiated state becomes equivalent to the supercooled liquid, where intrinsic thermal dynamics dominate.

The measurement of density fluctuations provided in Fig. 6.10 allows us to estimate the fictive temperature of the corresponding melt-quenched liquid. The blue dashed line represents the extrapolated behavior of the scattered signal in the supercooled liquid phase, assuming the linear increase with temperature $I \propto T$ (see Sec. 1.6) and imposing the continuity with the glassy regime at T_g which fixes the slop. This proportionality constant, following the framework presented in Sec. 1.6, in the SCL is linked to the low-frequency sound velocity as $I(0) = \rho(\rho v_{L,0}^2)^{-1} K_b T$. Forcing the blue dashed line to pass through the intensity at T_g is equivalent to assume a low frequency sound velocity of $\sim$ 1500 m/s. This value is close to the extrapolated value from high temperature measured by ultrasonic measurements reported in [Ana+08] of about 1400 m/s.

Unfortunately, this liquid regime could not be directly accessed due to sample crystallization. A direct measurement would have allowed us to determine the slope of the density fluctuation curve in the supercooled liquid without relying on an estimation. Nevertheless, this extrapolation leads to a remarkable result: the negative slope of the increase in density fluctuations induced by irradiation within the glass is comparable in modulus to the natural increase observed in the supercooled liquid phase. This suggests a direct correspondence between the irradiation-induced structural modifications and the thermally driven evolution of the liquid. Within this framework, the difference $T_g - T_f$ can be used to estimate the fictive temperature associated with the fully damaged state. In particular, fully irradiated germania at room temperature corresponds to a melt-quenched glass with a fictive temperature on the order of the melting temperature ($T_m \sim 1350$ K).

We conclude that low-temperature irradiation drives germania into states analogous to hyperquenched glasses, effectively enabling the production of configurations comparable to those obtained by direct quenching from the liquid.

6.5 Non-ergodicity factor from ps to ms timescale

We conclude this chapter, and this thesis, with a comparison between the dynamics measured by IXS and XPCS. These two techniques probe a similar dynamical quantity in different domains: the frequency domain and the time domain, respectively. The two observables introduced, $S(Q, E)$ and $F(Q, t)$, are related by a Fourier transform, which preserves the integral of the signal.

The non-ergodicity factor defined in Eq. 1.15 can therefore be evaluated in two

complementary ways. In XPCS experiments, which measure the square of the intermediate scattering function, we have seen it is directly related to the measured contrast C_Q through

$$C_Q = \beta(Q) f_Q^2,$$

where $\beta(Q)$ is a beamline-dependent constant. In our XPCS measurements, particular care was taken to keep $\beta(Q)$ constant with temperature. As a result, f_Q is proportional to $\sqrt{C_Q}$, with a proportionality factor independent of temperature. In the time domain, f_Q quantifies the relative contribution of fast decorrelation processes (such as vibrations) with respect to structural relaxation, with a timescale threshold in the ms-to-hours range.

In IXS experiments, an analogous quantity can be defined as the ratio between the elastic scattered intensity and the total scattered intensity. In our analysis, this is directly given by the fit parameter F_Q, which measures the fraction of correlations associated with static or quasi-static processes relative to the total. Since the Fourier transform preserves integrals, this definition is equivalent to that of f_Q, with the main difference being the probed timescale. In IXS, the instrumental resolution is of the order of meV, corresponding to a threshold in the ps range [Sco+03].

Figure 6.11 shows the comparison between F_Q obtained from IXS measurements (blue points, left axis) and the square root of the contrast $\sqrt{C_Q}$ measured by XPCS (orange points, right axis) as a function of temperature. The contrast could not be measured in absolute units, as the beamline contrast $\beta(Q)$ is not known and is difficult to estimate reliably. An experimental determination might be possible, for example, by using a cryostat to suppress vibrational contributions.

The figure clearly demonstrates the correspondence between the decrease of the non-ergodicity factor measured by IXS and the decrease of the contrast measured by XPCS. Apart from an overall proportionality factor, the agreement between $F_Q(T)$ and $\sqrt{C_Q(T)}$ is remarkable. This represents the first demonstration that XPCS can access the temperature dependence of the non-ergodicity factor in glasses.

The observed proportionality is consistent with the fact that germania is a strong glass, where secondary relaxation processes, occurring with intermediate time scales between vibrations and structural relaxation, have a very small weight, involving only small fraction of atoms. It would be particularly interesting to perform the same comparison on a fragile glass: if secondary relaxation processes exhibit a non-trivial temperature dependence similar to that of vibrational contributions, the proportionality between F_Q and $\sqrt{C_Q}$ would likely break down.

Finally, we note that this comparison has been performed on the fully damaged state of germania, rather than on the pristine glass. Performing the same measurement on the pristine glass would be extremely challenging, as it would require

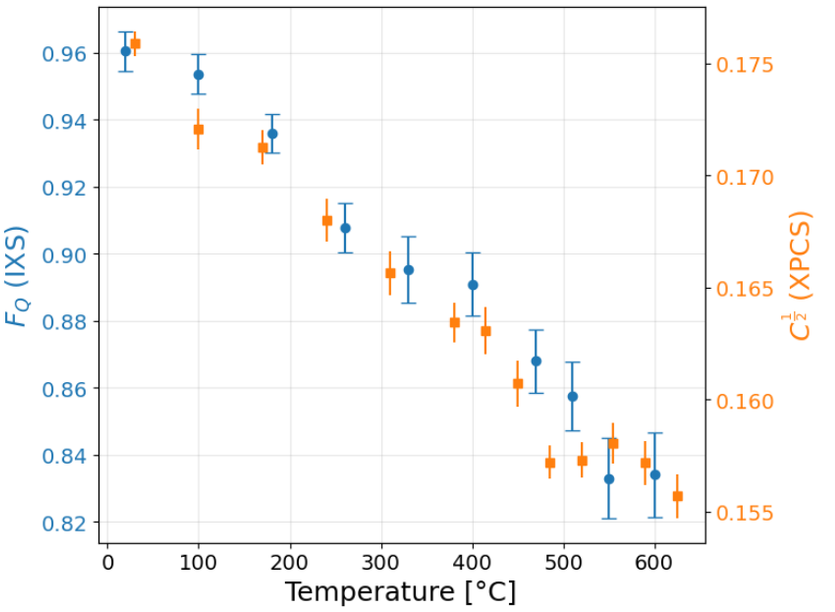

Figure 6.11: Comparison between the non-ergodicity factor measured by IXS and XPCS. Blue points (left axis) represent the elastic fraction F_Q obtained from IXS fits, while orange points (right axis) show the square root of the XPCS contrast, $\sqrt{C_Q}$, measured at low Q for different temperatures. Although the absolute scale of $\sqrt{C_Q}$ is not accessible due to the unknown beamline contrast, the two quantities exhibit the same temperature dependence, demonstrating their proportionality and confirming their common physical origin across different timescales.

limiting the absorbed dose to only a few MGy. Such experiments may instead be feasible on oxide glasses that are less sensitive to radiation damage, such as silica, which exhibits significantly slower irradiation-induced transformations [Alf24].

Conclusions

This thesis has presented a detailed investigation of the beam-induced dynamics and structural transformations of the strong glass former vitreous GeO_2 under X-ray irradiation. The observation that X-ray irradiation can trigger atomic rearrangements in disordered systems was first reported by Ruta *et al.* in 2017 [Rut+17]. In oxide and chalcogenide glasses, the absorption of photons leads to the formation of localized defects through radiolysis; the continuous creation and recombination of these defects can drive cooperative atomic rearrangements at the nanoscale. This induced dynamics is accompanied by a structural evolution of the glass, which, under irradiation, evolves toward a stationary state characterized by a well-defined structure, as recently reported by Baglioni *et al.* [Bag+24].

We used XPCS and IXS experiments to probe the X-ray induced transitions in vitreous GeO_2. The dynamics measured by XPCS demonstrate that, under continuous irradiation, the pristine glass initially exhibits non-stationary dynamics. During the first minutes of beam exposure, the beam-induced relaxation progressively slows down. After accumulating an absorbed dose of approximately 300 MGy, the system reaches a stationary state, referred to as the "fully damaged" or "fully irradiated" glass. In this regime, the dynamics stabilize, and the intensity autocorrelation function is well described by a stretched-exponential Kohlrausch-Williams-Watts (KWW) behavior over several decades in time.

Addressing this physical result has been possible thanks to two main data-analysis improvements. A novel multi-tau algorithm was introduced to compute the two-time correlation function (MT-2TC) and the intensity autocorrelation function. By computing the two-time correlation matrices (TTC) in quasi-logarithmic spacing in lag time, this method overcomes the severe memory limitations inherent to standard linear representations. This computational advancement extends the accessible time window by different decades and significantly improves the signal-to-noise ratio, particularly at long lag times. Crucially, it allows access to the regime of low lag-time to resolve the plateau preceding the initial decay. In addition, we implemented new detector corrections to accurately process the raw data. By applying a thresholding protocol to the flux distribution, we isolated anomalous, out-of-average pixels originating from detector-related hardware effects. Filtering out these structured patterns allowed us to successfully recover the expected Gaussian flux-per-pixel distribution, which is essential for accurate low-signal measurements.

This dynamic transition is coupled with a structural evolution. At room temperature, the structural transformation exhibits an exponential-like modification, saturating after about the same 300 MGy of absorbed dose. During this phase, the First Sharp Diffraction Peak (FSDP) widens by about 30%, reflecting an increase in medium-range disorder. Concurrently, the FSDP shifts to higher momentum transfer (Q) by approximately 1.3%, indicating an irradiation-induced densification of the glass matrix, while its height decreases. Conversely, low-Q measurements reveal an intensity increase of approximately 40%, which corresponds to an increase of spatial density fluctuations. Once the fully damaged state is reached, the structure becomes stationary. This state indicates that the rates of radiation-induced defect production and defect annihilation have reached a steady state.

Beyond the room-temperature behavior, the characteristics of the fully irradiated state exhibit a systematic dependence on the irradiation temperature. By investigating the system between room temperature and 100 K above the glass transition temperature, we established that the final stationary state is not unique, but its structural and dynamical properties are dictated by the sample temperature during X-ray irradiation. Structurally, the extent of the beam-induced modifications is inversely related to the temperature: irradiating the glass at lower temperatures results in a greater amplification of the spatial density fluctuations at low Q and a larger modification of the FSDP profile. Differently, dynamically, the steady-state relaxation time τ and the stretching exponent β extracted from the KWW model show little variation with temperature till, as already reported in literature, the standard thermal relaxation becomes faster than the beam-induced relaxation.

We also investigated the stability of this irradiated structure. The fully damaged state is stable in the glassy phase: once the X-ray induced transformation at a certain temperature is completed and the X-ray beam is switched off, the glass does not recover its pristine state. Instead, it preserves the irradiated structure, therefore its saturated defect concentration. This demonstrates that thermal annealing does not play a dominant role in governing defect annihilation in the glassy state: the saturation mechanism is instead dominated by radiation-induced processes. Only at temperatures close to or above the glass transition temperature (T_g), where intrinsic thermal structural relaxation becomes comparable to the experimental timescale, thermal annealing becomes effective, leading to a partial structural recovery toward the pristine structure. Furthermore, temperature-cycling experiments have shown that the structural transformation toward a temperature-specific, fully damaged state occurs only under irradiation, and that this fully irradiated state is independent of the sample's thermal and irradiation history.

Finally, Inelastic X-ray Scattering (IXS) measurements at small angles allowed us to disentangle the scattered signal into elastic (frozen-in) and inelastic (propagating

vibrational) density fluctuations. Modeled using a damped harmonic oscillator, the IXS results are consistent with the low-Q XPCS observations. They show that X-ray irradiation increases the frozen-in density fluctuations during the transition from the pristine to the fully damaged state, while vibrational density-fluctuations are not altered. As previously observed, the increase of density fluctuations from the pristine glass is higher the lower the irradiation temperature, in accordance with XPCS results.

We explained the temperature dependence of the fully irradiated state building a parallel with the standard melt-quenched glass with different fictive temperature, as discussed in the final chapter. As supported by Baglioni et al. [Bag+24], the fully irradiated structure, characterized by increased medium-range disorder (a broader FSDP) and enhanced spatial density fluctuations, resembles a glass quenched from a fictive temperature significantly higher than that of the pristine material ($T_f \sim T_g$). In a standard melt-quenching process, higher temperatures correspond to a larger concentration of equilibrium defects, which become frozen into the network upon cooling. Although the microscopic nature of X-ray-induced defects may differ from those generated purely thermally, their impact on the structure is remarkably similar. Continuous irradiation, therefore, drives the glass toward a unique stationary state that is exclusively controlled by the irradiation temperature. Because lower irradiation temperatures produce more pronounced structural changes, they correspond to a higher saturated defect concentration and, consequently, a higher effective fictive temperature. Specifically, irradiating the glass at room temperature yields a highly disordered structure analogous to a melt quenched from near its melting point ($T_f \sim T_m$). Conversely, irradiation close to the glass transition temperature does not significantly alter the glass network, leaving the effective fictive temperature of the final state close to that of the pristine glass.

We concluded the work by comparing the non-ergodicity factor measured by IXS with the speckle contrast measured by XPCS. The data show that the decrease with temperature of the non-ergodicity factor measured by IXS corresponds to the decrease of the square root of the contrast measured by XPCS. Apart from an overall proportionality factor due to the non-absolute measurement of the XPCS contrast, the scaling between $F_Q(T)$ and $\sqrt{C_Q(T)}$ is consistent. This direct proportionality holds because vitreous GeO_2 is a strong glass former. In this system, secondary relaxation processes, which occur on intermediate time scales between vibrations and structural relaxation, have a very small weight and involve only a small fraction of atoms. Ultimately, this demonstrates, for the first time, that XPCS can effectively access the temperature dependence of the non-ergodicity factor in glasses.

Extending this comparison to fragile glasses would be a natural next step. In fragile systems, secondary relaxations are more prominent and have their own

temperature dependencies. As a result, the direct proportionality between F_Q and $\sqrt{C_Q}$ is expected to break down, which could offer a new way to isolate these intermediate dynamics. Furthermore, it would be interesting to perform this measurement on systems that are not susceptible to X-ray damage, or where data can be collected fast enough before the beam-induced transformation occurs. This would allow us to test this relationship directly in the pristine glass, rather than in the fully damaged state, and to understand whether the X-ray induced transformation significantly alters the non-ergodicity of the glass.

Bibliography

[Ae13] Yoichi Aso and etal. **Interferometer design of the KAGRA gravitational wave detector**. *Phys. Rev. D* 88 (4 Aug. 2013), 043007. DOI: 10.1103/PhysRevD.88.043007. URL: https://link.aps.org/doi/10.1103/PhysRevD.88.043007 (see page 61).

[Ae14] F Acernese and etal. **Advanced Virgo: a second-generation interferometric gravitational wave detector**. *Classical and Quantum Gravity* 32:2 (Dec. 2014), 024001. DOI: 10.1088/0264-9381/32/2/024001. URL: https://doi.org/10.1088/0264-9381/32/2/024001 (see page 61).

[Ae15] J Aasi and etal. **Advanced LIGO**. *Classical and Quantum Gravity* 32:7 (Mar. 2015), 074001. DOI: 10.1088/0264-9381/32/7/074001. URL: https://doi.org/10.1088/0264-9381/32/7/074001 (see page 61).

[AG65a] Gerold Adam and Julian H Gibbs. **On the temperature dependence of cooperative relaxation properties in glass-forming liquids**. *The journal of chemical physics* 43:1 (1965), 139–146 (see page 16).

[AG65b] Gerold Adam and Julian H. Gibbs. **On the temperature dependence of cooperative relaxation properties in glass-forming liquids**. *The Journal of Chemical Physics* 43:1 (July 1965), 139–146. DOI: 10.1063/1.1696442 (see page 13).

[Alf+23] E. Alfinelli, F. Caporaletti, F. Dallari, A. Martinelli, G. Monaco, B. Ruta, M. Sprung, M. Zanatta, and G. Baldi. **Amorphous-amorphous transformation induced in glasses by intense x-ray beams**. *Physical Review B* 107 (2023), 054202. DOI: 10.1103/PhysRevB.107.054202 (see pages 100, 101, 113, 118).

[Alf24] Erica Alfinelli. **The effect of intense x-ray beams on oxide glasses unveiled by means of photon correlation spectroscopy**. Doctoral School in Physics, XXXVI Cycle. PhD thesis. Trento, Italy: Università degli Studi di Trento, 2024 (see page 156).

[Ana+08] A.V. Anan'ev, V.N. Bogdanov, B. Champagnon, M. Ferrari, G.O. Karapetyan, L.V. Maksimov, S.N. Smerdin, and V.A. Solovyev. **Origin of Rayleigh scattering and anomaly of elastic properties in vitreous and molten GeO2**. *Journal of Non-Crystalline Solids* 354:26 (2008), 3049–3058. ISSN: 0022-3093. DOI: 10.1016/j.jnoncrysol.2007.12.008. URL: https://www.sciencedirect.com/science/article/pii/S0022309308000264 (see pages 19, 149, 152–154).

[Ang85] C. A. Angell. “Strong and fragile liquids.” In: *Relaxations in Complex Systems*. Ed. by K. L. Ngai and G. B. Wright. Springfield, VA: National Technical Information Service, 1985, 3–11 (see page 22).

[Ang95] Charles A Angell. **Formation of glasses from liquids and biopolymers**. *Science* 267:5206 (1995), 1924–1935 (see pages 1–5).

[Ash+15] Giannis Ashiotis, Aurore Deschildre, Zubair Nawaz, Jonathan P. Wright, Dimitrios Karkoulis, Frédéric Emmanuel Picca, and Jérôme Kieffer. **The fast azimuthal integration Python library: pyFAI**. *Journal of Applied Crystallography* 48:2 (Apr. 2015), 510–519. DOI: 10.1107/S1600576715004306. URL: https://doi.org/10.1107/S1600576715004306 (see page 37).

[Bag+24] J. Baglioni, A. Martinelli, P. Sun, F. Dallari, F. Westermeier, M. Sprung, G. Grübel, and G. Monaco. **Uniqueness of glasses prepared via x-ray induced yielding**. *Reports on Progress in Physics* 87 (2024), 120503. DOI: 10.1088/1361-6633/ad91df (see pages 7, 102, 119, 127, 129, 132, 153, 157, 159).

[BB11] Ludovic Berthier and Giulio Biroli. **Theoretical perspective on the glass transition and amorphous materials**. *Reviews of modern physics* 83:2 (2011), 587 (see page 15).

[BH88] Ned E. Bibler and David G. Howitt. **Radiation Effects in Silicate Glasses - A Review**. *MRS Online Proceedings Library* 125:1 (1988), 263–284. ISSN: 1946-4274. DOI: 10.1557/PROC-125-263. URL: https://doi.org/10.1557/PROC-125-263 (see page 97).

[Bik17] Oier Bikondoa. **On the use of two-time correlation functions for X-ray photon correlation spectroscopy data analysis**. *Journal of Applied Crystallography* 50:2 (Apr. 2017), 357–368. DOI: 10.1107/S1600576717000577. URL: https://doi.org/10.1107/S1600576717000577 (see pages 50–52, 54).

[BK71] Werner H. Baur and Aijaz A. Khan. **Rutile-type compounds. IV. SiO_2, GeO_2 and a comparison with other rutile-type structures**. *Acta Crystallographica Section B: Structural Crystallography and Crystal Chemistry* 27:11 (1971), 2133–2139. DOI: 10.1107/S0567740871005398 (see page 22).

[Böh+93] Roland Böhmer, K. L. Ngai, C. A. Angell, and D. J. Plazek. **Nonexponential relaxations in strong and fragile glass formers**. *The Journal of Chemical Physics* 99:5 (1993), 4201–4209. DOI: 10.1063/1.466117 (see page 22).

[Bou08] Jean-Philippe Bouchaud. “Anomalous relaxation in complex systems: from stretched to compressed exponentials.” In: *Anomalous transport: foundations and applications*. Wiley Online Library, 2008, 327–345 (see pages 4, 11).

[Bov+05] L. E. Bove, E. Fabiani, A. Fontana, F. Paoletti, C. Petrillo, O. Pilla, and I. C. V. Bento. **Brillouin neutron scattering of v-GeO2**. *Europhysics Letters* 71:4 (July 2005), 563. DOI: 10.1209/epl/i2005-10125-0. URL: https://doi.org/10.1209/epl/i2005-10125-0 (see page 149).

[BP] R. Bartolini and Pduive23. *Synchrotron radiation schematic*. https://commons.wikimedia.org/w/index.php?curid=153996751. CC BY 3.0 (see page 41).

[Bru+26] Fabio Brugnara, Marco Cammarata, Yuriy Chushkin, Irene Festi, Massimo Granata, David Hofman, Matteo Leonardi, Daniele Marzi, Denis Nabari, Angela Trapananti, Simone Ziglio, Federico Zontone, Marco Zanatta, and Giacomo Baldi. **Time-resolved XPCS analysis across broad time-scales using multi-tau two-time correlations**. *Journal of Synchrotron Radiation* 33:3 (May 2026). DOI: 10.1107/S1600577526002171. URL: https://doi.org/10.1107/S1600577526002171 (see page 50).

[BSG70] Harold D. Bale, Robert E. Shepler, and Garry W. Gibbs. **X-Ray Diffraction from Neutron Irradiated Vitreous Silica**. *Journal of Applied Physics* 41:1 (Jan. 1970), 241–246. ISSN: 0021-8979. DOI: 10.1063/1.1658328. eprint: https://pubs.aip.org/aip/jap/article-pdf/41/1/241/18352347/241_1_online.pdf. URL: https://doi.org/10.1063/1.1658328 (see pages 94, 95, 118).

[Buc14] U. Buchenau. **Evaluation of x-ray Brillouin scattering data**. *Phys. Rev. E* 90 (6 Dec. 2014), 062319. DOI: 10.1103/PhysRevE.90.062319. URL: https://link.aps.org/doi/10.1103/PhysRevE.90.062319 (see page 144).

[BY80] Jean-Pierre Boon and Sidney Yip. **Molecular Hydrodynamics**. Reprinted by Dover Publications, 1991. New York: McGraw-Hill, 1980 (see pages 7, 144).

[BZ94] Umberto Balucani and Marco Zoppi. **Dynamics of the Liquid State**. Oxford Graduate Texts. Oxford, UK: Oxford University Press, 1994 (see pages 7, 9–11).

[Cav09] Andrea Cavagna. **Supercooled liquids for pedestrians**. *Physics Reports* 476:4-6 (2009), 51–124 (see pages 1, 5, 11).

[CCM12] Y. Chushkin, C. Caronna, and A. Madsen. **A novel event correlation scheme for X-ray photon correlation spectroscopy**. *Journal of Applied Crystallography* 45:4 (2012), 807–813. DOI: 10.1107/S0021889812023321. eprint: https://onlinelibrary.wiley.com/doi/pdf/10.1107/S0021889812023321. URL: https://onlinelibrary.wiley.com/doi/abs/10.1107/S0021889812023321 (see pages 49, 51).

[Chu+25] Yuriy Chushkin, Jonathan Correa, Alexandr Ignatenko, David Pennicard, Sabine Lange, Sergei Fridman, Sebastian Karl, Björn Senfftleben, Felix Lehmkühler, Fabian Westermeier, Heinz Graafsma, and Marco Cammarata. **Achieving nanosecond time resolution with a two-dimensional X-ray detector**. *Journal of Synchrotron Radiation* 32:5 (Sept. 2025), 1220–1227. DOI:

10.1107/S1600577525006599. URL: https://doi.org/10.1107/S1600577525006599 (see page 48).

[Chu20] Yuri Chushkin. **Deciphering the intrinsic dynamics from the beam-induced atomic motions in oxide glasses**. *Journal of Synchrotron Radiation* 27 (2020), 1247–1252. DOI: 10.1107/S1600577520008977 (see page 100).

[Cip+02] Luca Cipelletti, H Bissig, V Trappe, P Ballesta, and S Mazoyer. **Time-resolved correlation: a new tool for studying temporally heterogeneous dynamics**. *Journal of Physics: Condensed Matter* 15:1 (Dec. 2002), S257. DOI: 10.1088/0953-8984/15/1/334. URL: https://dx.doi.org/10.1088/0953-8984/15/1/334 (see pages 50, 51).

[Cor+24] Antoine Cornet, Alberto Ronca, Jie Shen, Federico Zontone, Yuriy Chushkin, Marco Cammarata, Gaston Garbarino, Michael Sprung, Fabian Westermeier, Thierry Deschamps, and Beatrice Ruta. **High-pressure X-ray photon correlation spectroscopy at fourth-generation synchrotron sources**. *Journal of Synchrotron Radiation* 31:3 (May 2024), 527–539. DOI: 10.1107/S1600577524001784. URL: https://doi.org/10.1107/S1600577524001784 (see pages 46, 48).

[CR14] Patrick Charbonneau and David R Reichman. **Dynamical heterogeneity and nonlinear susceptibility in supercooled liquids**. *Physical Review Letters* (2014) (see page 16).

[CR83] J. J. Curro and Ryong-Joon Roe. **Small-angle x-ray scattering study of density fluctuation in pressure-densified polystyrene glasses**. *Journal of Polymer Science: Polymer Physics Edition* 21:9 (1983), 1785–1796. DOI: 10.1002/pol.1983.180210914. eprint: https://onlinelibrary.wiley.com/doi/pdf/10.1002/pol.1983.180210914. URL: https://onlinelibrary.wiley.com/doi/abs/10.1002/pol.1983.180210914 (see pages 16–18).

[Cun16] Alessandro Cunsolo. "Using X-ray as a Probe of the Terahertz Dynamics of Disordered Systems – Complementarity with Inelastic Neutron Scattering and Future Perspectivess." In: *Neutron Scattering*. Ed. by Waldemar Alfredo Monteiro. London: IntechOpen, 2016. Chap. 1. DOI: 10.5772/62844. URL: https://doi.org/10.5772/62844 (see pages 29–31, 33, 144).

[CW99] Luca Cipelletti and D. A. Weitz. **Ultralow-angle dynamic light scattering with a charge coupled device camera based multispeckle, multitau correlator**. *Review of Scientific Instruments* 70:8 (Aug. 1999), 3214–3221. ISSN: 0034-6748. DOI: 10.1063/1.1149894. eprint: https://pubs.aip.org/aip/rsi/article-pdf/70/8/3214/19259265/3214_1_online.pdf. URL: https://doi.org/10.1063/1.1149894 (see pages 50–54).

[CZN24] William Chèvremont, Thomas Zinn, and Theyencheri Narayanan. **Improvement of ultra-small-angle XPCS with the Extremely Brilliant Source**. *Journal of Synchrotron Radiation* 31:1 (Jan. 2024), 65–76. DOI: 10.1107/S1600577523008627. URL: https://doi.org/10.1107/S1600577523008627 (see page 54).

[Dal+19] F. Dallari, G. Pintori, G. Baldi, A. Martinelli, B. Ruta, M. Sprung, and G. Monaco. **X-rays induced atomic dynamics in a lithium-borate glass**. *Condensed Matter Physics* 22:4 (2019), 43606. DOI: 10.5488/CMP.22.43606 (see pages 101, 118).

[De 59] Pierre-Gilles De Gennes. **Liquid dynamics and inelastic scattering of neutrons**. *Physica* 25:7-12 (1959), 825–839 (see page 15).

[DEC25] DECTRIS AG. *DECTRIS EIGER 4M / EIGER2 X 4M Detector Technical Documentation*. https://www.dectris.com/support/manuals-docs/eiger-x-for-synchrotron/eiger-x-4m/. DECTRIS AG. Baden-Daettwil, Switzerland, 2025 (see pages 48, 67).

[Deu26] Deutsches Elektronen-Synchrotron (DESY). *Coherence Beamline P10: Coherence Applications — PETRA III*. https://photon-science.desy.de/facilities/petra_iii/beamlines/p10_coherence_applications/index_eng.html. Accessed: 2026-03-18. 2026 (see pages 45, 46).

[Dev94] R.A.B. Devine. **Macroscopic and microscopic effects of radiation in amorphous SiO2**. *Nuclear Instruments and Methods in Physics Research Section B: Beam Interactions with Materials and Atoms* 91:1 (1994), 378–390. ISSN: 0168-583X. DOI: 10.1016/0168-583X(94)96253-7. URL: https://www.sciencedirect.com/science/article/pii/0168583X94962537 (see page 94).

[Die+95] S. B. Dierker, R. Pindak, R. M. Fleming, I. K. Robinson, and L. Berman. **X-Ray Photon Correlation Spectroscopy Study of Brownian Motion of Gold Colloids in Glycerol**. *Phys. Rev. Lett.* 75 (3 July 1995), 449–452. DOI: 10.1103/PhysRevLett.75.449. URL: https://link.aps.org/doi/10.1103/PhysRevLett.75.449 (see page 50).

[Din+11] R. Dinapoli, A. Bergamaschi, B. Henrich, R. Horisberger, I. Johnson, A. Mozzanica, B. Schmitt, X. Shi, and G. Theidel. **EIGER: Next generation single photon counting detector for X-ray applications**. *Nuclear Instruments and Methods in Physics Research Section A* 650 (2011), 79–83. DOI: 10.1016/j.nima.2010.12.005 (see page 36).

[DS01] Pablo G Debenedetti and Frank H Stillinger. **Supercooled liquids and the glass transition**. *Nature* 410:6825 (2001), 259–267 (see pages 1, 2, 5).

[Dur+05] Agnès Duri, Hugo Bissig, Véronique Trappe, and Luca Cipelletti. **Time-resolved-correlation measurements of temporally heterogeneous dynamics**. *Phys. Rev. E* 72 (5 Nov. 2005), 051401. DOI: 10.1103/PhysRevE.72.051401. URL: https://link.aps.org/doi/10.1103/PhysRevE.72.051401 (see pages 15, 45, 51, 52).

[DWS88] J. A. Erwin Desa, Adrian C. Wright, and Roger N. Sinclair. **A neutron diffraction investigation of the structure of vitreous germania**. *Journal of Non-Crystalline Solids* 99:2-3 (1988), 276–288. DOI: 10.1016/0022-3093(88)90024-3 (see page 23).

[EH12] Mark D Ediger and Peter Harrowell. **Perspective: Supercooled liquids and glasses**. *The Journal of chemical physics* 137:8 (2012), 080901 (see pages 1, 3, 11, 15).

[Ell91] Stephen R. Elliott. **Origin of the first sharp diffraction peak in the structure factor of covalent glasses.** *Physical review letters* 67 6 (1991), 711–714. URL: https://api.semanticscholar.org/CorpusID:36502836 (see pages 11, 35).

[Eur15] European Synchrotron Radiation Facility. *ID28 Beamline User Manual*. Accessed: 2026-03-14. Grenoble, France, 2015. URL: https://www.esrf.fr/UsersAndScience/Experiments/DynExtrCond/ID28/UserManual (see page 33).

[Fac25] European Synchrotron Radiation Facility. *ID10 - Soft interfaces and coherent scattering beamline*. Accessed: 2025-09-03. 2025. URL: https://www.esrf.fr/UsersAndScience/Experiments/CBS/ID10/ID10EH2 (see pages 45, 46, 67).

[Fav+17] V. Favre-Nicolin, Y. Chushkin, P. Cloetens, J. C. da Silva, S. Leake, B. Ruta, and F. Zontone. **Dynamics and Imaging Using Coherent X-rays at the European Synchrotron**. *Synchrotron Radiation News* 30:5 (2017), 13–18. DOI: 10.1080/08940886.2017.1364528. eprint: https://doi.org/10.1080/08940886.2017.1364528. URL: https://doi.org/10.1080/08940886.2017.1364528 (see page 48).

[FG79] E. J. Friebele and D. L. Griscom. "Radiation Effects in Glasses." In: *Treatise on Materials Science and Technology, Vol. 17*. Ed. by M. Tomozawa and R. H. Doremus. Chapter on radiation effects in silicate glasses. New York: Academic Press, 1979, 257–351. ISBN: 9780123418012 (see pages 82, 83, 87–89).

[FLM06] P. Falus, L. B. Lurio, and S. G. J. Mochrie. **Optimizing the signal-to-noise ratio for X-ray photon correlation spectroscopy**. *Journal of Synchrotron Radiation* 13:3 (May 2006), 253–259. DOI: 10.1107/S0909049506006789. URL: https://doi.org/10.1107/S0909049506006789 (see page 47).

[GMR08] G. Grübel, A. Madsen, and A. Robert, 953–995. In: *Soft Matter Characterization*. Ed. by Redouane Borsali and Robert Pecora. Dordrecht: Springer Netherlands, 2008. ISBN: 978-1-4020-4465-6. DOI: 10.1007/978-1-4020-4465-6_18. URL: https://doi.org/10.1007/978-1-4020-4465-6_18 (see pages 40, 42, 44).

[GNO71] G F J Garlick, J E Nicholls, and A M Ozer. **Electron spin resonance of electron irradiated germanium dioxide**. *Journal of Physics C: Solid State Physics* 4:14 (Oct. 1971), 2230. DOI: 10.1088/0022-3719/4/14/037. URL: https://doi.org/10.1088/0022-3719/4/14/037 (see page 89).

[Gol69] Martin Goldstein. **Viscous liquids and the glass transition: a potential energy barrier picture**. *The Journal of Chemical Physics* 51:9 (1969), 3728–3739 (see pages 5, 13).

[Goo84] J. W. Goodman. "Statistical Properties of Laser Speckle Patterns." In: *Laser Speckle and Related Phenomena*. Ed. by J. C. Dainty. Vol. 9. Topics in Applied Physics. Berlin: Springer-Verlag, 1984, 9–74 (see page 42).

[Göt09] Wolfgang Götze. **Complex dynamics of glass-forming liquids: A mode-coupling theory**. Vol. 143. Oxford University Press, USA, 2009 (see pages 2, 7).

[Gri11] David L. Griscom. **Trapped-Electron Centers in Pure and Doped Glassy Silica: A Review and Synthesis**. *Journal of Non-Crystalline Solids* 357:8 (2011). SiO_2, Advanced Dielectrics and Related Devices, 1945–1962. ISSN: 0022-3093. DOI: 10.1016/j.jnoncrysol.2010.11.011. URL: https://www.sciencedirect.com/science/article/pii/S0022309310008574 (see pages 86–90, 93).

[Gri85] David L. Griscom. **Nature of Defects and Defect Generation in Optical Glasses**. In: *Radiation Effects on Optical Materials*. Ed. by Paul W. Levy. Vol. 541. International Society for Optics and Photonics. SPIE, 1985, 38–59. DOI: 10.1117/12.975358. URL: https://doi.org/10.1117/12.975358 (see pages 79, 82–91, 93, 101).

[Gro22] Particle Data Group. **Review of Particle Physics**. *Prog. Theor. Exp. Phys.* (2022) (see page 74).

[Har+20] Charles R. Harris, K. Jarrod Millman, Stéfan J. van der Walt, Ralf Gommers, Pauli Virtanen, David Cournapeau, Eric Wieser, Julian Taylor, Sebastian Berg, Nathaniel J. Smith, et al. **Array programming with NumPy**. *Nature* 585:7825 (2020), 357–362 (see page 59).

[HM86] Jean-Pierre Hansen and Ian R. McDonald. **Theory of Simple Liquids**. 2nd. London: Academic Press, 1986 (see pages 8, 9, 11, 16).

[Hol] Bastian Holst. *Undulator radiation schematic*. https://commons.wikimedia.org/w/index.php?curid=37443811. CC BY-SA 3.0 (see page 41).

[Hua+13] P. Y. Huang, S. Kurasch, J. S. Alden, A. Shekhawat, A. A. Alemi, P. L. McEuen, J. P. Sethna, U. Kaiser, and D. A. Muller. **Imaging Atomic Rearrangements in Two-Dimensional Silica Glass: Watching Silica's Dance**. *Science* 342:6155 (2013), 224–227. DOI: 10.1126/science.1242248 (see page 98).

[Int23] Intel Corporation. *Intel® Math Kernel Library*. https://www.intel.com/content/www/us/en/developer/tools/oneapi/onemkl.html. 2023 (see page 59).

[Jae+16] Eberhard J. Jaeschke, Shaukat Khan, Jochen R. Schneider, and Jerome B. Hastings, eds. **Synchrotron Light Sources and Free-Electron Lasers: Accelerator Physics, Instrumentation and Science Applications**. Cham: Springer International Publishing, 2016. ISBN: 978-3-319-04507-8. DOI: 10.1007/978-3-319-04507-8 (see pages 38, 40).

[Jan18] Liesbeth M. C. Janssen. **Mode-coupling theory of the glass transition: A primer**. *Frontiers in Physics* 6 (2018), 97. DOI: 10.3389/fphy.2018.00097 (see pages 13, 14).

[JB25] Stuart D. Jackson and John Ballato. **Defect Centers in the Silicate Glasses: Basics, Implications, and Mitigation Strategies for the Generation of Visible Light**. *Laser & Photonics Reviews* 19:22 (2025), e00872. DOI: 10.1002/lpor.202500872. eprint: https://onlinelibrary.wiley.com/doi/pdf/10.1002/lpor.202500872. URL: https://onlinelibrary.wiley.com/doi/abs/10.1002/lpor.202500872 (see page 88).

[JG70] G. P. Johari and M. Goldstein. **Viscous liquids and the glass transition. II. Secondary relaxations in glasses of rigid molecules**. *The Journal of Chemical Physics* 53:6 (1970), 2372–2388. DOI: 10.1063/1.1674337 (see page 12).

[JGP90] Jacques G. H. Joosten, Erik T. F. Geladé, and Peter N. Pusey. **Dynamic light scattering by nonergodic media: Brownian particles trapped in polyacrylamide gels**. *Phys. Rev. A* 42 (4 Aug. 1990), 2161–2175. DOI: 10.1103/PhysRevA.42.2161. URL: https://link.aps.org/doi/10.1103/PhysRevA.42.2161 (see page 51).

[Jia+23] Z. Jiang, J. W. Strzalka, J. Wang, Q. Zhang, and E. M. Dufresne. *Beamline 8-ID-E Information*. https://www.aps.anl.gov/Beamlines/Directory/Details?beamline_id=243. Accessed: 2025-09-02. 2023 (see page 48).

[Jo+21] W. Jo, F. Westermeier, R. Rysov, O. Leupold, F. Schulz, S. Tober, V. Markmann, M. Sprung, A. Ricci, T. Laurus, A. Aschkan, A. Klyuev, U. Trunk, H. Graafsma, G. Grübel, and W. Roseker. **Nanosecond X-ray photon correlation spectroscopy using pulse time structure of a storage-ring source**. *IUCrJ* 8:1 (2021), 124–130. DOI: 10.1107/S2052252520015778. URL: https://doi.org/10.1107/S2052252520015778 (see page 48).

[Jor78] J. D. Jorgensen. **Compression mechanisms in α-quartz structures—SiO_2 and GeO_2**. *Journal of Applied Physics* 49:11 (1978), 5473–5478. DOI: 10.1063/1.324472 (see page 22).

[Kam+86] Kanichi Kamiya, S. Sakka, Y. H. Lee, and K. Matusita. **X-ray diffraction study of Na_2O-GeO_2 melts**. *Journal of Non-Crystalline Solids* 79:3 (1986), 285–294. DOI: 10.1016/0022-3093(86)90058-4 (see page 23).

[KB00] Willem K Kegel and Alfons van Blaaderen. **Direct observation of dynamical heterogeneities in colloidal hard-sphere suspensions**. *Science* 287:5451 (2000), 290–293 (see page 15).

[Kil95] Nicholas K. Kildahl. **Bond Energy Data Summarized**. *Journal of Chemical Education* 72:5 (1995), 423. DOI: 10.1021/ed072p423 (see page 84).

[Kir+96] S. Kirsch, V. Frenz, W. Schärtl, E. Bartsch, and H. Sillescu. **Multispeckle autocorrelation spectroscopy and its application to the investigation of ultraslow dynamical processes**. *The Journal of Chemical Physics* 104:4 (Jan. 1996), 1758–1761. ISSN: 0021-9606. DOI: 10.1063/1.470761. eprint: https://pubs.aip.org/aip/jcp/article-pdf/104/4/1758/19179358/1758_1_online.pdf. URL: https://doi.org/10.1063/1.470761 (see page 50).

[Kit05] Charles Kittel. **Introduction to Solid State Physics**. 8th ed. New York: John Wiley & Sons, 2005. ISBN: 978-0-471-41526-8 (see pages 80, 81).

[Kra+09] P. Kraft, A. Bergamaschi, Ch. Broennimann, R. Dinapoli, E. F. Eikenberry, B. Henrich, I. Johnson, A. Mozzanica, C. M. Schlepütz, P. R. Willmott, and B. Schmitt. **Performance of single-photon-counting PILATUS detector modules**. *Journal of Synchrotron Radiation* 16:3 (May 2009), 368–375. DOI: 10.1107/S0909049509009911. URL: https://doi.org/10.1107/S0909049509009911 (see page 36).

[Kri+17] N. M. Anoop Krishnan, Bu Wang, Yingtian Yu, Yann Le Pape, Gaurav Sant, and Mathieu Bauchy. **Enthalpy Landscape Dictates the Irradiation-Induced Disordering of Quartz**. *Phys. Rev. X* 7 (3 July 2017), 031019. DOI: 10.1103/PhysRevX.7.031019. URL: https://link.aps.org/doi/10.1103/PhysRevX.7.031019 (see pages 7, 94, 153).

[LAB+73] N. L. LABERGE, V. V. VASILESCU, C. J. MONTROSE, and P. B. MACEDO. **Equilibrium Compressibilities and Density Fluctuations in K2O–SiO2 Glasses**. *Journal of the American Ceramic Society* 56:10 (1973), 506–509. DOI: 10.1111/j.1151-2916.1973.tb12398.x. eprint: https://ceramics.onlinelibrary.wiley.com/doi/pdf/10.1111/j.1151-2916.1973.tb12398.x. URL: https://ceramics.onlinelibrary.wiley.com/doi/abs/10.1111/j.1151-2916.1973.tb12398.x (see pages 17–19).

[Lev+05] C. Levelut, A Faivre, R. Le Parc, B. Champagnon, J.-L. Hazemann, and J.-P. Simon. **In situ measurements of density fluctuations and compressibility in silica glasses as a function of temperature and thermal history**. *Phys. Rev. B* 72 (22 Dec. 2005), 224201. DOI: 10.1103/PhysRevB.72.224201. URL:

https://link.aps.org/doi/10.1103/PhysRevB.72.224201 (see pages 17, 19, 20, 142, 143).

[Lev+07] Claire Levelut, Rozenn Le Parc, Annelise Faivre, Ralf Brüning, Bernard Champagnon, Valérie Martinez, Jean-Paul Simon, Françoise Bley, and Jean-Louis Hazemann. **Density fluctuations in oxide glasses investigated by small-angle X-ray scattering**. *Journal of Applied Crystallography* 40:s1 (Apr. 2007), s512–s516. DOI: 10.1107/S0021889807000507. URL: https://doi.org/10.1107/S0021889807000507 (see pages 19, 142).

[Lum+00] D. Lumma, L. B. Lurio, S. G. J. Mochrie, and M. Sutton. **Area detector based photon correlation in the regime of short data batches: Data reduction for dynamic x-ray scattering**. *Review of Scientific Instruments* 71:9 (Sept. 2000), 3274–3289. ISSN: 0034-6748. DOI: 10.1063/1.1287637. eprint: https://pubs.aip.org/aip/rsi/article-pdf/71/9/3274/19283442/3274_1_online.pdf. URL: https://doi.org/10.1063/1.1287637 (see pages 48, 50, 51).

[Luo+11] Wenyun Luo, Zhongyin Xiao, Jianxiang Wen, Jianchong Yin, Zhenyi Chen, Zihua Wang, and Tingyun Wang. **Defect center characteristics of silica optical fiber material by gamma ray radiation**. In: *2011 Asia Communications and Photonics Conference and Exhibition (ACP)*. 2011, 1–6. DOI: 10.1117/12.905302 (see page 89).

[Mar+23] A. Martinelli, F. Caporaletti, F. Dallari, M. Sprung, F. Westermeier, G. Baldi, and G. Monaco. **Reaching the Yield Point of a Glass During X-Ray Irradiation**. *Physical Review X* 13 (2023), 041031. DOI: 10.1103/PhysRevX.13.041031 (see pages 61, 101, 102, 113, 115).

[Mar21] Alessandro Martinelli. **Density Relaxations Across the Glass Transition Under Equilibrium and Non-Equilibrium Conditions**. PhD thesis. Trento, Italy: Università degli Studi di Trento, Apr. 2021 (see page 46).

[Mas+04] C Masciovecchio, G Baldi, S Caponi, L Comez, S Di Fonzo, D Fioretto, A Fontana, A Gessini, SC Santucci, and F Sette. **Structural relaxation in liquid water by inelastic UV scattering**. *Physical Review Letters* 92:25 (2004), 255507 (see page 3).

[MCH06] Matthieu Micoulaut, Laurent Cormier, and G. S. Henderson. **The structure of amorphous, crystalline and liquid GeO_2**. *Journal of Physics: Condensed Matter* 18:45 (2006), R753–R784. DOI: 10.1088/0953-8984/18/45/R01 (see page 22).

[MFR16] A. Madsen, A. Fluerasu, and B. Ruta. "X-ray Photon Correlation Spectroscopy." In: *Synchrotron Light Sources and Free-Electron Lasers: Accelerator Physics, Instrumentation and Science Applications*. Ed. by E. J. Jaeschke, S. Khan, J. R. Schneider, and J. B. Hastings. Cham: Springer International Publishing, 2016,

1617–1641. DOI: 10.1007/978-3-319-14394-1_48. URL: https://doi.org/10.1007/978-3-319-14394-1_48 (see page 47).

[MGL07] John C Mauro, Prabhat K Gupta, and Roger J Loucks. **Continuously broken ergodicity**. *The Journal of chemical physics* 126:18 (2007) (see page 3).

[MKG59] J. W. MacKay, E. E. Klontz, and G. W. Gobeli. **Thermal and Radiation Annealing of Ge**. *Phys. Rev. Lett.* 2 (4 Feb. 1959), 146–148. DOI: 10.1103/PhysRevLett.2.146. URL: https://link.aps.org/doi/10.1103/PhysRevLett.2.146 (see page 93).

[Nat15] National Institute of Standards and Technology (NIST). *Standard Reference Material 660c: Line Position and Line Shape Standard for Powder Diffraction (Lanthanum Hexaboride Powder)*. Certificate. 2015. URL: https://tsapps.nist.gov/srmext/certificates/660c.pdf (see page 36).

[Nga11] K. L. Ngai. **Relaxation and Diffusion in Complex Systems**. 1st ed. New York, NY: Springer, 2011 (see page 13).

[NL96] Jörg Neuefeind and K.-D. Liss. **Bond angle distribution in amorphous germania and silica**. *Berichte der Bunsengesellschaft für physikalische Chemie* 100:8 (1996), 1341–1349. DOI: 10.1002/bbpc.19961000819 (see page 23).

[NM68] A. Napolitano and P. B. Macedo. **Spectrum of Relaxation Times in GeO_2 Glass**. *Journal of Research of the National Bureau of Standards Section A: Physics and Chemistry* 72A:4 (1968), 425–433. DOI: 10.6028/jres.072A.034 (see page 127).

[OGP21] Nadège Ollier, Sylvain Girard, and Sylvain Peuget. **3.13**, 405–414. In: *Encyclopedia of Glass Science, Technology, History, and Culture*. John Wiley & Sons, Ltd, 2021. ISBN: 9781118801017. DOI: 10.1002/9781118801017.ch3.13. eprint: https://onlinelibrary.wiley.com/doi/pdf/10.1002/9781118801017.ch3.13. URL: https://onlinelibrary.wiley.com/doi/abs/10.1002/9781118801017.ch3.13 (see pages 83, 88, 90, 92, 94, 96, 97).

[Pec85] Robert Pecora, ed. **Dynamic Light Scattering. Applications of Photon Correlation Spectroscopy**. New York: Plenum Press, 1985, XIV+420. ISBN: 978-0-306-41790-0. DOI: 10.1007/978-1-4613-2389-1 (see pages 37, 38, 43, 44, 48).

[Per+17] Fivos Perakis, Katrin Amann-Winkel, Felix Lehmkühler, Michael Sprung, Daniel Mariedahl, Jonas A. Sellberg, Harshad Pathak, Alexander Späh, Filippo Cavalca, Daniel Schlesinger, Alessandro Ricci, Avni Jain, Bernhard Massani, Flora Aubree, Chris J. Benmore, Thomas Loerting, Gerhard Grübel, Lars G. M. Pettersson, and Anders Nilsson. **Diffusive dynamics during the high-to-low density transition in amorphous ice**. *Proceedings of the National Academy of Sciences* 114:31 (2017), 8193–8198. DOI: 10.1073/pnas.1705303114.

eprint: https://www.pnas.org/doi/pdf/10.1073/pnas.1705303114. URL: https://www.pnas.org/doi/abs/10.1073/pnas.1705303114 (see page 54).

[PG72] G.E. Palma and R.M. Gagosz. **Optical absorption in fused silica during irradiation: Radiation annealing of the C-BAND**. *Journal of Physics and Chemistry of Solids* 33:1 (1972), 177–189. ISSN: 0022-3697. DOI: 10.1016/S0022-3697(72)80065-9. URL: https://www.sciencedirect.com/science/article/pii/S0022369772800659 (see pages 92, 93).

[PH23] Charlotte F. Petersen and Peter Harrowell. **Direct measurement of the structural change associated with amorphous solidification using static scattering of coherent radiation**. *The Journal of Chemical Physics* 159:24 (Dec. 2023), 244506. ISSN: 0021-9606. DOI: 10.1063/5.0177251. eprint: https://pubs.aip.org/aip/jcp/article-pdf/doi/10.1063/5.0177251/18280168/244506_1_5.0177251.pdf. URL: https://doi.org/10.1063/5.0177251 (see page 38).

[Phi81] William Andrew Phillips. **Amorphous solids: low-temperature properties**. Springer Berlin, 1981 (see page 4).

[Pin+19] G. Pintori, G. Baldi, B. Ruta, and G. Monaco. **Relaxation dynamics induced in glasses by absorption of hard x-ray photons**. *Physical Review B* 99 (2019), 224206. DOI: 10.1103/PhysRevB.99.224206 (see pages 99–101).

[Pin+22] G. Pintori, G. Baldi, F. Dallari, A. Martinelli, M. Sprung, and G. Monaco. **X-ray induced dynamics in borate glasses with different network connectivity**. *Physical Review B* 105 (2022), 104207. DOI: 10.1103/PhysRevB.105.104207 (see page 101).

[PJR15] Tomás Pérez-Castañeda, Rafael J Jiménez-Riobóo, and Miguel Angel Ramos. **Do two-level systems and boson peak persist or vanish in hyperaged geological glasses of amber?** *Philosophical Magazine* 96:7-9 (2015), 774–787. DOI: 10.1080/14786435.2015.1118683 (see page 6).

[PK68] William Primak and Robert Kampwirth. **The Radiation Compaction of Vitreous Silica**. *Journal of Applied Physics* 39:12 (Nov. 1968), 5651–5658. ISSN: 0021-8979. DOI: 10.1063/1.1656029. URL: https://doi.org/10.1063/1.1656029 (see pages 85, 96, 118, 119).

[POH00] Fan Piao, William G. Oldham, and Eugene E. Haller. **The Mechanism of Radiation-Induced Compaction in Vitreous Silica**. *Journal of Non-Crystalline Solids* 276:1 (2000), 61–71. ISSN: 0022-3093. DOI: 10.1016/S0022-3093(00)00263-5. URL: https://www.sciencedirect.com/science/article/pii/S0022309300002635 (see page 94).

[Pri+64] William Primak, Edward Edwards, David Keiffer, and Herman Szymanski. **Ionization Expansion of Compacted Silica and the Theory of Radiation-Induced Dilatations in Vitreous Silica**. *Phys. Rev.* 133 (2A Jan. 1964), A531–A535. DOI: 10.1103/PhysRev.133.A531. URL: https://link.aps.org/doi/10.1103/PhysRev.133.A531 (see pages 96, 118, 119).

[Pri78] William Primak. **Dependence of the compaction of vitreous silica on the ionization dose**. *Journal of Applied Physics* 49:4 (Apr. 1978), 2572–2572. ISSN: 0021-8979. DOI: 10.1063/1.325069. eprint: https://pubs.aip.org/aip/jap/article-pdf/49/4/2572/18379840/2572_1_online.pdf. URL: https://doi.org/10.1063/1.325069 (see pages 118, 119).

[RB25] Ernst A. Rössler and Manuel Becher. **Relaxation spectra of molecular glass formers probed by tandem Fabry–Perot interferometry and photon correlation spectroscopy: A critical re-assessment**. *The Journal of Chemical Physics* 163:5 (Aug. 2025), 054510. ISSN: 0021-9606. DOI: 10.1063/5.0273910. eprint: https://pubs.aip.org/aip/jcp/article-pdf/doi/10.1063/5.0273910/20630765/054510_1_5.0273910.pdf. URL: https://doi.org/10.1063/5.0273910 (see page 65).

[RBB+23] P. Raimondi, C. Benabderrahmane, P. Berkvens, et al. **The Extremely Brilliant Source storage ring of the European Synchrotron Radiation Facility**. *Communications Physics* 6 (2023), 82. DOI: 10.1038/s42005-023-01195-z. URL: https://doi.org/10.1038/s42005-023-01195-z (see page 48).

[Roe83] Ryong-Joon Roe. **Density fluctuation in a "Theorist's ideal glass"**. *The Journal of Chemical Physics* 79:2 (July 1983), 936–938. ISSN: 0021-9606. DOI: 10.1063/1.445870. eprint: https://pubs.aip.org/aip/jcp/article-pdf/79/2/936/18942711/936_1_online.pdf. URL: https://doi.org/10.1063/1.445870 (see pages 17, 18).

[Rut+12] Beatrice Ruta, Yuriy Chushkin, Giulio Monaco, Luca Cipelletti, Eloi Pineda, Pere Bruna, Valentina M Giordano, and Marta Gonzalez-Silveira. **Atomic-scale relaxation dynamics and aging in a metallic glass probed by x-ray photon correlation spectroscopy**. *Physical review letters* 109:16 (2012), 165701 (see page 3).

[Rut+13] B. Ruta, G. Baldi, G. Monaco, and Y. Chushkin. **Compressed correlation functions and fast aging dynamics in metallic glasses**. *The Journal of Chemical Physics* 138:5 (Feb. 2013), 054508. ISSN: 0021-9606. DOI: 10.1063/1.4790131. eprint: https://pubs.aip.org/aip/jcp/article-pdf/oi/10.1063/1.4790131/13310160/054508_1_online.pdf. URL: https://doi.org/10.1063/1.4790131 (see page 49).

[Rut+14] B. Ruta, G. Baldi, Y. Chushkin, B. Rufflé, L. Cristofolini, A. Fontana, M. Zanatta, and F. Nazzani. **Revealing the fast atomic motion of network glasses**. *Nature Communications* 5 (2014), 3939. DOI: 10.1038/ncomms4939 (see page 98).

[Rut+17] B. Ruta, F. Zontone, Y. Chushkin, G. Baldi, G. Pintori, G. Monaco, B. Rufflé, and W. Kob. **Hard X-rays as pump and probe of atomic motion in oxide glasses**. *Scientific Reports* 7 (2017), 3962. DOI: 10.1038/s41598-017-04271-x (see pages 61, 98, 100, 101, 117, 157).

[Sal+07] Philip S Salmon, Adrian C Barnes, Richard A Martin, and Gabriel J Cuello. **Structure of glassy GeO2**. *Journal of Physics: Condensed Matter* 19:41 (Sept. 2007), 415110. DOI: 10.1088/0953-8984/19/41/415110. URL: https://doi.org/10.1088/0953-8984/19/41/415110 (see pages 11, 119).

[Sch83] K. Schätzel. **Noise in Photon Correlation and Photon Structure Functions**. *Optica Acta: International Journal of Optics* 30:2 (1983), 155–166. DOI: 10.1080/713821145. eprint: https://doi.org/10.1080/713821145. URL: https://doi.org/10.1080/713821145 (see page 52).

[Sch87] K. Schätzel. **Correlation techniques in dynamic light scattering**. *Applied Physics B* 42:4 (1987), 193–213. ISSN: 1432-0649. DOI: 10.1007/BF00693937. URL: https://doi.org/10.1007/BF00693937 (see page 50).

[Sci05] Francesco Sciortino. **Potential energy landscape description of supercooled liquids and glasses**. *Journal of Statistical Mechanics: Theory and Experiment* 2005:05 (2005), P05015 (see pages 5, 6).

[Sco+03] Tullio Scopigno, Giancarlo Ruocco, Francesco Sette, and Giulio Monaco. **Is the fragility of a liquid embedded in the properties of its glass?** *Science* 302:5646 (2003), 849–852. DOI: 10.1126/science.1089446 (see pages 13, 21, 145, 155).

[Shp14] Oleg G. Shpyrko. **X-ray photon correlation spectroscopy**. *Journal of Synchrotron Radiation* 21:5 (2014), 1057–1064. DOI: 10.1107/S1600577514018232. eprint: https://onlinelibrary.wiley.com/doi/pdf/10.1107/S1600577514018232. URL: https://onlinelibrary.wiley.com/doi/abs/10.1107/S1600577514018232 (see page 47).

[SI64] G. S. T. Smith and Patricia B. Isaacs. **The crystal structure of quartz-like GeO_2**. *Acta Crystallographica* 17:7 (1964), 842–846. DOI: 10.1107/S0365110X64002143 (see page 22).

[Sid23] D. L. Sidebottom. **Generic α relaxation in a strong GeO_2 glass melt**. *Phys. Rev. E* 107 (1 Jan. 2023), L012602. DOI: 10.1103/PhysRevE.107.L012602. URL: https://link.aps.org/doi/10.1103/PhysRevE.107.L012602 (see pages 14, 124).

[SN04] Alexei P. Sokolov and Vladimir N. Novikov. **Fast relaxation in disordered systems: From a double well to a cage**. *Philosophical Magazine* 84:13–16 (2004), 1355–1360. DOI: 10.1080/14786430410001669305 (see page 12).

[Spr+23] M. Sprung, F. Westermeier, D. Weschke, R. Rysov, W. Roseker, and N. D. Anthuparambil. *P10 – Coherence Application Beamline*. https://photon-science.desy.de/facilities/petra_iii/beamlines/p10_coherence_applications/unified_data_sheet_p10/index_eng.html. Accessed: 2025-09-02. 2023 (see page 48).

[Squ78] Gordon Leslie Squires. **Introduction to the Theory of Thermal Neutron Scattering**. Reprinted with corrections, 1996 and 2012. Cambridge: Cambridge University Press, 1978 (see page 9).

[ST23] Jennifer Scott and Miroslav Tůma, 1–18. In: *Algorithms for Sparse Linear Systems*. Cham: Springer International Publishing, 2023. ISBN: 978-3-031-25820-6. DOI: 10.1007/978-3-031-25820-6_1. URL: https://doi.org/10.1007/978-3-031-25820-6_1 (see page 51).

[Ste18] Jessica Steinlechner. **Development of mirror coatings for gravitational-wave detectors**. *Philosophical Transactions of the Royal Society A: Mathematical, Physical and Engineering Sciences* 376:2120 (2018), 20170282 (see page 61).

[Sut+03] Mark Sutton, Khalid Laaziri, F. Livet, and F. Bley. **Using coherence to measure two-time correlation functions**. *Opt. Express* 11:19 (Sept. 2003), 2268–2277. DOI: 10.1364/OE.11.002268. URL: https://opg.optica.org/oe/abstract.cfm?URI=oe-11-19-2268 (see pages 50, 51).

[Sut08] Mark Sutton. **A review of X-ray intensity fluctuation spectroscopy**. *Comptes Rendus. Physique* 9:5–6 (2008), 657–667. DOI: 10.1016/j.crhy.2007.04.008. URL: https://comptes-rendus.academie-sciences.fr/physique/articles/10.1016/j.crhy.2007.04.008/ (see page 47).

[Too46] Arthur Q Tool. **Relation between inelastic deformability and thermal expansion of glass in its annealing range**. *Journal of the American Ceramic Society* 29:9 (1946), 240–253. DOI: 10.1111/j.1151-2916.1946.tb11592.x (see page 3).

[Tra+98] U Tracht, Manfred Wilhelm, Andreas Heuer, H Feng, K Schmidt-Rohr, and Hans Wolfgang Spiess. **Length scale of dynamic heterogeneities at the glass transition determined by multidimensional nuclear magnetic resonance**. *Physical Review Letters* 81:13 (1998), 2727 (see page 15).

[Van54] Léon Van Hove. **Correlations in space and time and Born approximation scattering in systems of interacting particles**. *Physical Review* 95:1 (July 1954), 249–262 (see page 8).

[Wee+00] Eric R Weeks, John C Crocker, Andrew C Levitt, Andrew Schofield, and David A Weitz. **Three-dimensional direct imaging of structural relaxation near the colloidal glass transition**. *Science* 287:5453 (2000), 627–631 (see page 16).

[WIE18] Bin Wu, Takuya Iwashita, and Takeshi Egami. **Atomic Dynamics in Simple Liquid: de Gennes Narrowing Revisited**. *Phys. Rev. Lett.* 120 (13 Mar. 2018), 135502. DOI: 10.1103/PhysRevLett.120.135502. URL: https://link.aps.org/doi/10.1103/PhysRevLett.120.135502 (see page 15).

[WP65] R. A. Weeks and T. Purcell. **Electron Spin Resonance and Optical Absorption in GeO2**. *The Journal of Chemical Physics* 43:2 (July 1965), 483–491. ISSN: 0021-9606. DOI: 10.1063/1.1696768. eprint: https://pubs.aip.org/aip/jcp/article-pdf/43/2/483/18839575/483_1_online.pdf. URL: https://doi.org/10.1063/1.1696768 (see page 89).

[WSI03] T. Watanabe, K. Saito, and A. J. Ikushima. **Fictive temperature dependence of density fluctuation in SiO2 glass**. *Journal of Applied Physics* 94:8 (Oct. 2003), 4824–4827. ISSN: 0021-8979. DOI: 10.1063/1.1608477. eprint: https://pubs.aip.org/aip/jap/article-pdf/94/8/4824/18704885/4824_1_online.pdf. URL: https://doi.org/10.1063/1.1608477 (see page 19).

[Zac44] William H. Zachariasen. **Theory of X-Ray Diffraction in Crystals**. New York: Dover Publications, 1944 (see page 31).

[Zha+16] Qingteng Zhang, Eric M. Dufresne, Pawel Grybos, Piotr Kmon, Piotr Maj, Suresh Narayanan, Grzegorz W. Deptuch, Robert Szczygiel, and Alec Sandy. **Submillisecond X-ray photon correlation spectroscopy from a pixel array detector with fast dual gating and no readout dead-time**. *Journal of Synchrotron Radiation* 23:3 (May 2016), 679–684. DOI: 10.1107/S1600577516005166. URL: https://doi.org/10.1107/S1600577516005166 (see page 48).

[Zha+17] Q. Zhang, D. Bahadur, E. M. Dufresne, P. Grybos, P. Kmon, R. L. Leheny, P. Maj, S. Narayanan, R. Szczygiel, S. Ramakrishnan, and A. Sandy. **Dynamic Scaling of Colloidal Gel Formation at Intermediate Concentrations**. *Physical Review Letters* 119:17 (2017), 178006. DOI: 10.1103/PhysRevLett.119.178006. URL: https://doi.org/10.1103/PhysRevLett.119.178006 (see page 48).

[Zha+18] Qingteng Zhang, Eric M. Dufresne, Suresh Narayanan, Piotr Maj, Anna Koziol, Robert Szczygiel, Pawel Grybos, Mark Sutton, and Alec R. Sandy. **Sub-microsecond-resolved multi-speckle X-ray photon correlation spectroscopy with a pixel array detector**. *Journal of Synchrotron Radiation* 25:5 (Sept. 2018), 1408–1416. DOI: 10.1107/S1600577518009074. URL: https://doi.org/10.1107/S1600577518009074 (see page 48).

[Zha+21] Qingteng Zhang, Eric M. Dufresne, Yasukazu Nakaye, Pete R. Jemian, Takuto Sakumura, Yasutaka Sakuma, Joseph D. Ferrara, Piotr Maj, Asra Hassan, Divya Bahadur, Subramanian Ramakrishnan, Faisal Khan, Sinisa Veseli, Alec R. Sandy, Nicholas Schwarz, and Suresh Narayanan. **20μs-resolved high-throughput X-ray photon correlation spectroscopy on a 500k pixel detector enabled by data-management workflow**. *Journal of Synchrotron Radiation* 28:1 (Jan. 2021), 259–265. DOI: 10.1107/S1600577520014319. URL: https://doi.org/10.1107/S1600577520014319 (see page 48).

[Zig24] Simone Ziglio. **Structural Evolution and Phase Transition in GeO_2: Glass Transition, Crystallization and Melting**. MA thesis. Università degli Studi di Padova, Dipartimento di Fisica, 2024 (see page 23).